Engineering Excited State Transport and Relaxation in Organic Semiconductors

A Dissertation
SUBMITTED TO THE FACULTY OF
UNIVERSITY OF MINNESOTA
BY

Deepesh Rai

IN PARTIAL FULFILLMENT OF THE REQUIREMENTS
FOR THE DEGREE OF
DOCTOR OF PHILOSOPHY

Russell J. Holmes, Advisor

May 2020

Acknowledgements

First, I would like to thank my advisor Professor Russell Holmes for his guidance and steadfast support during my entire journey as a Ph.D. at the University of Minnesota. His insightful questioning, technical acumen and the highest standards for research works have been an inspiration for me. I would like to thank all past and present members of Holmes research group, Matt, Yunlong, Tyler, Tom, Ian, Kyle, Tao, Catherine, John, Kaicheng, Nolan, and Robert, for engaging dialogue and friendship. I would especially like to acknowledge Matt for his help during my initial years.

I would like to thank those who contributed directly to the work presented in this dissertation, John, and Javier. I am very grateful to have been supported by National Science Foundation (NSF) Electronics, Photonics and Magnetic Devices under ECCS-1509121 and Solid-State and Materials Chemistry under DMR-1708177. I am also grateful to have been funded by Frank & Janis Bates Fellowship (2014-2015); Robert V. Mattern Fellowship (2014-2015) during my first year at the University of Minnesota.

Last but not the least, I need to thank my family and friends for their constant love and support. I would not have been able to get through this experience without their support.

Dedication

I dedicate this dissertation to my family and friends- Krishna, Navita Rai, Santosh Rai, Deepali Porwal, Deepak Porwal, Piyush Rai, Karteek Agarwal, Anasuya Devi Dasi, Gopika Devi Dasi, Purnendu Krishna Das

Abstract

Organic semiconductors are an important class of optoelectronic materials that are characterized by high degree of conjugation within the molecule. These are thin films of conjugated molecules in organic optoelectronic devices such as organic light-emitting devices (OLEDs) and organic photovoltaic cells (OPVs). In organic semiconductors, the excited state is characterized by a tightly bound electron-hole pair called an exciton. The migration and relaxation of the exciton strongly dictates material optical properties, as well as the subsequent design and operation of semiconductor devices. For example, OPVs rely on the efficient harvesting and dissociation of photogenerated excitons at heterointerfaces in the device layer stack. The transport of long-lived dark excitons is of special interest as they play an important role as energetic intermediates in OLEDs while also being a potential active material in OPVs. Despite this, their spatial migration is challenging to probe accurately. The focus of this thesis is on demonstrating new characterization techniques to track exciton migration as well as on engineering unique device architectures for enhancing energy transport in OPVs. This work has brought insight into the role of spin and molecular structure in impacting exciton diffusion using a novel sensitizer-based methodology to selectively excite and probe dark exciton transport. Furthermore, the normally diffusive aspect of energy transport is overcome by excitonic gates that required development of new experimental and modeling tools.

Table of Contents

List of Figures

using the phosphorescent sensitizer-based approach. C545T singlet excitons in a neat film emit at a peak wavelength λ=575 nm. The structure is pumped at a wavelength of λ=370 nm where the majority of excitons are generated in the injection layer of 4P-NPB. Excitons diffusing through C545T are harvested using a film of 45 wt.% PtTPTBP doped in mCP. (b) Experimental and simulated (line) transport efficiency as a function of transport layer thickness. An L_D of (12.2 $\pm$ 0.7) nm is extracted from KMC simulations. (c) Representative photoluminescence spectra for the architectures (4P-NPB/C545T (10 nm)/mCP and 4P-NPB/C545T (10 nm)/HATCN) used to probe the singlet diffusion length of C545T using thickness dependent photoluminescence quenching. (d) Photoluminescence ratio versus thickness for determination of singlet L_D of C545T. An L_D of (12.4 $\pm$ 0.8) nm is extracted by fitting experimental data using a 1D steady-state diffusion equation. 65

Figure 5.6 (a) Architectures used to extract the transport efficiency and triplet L_D for NPD as a function of thickness. The structure is pumped at a wavelength of λ=470 nm where the majority of excitons are generated in $Ir(ppy)_3$ injection layer. (b) Absorption coefficient (open symbols) and normalized photoluminescence (solid symbols) for the materials of interest. Spectra for PtOEP are collected for films of 15 wt.% PtOEP in TCTA. (c) Representative photoluminescence spectra for multilayer structures (15 wt.% PtOEP:TCTA/NPD (30 nm)/$Ir(ppy)_3$ and 15 wt.% PtOEP:TCTA/NPD (20 nm)/TCTA (10 nm)/$Ir(ppy)_3$) used to probe the triplet diffusion length of NPD using the phosphorescent sensitizer-based approach. (d) Experimental (symbols) and simulated (line) transport efficiency as a function of transport layer thickness. The η_T versus thickness is plotted for

List of Tables

List of Abbreviations

OPV ..... Organic Photovoltaic
OLED..... Organic Light Emitting Devices
LUMO.....Lowest Unoccupied Molecular Orbital
HOMO .....Highest Occupied Molecular Orbital
L_D ..... Exciton Diffusion Length
CT state.....Charge Transfer state
PL..... Photoluminescence
S_0 .....Singlet ground state
S_1 .....First excited singlet state
T_1.....First triplet excited state
η_T ..... Transport Efficiency
η_{EQE}..... External Quantum Efficiency
η_{IQE} .....Internal Quantum Efficiency
η_D .....Diffusion Efficiency
η_{CC} .....Charge Collection Efficiency
k.....Extinction Coefficient
KMC ..... kinetic Monte Carlo
τ .....mean exciton lifetime
D ..... Diffusion Coefficient
ρ.....Molecular Density
D-A..... Donor-Acceptor
PHJ ..... Planar Heterojunction
R_0..... Förster Radius
η_{PL}.....Photoluminescence Efficiency
η_{OC} .....Outcoupling Efficiency
n ..... refractive index

1 Applications of Organic Semiconductor Devices

Organic semiconductors are carbon based conjugated small molecules or polymers, offering a remarkable array of optical, mechanical and electronic properties. They are currently employed in a variety of applications such as organic photovoltaics (OPVs),[1–3] organic light-emitting devices (OLEDs),[4–7] radio frequency identification devices (RFID),[8–10] photodetectors,[11–15] and biosensors.[16–19] They have the great potential of being employed in the healthcare sector as well as for smart electronic textiles.[20–25] Smart textiles can sense and respond to various thermal and mechanical conditions by sending data to other devices. Organic semiconductors can be processed at low temperature and are highly compatible with roll-roll processing and flexible substrates.

Figure 1.1 (a) Flexible and rollable OLED TV (LG). (b) OLED display in iPhone X and Apple Watch. (c) Samsung Fold with flexible OLED display.

1.1 Organic Light-Emitting Devices

OLEDs are solid state devices consisting of an emissive electroluminescent organic semiconductor layer that emits light on application of current through the device. Since an OLED display works without a backlight, it can display deep black levels. OLED technology offers improved image quality in terms of brightness, contrast ratio, faster refresh rate, and large fields of view (about 170 degrees) as compared to conventional liquid crystal display technology which utilizes a white backlight in combination with color filtering to produce the image.[5] Furthermore, the fabricated OLED device is extremely thin (100-500 nm) without any need of high temperature during its manufacturing. Technological advancement in this field has enabled creation of unique products such as flexible and foldable displays (Fig. 1.1) and transparent display screens.[26–30]

1.2 Organic Photovoltaic Cells

Organic photovoltaic cells (OPVs) are fabricated from small molecule or polymer organic semiconductor thin films. They are an attractive renewable energy technology due to their

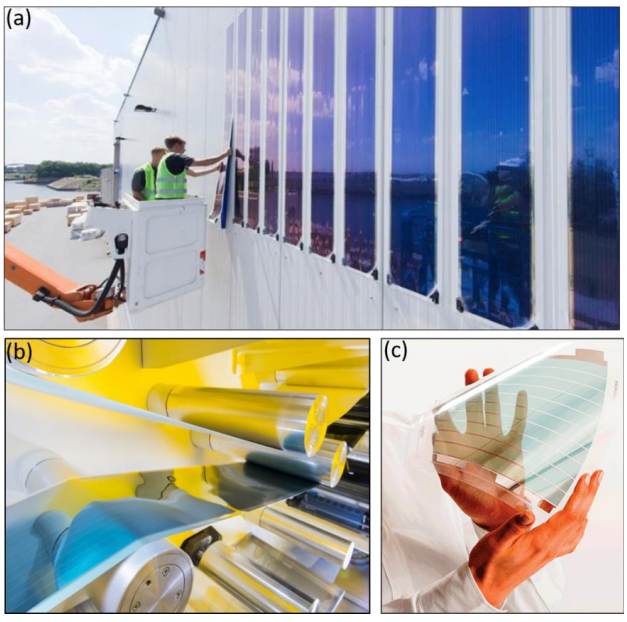

Figure 1.2 (a) Integration of OPVs on building walls. (b) Vacuum roll-to-roll production (c) Ultra-thin flexible semitransparent panels (Heliatek).[31]

compatibility with high throughput large-area fabrication methods, mechanical flexibility, abundant raw materials, and overall potential for low-cost production.[32–35] Additionally, the tunable absorption properties of organic semiconductors can help to generate power using the infrared and UV regions of the solar spectrum which makes them highly suitable for various applications, such as transparent windows for building integrated photovoltaics (BIPV) and implementation in electronic devices such as mobile phones, smartwatches and electric cars to constantly charge and extend the battery life. (Fig 1.2).[36] The current OPV power conversion efficiencies have exceeded 16% for single-junction solar cells,[37–39] 17.3% for multijunction organic solar cells,[40] and a module efficiency of over 10%. In transparent solar cell technology it has achieved a record power conversion efficiency of 9.8% and an average transparency of 38.3%.[41]

1.3 Scope of Present Work

This thesis explores questions related to excited-state transport in organic semiconductor thin films. The excited state in organic semiconductor exist as a bound electron-hole pair, also known as exciton. The transport of long-lived dark exciton is of special interest as they play an important role as energetic intermediates in OLEDs as well as a potential active material in OPVs. However, their migration is specifically challenging to probe accurately. The focus of this thesis is on demonstrating a new characterization technique to track exciton migration as well as on engineering unique device architectures for enhancing energy transport in OPVs. The effect of subtle changes in molecular structure in substantially impacting excited state transport is investigated.

Furthermore, solar cell architectures that exploit exciton gates to bias exciton migration, thereby overcoming the normally diffusive aspect of energy transport are developed.

2 Excited States in Organic Semiconductors

This chapter is designated to provide the fundamentals of molecular excited state behavior in organic semiconductors. For a more detailed discussion on this topic readers are referred to work by Köhler and Bässler.[42]

2.1 Properties of Organic Semiconductors

2.1.1 Molecular Conjugation

Organic semiconductors are carbon based conjugated small molecules or polymers. The conjugated carbon atoms are sp^2 hybridized which gives rise to three σ bonds and one π bond. The molecular σ orbital arises due to constructive interference of two electron wavefunctions where the electron density between nuclei leads to the bonding character of this orbital. The destructive interference of two electron wavefunctions leads to reduced electron density between the nuclei. The resultant bond is referred as a σ^* antibonding orbital since

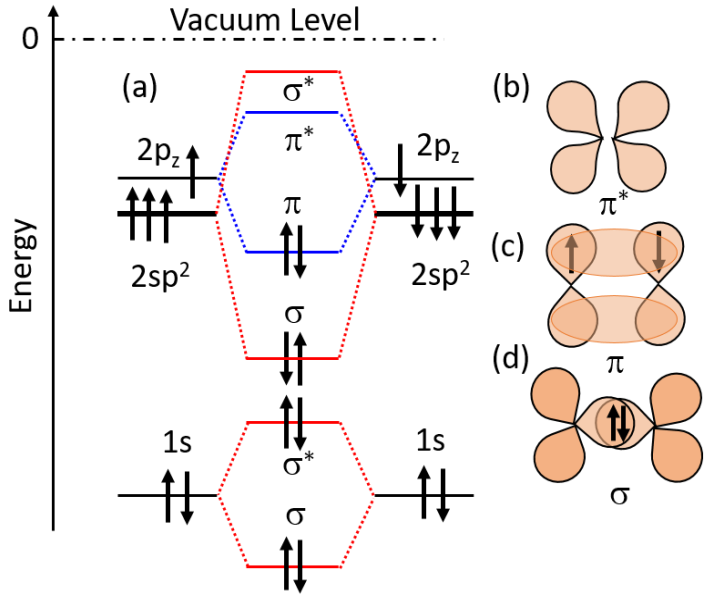

Figure 2.1 (a) Molecular orbital diagram of C=C. (b) p orbitals in a π^* anti-bond (c) p orbitals in π bond (d) sp^2 hybridized orbitals in σ bond.

the repulsion between nuclei is not screened by the electron density. The energy associated with the two orbitals is $E_{\pm}=(\alpha \pm \beta)/(1+S)$ where S is the overlap integral, α is the Coulomb integral and β is the exchange integral. The overlap integral is a measure of extent to which orbitals on two nuclei overlap, Coulomb integral measures the electrostatic attraction between the electron density of one nucleus with the other nucleus, and the exchange integral represents interaction between overlap of the two electron wavefunction and the nucleus. The energy splitting between two molecular orbitals is mainly controlled by exchange integral. The three sp^2 hybridized orbitals are distributed on a plane with an angle of 120^o between them, each lying along internuclear axis with other atoms. The higher value of exchange integral is due to large overlap of electron density between two carbon atoms results in large amount of splitting between σ bonding and σ^* antibonding orbitals. The interaction the of $2p_z$ orbitals leads to the formation of π bonding and π^* antibonding orbitals. The location of electron density away from internuclear axis results in the lower splitting between the two orbitals as compared to σ and σ^*. Figure 2.1 illustrates the interaction between two carbon atoms. The higher occupied molecular orbital (HOMO) is the π orbital and the lowest unoccupied molecular orbital (LUMO) is an empty π^* orbital. These orbitals are often referred as frontier orbitals and the ability of a molecule to partake in optical processes such as absorption and emission, depends upon the transition between HOMO and LUMO orbitals. For large π orbital extended over several carbon atoms, the weaker splitting between LUMO and HOMO orbital leads to transition in the visible region

of light spectrum. Thus, making the molecule more relevant for optoelectronic applications.

2.1.2 Spin Singlet and Triplet States

The electronic wavefunction provides information about the electron's spatial coordinates and the positions of nuclei. For a fixed nuclei position, the probability of finding the electron can be described by the square of electron wavefunction. However, the electron wavefunction is not sufficient to describe the complete state of the system. It is necessary to consider the role of electron spin which can be incorporated by introducing a spin wavefunction.

The spin state of a molecule can be calculated by summing the spin of all electrons in all orbitals. However, in filled orbitals the antiparallel spin of two electrons contributes zero to the net spin. Therefore, it is sufficient to describe the spin state of the system by considering the spin of unpaired electrons in the excited state configuration of the molecule. Molecule configurations with antiparallel and parallel spins are referred as singlet and triplet states, respectively. The unpaired electrons in the excited state is a two-particle system. The spin state of the system is described by spin angular momentum operator $\hat{S}^2$ and its z component $\hat{S}$ with eigenvalues S and M_s. There are four eigenstates for the system. The full electron wavefunction is the product of the spatial and spin wavefunctions. The four spin wavefunctions (ψ_{Spin}) are:[43]

$$\psi_{\mathrm{Spin,T_-}} = |\uparrow\uparrow> \text{ yielding } \mathrm{S} = 1 \text{ and } \mathrm{M_s} = 1$$

$$\psi_{\mathrm{Spin,T_0}} = \frac{1}{\sqrt{2}}(|\uparrow\uparrow> + |\downarrow\downarrow>) \text{ yielding } \mathrm{S} = 1 \text{ and } \mathrm{M_s} = 0$$

$$\psi_{\mathrm{Spin,T_-}} = |\downarrow\downarrow> \text{ yielding } S = 1 \text{ and } M_s = -1$$

$$\psi_{\mathrm{Spin,S_0}} = \frac{1}{\sqrt{2}}(|\uparrow\uparrow> - |\downarrow\downarrow>) \text{ yielding } S = 0 \text{ and } M_s = 0$$

The first three spin wavefunction are always in phase, differing only in the z^{th} component of the spin and are referred as triplets. While the fourth spin wavefunction ($\psi_{\mathrm{Spin,S_0}}$) is 180^0 out of phase and is referred as singlet state. The energy of the singlet and triplet states differ by twice the value of exchange integral. The exchange integral scales exponentially with the overlap of electron and hole wavefunction.[44] The smaller value of exchange energy (0.2-0.5 eV) will occur when HOMO and LUMO orbitals are located on two different part of the molecule. [43]

2.1.3 Molecular Vibrations

The potential energy of the ground state or excited state of the molecule depends upon the positions of atomic nuclei. The nuclei in a real molecule oscillate around their equilibrium position with a certain vibrational frequency ω and associated energy (n+1/2) $\hbar\omega$, where n is the harmonic or energy level. The atoms in a molecule form a system of coupled oscillators. The vibrational motion of the nucleus can be described by a separate wavefunction, Ψ_{vib}. Thus, the total wavefunction is approximated as the product of electronic, spin and vibrational wavefunction. The vibrational energy of the modes is experimentally measured using Raman spectroscopy or by Fourier transform infrared spectroscopy (FTIR). The vibrational modes are also reflected in absorption and emission spectra of the molecule. Typical vibrational modes that occur in organic molecules are C-C, C=C stretching modes, C-H in plane bond stretching, phenyl ring torsion.[45]

2.1.4 Optical Absorption and Emission

In organic molecule photon absorption and emission involves an electronic transition between ground and excited state potential energy curves. The different vibrational sublevels are represented by horizontal lines on a potential energy diagram (Fig. 2.2). The resulting absorption and emission spectra are the superposition of energy transitions between different vibrational level of ground and excited state. The transition rate between initial state Ψ_i and final state Ψ_f is given by Fermi's golden rule:[42,46,47]

$$k_{if} = \frac{2\pi}{\hbar} | < \Psi_f | \widehat{H'} | \Psi_i > |^2 \rho \quad (2.1)$$

where ρ is the density of final states, $\widehat{H'}$ is the perturbing Hamiltonian operator that causes the transition. The total molecular wavefunction can be expressed as $\Psi_{total} = \Psi_{el}\, \Psi_{spin} \Psi_{vib}$, while the dipole operator is êr, and is used in the perturbing Hamiltonian, $\widehat{H'}$. The dipole operator acts only on the electronic wavefunction with the spin and vibrational wavefunctions are insensitive to the electric field. Therefore, they can be treated as constant, leading to the following expression:[45]

$$k_{if} = \frac{2\pi}{\hbar} | < \Psi_{el,f} | e\hat{r} | \Psi_{el,i} > |^2 \, | < \Psi_{spin,f} | \Psi_{spin,i} > |^2 \, | < \Psi_{vib,f} | \Psi_{vib,i} > |^2 \quad (2.2)$$

Thus, the optical transition rate depends on three factors: electronic, vibrational and spin. If any of these factors is zero, the transition is forbidden.

The electronic factor $| < \Psi_{el,f} | e\hat{r} | \Psi_{el,i} > |$ is non-zero if the transition is dipole allowed, i.e. the excited state is antibonding orbitals denoted as σ^* and π^*. The electronic factor also depends on the overlap of the initial and final state wavefunctions. The transition

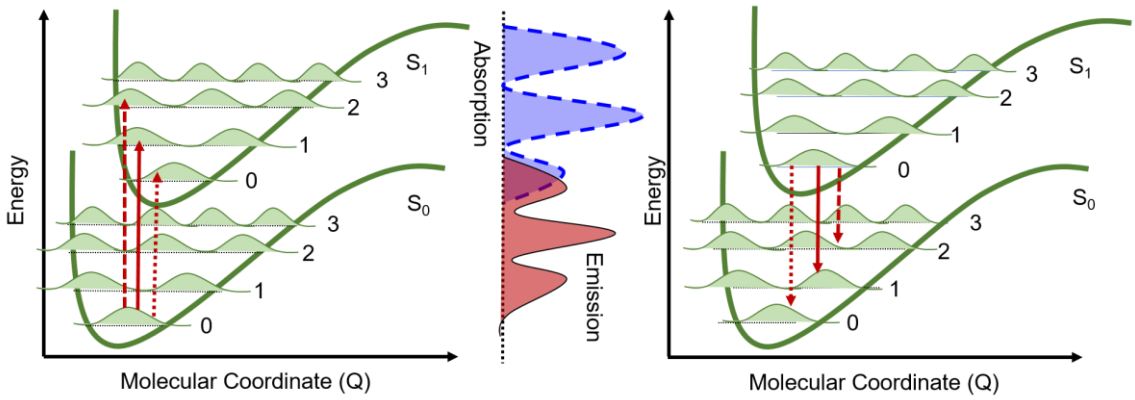

Figure 2.2 Schematic of a potential energy curve for ground and excited state with the overlap of vibrational wavefunction determines shape of absorption (left) and emission spectra (right).

rate is higher between orbitals that are centered on the same parts of the molecule (ex. $\pi - \pi^*$ transition) and is lower between orbitals that occupy different space (ex. A charge-transfer state transition, $n - \pi^*$ transition).[42,48,49]

The vibrational factor controls the spectral shape of the absorption and emission. The energy of vibrational quanta lies between 100-300 meV, therefore at room temperature the lowest vibrational state is populated.[42,50–52] The absorption takes place from the zeroth vibrational level of the ground state to the m^{th} vibrational level of the excited state. The intensity of the transition is controlled by the overlap of vibrational wavefunctions, $|<\Psi_{vib,f}|\Psi_{vib,i}>|^2$ also known as Franck-Condon-factor F, which gives the probability of transition between vibrational states. The excited state configuration coordinate is displaced by ΔQ with respect to ground state potential energy curve (Fig 2.2). In the excited state, equilibrium spacing between atomic cores is increased because of one of the electrons in an antibonding orbital which reduces the overall electron density between atomic cores. For a stiff molecule, the 0^{th}-0^{th} transition between ground and excited state is dominant due

to small displacement along molecular coordinates, while for flexible molecules transition between higher vibrational levels such 0^{th}-1^{st} form the peak of the distribution.[42]

The spin factor $| < \Psi_{spin,f} | \Psi_{spin,i} > |^2$ takes two values, 0 if spins of initial and final state differ and 1 if they are same. Thus, the transition such as $S_0 \rightarrow S_1$ and $T_1 \rightarrow T_n$ are spin allowed, while the transition such as $T_1 \rightarrow S_0$ are spin forbidden. However, spin forbidden transitions can acquire a finite transition rate if by some perturbation the wave function obtains a contribution from opposite spin wavefunction.[53]

The mechanism of spin-orbit coupling can provide such mixing. In spin-orbit coupling, the change in spin angular momentum of an electron is compensated by an opposite change in orbital angular momentum, since the total angular momentum is conserved during optical transition.[42,43] The amount of mixing between pure triplet excited state and singlet excited state will depend upon wavefunction overlap after spin-orbit coupling, separation in energy between two states, and magnitude of perturbing Hamiltonian which varies as fourth power of atomic charge.[43,54] Thus, incorporation of heavy metal atom such as iridium or platinum in chromophore results in strong phosphorescence (radiative emission from triplet state).[55]

2.1.5 Non-radiative Transitions

Non-radiative transitions are isoenergetic transitions between the 0^{th} vibrational level of initial state and k^{th} vibrational level of the final state, as represented by a horizontal arrow in Figure 2.3. The transition is followed by thermal relaxation which is a fast and irreversible dissipation of vibrational energy to the surroundings. The thermal relaxation is represented by sequence of vertical arrows (Fig. 2.3). The non-radiative transition between states of same spin fold such as $S_1 \rightarrow S_0$ and $T_2 \rightarrow T_1$ are referred to as internal conversion, while transitions between different spin manifolds such as $S_1 \rightarrow T_1$ and $T_1 \rightarrow S_0$ are referred to as intersystem crossing. Siebrand derived the rate of intersystem by going beyond the Born–Oppenheimer approximation as:[53,56–61]

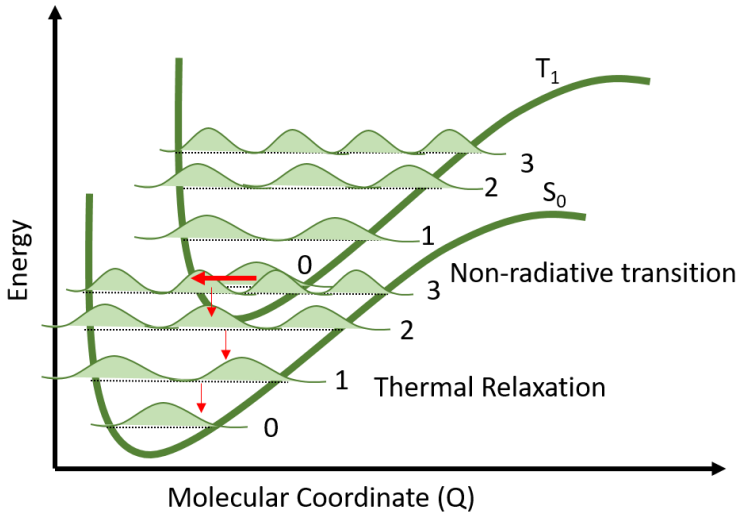

Figure 2.3 Potential energy diagram illustrating a nonradiative transition from T_1 to S_0, followed by thermal relaxation.

$$k_{if} = \frac{2\pi}{\hbar} \rho J^2 F \quad (2.2)$$

where the Franck-Condon factor F is the overlap of the overall vibrational wavefunction of the initial and final states $| < \Psi_{vib,f} | \Psi_{vib,i} > |^2$, and J contains the electronic coupling between two states. The Franck-Condon factor, F for the general case of a distorted

oscillator depends exponentially on the energy difference between the initial and final states. This is reflected by the energy gap law as:

$$k_{if} \propto \exp\left(-\gamma \frac{2\pi\,\Delta E}{h\,\omega_m}\right) \quad (2.3)$$

where $\frac{h\,\omega_m}{2\pi}$ is the energy of the highest frequency mode and γ depends on molecular parameters. The electronic coupling contains the electronic and spin wavefunction and the selection rules for spin, symmetry and parity are like radiative decay.

2.2 Excitons

Excitons are charge neutral quasiparticles consisting of Coulombically bound electron-hole pairs. Excitons are classified based on binding energy and spatial extent into three types as Wannier-Mott, Frenkel and charge-transfer excitons (Fig. 2.4).

2.2.1 Wannier-Mott Excitons

Wannier-Mott excitons are frequently found in inorganic crystalline semiconductors.[47,48] The Columbic attraction between the electron and hole is weak due to the large dielectric constant. The typical binding energy for these excitons is around 5 meV.[43,64] The thermal energy at room temperature (25.9 meV) is large enough to dissociate these excitons. Therefore, Wannier excitons exist only at low temperature. The binding energy corresponds to a separation between (5-10) nm between electron and hole, which exceeds the interatomic spacing.[43]

2.2.2 Frenkel Excitons

In organic semiconductors the excited state is a tightly bound electron-hole pair, called a Frenkel exciton. The binding energy reflects the low dielectric constant of these

materials, and is ~0.3-0.5 eV.[65,66] For triplet excitons, the binding energy is larger due to the exchange interaction between the electron and hole of the same spin orientation.[43] In amorphous organic semiconductor films the exciton is localized on a single molecule,[67] while in organic crystals large intermolecular coupling between molecules results in exciton delocalization. The spontaneous dissociation of exciton requires heterojunction interface of energetically dissimilar materials, such that the net energy is lower than that of the exciton.

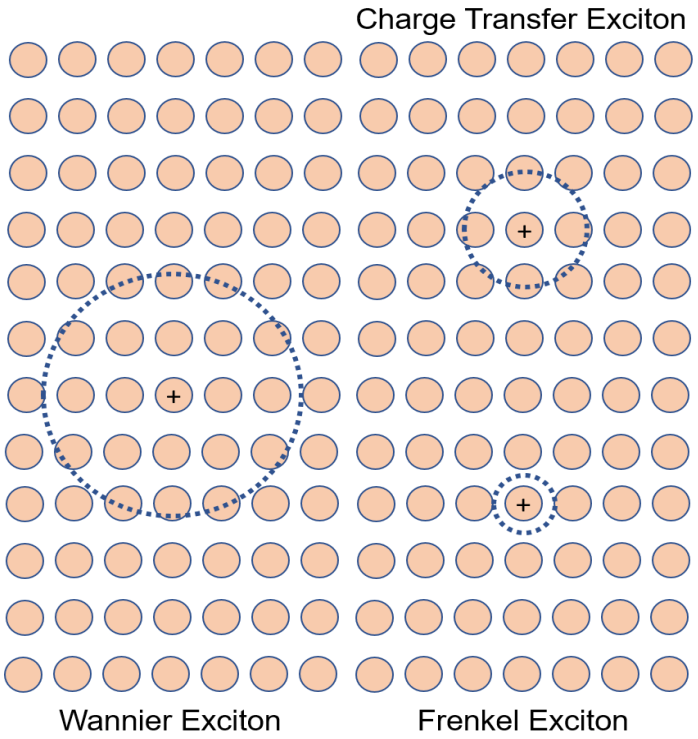

Figure 2.4 Diagram illustrating spatial extent of Wannier exciton, Frenkel exciton and Charge Transfer exciton in a molecular lattice.

2.2.3 Charge-Transfer Excitons

Charge transfer (CT) excitons can be described as an intermediate between Frenkel and Wannier-Mott excitons. In OPVs, these are formed between donor and acceptor heterojunction before dissociation to free carriers.[68–70] In several cases, CT states can exist in the bulk of organic semiconductors.[71] The binding energy of these excitons can range

from 0.1 eV to 0.3 eV, which corresponds to an exciton radius of (0.5 nm to 5 nm).[69,72] The CT state excitons have also been observed in two-dimensional metal chalcogenides and transition metal oxides.[73,74]

2.3 Exciton Energy Transfer

Excitons migrate from molecule to molecule via several energy transfer mechanisms known as cascade energy transfer, Förster energy transfer, and Dexter energy transfer.

2.3.1 Cascade Energy Transfer

The photon emitted from exciton recombination can be reabsorbed by a second molecule. Energy transfer mediated by a real photon is often referred as cascade or radiative energy transfer.[47,75–77] The efficiency of radiative transfer depends upon the overlap between the emission and absorption spectra of a given material. In organic semiconductor thin films, this mechanism should be considered when there is small Stokes shift (difference between the spectral position of first absorption band peak and the emission peak) as well as no competition from other energy transfer mechanisms.[75] The percentage of reabsorbed photons depends upon the thickness of the organic thin film. Typically, it starts to play role when thickness approaches absorption path length (100-200 nm) of the material.[78]

2.3.2 Förster Energy Transfer

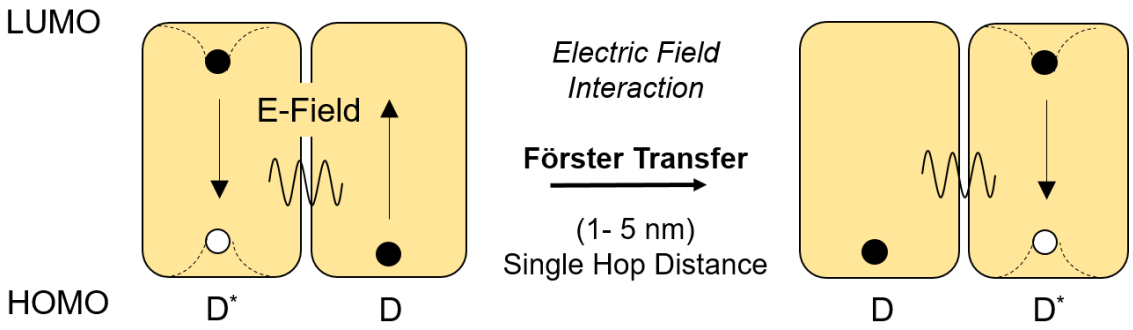

Figure 2.5 Schematic representation of electron pathway for Förster energy transfer. The transfer proceeds via Coulombic (dipole) coupling between donor (D*) and acceptor (D) molecules.

Förster transfer is a non-radiative energy transfer mechanism observed for fluorescent singlet excitons. The energy transfer occurs via dipole coupling between donor and acceptor molecules. The energy transfer between two dipoles separated in space is:[79]

$$k_F(d) = \frac{1}{\tau}\left(\frac{R_0}{d}\right)^6 \qquad (2.4)$$

where τ is the exciton lifetime and R_0 is the Förster radius which is separately defined as:[75]

$$R_0^6 = \frac{9\eta_{PL}\kappa^2}{128\pi^5}\int \frac{\lambda^4 F_D(\lambda)\sigma_A(\lambda)d\lambda}{n(\lambda)^4} \quad (2.5)$$

where η_{PL} is the photoluminescence efficiency, κ is the dipole orientation factor (taken as $0.845\sqrt{\frac{2}{3}}$ for randomly oriented rigid dipoles),[80] n is the wavelength dependent refractive index of the donor film, F_D is the normalized fluorescence spectrum, σ_A is the acceptor absorption cross-section, and λ is the wavelength. Förster transfer may occur over a relatively long length scale (typically in the range 1-5) nm as compared to intermolecular space on the order of d=1 nm or less. [78,81–83]

The energy transfer from a donor molecule to a plane of acceptor layer (k_{Fp}) or thick acceptor layer (k_{Fs}) is given by:[84–86]

$$k_{Fp}(d) = \frac{\pi \rho_A}{2\tau} \frac{R_0^6}{d^4} \quad (2.6)$$

$$k_{Fs}(d) = \frac{\pi \rho_A}{6\tau} \frac{R_0^6}{d^3} \quad (2.7)$$

where ρ_A is the molecular density of acceptor (per unit area or volume, respectively), d is the distance from the donor to the acceptor plane or slab.

2.3.3 Dexter Energy Transfer

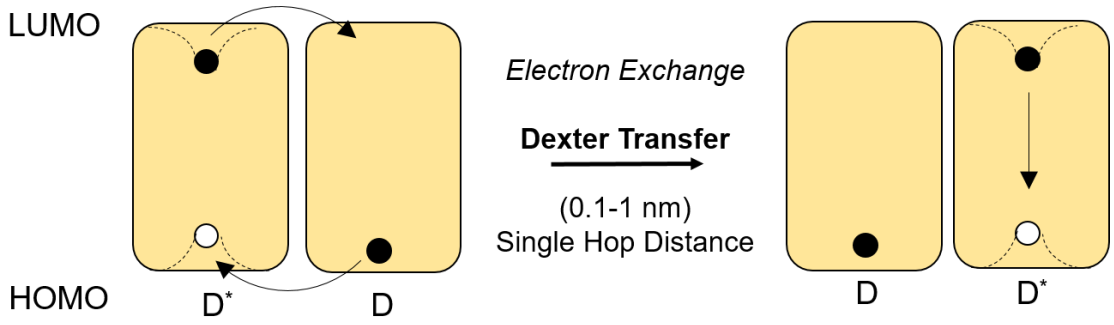

Figure 2.6 Schematic representation of the electron pathway for the Dexter energy transfer. The transfer proceeds via electron exchange.

Dexter energy transfer is a short-range non-radiative energy transfer mechanism, dominant for non-luminescent singlet or triplet excitons. The energy transfer is typically mediated by electron exchange between two molecules. The subsequent transfer rate is defined as: [87–89]

$$k_{Dexter} = \frac{2\pi}{\hbar} K^2 \exp\left(-\frac{2d}{L}\right) \int F_D(E)\, \sigma_A(E) dE \quad (2.8)$$

where F_D and σ_A are normalized donor and acceptor emission and absorption spectra, respectively, d is the intermolecular separation, L is the effective average orbital radius for

the excited and unexcited state of donor and acceptor, and K is a constant that reflects the specific orbital interactions. The electron exchange in Dexter transfer occurs over a short length scale of (0.1-1) nm since the transfer requires orbital overlap with adjacent acceptor molecule.

2.4 Exciton Transport

Exciton diffusion is modeled as an ensemble of self-energy transfer hopping events. For an isotropic medium exciton diffusion can be modeled as nearest neighbor hopping event. A generalized diffusion coefficient is written as[75,76,90]

$$D = \frac{A}{6}\sum_N d^2 k_{ET}(d) \quad (2.9)$$

where A is a geometric factor accounting for disorder in the thin film, d is the distance of single hopping event, and k_{ET} is the energy transfer rate to a specified lattice point of set N. The k_{ET} can be Förster or Dexter energy transfer rate depending upon the dominant energy transfer mechanism in the film. When considering the motion of an exciton along one-dimensional infinite array the mean displacement is zero since it has an equal probability of moving right or left. However, the mean square displacement is non-zero and is written as $< x^2 > = D * t$, where

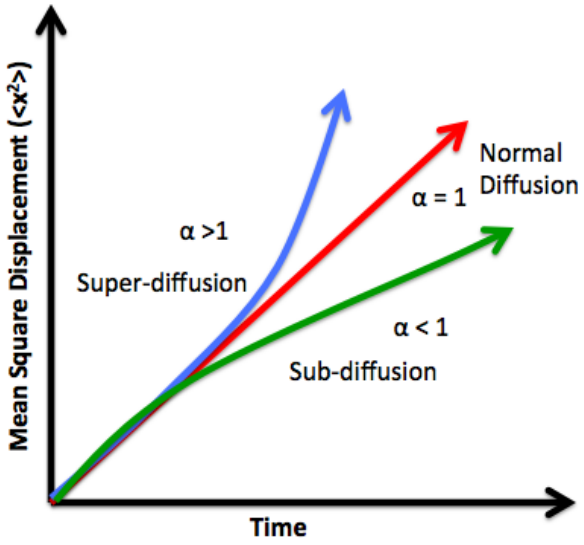

Figure 2.7 Diagram for the mean-squared displacement versus time highlighting the difference between normal diffusive, sub-diffusive, and super-diffusive motion.

D is the diffusion coefficient and t is the time. For the normal diffusion motion, the characteristic diffusion length, the L_D is given by:

$$L_D = \sqrt{< x^2 >} = \sqrt{D\tau} \qquad (2.10)$$

For normal diffusion, the mean square displacement linearly increases with time. Any deviation from it will result in anomalous diffusion. A more generalized expression for displacement is given by:[91]

$$<x^2> = \beta * t^{\alpha} \qquad (2.11)$$

where β is proportionality constant related to D and $\alpha < 1$ represents sub-diffusive and $\alpha > 1$ super-diffusive motion. Figure 2.7 illustrates traces for normal and anomalous diffusive region.

2.5 Exciton Interactions and Quenching Processes

Excitons in organic semiconductors can be subject to various bimolecular interactions during its lifetime. This section highlights different exciton interaction processes.

2.5.1 Exciton-Exciton Annihilation and Triplet Fusion

Exciton-exciton annihilation is a non-radiative process where the energy of one exciton is transferred to an already excited molecule, thereby promoting the exciton into a second excited state.[43,78] Subsequently, the exciton thermally relaxes back to the first excited state losing excess energy to the surrounding. The rate of this bimolecular process depends on exciton density squared. Exciton annihilation occurs both for singlet and triplet

excitons. In the triplet-triplet annihilation, two triplets annihilate to form an intermediate state X that can be converted to either a singlet or triplet state according to the following exothermic reaction as either singlet or triplet state according to the following exothermic reaction as:[92,93]

$$T_1 + T_1 \xrightarrow{k_{ss}^T} T_n + S_o \rightarrow T_1 + S_o$$

$$T_1 + T_1 \xrightarrow{k_{TT}^S} S_n + S_o \rightarrow S_1 + S_o$$

where T_1 represents the triplet excited state, S_1 the singlet excited state, and S_o the ground state of the molecule. The rate constant for generation of singlets and triplets from TTA are given as k_{TT}^S and k_{TT}^T respectively. When the singlet excitons are generated, the process is also referred as triplet fusion where the generated singlet exciton may decay radiatively. The emission is called delayed fluorescence since its transient decay can be much longer than decay time of singlet excitons. The singlet state energy must be less than or equal to the sum of two triplet state ((E(S) ~ < 2E(T)). Generally, the exciton-exciton annihilation is dominant for high exciton densities when the two excitons have high probability of encounter. It is especially observed in long-lived triplet excitons compared to short-lived singlet state.

2.5.2 Singlet Fission

Singlet fission is a photophysical process in which singlet exciton is converted to two triplet exciton pairs (Fig. 2.8).[94,95] The generated triplet exciton must be harvested to increase photogeneration efficiency in organic photovoltaic devices. The process has

gained renewed interest as a promising candidate for surpassing the Shockley-Queisser limit for energy conversion in a single junction solar cell. It has been observed in selected number of organic semiconductor materials, with triplet energy nearly half of singlet energy (E(S) ~ 2E(T)). When combined with conventional silicon-based photovoltaic cells, singlet-fission materials offer a route to improve spectral coverage by direct charge generation or reduced thermalization loss via down conversion.[96,97]

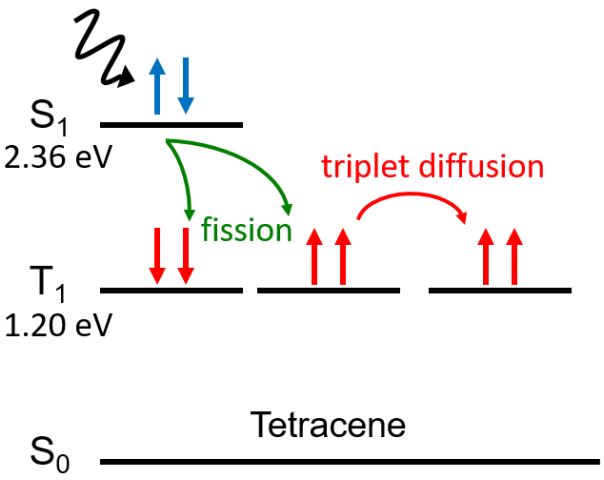

Figure 2.8 Schematic of singlet fission in an archetypical organic semiconductor molecule Tetracene.

2.5.3 Exciton-Polaron Quenching

Exciton polaron quenching constitute one of the major loss mechanism in organic optoelectronic devices, particularly at high exciton density.[98–101] The rate of quenching is proportional to the product of exciton density and polaron density. The proportionality constant depends upon the polaron diffusion coefficient and exciton polaron capture radius.[100] The exciton polaron quenching mainly occurs via Förster energy transfer and no orbital overlap is required for this process.[102]

2.6 Summary

In this chapter, electronic and optical properties of excited state in organic semiconductor are discussed. The excitons in organic semiconductor migrate from molecule to another through energy transfer between them. The energy transfer can be of different types based on mechanism of transfer. Ensemble of self-energy transfer event during the lifetime of exciton determines the characteristic diffusion length. Excitons can also be subjected to various bimolecular interactions during its lifetime. The physics introduced here will be used in later chapter for interpreting and understanding the exciton transport in organic semiconductor thin films.

3 Fabrication and Characterization of Organic Semiconductor Devices

The previous chapter described the electronic and optical properties of organic semiconductors. The application of organic semiconductors in devices requires them to be deposited as thin film with high uniformity and repeatability. This chapter discusses conventional techniques used for the fabrication of organic semiconductor thin films. The chapter further describes experimental techniques required for interpreting and understanding the exciton transport in organic semiconductor thin films. This chapter also looks into the processes which lead to photoconversion in OPVs, device architectures which are able to accomplish these processes efficiently.

3.1 Thin Film Deposition Techniques

3.1.1 Vacuum Based Deposition

Vacuum thermal evaporation involves resistively heating the source material in tantalum doped tungsten boats in a vacuum environment with pressure ranging from 10^{-7} Torr to 10^{-6} Torr. As the boat is heated, sublimation produces a vapor plume from the source. The vapor plume condenses on a substrate to create a uniform film with excellent control and repeatability.[103–105] The high vacuum is essential for thin film purity as background gases can lead to contamination of the deposited film. The molecular mean free path (λ_{mean}), the average distance between two successive collision is:[106,107]

$$\lambda_{mean} = \frac{k\,T}{\sqrt{2}\,\pi\,d^2 P} \qquad (3.1)$$

where d is the molecular diameter and P is the deposition pressure in the chamber. The λ_{mean} is 12.1 m for a molecule with an average diameter of 1 nm at 250 ºC and a deposition pressure of 10^{-6} Torr. The much greater mean free path than chamber length allows molecule a line of sight during deposition. The deposition rate is measured by a cooled quartz crystal microbalance (QCM) placed near the source. The rate is controlled via a closed loop PID controller. When the desired rate is reached, the shutter opens, and deposition begins. The substrate holder is rotated to provide thickness uniformity (± 1 nm) across different samples. The advantage of thermal evaporation lies in constructing multilayer architectures and co-deposition of several small molecule organic semiconductor materials without concern of delamination or dissolution of previous layer. The high film uniformity across substrate as well as good run to run reproducibility are the

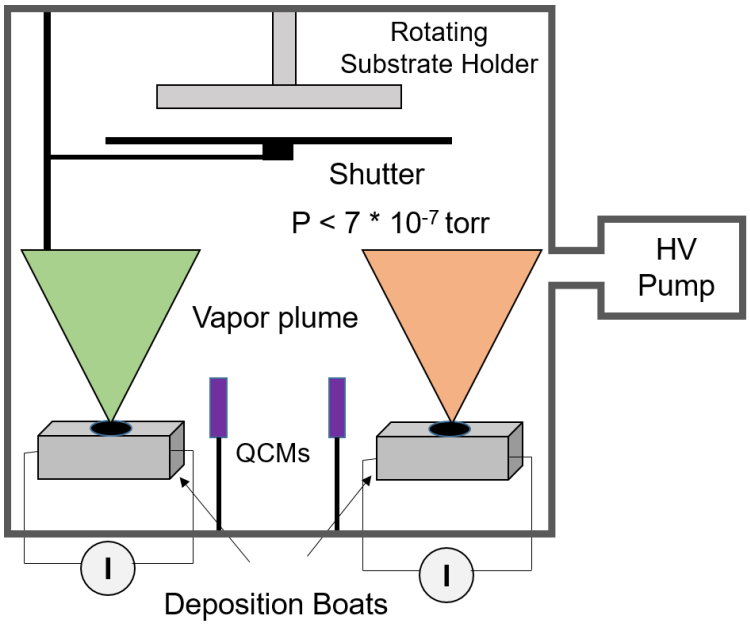

Figure 3.1 Schematic of vacuum based thermal evaporator system. Source material is resistively heated in a tantalum doped tungsten boat. Vapor plume from the source material uniformly spreads as it moves away from the source and which can then be condensed on a substrate to form uniform film.

key features of this technique. The deposition system used in this thesis is an eight-source vacuum thermal evaporation chamber. The multiple sources provide facility for co-depositing up to four materials.

Other vacuum based thin film deposition methods are organic molecular beam deposition (OMBD),[108,109,110,111] laser deposition,[112,113] hot wall deposition,[114,115] and organic vapor phase deposition (OVPD). [26–29] These techniques differ in terms of deposition pressure, method of heating (laser ablation in laser deposition), and the introduction of carrier gas for transportation of organic vapors (OVPD, hot wall deposition).

3.1.2 Solution Based Deposition

There are several solution processing methods applied to organic semiconductors including inkjet printing,[120–124] screen printing,[125,126] solution casting,[127] and spin coating.[37,38,40,128,129] At a laboratory scale, spin-coating is often applied to form thin films of materials whose molecular weight prevents the use of vacuum processing. The material of interest is dissolved in a solvent and dropped on a spinning substrate. The substrate is spun at high speed (>1000 rpm), and

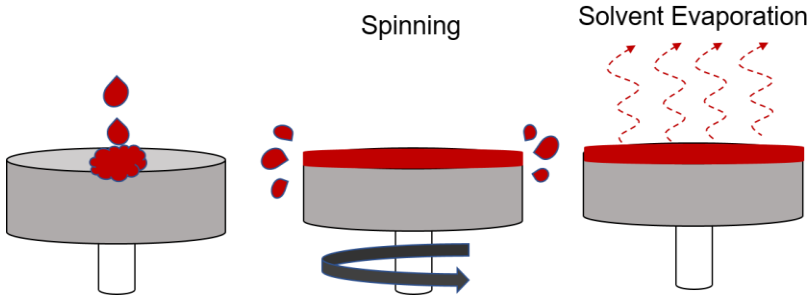

Figure 3.2 Schematic of the spin coating process. The solution is droped at the center of stage. As the stage is rotated the equilibrium between centripetal force and surface tension of the liquid, yields a uniform film.

the liquid uniformly distributes due to equilibrium between centripetal force and surface tension.[130,131] This stage is followed by uniform evaporation of the solvent. Final thickness of the deposited film is controlled by the rotation speed, viscosity of the coating solution and concentration of deposited material in the solvent.

3.2 Thin Film Characterization

This section provides measurement techniques to probe optical properties in organic semiconductor thin films.

3.2.1 Photoluminescence Efficiency

The photoluminescence efficiency (η_{PL}) is the absolute quantum yield of light emission from organic semiconductor thin film and is defined as:

$$\eta_{PL} = \frac{k_R}{k_R + k_{NR}} \quad (3.2)$$

where k_R and k_{NR} are the radiative and non-radiative decay rates of the exciton. Experimentally η_{PL} is measured as the ratio between number of photons emitted and number of photons absorbed by the sample. All the emission from the sample is collected by placing it in an integrating sphere with highly reflective coating. The number of photons absorbed by the sample is calculated by measuring the difference in integrated pump intensity with and without the presence of organic semiconductor film on quartz substrate. The pump wavelength must be selected to avoid overlap with emission spectra. The emission and pump spectra must be multiplied with wavelength and intensity correction factor of the instrument to ensure accurate account of photons. The η_{PL} can reach unity by

diluting the emissive species in a large energy gap host material. This action decreases non-radiative decay rates due to reduction in phonon-mediated decay pathways.[55]

3.2.2 Transient Photoluminescence

Transient photoluminescence measurement is widely used in fluorescence spectroscopy to excited state decay. The lifetime (τ) of the exciton can be generally defined as the inverse of all rates that deactivate the singlet or triplet:

$$\tau = \frac{1}{(k_R + k_{ISC} + k_{NR})} \quad (3.3)$$

where k_R and k_{NR} are radiative and non-radiative decay rates respectively and k_{ISC} is the intersystem crossing rate from singlet to triplet excited state. For fluorescent materials, $k_{ISC} = 0$ and τ is on the order of 10^{-9} s. In phosphorescent materials, the rate of intersystem crossing ($k_{ISC} \sim 10^9$ s^{-1} to 10^{11} s^{-1}) competes with radiative and non-radiative singlet decay rate.[46,47] This results in an appreciable triplet population, which decays radiatively ($k_{R,T}$) as phosphorescence or non-radiatively ($k_{NR,T}$) to the ground state. Since triplet states require spin-orbit coupling to decay radiatively to the ground state, the decay is much slower than for singlets. The singlet exciton lifetime can be measured using time correlated single photon counting (TCSPC). For the work in this thesis, TCSPC is carried out using a high repetition rate picosecond or femtosecond light source and a highly sensitive avalanche photodiode or high-speed photomultiplier tube. In TCSPC, the conditions are adjusted to detect less than 1 photon per excitation pulse, in fact the photon count rate is 1 photon per 100 excitation pulse.[132] The arrival time of the emitted photon from the film after excitation pulse is stored in a histogram. When less than 1 photon is detected per excitation pulse, the

histogram represents the optical decay of the excited state. The measurement of time difference is recorded using a constant function discriminator and time to amplitude convertor. The measured intensity decay is a convolution with the instrument response function (IRF). The IRF represent the shortest time profile that can be measured by the instrument. It is the response of the instrument to zero lifetime sample, which is typically collected through a roughened glass substrate or colloidal silica.

In this work, exciton lifetimes >20 ns are measured using a nitrogen laser at a wavelength of λ = 337 nm which provides ~ 1 ns pulse width. The repetition rate of the laser can also be driven externally using a pulse generator. The photoluminescence transients are recorded with an amplified silicon photodetector attached to a fast oscilloscope for read-out.

3.2.3 Film Thickness and Optical Constants

Optical constants and film thickness are the two key parameters that are required for optimizing organic semiconductor thin film architectures. It is generally extracted using ellipsometry which measures changes the change in light polarization as it reflects from a film. The polarization change is quantified by an amplitude ratio ψ, and a phase difference Δ, using a common ellipsometry parameter ρ defined as the ratio of the complex Fresnel reflection coefficient (R) between p and s polarized light:

$$\rho = \frac{R_p}{R_s} = \tan(\psi)\, e^{i\Delta} \quad (3.4)$$

The incident light is linear for both s-polarized and p-polarized component of incident light. The thickness of the thin film is determined from the interference between light reflecting from the surface and light travelling through the entire film and returning to the surface. The resultant interference contains information about both phase and amplitude. The phase information is very sensitive to the film thickness with a sensitivity of sub-monolayer thickness. The typical range of thickness measurement ranges from sub-nanometer to sub-microns. The interference oscillation for film thicknesses greater than one micron is difficult to resolve and thus requires other techniques for measurement. To extract film thickness, a model is constructed to describe the sample. The most common model for isotropic, non-absorbing films uses Cauchy's equation for the dispersion of refractive index with wavelength:

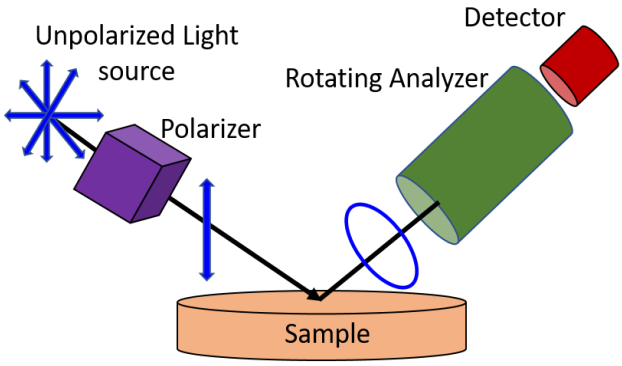

Figure 3.3 Diagram illustrating common ellipsometer configuration, rotating analyzer (RAE), polarizer, detector, light source. rotating polarizer (RPE).

$$n(\lambda) = A + \frac{B}{\lambda^2} + \frac{C}{\lambda^4} \quad (3.5)$$

This in turn can be used to calculate film thickness by fitting experimental data. The best result for the fit must corresponds to the lowest mean squared error (MSE). To fit optical constants, the film thickness is fixed, and the model is varied to iteratively fit n and k at

each wavelength to produce the measured signal. In this thesis, optical constants and film thickness are collected using a Woollam VASE VB-400 ellipsometer with an autoretarder.

3.3 Organic photovoltaic devices

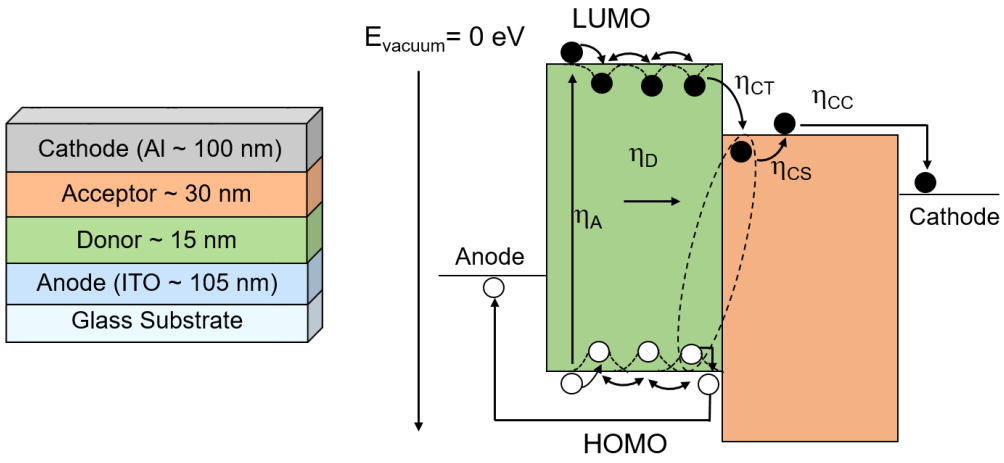

Figure 3.4 (a) Schematic representation of device architecture for a conventional bilayer OPV. (b) Energy level diagram for an OPV. Incident photons are absorbed with an efficiency, η_A, generating excitons. Excitons diffuse to the D-A interface, characterized by diffusion efficiency (η_D). At the heterointerface, excitons dissociate to form CT state between donor and acceptor molecules. The CT state then separates into charges with an efficiency (η_{CS}). These charges are collected at their respective electrodes with an associated collection efficiency, η_{CC}.

OPVs are constructed by forming heterojunction between energetically two dissimilar small organic semiconductor molecules or polymers. Figure 3.4a shows bilayer architecture in its simplest form, consisting of two organic layers sandwiched between transparent conducting anode, usually indium-tin-oxide (ITO) deposited on glass substrate, and metallic cathode, generally aluminum or silver. Figure 3.4b illustrates the working mechanism for an OPV. When the device is illuminated from the ITO side, excitons are

generated in donor and acceptor layer with an absorption efficiency $\eta_A(\lambda)$, which depends on the absorption coefficient of the material at the wavelength of incident photon and thickness of the layer. The photogenerated excitons then diffuse towards donor-acceptor hetero-interface, characterized by diffusion efficiency (η_D), which depends on the exciton L_D of the two material. Upon reaching the D-A interface, the electron is transferred from the LUMO of the donor to the LUMO of the acceptor with an efficiency η_{CT}, forming an intermediate coulombically bound CT state. If the HOMO-LUMO offset between donor and acceptor layer is greater than the binding energy of exciton, the process is exothermic and occurs at time scale 10^{-9}-10^{-12} s and is generally assumed to be 100%.[133] The CT state separates into free charges, dictated by the charge separation efficiency (η_{CS}). The η_{CS} depends upon the built-in electric field and thermal energy.[134,135]

The free charges are finally collected at respective electrodes, determined by the charge collection efficiency (η_{CC}). The product of five efficiencies determines the device external quantum efficiency (η_{EQE}) which is the ratio between number of charges collected at the electrodes to the total number of incident photons as:

$$\eta_{EQE} = \eta_A(\lambda) \times \eta_D(L_D) \times \eta_{CT}(V) \times \eta_{CS}(V) \times \eta_{CC}(V) \quad (3.6)$$

The key limitation in organic photovoltaic device is a trade-off between exciton L_D (~10 nm) and the optical absorption length (~100 nm).[2,75,78] Many of the photogenerated excitons will not reach the heterointerface to generate current. Indeed, state-of-the-art OPVs have overcome this trade-off and realize high efficiency through the use of a bulk heterojunction (BHJ) architecture where donor and acceptor materials are blended in a

single layer.[40,136,137] While this approach circumvents the short exciton diffusion length (L_D) by increasing the area of the dissociating donor-acceptor interface, it has presented new challenges in engineering morphology for efficient exciton and charge transport.

Several works have also attempted to directly increase the value of L_D via molecular design and morphology engineering.[138–145] In fact, anisotropic exciton diffusion is observed in polymer chromophores to be 100 times faster along co-facial π- π aggregates than in the lateral direction between aggregates. Significant enhancement in exciton diffusivity is achieved by increasing the molecular weight of polymer chromophore which increases chain aggregation and exciton delocalization.[145] Similarly, molecular modification by adding steric bulk in small molecules leads to enhancement in singlet L_D, originating from gains in the Förster radius for energy transfer.[140]

Indeed, the largest values of L_D have been realized in large-grained polycrystalline thin films and molecular crystals.[75,89,146–149] While at the same time it is non-trivial because there are a certain range of angles along which exciton hopping is maximized and thus it is difficult to say whether increase crystallinity will improve L_D.[150–154] There also has been a wide variety of work measuring L_D in oligocene single crystals, however their implementation in OPVs has been limited.[148] Nevertheless, the crystalline order in OPV design can be introduced through the engineering of polycrystalline films via thermal annealing. In fact, large grain size can approach limit for single crystalline films.[146] The critical factor determining L_D in these films is the non-radiative quenching at the grain boundaries which is orders of magnitude larger than those present in single crystals.[75,146]

In spite of the fact that the introduction of crystallinity through thermal annealing improves L_D, it is not a general trend.[150–153] Incorporation of organic semiconductor nanofibers comprising of crystalline core and segmented corona have recently emerged as a possible route to achieve L_D similar to molecular crystals. Self-assembly of molecular aggregates and conjugated polymers in solution has been shown as a promising method to achieve core-corona nanofibers.[149,155] Prior work has also demonstrated how variations in intermolecular separation can lead to increases in the L_D by optimizing the various parameters responsible for dipole-mediated Förster energy transfer.[90,156]

Many researchers in the field have also noted of a potential opportunity in enhancing L_D through the utilization of long-lived triplet excitons. The photogenerated singlet excitons can be converted to triplet excitons through the incorporation of phosphorescent sensitizer into the active layer.[157–160] Indeed, triplet diffusion lengths >100 nm have been reported for several organic semiconductor materials.[78] However, frequently different

Table 3.1 Measured values of triplet L_D reported for archetypical organic semiconductor materials

values of the triplet L_D have been published for the same material (Table 3.1). Different

Material	L_D (nm)	Method	Phase
NPD	6–87	Photocurrent,[158], remote sensing in tri-layers[161]	Amorphous
Alq_3	14-140	Remote sensing in LED configuration,[162] annihilation,[163] delayed PL[164]	Amorphous
CBP	8.3–300	Remote sensing in LED configuration,[165–167] PL quenching,[168] photocurrent[169]	Amorphous

values arise from different measurement techniques and the underlying assumptions of them. In Chapter 5 of this thesis various photoluminescence and charge-carrier based exciton L_D measurements are described. In Chapter 6, the limitation of these techniques in accurately measuring dark triplet L_D are mentioned and a novel sensitizer-based methodology to accurately to probe dark triplet L_D is demonstrated for several archetypical organic semiconductor materials.

3.4 Summary

In this chapter, deposition techniques for fabricating organic semiconductor thin films are presented. The key optical properties for characterizing excited state behavior in fabricated thin films are explored. The chapter also investigated the factors that determine the component efficiencies of the photoconversion process in an OPV. Several device designs to overcome the trade-off between exciton diffusion and optical absorption length are discussed. The necessity for accurate probe of dark long-lived triplet excitons is recognized. The techniques and concepts introduced here will be used in later chapter for interpreting and understanding the exciton transport in organic semiconductor thin films.

4 Experimental Probes and Theoretical Modeling of Exciton Diffusion

The previous chapter discussed about the importance of exciton diffusion as the key bottleneck limiting the photoconversion efficiency in an OPV. As such, it is critically important to accurately characterize the magnitude of L_D in order to gain control over material selection as well as device architecture to optimize diffusion and yield a more efficient device. Here, a summary of different techniques for probing L_D are presented, and broadly characterized as photoluminescence-based or charge carrier-based. In addition to presenting methods for extracting L_D, the constraints of each technique will also be considered.

4.1 Optical Transfer Matrix Formalism and Exciton Diffusion Modelling

This section focuses on modeling short-circuit photocurrent spectra of an organic thin film photovoltaic device. In a conventional silicon photovoltaic cell where film thickness is much greater than wavelength of light, it is a common practice to assume an exponential decay of optical intensity along the direction of propagation. However, the overall thickness is ~100 nm for OPVs, and interference effects become important.

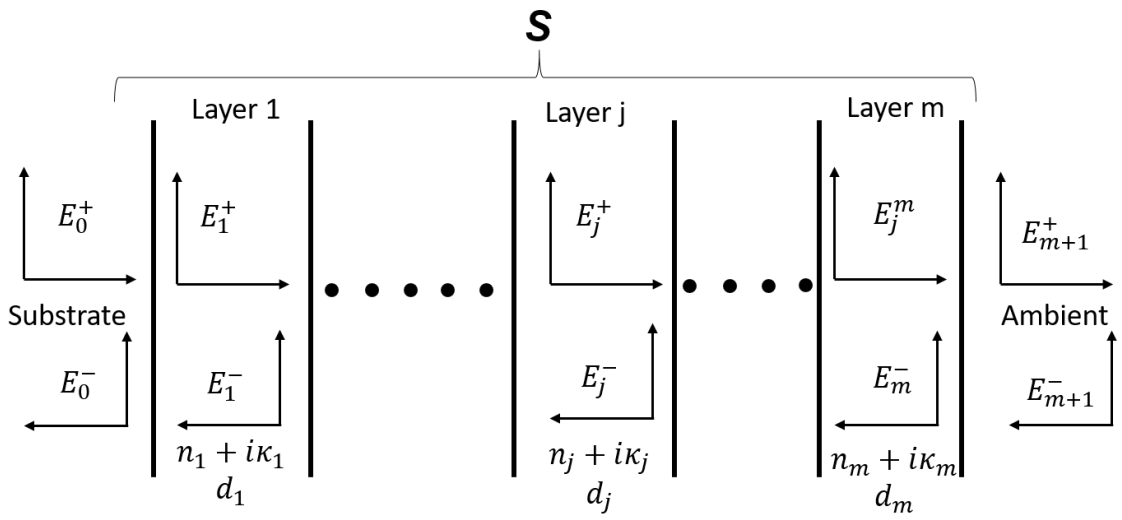

Figure 4.1 Generalized multilayer structure having m layers between semi-infinite transparent substrate and ambient. Each layer is described by thickness d_j and complex index of refraction.

The optical transfer matrix model by Pettersson et al.[170] is commonly used to take into account the distribution of exciting optical electric field intensity inside the thin film structure. The model employs an optical transfer matrix approach to solve for the reflection and transmission coefficient of the electromagnetic field in a multilayer structure. The model assumes that the layers are isotropic, homogeneous and parallel-flat interfaces such that the incident light at the device can be described by plane waves. The 2×2 scattering matrices are used to describe the plane wave incident on a multilayer structure having m layers between a semi-infinite transparent ambient and a semi-infinite substrate (Fig. 3.4). The total system transfer matrix (S) relating electric field at substrate and ambient is given by

$$\begin{bmatrix} E_o^+ \\ E_o^- \end{bmatrix} = S \begin{bmatrix} E_{m+1}^+ \\ E_{m+1}^- \end{bmatrix} \quad (4.1)$$

where S is constructed by using the interface matrix (I) and layer matrix (L) as:

$$S = \begin{bmatrix} S_{11} & S_{12} \\ S_{21} & S_{22} \end{bmatrix} = \left(\prod_{v=1}^{m} I_{(v-1)v}\, L_v\right) I_{m\,(m+1)} \quad (4.2)$$

where $I_{jk} = \frac{1}{t_{jk}} \begin{bmatrix} 1 & r_{jk} \\ r_{jk} & 1 \end{bmatrix}$, r_{jk} and t_{jk} are Fresnel reflection and transmission coefficient at interface *jk*, and layer matrix through layer *j* is given as $L_j = \begin{bmatrix} e^{-i\,(2\pi \frac{q_j d_j}{\lambda})} & 0 \\ 0 & e^{-i\,(2\pi \frac{q_j d_j}{\lambda})} \end{bmatrix}$, d_j is the layer thickness, $q_j = \tilde{n}_j \cos(\phi_j)$, the complex index of refraction $\tilde{n}_j = \eta_j + i\kappa_j$ is a function of wavelength of incident light and ϕ_j is the angle of refraction in layer j. The time average of energy absorbed per second at position x in layer j is given as:

$$Q_j(x) = \frac{1}{2}\, c\, \epsilon_o \alpha_j \eta_j \left| E_j^{+}(x) + E_j^{-}(x) \right|^2 \quad (4.3)$$

where the absorption coefficient $\alpha_j = \frac{4\pi\, \kappa_j}{\lambda}$, c is the speed of light, ϵ_o is the permittivity of free space, η_j is the refractive index and $\left| E_j^{+}(x) + E_j^{-}(x) \right|^2$ is the modulus square of electric field in layer j. The transport of photogenerated excitons in active layer is given by standard diffusion equation:

$$\frac{\partial n}{\partial t} = D\, \frac{d^2 n}{dx^2} - \frac{n}{\tau} + \theta_1\, \frac{Q\,(x)}{h\,\nu} \quad (4.4)$$

where n is the exciton density, D is the diffusion coefficient, τ is the mean exciton lifetime, θ_1 is the quantum efficiency of exciton generation, $h\nu$ is the excitation energy of the incident light. The first term represents exciton diffusion, second term is the exciton recombination, and third term represents exciton generation rate. Equation 3.9 is solved by

specifying the boundary at two interfaces. At the heterojunction between donor and acceptor layer the boundary condition is $n = 0$ at x=d_j for donor layer and x=0 for acceptor layer represent dissociation excitons reaching the interface. The short circuit photocurrent for donor layer is given as $J_{photo} = q\ \theta_2\ D\ \frac{\partial n}{\partial x}|_{x=d_j}$, while photocurrent for acceptor layer is given by $J_{photo} = q\ \theta_2\ D\ \frac{\partial n}{\partial x}|_{x=0}$, q is the electron charge and θ_2 is the exciton dissociation efficiency at the interface. The external quantum efficiency (EQE) of a photovoltaic device described as the ratio between number of charge carriers contributing to photocurrent and the number of incident photon is given as:

$$EQE\ (\%) = 1240\ \times \frac{J_{photo}}{\lambda\ I_o} \quad (4.5)$$

where I_o is the intensity and λ is the wavelength of the incident light. The readers are referred to the detailed code implementing the transfer matrix model in Appendix G.

4.2 Kinetic Monte Carlo Formalism

A Kinetic Monte Carlo formalism is employed in solving the exciton diffusion equation when the interfacial boundary conditions for excitons are unknown. The KMC resolves the unknown boundary condition by using the known imbalance in energy transfer rates.[86,156,171] The block diagram representing KMC formalism is show in Fig 4.2a. This approach divides each layer of the architecture into bins that are 1 nm thick. Each bin is assigned a set of local generation, energy transfer, and natural decay rates for the various events that can affect the exciton during its lifetime. Generation rates are calculated using an optical transfer matrix formalism as described in section 4.1.[170] Each of the rates except

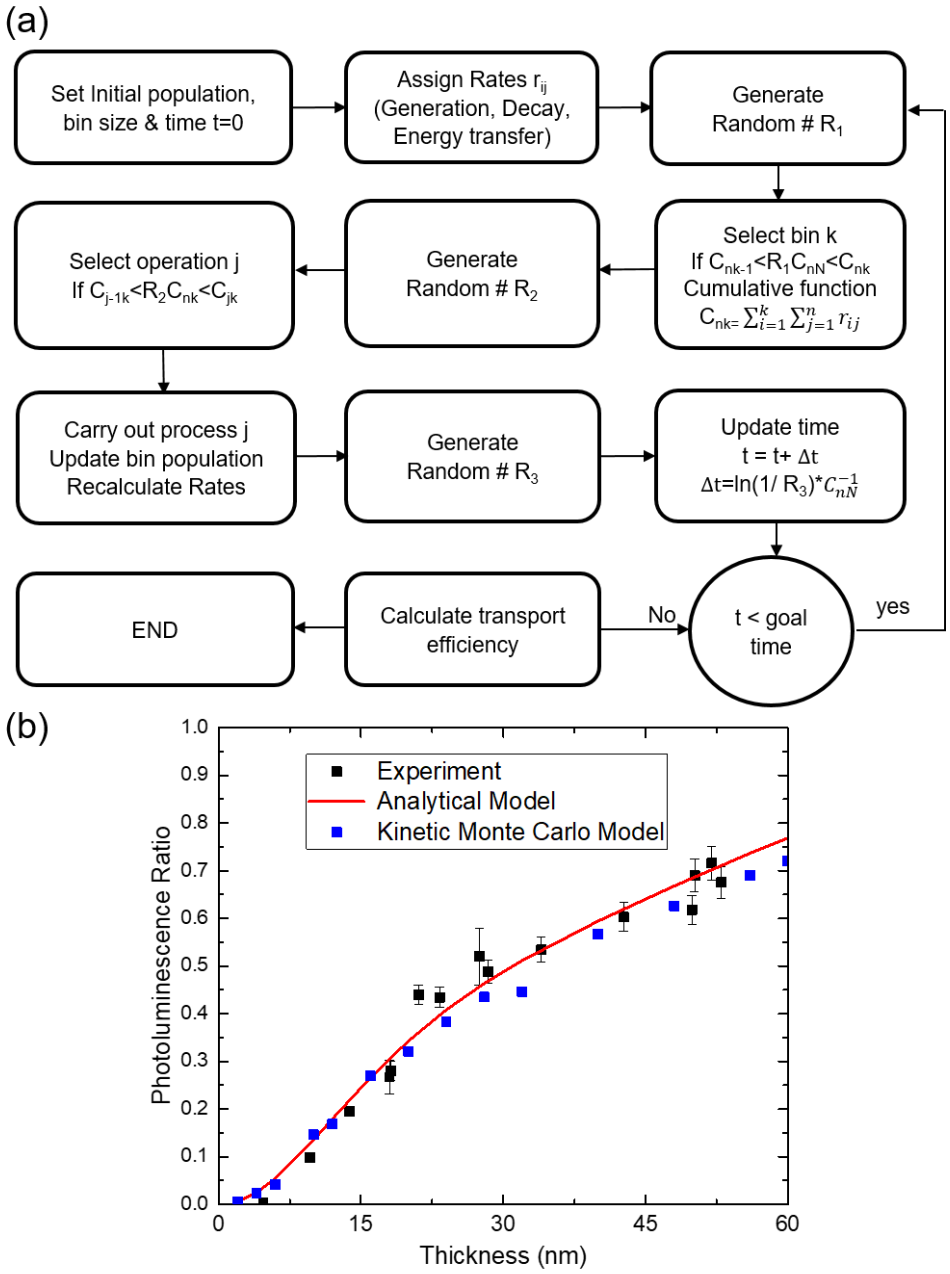

Figure 4.2 (a) Block diagram representation of the algorithm used to simulate the time evolution of the exciton density using a Kinetic Monte Carlo formalism. (b) Photoluminescence ratio fitting (quenched film PL divided by unquenched film PL) of C545T using both Kinetic Monte Carlo and analytical models of exciton diffusion. The extracted singlet exciton diffusion length is (12.7 ± 0.7 nm).

generation are then weighted by the bin populations. For each bin k, a cumulative function (C_{nk}) then sums all the rates from all n possible operations. The $C_{nN,}$ then sums the cumulative sum (C_{nk}) from all N bins in the system. A random number between 0 and C_{nN} then selects a bin, such that the probability to select a bin k is proportional to C_{nk}. For each selected bin k, a random number between 0 and C_{nk} selects a operation to be carried out. The operation is then performed for the selected bin and the exciton population is updated. Following this a random number is generated to update the time. This cycle repeats untill the simulation time is less than the goal time. The goal time in the KMC model is determined by the time the KMC simulation takes to reach steady state. The convergence to steady state is checked by assigning different initial bin populations and monitoring the rate of change in bin population as a function of time. It has been found that the simulation reaches steady state within 100 exciton lifetimes. The KMC model used in this thesis has been verified with experimental data and an analytical model [170] for diffusion in a single layer of 2,3,6,7-tetrahydro-1,1,7,7, tetramethyl-1H,5H,11H- 10(2-benzothiazolyl) quinolizine[9,9a,1gh] coumarin (C545T) with 1,4,5,8,9,11-hexaazatriphenylene hexacarbonitrile (HATCN) as an adjacent quencher (Fig. 4.2b).

4.3 Photoluminescence Based Diffusion Length Measurement

4.3.1 Thickness Dependent Photoluminescence Quenching

Thickness dependent photoluminescence (PL) quenching measurements are used to experimentally measure the exciton diffusion length (L_D) in luminescent films.[90,172] The general scheme for this measurement is shown in Fig. 4.3a. Excitons are optically

generated in the luminescent film with and without the presence of an adjacent quenching layer (electron or hole accepting material). Generated excitons that reach the quencher, as determined by its characteristic L_D are dissociated, thereby decreasing the PL.

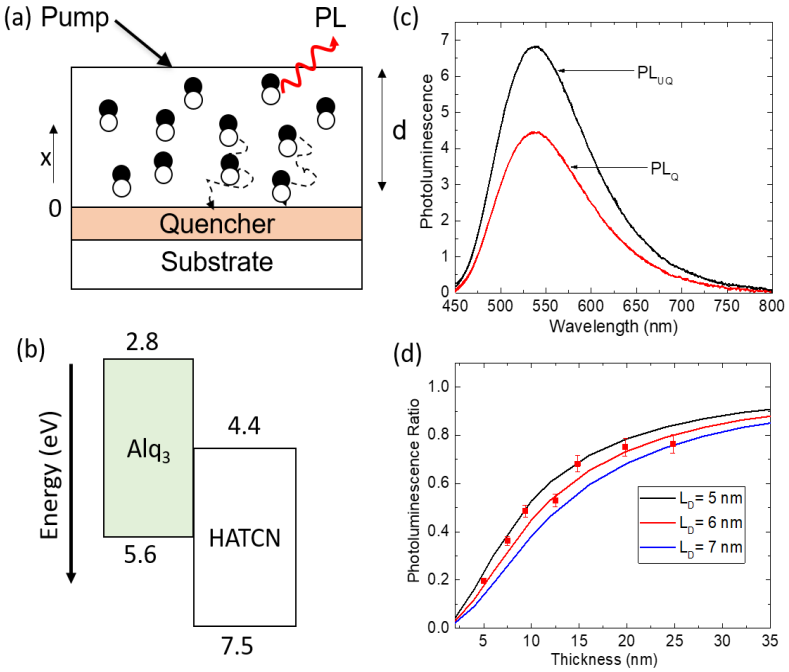

Figure 4.3 (a) Schematic of the PL quenching technique for the measurement of L_D. (b) Energy level diagram for an archetypical donor molecule Alq_3 and quencher HATCN. (c) Representative photoluminescence spectra of quenched and unquenched sample of Alq_3. (d) Experimental and fitted PL ratio data as a function of layer thicknesses.

Figure 4.3b shows the schematic of energy level diagram for an archetypical donor tris-(8-hydroxyquinoline)aluminum (Alq_3) and quencher HATCN. The PL is collected as a function of the luminescent film thickness both with and without the presence of quencher. Using PL spectra, an experimental PL ratio is constructed by dividing the integrated PL from the quenched sample (PL_Q) and unquenched sample (PL_{UQ}) (Fig. 4.3 c) as:

$$Exp.PL\ Ratio = \frac{\int_0^d PL_Q(\lambda)d\lambda}{\int_0^d PL_{UQ}(\lambda)d\lambda} \quad (4.6)$$

The PL ratio can then be modeled by integrating the exciton densities in each film calculated by solving standard diffusion equation Eq. 4.4 with the boundary condition between the luminescent film and quencher interface is $n = 0$ at x = 0 which represents dissociation of excitons reaching the interface. While the boundary conditions between luminescent film and exciton blocking layer or air is $\frac{\partial n}{\partial x} = 0$ at x = d, representing reflecting interface for excitons. In general, as the thickness of the luminescent film increases, a smaller percentage of optically generated excitons can reach the interface and be quenched, leading to a larger PL ratio. Iterative fitting is used to fit the experimentally measured PL ratios to extract L_D. For Alq_3, an L_D of (5.9 ± 0.6) nm is extracted from the measurement (Fig. 4.3 d).

4.3.2 Spectrally Resolved Photoluminescence Quenching

Spectrally resolved photoluminescence quenching (SRPLQ) instead employs a variation in pump wavelength for a given emission wavelength of a luminescent film.[146,173–175] This method allows the use of single thick film to extract L_D as compared to thickness dependent PL quenching. The spatial variation in the exciton distribution inside the film corresponds to the optical constants measured using ellipsometer. The PL ratio is calculated by measuring the PL intensity of the sample in the presence of quencher divided by the PL intensity without a quencher for a given emission wavelength (Fig. 4.4). SRPLQ can provide information about L_D of different features, such as an aggregate peak in the emission spectra.[176]

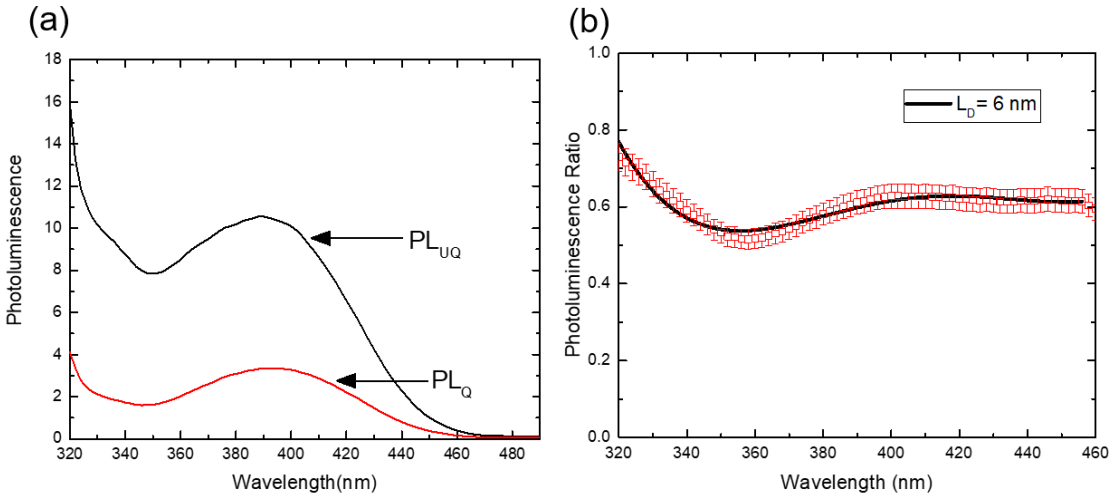

Figure 4.4 (a) Representative photoluminescence spectra of quenched and unquenched sample (b) Experimental and fitted PL ratio data as a function of excitation wavelength.

4.3.3 Transient Photoluminescence Quenching

Transient photoluminescence quenching measurement employs recording the PL decay from luminescence film in time-domain instead of steady-state output from the film. The transient PL approach is less sensitive to variations in luminescent intensity from the sample since the decay curve can be normalized to its maximum value. It can also offer additional insight into exciton dynamics that are not accessible from a steady state PL quenching measurement alone. The measurement is conducted in either in bilayer[177–180] or bulk quenching architectures.[153,181–184] In a bilayer architecture, the PL decay is recorded from quenched and unquenched sample for various layer thickness. The PL intensity at time t is proportional to the exciton density integrated over the thickness of the film. The exciton D is extracted by solving standard diffusion equation 4.4 in transient regime for the

quenched film, where τ is determined from the unquenched sample. The generation term in diffusion equation is given by g(x) $\delta\ (t - t_0)$ where δ is a delta type function and g(x) is determined from optical transfer matrix model. In bulk quenching architecture, luminescent material is blended with a small amount of quencher (0-10 wt.%). The PL decay is recorded for blended sample for various layer quencher concentration. The relative quenching efficiency is determined by integrating time-resolved PL for the blend and pristine organic semiconductor films respectively. The PL decay can be analyzed using Monte Carlo simulation[153,161,185] or Stern-Volmer model[132,185].

4.3.4 Photoluminescence Imaging

Photoluminescence imaging involves direct observation of exciton motion by imaging PL in both steady-state and transient regimes.[186–188] The method involves focusing a collimated laser beam through a microscope objecting lens unto the sample (Fig. 4.5). The PL from the excitons diffusing away from the excitation spot is spatially mapped using streak camera or single photon counting detecting avalanche photodiode. The image from the sample is then mapped to time-dependent exciton density as a function of position, convoluted with point spread function (PSF) of the imaging optics. The technique cannot resolve L_D greater than the spatial resolution of the imaging optics. Due to recent development in imaging optics this limit has been reduced to ~ 250 nm.[186] The technique is ideal for measuring exciton diffusion in single crystals or polycrystalline films of organic

semiconductors where long L_D observed. Additionally, temporal domain direct imaging can reveal information about the effect of morphology on time evolution of diffusivity.[188] This technique also requires the material to be emissive, however it can also map dark triplet excitons in endothermic singlet fission materials, where delayed fluorescence due to triplet-triplet annihilation is detected as a function of time. The delay fluorescence image is modelled using the diffusion equation with annihilation term.

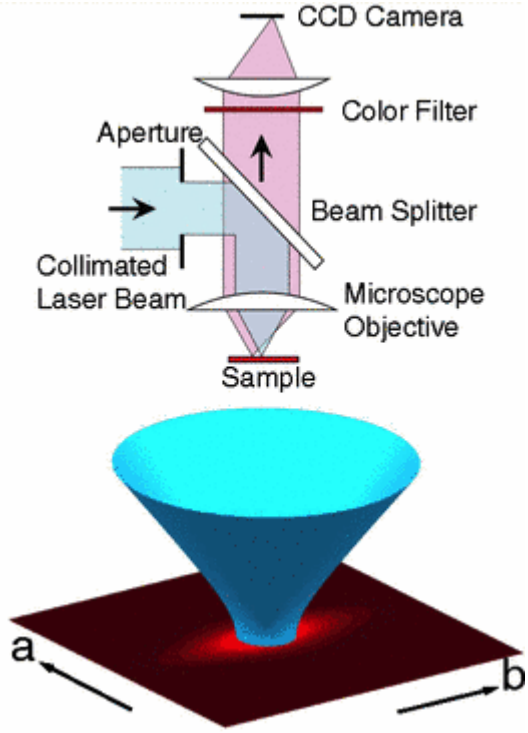

Figure 4.5 Experimental setup for exciton diffusion length measurement using photoluminescence imaging. (Reused by permission from American Physical Society Publishing: Physical Review Letters ref. 187, copyright 2011)

4.3.5 Transient Absorption Microscopy

Femtosecond transient absorption microscopy (TAM) employs direct imaging of singlet and triplet population in both space and time.[189–194] The singlet and triplet absorption transition peaks are first identified by performing polarization-dependent transient absorption spectroscopy. Exciton transport is then imaged by fixing the pump beam while the probe beam is scanned relative to the pump (Fig. 4.6). Different probe beams are selected to pump singlet and triplet states. The spatial distribution of the

differential transmission (ΔT) of the probe beam signal is then measured as a function of pump-probe delay times. The measurement of exciton L_D is limited by the spatial resolution of TAM which is the smallest measurable change in the excited-state population profile and not directly by the diffraction limit. The measurement take place at high photon flux which requires considering various bimolecular recombination rate such as triplet-triplet annihilation, singlet-triplet annihilation, and triplet-triplet fusion.

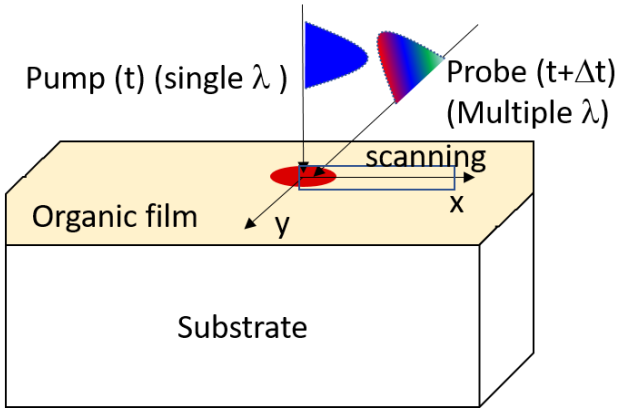

Figure 4.6 Generalized scheme for measuring exciton diffusion using transient absorption microscopy. Exciton diffusion is mapped by fixing the pump beam and spatially mapping the transmission from probe beam as a function of delay time.

4.3.6 Transient Exciton-Exciton Annihilation

The exciton L_D can also be extracted by studying exciton-exciton annihilation event as a function of pump intensity. The annihilation rate constant depends upon excitation intensity and diffusivity of excitons. The annihilation rate constant (γ) and exciton lifetime (τ) can be extracted from transient PL decay[180,195,196] or transient absorption curve[197,198]. For an isotropic diffusion and excition-exciton annihilation, the diffusivity (D) can be related to γ using Smoluchowski equation:[199]

$$\gamma = 4\pi R_a D \left(1 + \frac{R_a}{\sqrt{2\pi D t}}\right) \quad (4.7)$$

where R_a is the annihilation radius. It is difficult to measure it experimentally and often takes value as average intermolecular spacing assuming a simple cubic lattice.

4.3.7 Measurement in OLED Configuration

Exciton L_D can also be measured in an OLED through the use of an appropriate structure.[162–164,167,200] The exciton in the material of interest is electrically generation and confined to a thin layer adjacent to either hole or electron blocking layer. The excitons that diffuse through the host layer (spacer) can then be detected using a phosphorescent or fluorescent sensing layer positioned at different distance from the generation zone (Fig. 4.7). The triplet or singlet exciton density within the material of interest is measured by recording phosphorescence or fluorescence from the sensitizer as function of distance (L) from the recombination zone. The profile is then modelled to fit for exciton L_D. This measurement requires taking into account cavity effects on the outcoupling efficiency of the sensitizer, direct generation of excitons in the sensing layer, and boundary conditions at sensitizer and

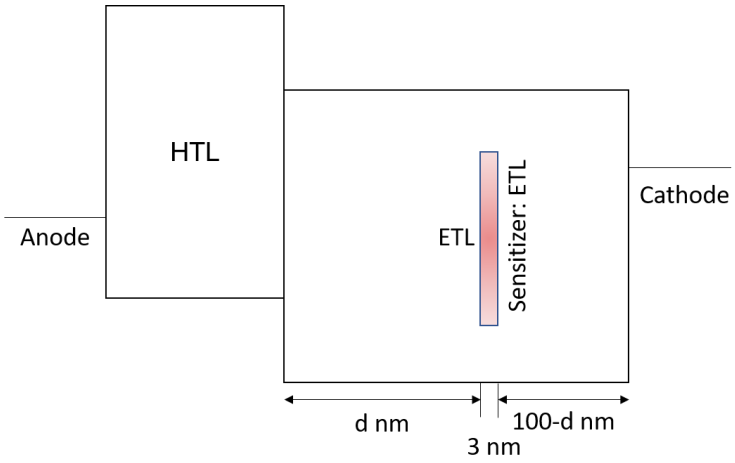

Figure 4.7 The OLED layer stack for measuring exciton diffusion length in electron transport layer. The excitons are generated in a thin layer adjacent to hole transport layer (HTL)and electron transport layer (ETL). The excitons that diffuse through the ETL (material of interest) can then be detected using a phosphorescent or fluorescent sensing layer positioned at different distance from the generation zone.

spacer layer. It is difficult to evaluate the effect of bimolecular quenching rates such as triplet-triplet annihilation and triplet polaron annihilation in this measurement.

4.4 Charge Carrier Based Diffusion Length Measurement

4.4.1 Photocurrent Based Measurement

A photocurrent based measurement is often used to measure exciton L_D for non-luminescent materials.[158,159,169,201–206] In these measurements, a material of interest is incorporated in a bilayer OPV architecture as a donor or acceptor layer and the device η_{EQE} is fit for L_D using an optical interference model and solution to the diffusion equation (Section 4.1). Recall from Chapter 3, that the η_{EQE} is a product of five efficiencies representing the steps of photoconversion. While good fits to the experimental data are often achieved using this measurement, the analysis requires assumptions about the charge separation η_{CS} and collection η_{CC} efficiencies respectively. If η_{CS} and η_{CC} are naively assumed to be unity, the fitting algorithm will incorporate photogenerated charge carrier losses into η_D and thus underestimate extracted L_D. Separate device-based methods can be used to measure these efficiencies. Chapter 9 of this thesis introduces a photocurrent ratio methodology which overcomes the limitation of conventional η_{EQE} based measurement.

4.4.2 Photovoltage Measurement

The L_D can also be determined by measuring photovoltage in an OPV at open-circuit.[207,208] In a bilayer OPV, photogenerated excitons diffuse towards a D-A interface consistent with the L_D of the material, forming an interfacial CT state. The resultant CT

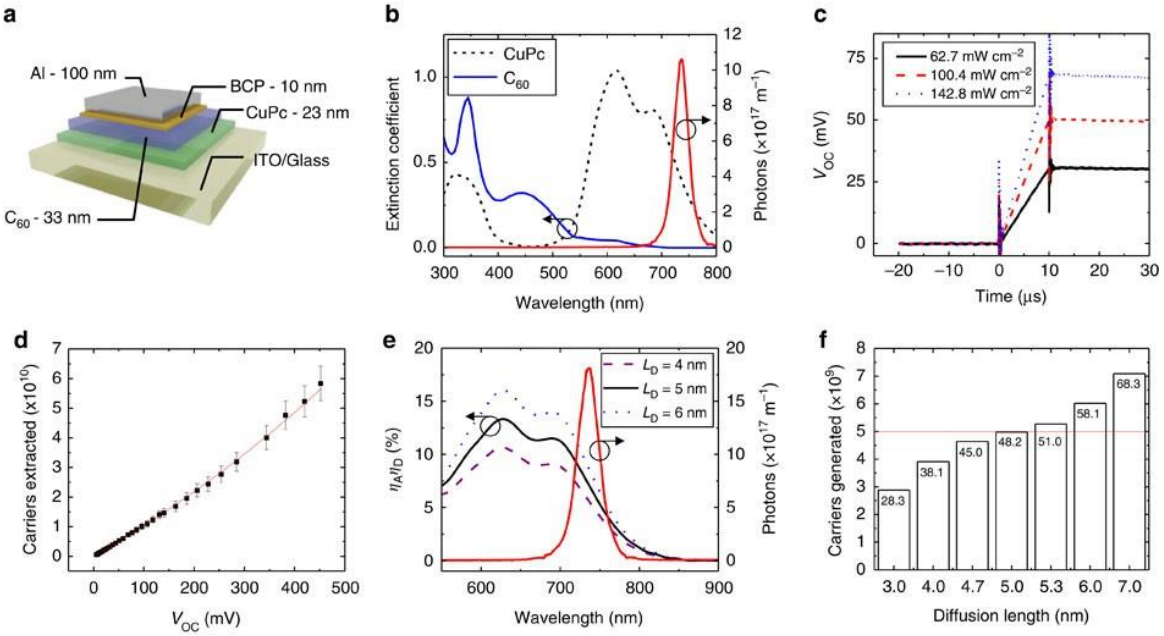

Figure 4.8 (a) Architecture for the planar heterojunction OPV based on the donor-acceptor pairing of CuPc-C_{60}. (b) Comparison of the extinction coefficients for CuPc and C_{60} as well as the spectrum of the LED pulse (λpeak=735 nm) used to pump CuPc. (c) Photovoltage rises recorded when pumping CuPc with the λ=735 nm LED at intensities of 62.7 mW cm^{-2} (black), 100.4 mW cm^{-2} (red) and 142.8 mW cm^{-2} (blue). (d) Relationship between charge carriers and voltage in the CuPc-C60 device obtained using the charge extraction method and an exponential fit to the data. The error bars represent the standard deviation across eight devices. (e) Simulated $\eta_A\eta_D$ curves for three CuPc L_D values with a constant C_{60} L_D of 12.1 nm compared with the time integrated LED pump spectrum. (f) Comparison of the predicted number of charge carriers generated (for multiple values of the CuPc L_D) to the photovoltage-based measurement (horizontal line). The V_{OC} (in millivolts) that would be measured for the corresponding number of charge carriers is labelled for each bar. (Reused from Springer nature: nature communication, ref. 207, copyright 2017 under the Creative Commons Attribution 4.0 International License)

state is dissociated to generate free charge carriers which occupy sites of disparate potential energy, producing a measurable photovoltage. In this measurement, the device is held at open-circuit and first illuminated at a select wavelength for photogeneration of excitons in donor or acceptor layer (Fig 4.8b). The photovoltage is recorded until a steady-state voltage is reached (Fig. 4.8c). Then, simultaneously, the illumination is turned off and the device

is switched to short-circuit recording resultant current transient. The integral of the current transient yields the number of charge carriers stored in the OPV, determining the relationship between the number of carriers and the photovoltage (Fig. 4.8d). The measurement is recorded as a function of illumination intensity resulting in a linear relationship between number of photogenerated excitons, free charge carriers and magnitude of photovoltage.[209–211] Non-geminate recombination is insignificant in comparison to charge collected using current transient, which results in unity η_{CC}. The L_D can be extracted by modeling η_A as a function of wavelength using optical transfer matrix formalism and η_D of the device using standard exciton diffusion equation (Eq. 4.4, Fig. 4.8e). The number of carriers that would be generated from exciton dissociation (n_{gen}) as a function of L_D is given by:

$$n_{gen} = \int \eta_A(\lambda)\, \eta_D(\lambda, L_D) Pinc(\lambda) d\lambda \quad (4.8)$$

where P_{inc} is the number of incident photons. The values of L_D are then iterated to match n_{gen} with measured number of charge carriers (Fig. 4.8f). In this measurement, the extracted L_D will be an underestimate if η_{CS} is non-unity due to rapid geminate recombination of CT state. This measurement does not account for loss due to exciton-polaron quenching.

4.4.3 Microwave Spectroscopy

Time-resolved microwave conductivity is an electrode-less technique that measures the time dependent change in reflected power from a microwave cavity, inside of which a bilayer architecture of the material of interest and the quenching medium is located.[212–217] A variation in reflected power results from a change in conductivity of the quenching film

which depends upon number of photogenerated charge carriers, and hence L_D. The measurement is insensitive to charge carrier collection losses, however it requires a quenching medium, often TiO_2, to be more conductive than organic semiconductor film. The technique can probe non-emissive materials and is insensitive to non-geminate recombination losses, however rapid geminate recombination affects measured L_D. Furthermore, the degree of geminate recombination will be different for TiO_2 than an acceptor used in an OPV.

4.4.4 Surface Photoconductivity

Surface photoconductivity measurements can used to determine exciton L_D in single crystals.[147] In this measurement, the change in surface conductivity results from dissociation of photogenerated excitons diffusing to the surface from the bulk. The surface conductivity is measured by depositing electrodes on top of the surface of single crystal. At the surface, excitons can dissociate either through surface defects or in the presence of a quenching material. Photocurrent excitation spectra is collected as function of wavelength and polarization angle. The polarization angle is defined as the angle between linearly polarized light and high mobility axis of single crystal. Changing the polarization angle results in periodic variation in surface conductivity due to the angular dependence of absorption coefficient. The relative amplitude of the photoconductivity variation is then fit to obtain L_D. Longer L_D will overcome variable absorption length and show smaller variation in surface photoconductivity while the shorter L_D will show large difference in surface photoconductivity.

4.5 Summary

In this chapter, exciton diffusion modelling techniques used in this thesis are presented. Different PL-based and charge-based techniques for L_D are reviewed. While PL-based techniques probe excitons which fail to reach a dissociating interface, charge carrier-based techniques probe the number of excitons which are successfully dissociated at a D-A to extract exciton L_D. In addition to presenting the method for extracting L_D, the constraints of each techniques are recognized.

5 Measurement of Triplet Diffusion Length in Organic Semiconductor Thin Films

This chapter is a summary and extension of published work in journal of materials chemistry C entitled “Measurement of the Triplet Exciton Diffusion Length in Organic Semiconductors.”[218] This work is supported by National Science Foundation (NSF) Electronics, Photonics and Magnetic Devices under ECCS-1509121. The author acknowledges C. Clark for X-ray diffraction measurements of as-grown thin films of active materials.

5.1 Background

Chapter 3 discussed in detail the critical role of exciton transport in an organic photovoltaic cell and the importance of enhancing L_D through the utilization of long-lived triplet excitons. Several methodologies to probe exciton migration were discussed in Chapter 4, however direct probing of exciton migration using photoluminescence-based measurements cannot be applied due to non-emissive nature of triplet excitons. Frequently, device-based measurements are used to indirectly probe triplet diffusion via the byproducts of their dissociation in an OPV or by transfer to a luminescent species. Specifically, these include the fitting of external quantum efficiency spectra in OPVs,[158,159,201,205,206] photovoltage measurements,[207,208,219] photoconductivity measurements,[147] microwave spectroscopy,[220–222] and a variety of measurements in OLED configurations.[162–164,167,200]

While capable of yielding a value for the exciton diffusion length (L_D), device-based methods can be limited in their ability to measure the intrinsic value of L_D due to unknown recombination losses or interfacial energy transfer rates.[206] Further, the roles of triplet-triplet annihilation, triplet-polaron quenching, exciton formation zone migration, and the contribution from singlet diffusion are also difficult to evaluate. Consequently, there is frequently disagreement among different methods of measurement for the triplet L_D. While non-device-based methods ultrafast transient absorption microscopy (TAM)[189,190,223] are capable of probing the intrinsic diffusion length of both non-radiative triplets as well as mobile singlets excitons, however, the measurement takes place at high photon flux which requires taking into account various bimolecular recombination rate such as triplet-triplet annihilation, singlet-triplet quenching, and triplet-triplet fusion. It is for these reasons that the direct probing of non-radiative triplets using a phosphorescent sensitizer[161,168] is of particular interest, due to its ability to distinguish between singlet and triplet transport, as well as prevent bimolecular triplet quenching mechanisms. However, in this method, the quenching efficiency of triplet excitons by the phosphorescent sensitizer is seldom known quantitatively, and hence can cause inaccuracy in reported values. Here, we develop a methodology to resolve this issue and apply the technique to extract the triplet L_D for a variety of materials.

5.2 Phosphorescent Sensitizer-Based Methodology

Figure 5.1a shows a phosphorescent sensitizer-based methodology for measuring dark triplet excitons in organic semiconductor thin films. Singlet excitons are optically

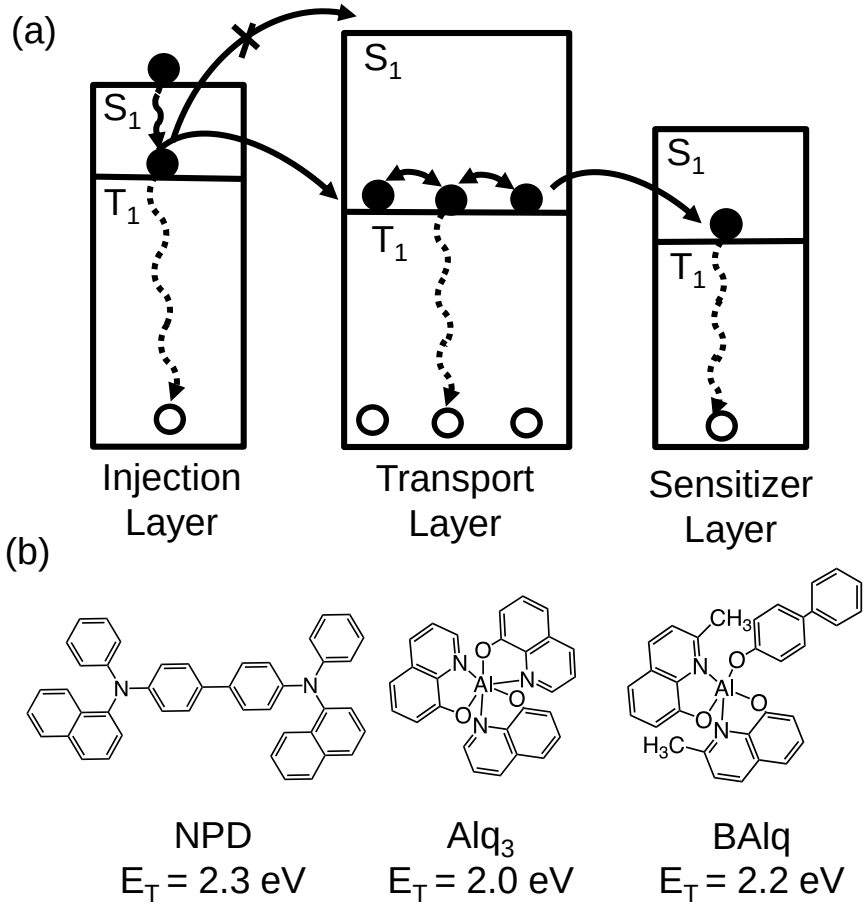

Figure 5.1 (a) A generalized scheme for probing the diffusion length of non-radiative triplet excitons in organic semiconductor thin films. Excitons are injected into the transport layer by energy transfer from an adjacent phosphorescent injection layer. Excitons diffuse through the material of interest (transport layer) before undergoing energy transfer to the phosphorescent sensitizer layer. The triplet energy levels of the three layers are selected to ensure downhill energy transfer from the injection layer to the sensitizer layer. (b) Molecular structure and triplet energy (E_T) of three archetypical fluorescent semiconductors investigated in this study.

generated in a thin phosphorescent injection layer which undergoes rapid intersystem crossing due to spin-orbit coupling.[224] The resulting triplets are injected directly into the triplet energy level (E_T) of an adjacent transport layer (*i.e.* the material of interest), with

transfer from the injection layer to the singlet level of the transport layer being frustrated by its endothermicity.[225] Triplet excitons that diffuse through the full thickness of the transport layer may undergo energy transfer to a low-energy phosphorescent sensitizer layer, leading to measurable photoluminescence.[161,226] Exciton diffusion in the transport material is therefore characterized by a transport efficiency (η_T), defined as the ratio of the exciton collection rate by the sensitizer and the exciton injection rate into the transport layer. Experimentally, η_T is calculated based on the reduction (increase) of photoluminescence (PL) from the injector (sensitizer) in the presence of the transport layer versus a wide energy gap exciton blocking layer ($\Delta PL^{Injector}$ and $\Delta PL^{Sensitizer}$, respectively) as:

$$\eta_T = \frac{\Delta PL^{Sensitizer}}{\Delta PL^{Injector}} \times \frac{\eta^{PL}_{Injector}}{\eta^{PL}_{Sensitizer}} \quad (5.1)$$

In Eq. (5.1), $\eta^{PL}_{Injector}$ and $\eta^{PL}_{Sensitizer}$ are the outcoupled PL efficiencies of the injector and sensitizer layers. The outcoupled PL efficiencies are determined experimentally as discussed in the Appendix D.

In Eq. (5.1), the assumption is made that any changes in PL from the injector and sensitizer layers come from the transport of excitons through the material of interest. For this to be accurate, the short-range quenching of excitons in the material of interest by the sensitizer must be efficient. Without knowledge of the quenching efficiency, the extracted L_D may not reflect the intrinsic behavior of the material. Here, we extract the transfer rate (k_Q) from the transport layer to the phosphorescent sensitizer by varying the concentration of the sensitizer in a non-quenching host. In this way, the number of quenching sites (and

the quenching efficiency) at the interface is also varied in a predictable manner. Increasing the sensitizer concentration leads to a concomitant increase in η_T until the quenching efficiency reaches unity.

In this chapter, η_T is measured as function of thickness in order to track the injected triplet exciton density reaching the sensitizer layer. In parallel, measurements of η_T as a function of sensitizer concentration are used to extract k_Q and determine an appropriate boundary condition for the exciton density. A kinetic Monte Carlo (KMC) formalism described in previous chapter 4 is used to model the dependence of η_T and extract the triplet diffusion length of the transport layer.[171,227] The injected triplet exciton density in the transport layer is kept small (~10^{15} cm^{-3}) to avoid triplet-triplet annihilation.[228] The triplet diffusion length is probed in thin films of the archetypical organic semiconductors N,N′-di(1-naphthyl)-N,N′-diphenyl-(1,1′-biphenyl)-4,4′-diamine (NPD), tris-(8-hydroxyquinoline)aluminum (Alq_3) and bis-(8-hydroxy-2-methylquinoline)-(4-phenylphenoxy)aluminum (BAlq). The method is validated against thickness dependent photoluminescence quenching measurements for singlet exciton diffusion in both Alq_3 and C545T.

5.3 Experimental Details

All thin films are deposited using vacuum thermal sublimation (base pressure <$7x10^{-7}$ Torr) at a total rate of 0.1 nm s^{-1} on glass substrates. Substrates are pre-cleaned by sequentially sonicating in tergitol solution, deionized water, and acetone, followed by rinsing in isopropanol. Material optical constants and film thicknesses are measured using

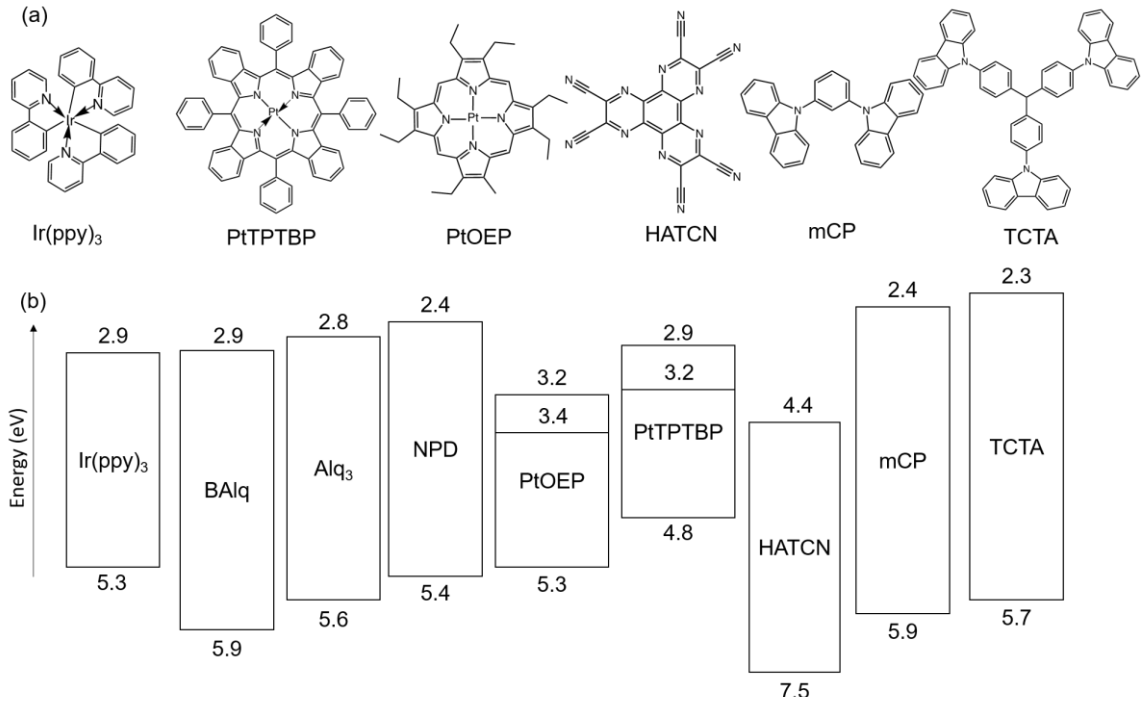

Figure 5.2 (a) Molecular structures and (b) energy level of active materials used in the chapter

a J. A. Woollam variable-angle spectroscopic ellipsometer (Cauchy model). Active materials of N, N'-di-1- naphthalenyl-N,N'-diphenyl [1,1':4',1'':4'',1'''-quaterphenyl]-4,4'''-diamine (4P-NPB), tris[2-phenylpyridinato-C2,N]iridium(III) ($Ir(ppy)_3$), tris(4-carbazoyl-9-ylphenyl)amine (TCTA), 1,3-Bis(N-carbazolyl)benzene (mCP), NPD, C545T and Alq_3 are purchased from Luminescence Technology Corporation; BAlq is purchased from Sigma Aldrich, and platinum octaethylporphyrin (PtOEP) and platinum tetra-phenyl-tetra-benzo-porphyrin (PtTPTBP)[229,230] is purchased from Frontier Scientific. The HATCN[231] is used as a quencher for measuring the singlet L_D of Alq_3 and C545T is purchased from Luminescence Technology Corporation. In this work, the quenching efficiency of HATCN is assumed to unity, due to its favorable energy offset for electron

transfer.[232] Photoluminescence spectra are measured under N_2 purge using a Photon Technology International QuantaMaster 400 Fluorometer equipped with a photomultiplier detection system. Samples are excited at an angle of 70^o to sample normal using a monochromatic Xe lamp. The incident light intensity is measured using a S2281 silicon photodiode with a mask of 0.36 cm^2 area. To check for the presence of triplet-triplet annihilation in our measurements, PL spectra are collected at two different pump intensities using a neutral density filter (OD = 0.5). The experimental data is fitted using a non-linear least squares methodology where fit error in the calculation of L_D represents a 95% confidence interval. To detect any crystallinity in the transport layers, X-ray diffraction measurements are carried out at an incident angle of 8 degrees, while samples are scanned using a 2D detector which spans from $2\theta = 1$ degree to 53 degrees. Triplet energy levels for $Ir(ppy)_3$ and the sensitizer molecules are determined from room temperature phosphorescence spectra. All other triplet energy levels referenced in this work are determined using the first peak of the phosphorescence taken from literature. [164,233,234]

5.4 Methodology Validation

To demonstrate the validity of the phosphorescent sensitizer-based technique, the method is first applied to measure the singlet diffusion length of Alq_3 and the result compared to well-established thickness-dependent PL quenching-methods.[172] In the generalized scheme of Fig. 5.1a, singlet excitons are injected from fluorescent 4P-NPB into Alq_3 by optical pumping at a wavelength of λ=380 nm, where absorption occurs mainly i4P-NPB (Fig. 5.3 b). An injector layer of 4P-NPB is chosen due to its favorable spectral

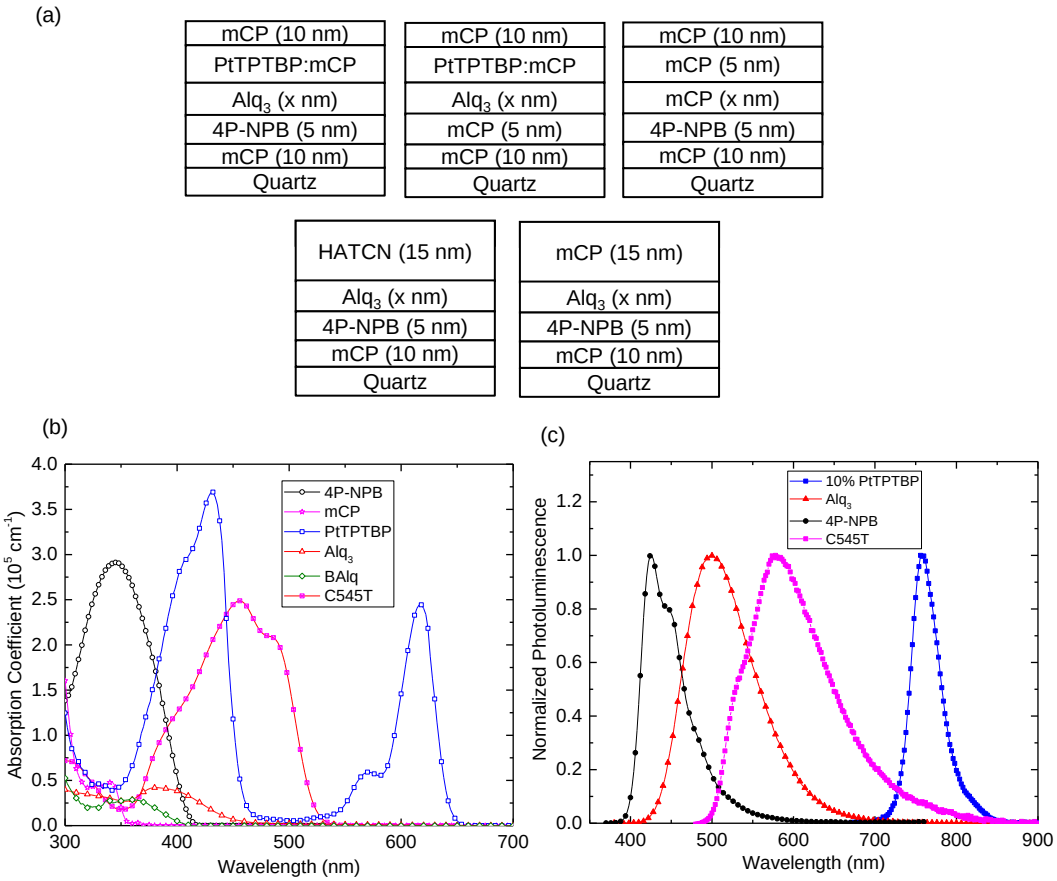

Figure 5.3 (a) Device architecture for measuring the singlet exciton diffusion length of Alq_3 using the phosphorescent sensitizer-based approach and thickness dependent photoluminescence quenching. The excitons diffusing through Alq_3 are captured using 10 wt.% PtTPTBP doped in mCP. (b) Absorption coefficient of Alq_3, BAlq, C545T, 4P-NPB, mCP and PtTPTBP. The absorption coefficient is calculated from the extinction coefficient extracted from ellipsometric measurements on a 30-nm-thick film deposited on a glass substrate. (c) Normalized photoluminescence of Alq_3, C545T, 4P-NPB and 10 wt.% PtTPTBP in mCP.

overlap with the absorption spectrum of Alq_3 (Fig. 5.3 for active material emission and absorption spectra), enabling efficient Förster energy transfer. Excitons migrate through Alq_3 and are detected by monitoring phosphorescence from a sensitizer layer of PtTPTBP at λ=770 nm. The exciton transport efficiency is extracted by comparing changes in PL

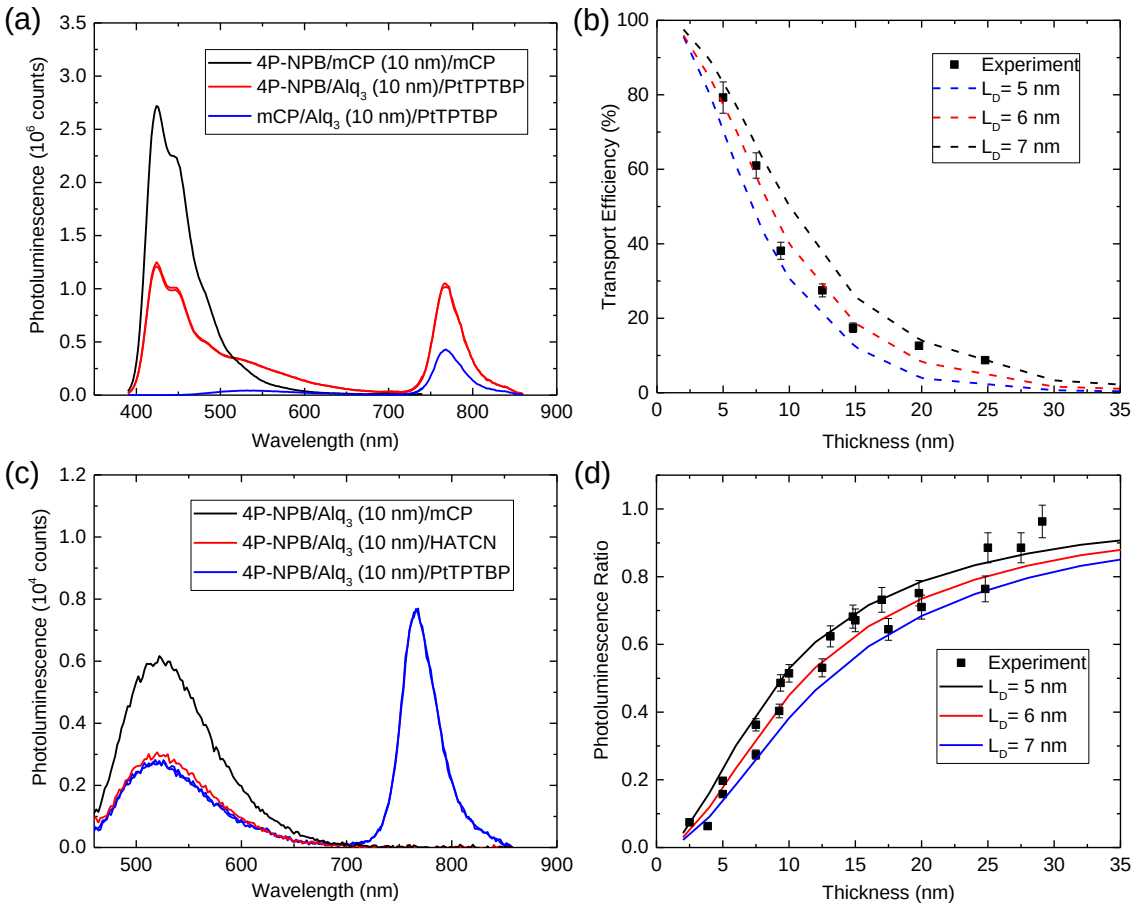

Figure 5.4 (a) Photoluminescence spectra collected for the multilayer structures (4P-NPB/mCP (x nm)/mCP or 4P-NPB/Alq_3 (x nm)/10 wt.% PtTPTBP:mCP and mCP/Alq_3 (x nm)/10 wt.% PtTPTBP:mCP) used to extract the singlet diffusion length of Alq_3 using the phosphorescent sensitizer-based approach. The structure is pumped at a wavelength of λ=380 nm where a majority of excitons are generated in the 4P-NPB injection layer. The excitons that diffuse through Alq_3 are detected using 10 wt.% PtTPTBP doped in mCP. (b) Experimental and simulated (lines) transport efficiency as a function of transport layer thickness. The L_D is extracted from a KMC simulation. (c) Photoluminescence spectra used to extract the singlet diffusion length of Alq_3 using thickness dependent PL quenching. The structure (4P-NPB/Alq_3 (x nm)/mCP and 4P-NPB/Alq_3 (x nm)/HATCN) is pumped at a wavelength of λ=440 nm where all the excitons are generated in Alq_3. (d) Photoluminescence ratio versus thickness for determination of the singlet exciton diffusion length of Alq_3.

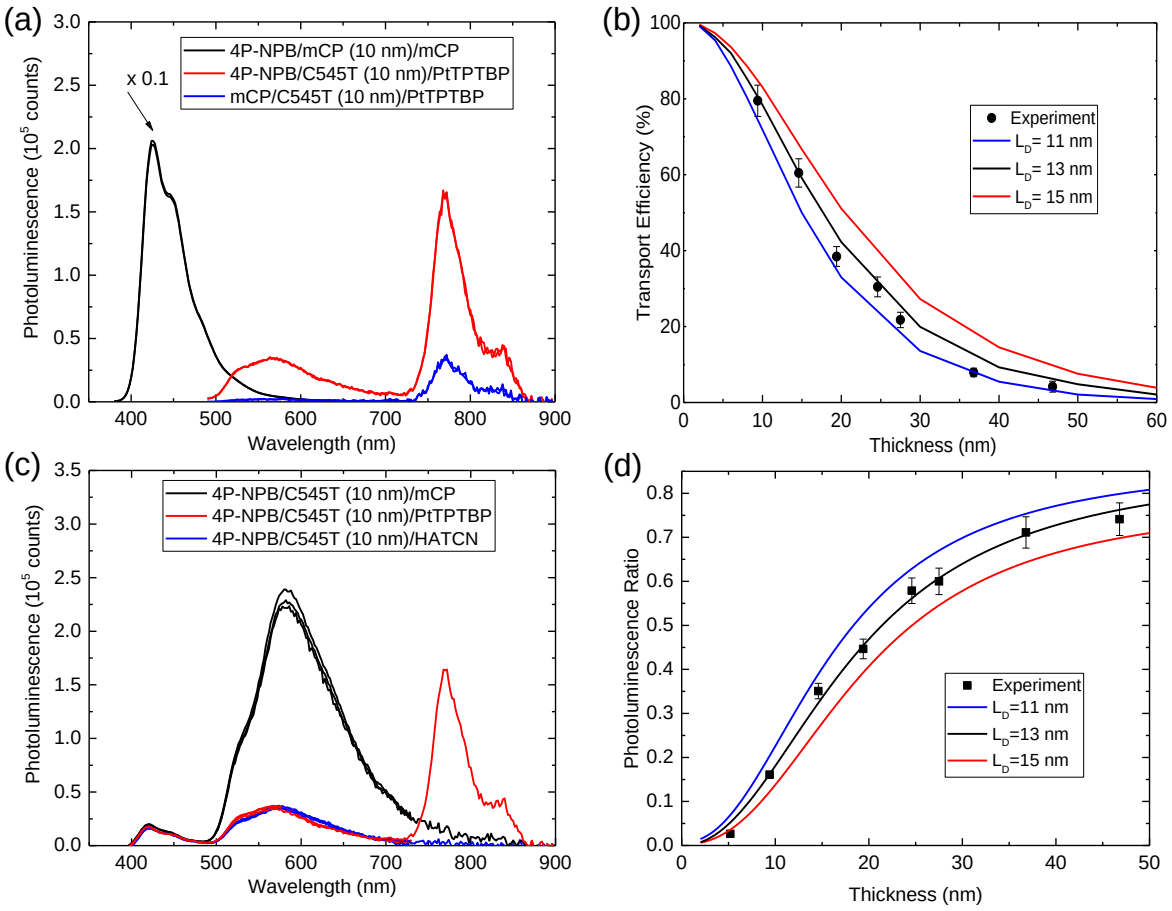

Figure 5.5 (a) Representative photoluminescence spectra for the architectures (structures (4P-NPB (5 nm)/mCP (10 nm)/mCP(15 nm), 4P-NPB (5 nm)/C545T (10 nm)/45 wt.% PtTPTBP:mCP (5 nm)/mCP (10 nm), and mCP (5 nm)/C545T (10 nm)/ 45 wt.% PtTPTBP:mCP (5 nm)/mCP (10 nm)) used to probe the singlet diffusion length of C545T using the phosphorescent sensitizer-based approach. C545T singlet excitons in a neat film emit at a peak wavelength λ=575 nm. The structure is pumped at a wavelength of λ=370 nm where the majority of excitons are generated in the injection layer of 4P-NPB. Excitons diffusing through C545T are harvested using a film of 45 wt.% PtTPTBP doped in mCP. (b) Experimental and simulated (line) transport efficiency as a function of transport layer thickness. An L_D of (12.2 $\pm$ 0.7) nm is extracted from KMC simulations. (c) Representative photoluminescence spectra for the architectures (4P-NPB/C545T (10 nm)/mCP and 4P-NPB/C545T (10 nm)/HATCN) used to probe the singlet diffusion length of C545T using thickness dependent photoluminescence quenching. (d) Photoluminescence ratio versus thickness for determination of singlet L_D of C545T. An L_D of (12.4 $\pm$ 0.8) nm is extracted by fitting experimental data using a 1D steady-state diffusion equation.

from PtTPTBP and 4P-NPB (Fig. 5.4a) in the case when the injector layer of 4P-NPB is present, and where it is replaced by a non-absorbing, wide energy gap spacer layer of mCP.

In this way, the increase in photoluminescence from PtTPTBP due to energy transfer from 4P-NPB can be isolated from direct optical excitation (*i.e.* where the injection layer of 4P-NPB is replaced with mCP). The η_T is calculated using Eq. (5.1) and the associated architecture for measurement is shown in Fig. 5.3a. The KMC modelling of experimentally measured η_T as a function of Alq_3 thickness results in a singlet L_D of (5.9 ± 0.6) nm (Fig. 5.4b).

The architecture for comparing the phosphorescent sensitizer technique against thickness-dependent PL quenching for Alq_3 singlets is also shown in Fig. 5.3a. This method requires the measurement of PL from the material of interest both with and without an adjacent quenching layer, with the ratio of these two quantities fit as a function of thickness for L_D. Here, the sensitizer layer is replaced by a top quenching layer of HATCN or an exciton blocking layer of mCP for the quenched and unquenched samples, respectively. Singlets are generated in Alq_3 by optical pumping at a wavelength of λ=440 nm, where absorption occurs mainly in Alq_3. A PL ratio is calculated as a function of Alq_3 layer thickness as the ratio of the integrated PL spectrum with and without an adjacent quenching layer (Fig. 5.4c). The analytical modelling of the experimentally measured PL ratio also yields a singlet L_D of (5.6 ± 0.4) nm (Fig. 5.4d),[170] validating the sensitizer-based

technique. The method is also verified for the organic fluorescent dye C545T which results in a L_D of (12.2 $\pm$ 0.7) nm as shown in Fig. 5.5.

5.5 *Application to Archetypical Organic Semiconductor Materials*

Triplet exciton diffusion is examined for three archetypical organic molecules: NPD, Alq_3 and BAlq. Thin films of these materials show no scattering peaks in X-ray diffraction, consistent with previous reports showing that as-grown films of these materials are amorphous.[235,236] All three of these materials are used frequently as transport layers in OLEDs and there is disagreement among the reported L_D values for both NPD and Alq_3 (Chapter 3, Table 3.1).[78] Here, the case of NPD is considered first to demonstrate the methodology in detail using the architecture of Fig. 5.6a. Using a phosphorescent injector layer of $Ir(ppy)_3$ (E_T = 2.4 eV),[164] the system is pumped at a wavelength of λ=470 nm, where absorption only occurs in $Ir(ppy)_3$ and no singlet excitons are generated in NPD (Fig. 5.6b). Triplets are injected into NPD and those that migrate through the layer may undergo energy transfer to a sensitizer layer of PtOEP (E_T = 1.9 eV)[164] doped in a wide energy gap host of TCTA (E_T = 2.8 eV).[234] The η_T is extracted by comparing the photoluminescence from PtOEP and $Ir(ppy)_3$ in the case when the transport layer of NPD is present, and where it is replaced by a wide gap spacer layer of TCTA (Fig. 5.6c). The photoluminescence spectra in Fig. 5.6c are deconvoluted using the separately measured photoluminescence spectra of PtOEP and $Ir(ppy)_3$ (Fig. 5.6b). The decrease in photoluminescence from $Ir(ppy)_3$ when adjacent to NPD reflects triplet exciton injection into NPD. Similarly, the

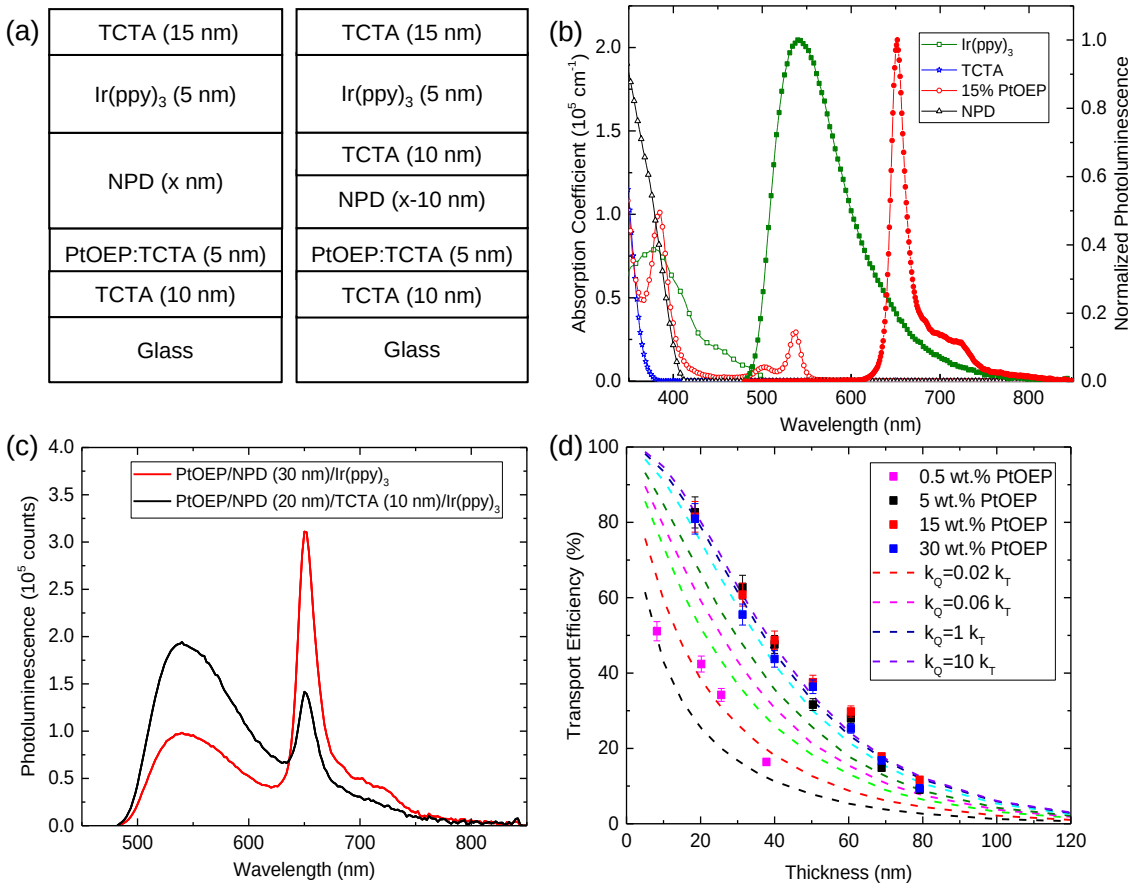

Figure 5.6 (a) Architectures used to extract the transport efficiency and triplet L_D for NPD as a function of thickness. The structure is pumped at a wavelength of λ=470 nm where the majority of excitons are generated in $Ir(ppy)_3$ injection layer. (b) Absorption coefficient (open symbols) and normalized photoluminescence (solid symbols) for the materials of interest. Spectra for PtOEP are collected for films of 15 wt.% PtOEP in TCTA. (c) Representative photoluminescence spectra for multilayer structures (15 wt.% PtOEP:TCTA/NPD (30 nm)/$Ir(ppy)_3$ and 15 wt.% PtOEP:TCTA/NPD (20 nm)/TCTA (10 nm)/$Ir(ppy)_3$) used to probe the triplet diffusion length of NPD using the phosphorescent sensitizer-based approach. (d) Experimental (symbols) and simulated (line) transport efficiency as a function of transport layer thickness. The η_T versus thickness is plotted for various values of transfer rate (k_Q) to the sensitizer relative to bulk energy transfer (k_T) for a fixed NPD triplet L_D=30 nm.

corresponding increase in photoluminescence from PtOEP reflects triplet excitons that diffuse through NPD and undergo energy transfer into the sensitizer layer. The boundary condition at the interface between NPD and the sensitizer layer is determined by increasing the concentration of PtOEP molecules from 0.5 wt.% to 30 wt.%. In Fig. 5.6d, the experimentally measured values of η_T as a function of NPD thickness are similar for PtOEP concentrations >5 wt.%, signifying that all excitons reaching the interface are quenched. The boundary condition is implemented in the KMC model by varying k_Q to the sensitizer

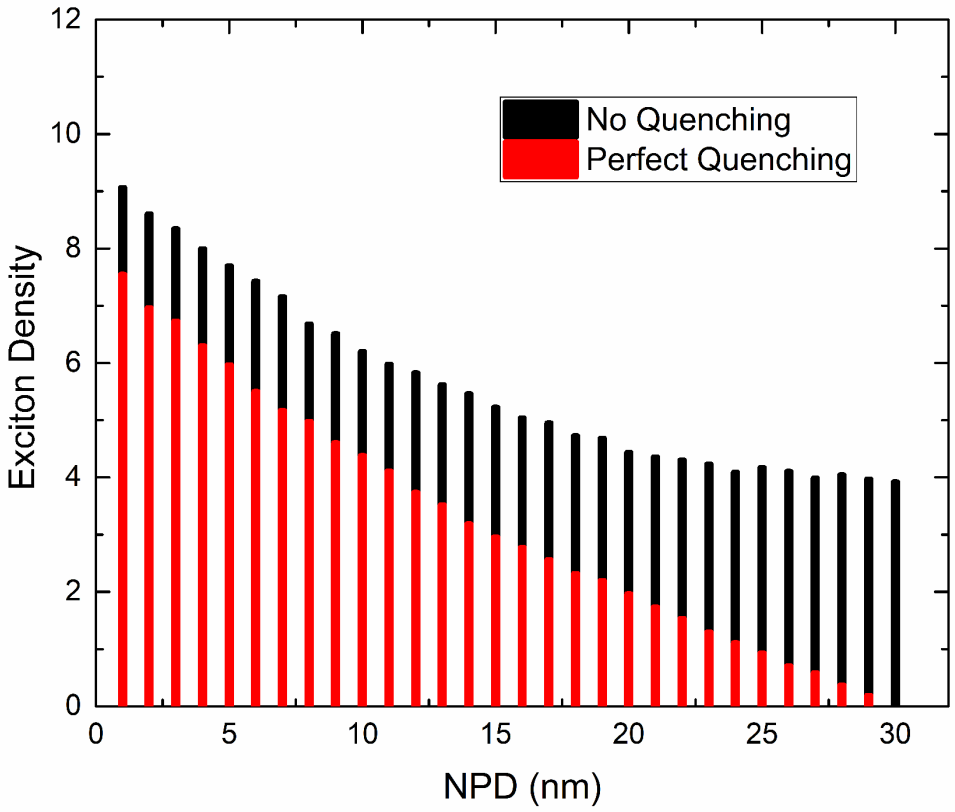

Figure 5.7 Simulated exciton density profile inside transport layer, NPD under no quenching and perfect quenching by sensitizer.

layer with respect to energy transfer (k_T) within the layer. The k_T can linked to the exciton diffusivity (D) and L_D as described by Eq. 2.9 in Chapter 2. The KMC modelling of the experimentally measured dependence of η_T on NPD thickness yields $L_D = (29.8 \pm 1.1)$ nm for the triplet of NPD (Fig. 5.6b). The measured L_D is larger than that previously obtained by fitting device photocurrent, likely reflecting device specific recombination losses.[158] The measured L_D for NPD is smaller than the previous related work which has doped a discontinuous sensitizer layer into the transport layer and assumed that the sensitizer does not significantly affect the underlying triplet density, such that the sensitizer emission can be fit with an exponential decay curve.[161] The current work suggests that accurate determination of the triplet L_D depends upon both the sensitizer concentration and boundary condition assumptions (Fig. 5.7). Inaccurate assumptions for a given sensitizer concentration can lead to either overestimation or underestimation of L_D. For example, in the current work, the incorrect assumption of perfect quenching by 0.5 wt.% PtOEP would yield an underestimated triplet L_D = 12 nm. Similarly, assuming here that the sensitizer does not affect the exciton density in the case of quenching by 15 wt.% PtOEP yields an overestimated triplet L_D = 52 nm.

The triplet exciton diffusion lengths of Alq_3 and BAlq are similarly determined using a sensitizer of PtTPTBP (E_T = 1.6 eV) doped in mCP (E_T = 2.9 eV)[233]. The triplets are injected by optically pumping $Ir(ppy)_3$ at a wavelength of λ=470 nm. Triplets diffusing through the transport layer are probed for two different concentration of sensitizer (5 wt.% and 15 wt.% PtTPTBP) in order to check the quenching efficiency of excitons reaching the

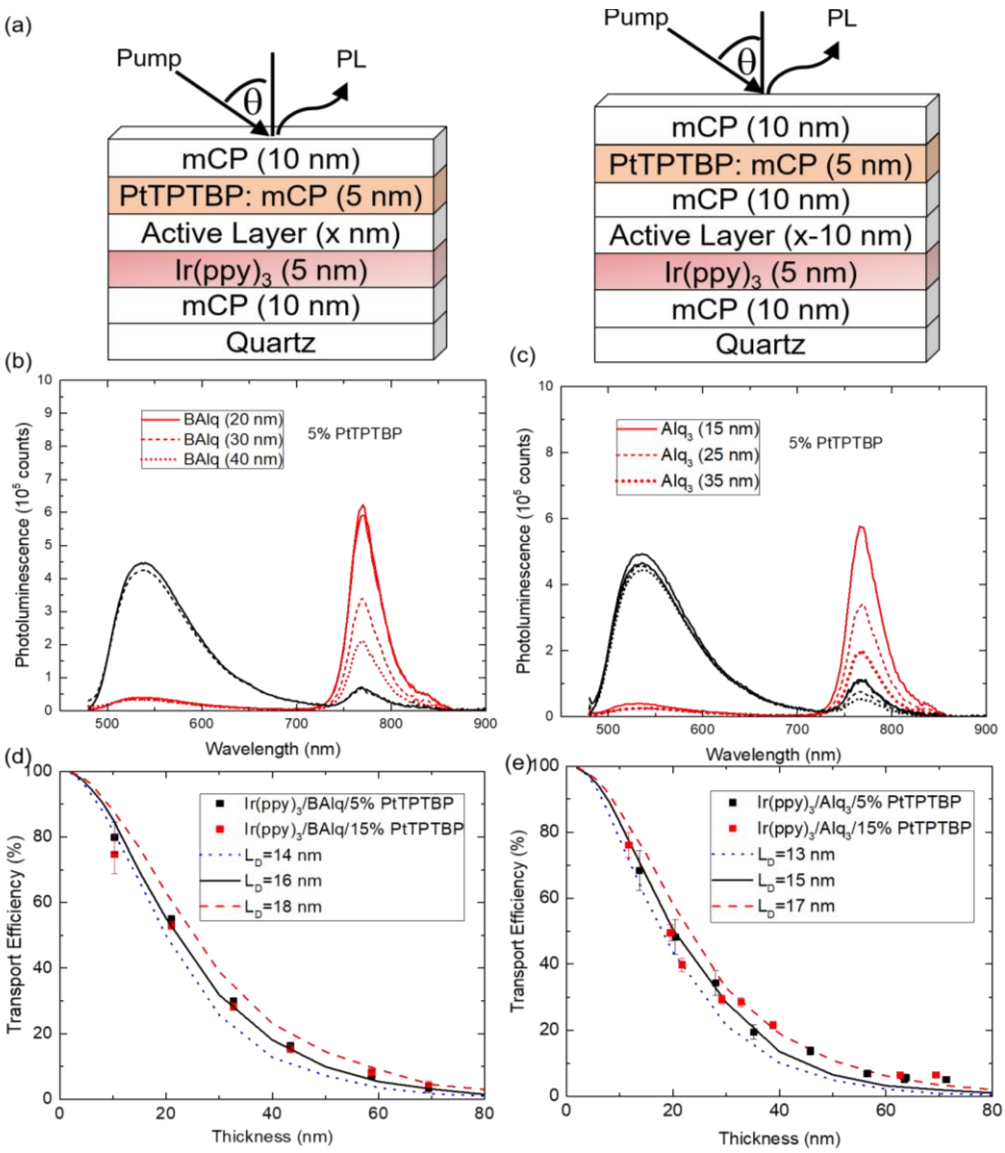

Figure 5.8 (a) Device architecture to probe triplet L_D of BAlq and Alq_3. Photoluminescence spectra collected for the multilayer used to extract the triplet diffusion length of BAlq (b) and Alq_3 (c) using the phosphorescent sensitizer-based approach. The structure is pumped at a wavelength of λ=470 nm where a majority of excitons are generated in the $Ir(ppy)_3$ injection layer. The excitons that diffuse through BAlq or Alq_3 are detected using 5 wt.% PtTPTBP doped in mCP. Experimental (symbols) and simulated (lines) transport efficiency as a function of BAlq (d) and Alq_3 (e) thickness for different values of the triplet L_D. Multiple sensitizer concentrations are considered to ensure unity quenching at the transport layer-sensitizer interface.

sensitizer interface. The η_T is calculated using Eq. (5.1) from the measured photoluminescence of PtTPTBP and $Ir(ppy)_3$ for the case when the transport layer of BAlq or Alq_3 is present, and when it is replaced by a wide gap spacer layer of mCP (Fig. 5.8a-c). The KMC modelling of the experimentally determined η_T as a function of BAlq and Alq_3 thickness yield L_D values of (16.6 $\pm$ 1.0) nm and (15.2 $\pm$ 0.9) nm respectively (Fig. 5.8d-e). The agreement in η_T for two different sensitizer concentrations suggests efficient quenching at the transport layer and sensitizer interface. The measured L_D for Alq_3 is consistent with the value of (14 $\pm$ 9) nm previously reported by Baldo et al.[164] using transient analysis of phosphorescence in an OLED.

In addition to offering a means to accurately probe the diffusion of dark triplet excitons, the phosphor sensitized methodology is attractive for its ability to separately probe singlet or triplet exciton transport. Indeed, by simply varying the injecting layer, either the singlet or triplet of the material of interest can be excited. For example, in Alq_3 we find here a singlet diffusion length of L_D = (5.9$\pm$ 0.6) nm and a triplet diffusion length of L_D = (15.2 $\pm$ 0.9) nm in the same architecture, simply by changing the injection layer from 4P-NPB to $Ir(ppy)_3$. Certainly, the Alq_3 triplets have long L_D as compared to its singlets due to an increased lifetime.[2,75,78] However, the corresponding increase in L_D is likely throttled by slow short-range Dexter energy transfer for amorphous organic semiconductor thin films.[237] By coupling measurements of this type with additional time-domain investigations, additional insight can be gained into the factors that impact singlet and triplet migration. Further, the ability to selective pump the singlet and triplet states

should have great utility in decoupling the more complex exciton transport that exists in materials exhibiting singlet fission or TADF.[238] The tri-layer stack used in current work may also be extended to solution-processed active materials. For example, the use of orthogonal solvents is increasingly being demonstrated to prevent re-dissolving in multilayer stacks.[239–244] Further, the combination of a solution-processed bottom layer and vapor-processed top layer would reduce the issue of re-dissolving to only the bottom interface.

5.6 Summary

In this chapter a phosphorescent sensitizer-based methodology to accurately extract the exciton diffusion length of non-radiative triplet excitons in organic semiconductor thin films is presented. In order to confirm the validity of the technique, we first extract the L_D of luminescent singlet excitons in thin films of Alq_3 and C545T, comparing the result to conventional photoluminescence measurements. For measurement of non-radiative triplet excitons, excitons are injected by energy transfer from an adjacent phosphorescent layer. By measuring the transport efficiency of excitons across the material of interest, triplet L_D values in the range of 15-30 nm are obtained. The method is also attractive in that values for the singlet and triplet L_D be extracted for a given material in a common architecture by varying only the exciton injecting material.

6 Impact of Molecular Structure on Singlet and Triplet Diffusion

This chapter is a summary and extension of published work in journal of materials chemistry C entitled “Impact of molecular structure on singlet and triplet exciton diffusion in phenanthroline derivatives”[245] The author acknowledges collaborators John S. Bangsund for outcoupled PL efficiency simulations and atomic force microscopy (AFM) measurements and Javier Garcia Barriocanal for X-ray reflectivity measurement. This work is supported by National Science Foundation (NSF) Solid-State and Materials Chemistry under DMR-1708177 and Electronics, Photonics and Magnetic Devices under ECCS-1509121. The author acknowledges C.P. Clark for X-ray diffraction measurements and Dr. Andrew Healy for measuring singlet exciton lifetimes using TCSPC.

6.1 Background

The previous chapter discussed a phosphorescent sensitizer-based methodology to accurately determine dark triplet exciton diffusion length. In this chapter, the methodology is used to present a systematic study of the impact of subtle changes in molecular structure on the singlet and triplet exciton diffusion lengths.

In terms of exciton transport, spin singlet and triplet excitons diffuse via different mechanisms, due mainly to the fact that singlets may undergo radiative recombination while triplets are often dark.[171] The previous chapter noted the role of spin in impacting in

impacting exciton L_D for archetypical organic semiconductor molecules, NPD and Alq_3. This difference in mechanism also implies that the handles available for tuning the exciton diffusion length (L_D) may enhance the transport of one spin state while not favorably impacting the other.[237] Reduced intermolecular spacing is typically considered as a route to improve exciton transport however, even here care must be taken to avoid increasing non-radiative decay and reducing the exciton lifetime. Several studies have reported on the role of molecular functionalization and crystallization in enhancing singlet exciton transport.[138,140,145–147,150,153,246] There are however fewer studies of triplet excitons as they are often non-radiative and hence incompatible with common photoluminescence-based techniques. Furthermore, few efforts have sought to systematically compare the role of functionalization on both singlet and triplet states.[187,247] As such, there exists a need for experimental methodologies that permit the investigation of singlet and triplet diffusion in a common set of samples that could experimentally elucidate the fundamental difference in transport behavior between these states.

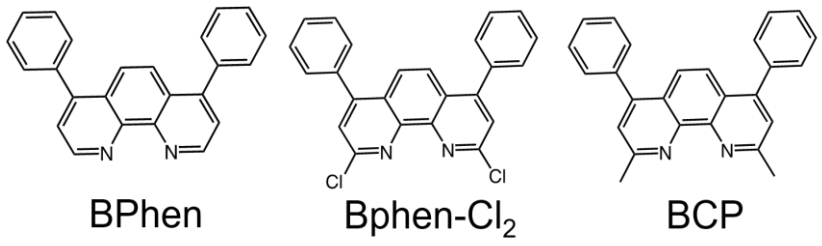

Figure 6.1 Molecular structures of the phenanthroline derivatives considered in this chapter.

In this chapter, we examine singlet and triplet exciton diffusion as a function of molecular functionalization in phenanthroline derivatives, offering a useful contrast of the factors governing the migration of each state. Phenanthrolines have long been used as

electron transport materials and exciton blocking layers in organic light-emitting devices (OLEDs)[248–251] and organic photovoltaic cells (OPVs)[252–254], and are examined here for the availability of several derivatives namely, 4,7-diphenyl-1,10-phenanthroline (BPhen), 2,9-dichloro-4,7-diphenyl-1,10-phenanthroline (BPhen-Cl_2), and 2,9-dimethyl-4,7-diphenyl-1,10-phenanthroline (BCP), where steric bulk and intermolecular spacing are tailored by substitution of -H, -Cl and -CH_3 on the phenanthroline core (Fig. 6.1). Changes in intermolecular spacing also lead to changes in molecular photophysics, and measurements of exciton transport are complemented by detailed spectroscopic investigations. Thus, a systematic understanding for the role of functionalization on singlet and triplet diffusion is established.

6.2 Experimental Details

BPhen, BPhen-Cl_2, BCP, mCP and HATCN are purchased from Luminescence Technology Corporation; PtOEP is purchased from Frontier Scientific. For thickness dependent PL quenching measurements, a unity quenching efficiency is assumed for HATCN due to the favorable energy offset for electron transfer.[206,231] Photoluminescence spectra are measured in a Photon Technology International QuantaMaster 400 Fluorometer equipped with a photomultiplier detection system. Structures are excited using a Xe lamp attached to a monochromator, at an angle of 70^{o} from substrate normal. Photoluminescence efficiencies are measured in an integrating sphere using a previously published methodology.[255]. Singlet exciton lifetimes are measured using a PicoQuant time correlated single photon counting (TCSPC) system, pumped using a regeneratively amplified

Ti:sapphire laser system producing ~80 fs, λ = 900 nm pulses at a repetition rate of 40 MHz. A λ = 300 nm excitation pulse is then obtained using a nonlinear harmonic generation system equipped with a BBO crystal for tripling the frequency of the excited pulse. A closed cycle Janis CSS-150 He optical cryostat is used to measure triplet photoluminescence spectra and lifetimes at 10 K. Samples are pumped at a wavelength of λ = 337 nm using a N_2 laser which provides ~ 1 ns pulse width. The emission spectrum from the sample is detected using a FERGIE integrated spectrograph (Princeton Instruments), with spectrum acquisition triggered externally with a pulse generator after a 5 ms delay from the laser pulse. The repetition rate of the laser is kept at 0.25 Hz. Triplet photoluminescence spectra are measured for different delay times to obtain the triplet lifetime. X-ray reflectivity is measured on a 20-nm-thick film of the active material deposited on a Si substrate using a PANalytical X'pert Pro instrument. The experimental data is simulated using GenX software to obtain thin film density, surface roughness and film thickness. The film thickness is independently checked with values from ellipsometer. The film crystallinity is checked using X-ray diffraction measurements at an incident angle of 8 degrees, while sample is being scanned using a 2D detector which spans from $2\theta = 1$ degree to 53 degrees. Experimental data for singlet and triplet L_D measurements is fitted using a non-linear least square methodology where error in the fit value represents 95% confidence interval.

6.3 *Singlet Exciton Behavior*

Figure 6.2b shows the thin film extinction coefficient and photoluminescence (PL) behavior of the active materials of interest in this work. The PL collected at room temperature is fluorescence from the singlet state. The phosphorescence spectra shown are collected at 10 K at long times under pulsed laser excitation (Fig. 6.2 a). Spectrum acquisition is triggered by a pulse generator with a 5 ms delay after the laser pulse to reject short time luminescence and only collect long-lived triplet phosphorescence. As-deposited films showed no evidence of crystallinity in X-ray diffraction (XRD) measurements. Fine differences in the intermolecular spacing with functionalization are probed by measuring film density using X-ray reflectivity (XRR). The film thickness, density, and roughness are

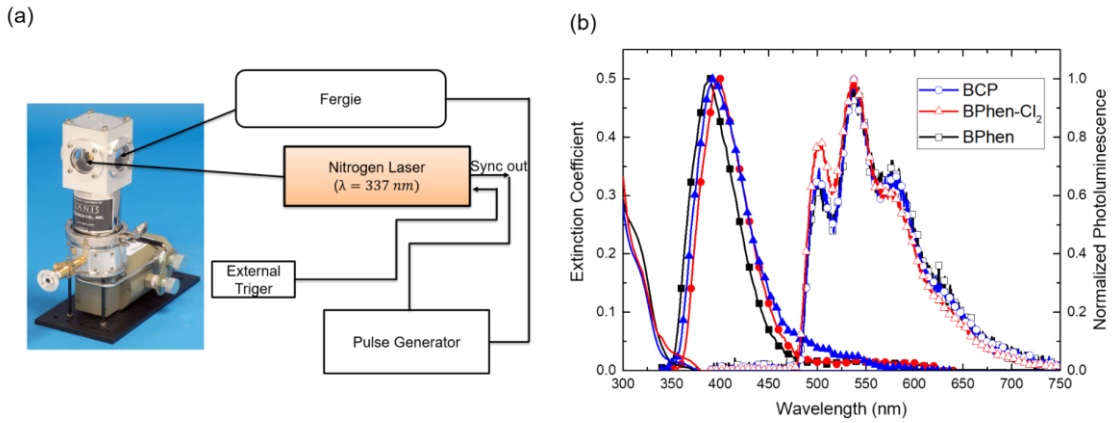

Figure 6.2 (a) Schematic of the setup for the measurement of phosphorescence spectra. (b) Thin film fluorescence (closed symbols) and extinction spectra (solid lines) for the molecules in (a) taken at room temperature. Low temperature phosphorescence spectra (open symbols) are collected at 10 K at long times after pulsed excitation to avoid detection of fluorescence.

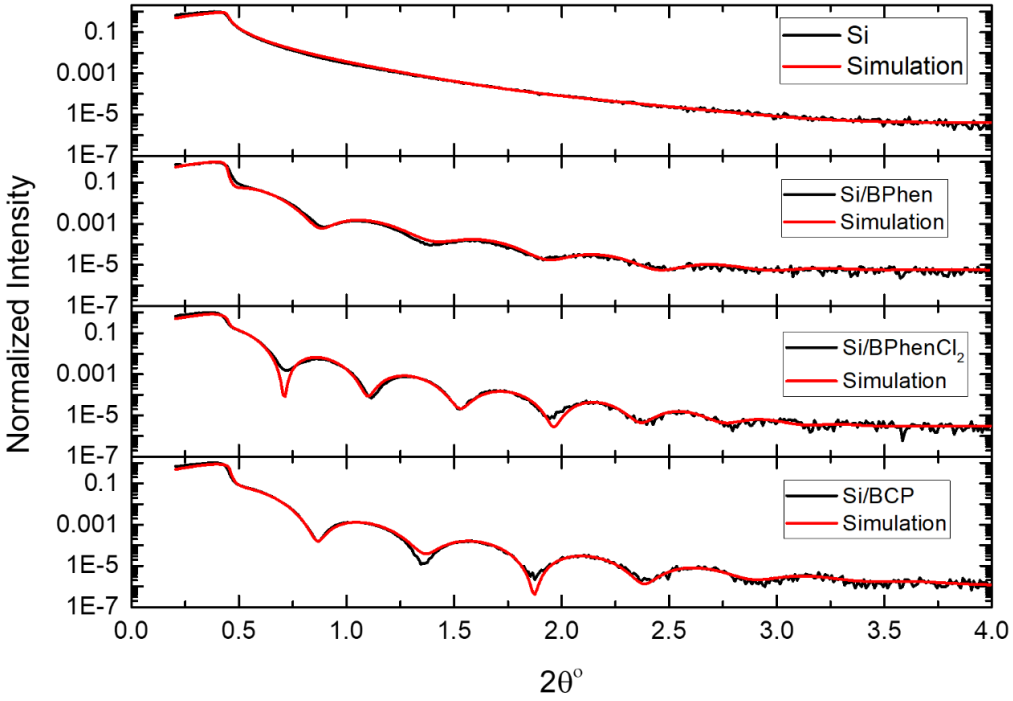

Figure 6.3 X-ray reflectivity on 20-nm-thick films (on a Si substrate) of BPhen, BPhen-Cl_2 and BCP. Data analysis is performed using GenX software with film thickness, density and roughness as fitting parameters. The extracted film thicknesses are within 5% of the values extracted from ellipsometry. The film roughness obtained from the fit is about 1.2 nm which is in close agreement with roughness value (RMS < 0.7 nm) obtained using atomic force microscopy (AFM).

used as fitting parameters for XRR experimental data analysis (Fig. 6.3). The fit parameters along with independent measurements of film thickness using ellipsometry are shown in Table 6.1. XRR analysis yields extracted molecular densities of (1.87 ± 0.03) nm^{-3} for BCP, (2.04 ± 0.03) nm^{-3} for BPhen-Cl_2, and (2.26 ± 0.03) nm^{-3} for BPhen, consistent with previous reports for BPhen and BCP.[256]

Table 6.1 XRR fit parameters for thin films of phenanthroline derivatives**.** The experimental data is simulated using GenX software to obtain thin film molecular density (ρ), surface roughness (σ_R) and film thickness. Values are compared against literature value of ρ.[256,257]

Layer	XRR Thickness (nm)	ρ (nm^{-3})	σ_R (nm)	Ellipsometer Thickness (nm)	ρ (Lit.) (nm^{-3})
Si		50	0-0.4		50
SiO_2	1-3	22.0	1-3	1.5	20.7-22.5
BPhen	16.2	2.26	1.1	15.4	2.27 ± 0.02
$BPhenCl_2$	20.8	2.04	1.2	20.5	
BCP	16.1	1.87	1.2	15.8	1.87 ± 0.02

The singlet L_D for each material of interest is extracted using thickness dependent PL quenching. Thin film fluorescence is measured with and without the presence of an adjacent top quenching layer of HATCN (See Appendix E, Fig. E1 for spectra).[172] The PL ratio (quenched to unquenched) is measured as a function of active layer thickness and fit to yield the singlet L_D. Table 6.2 lists the singlet L_D values extracted for BPhen and its derivatives, obtained by analytical modelling of the associated PL ratio (Fig. 6.4). Extracted values of L_D are < 1 nm for BPhen, (3.9 ± 1.1) nm for BCP, (5.4 ± 1.2) nm for BPhen-Cl_2. It is worth noting that if fit explicitly, the data in Fig. 6.4 for BPhen yields L_D = (0.8 ± 0.3) nm. This value is below the estimated resolution limit of 1 nm of the technique.

The observed trend in singlet L_D can be considered in terms of Förster theory by considering how changes in intermolecular spacing and the self-R_0 (Table 6.2) impact L_D. Singlet L_D values for the BPhen derivatives scale linearly with the ratio R_0^3/d^2 as expected based on Equations 2.4 , 2.9 and 2.10 from Chapter 2. This ratio is largest for $BPhenCl_2$,

which reflects a high degree of spectral overlap between fluorescence and absorption spectra.

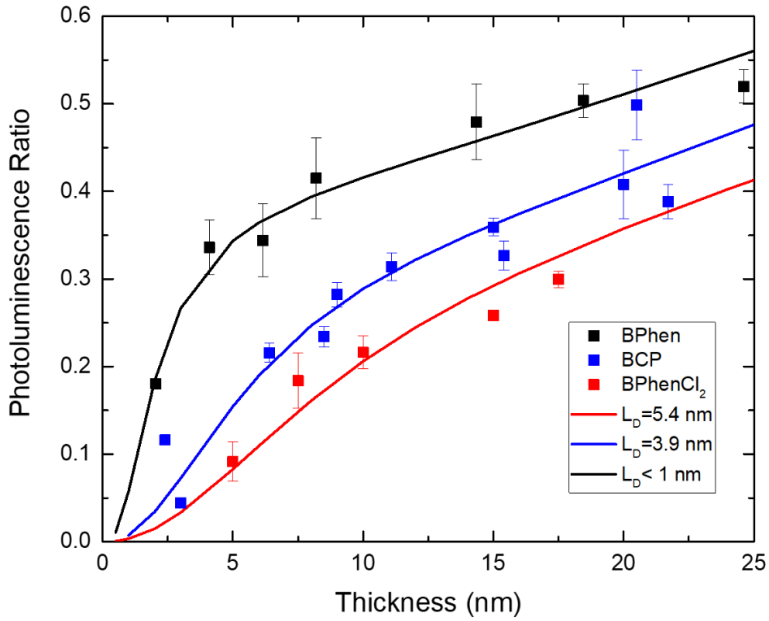

Figure 6.4 Photoluminescence ratios (with and without an adjacent HATCN quenching layer) for BPhen and its derivatives with the corresponding exciton diffusion length (L_D) extracted from the data.

Table 6.2 Exciton transport and photophysical parameters for phenanthroline thin films

Materials	Singlet L_D (nm)	Singlet τ (ns)	Singlet η_{PL} (%)	Self-R_0 (nm)	Triplet L_D (nm)	Triplet τ (ms) (10 K)
BPhen	<1	0.58 ± 0.03	2.5 ± 0.5	0.59 ± 0.01	15.4 ± 0.4	455.2 ± 7.9
BPhen-Cl_2	5.4 ± 1.2	0.48 ± 0.01	9.4 ± 0.9	0.84 ± 0.01	8.0 ± 0.7	313.7 ± 19.5
BCP	3.9 ± 1.1	1.24 ± 0.01	21.6 ± 2.2	0.85 ± 0.01	4.0 ± 0.5	633.1 ± 59.8

6.4 *Triplet Exciton Behavior*

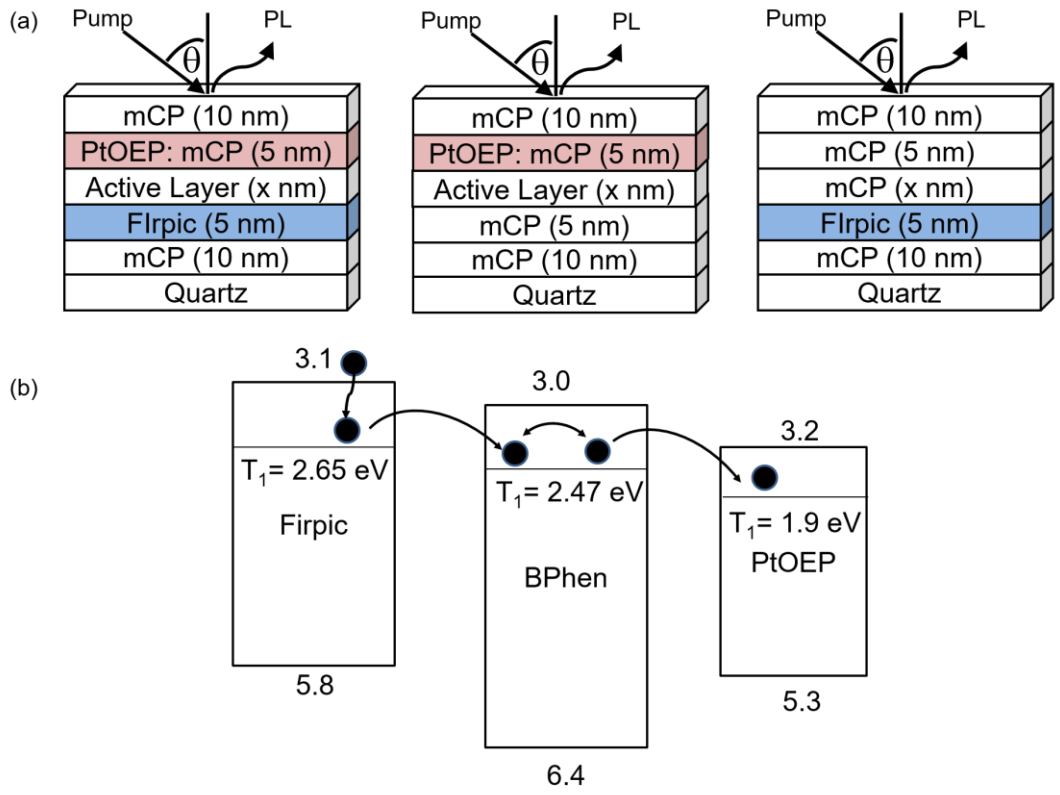

Figure 6.5 (a) Multilayer thin film architecture for investigating the triplet L_D for BPhen and its derivatives. (b)The structure is pumped at a wavelength of λ=430 nm where a majority of excitons are generated in the FIrpic injection layer. The excitons that diffuse through BPhen and its derivatives are detected using 5 wt.% PtOEP doped in mCP.

Figure 6.5a shows the device architecture for measuring the triplet L_D in BPhen and its derivatives using a phosphorescent sensitizer based method.[218] A layer of (4,6-difluorophenyl)pyridinato-C2,N](picolinato)iridium(III) (FIrpic) (triplet energy, E_T = 2.65 eV) injects triplets into the phenanthroline of interest (E_T = 2.47 eV for all three materials). Injected triplets that migrate through the full thickness of the active layer are detected using a sensitizer of platinum octaethylporphyrin (PtOEP) (E_T = 1.9 eV)[233] doped in the wide

energy gap host 1,3-bis(N-carbazolyl)benzene (mCP) (E_T = 2.9 eV) (Fig. 6.5b). Exciton diffusion in the active layer is defined in terms of a transport efficiency (η_T) as:[218,227]

$$\eta_T = \frac{\Delta PL^{PtOEP}}{\Delta PL^{FIrpic}} \times \frac{\eta^{PL}_{Firpic}}{\eta^{PL}_{PtOEP}} \quad (6.1)$$

where η^{PL}_{Firpic} and η^{PL}_{PtOEP} are the outcoupled PL efficiencies of the FIrpic and PtOEP layers. The outcoupling efficiency ratio in the absence of the active layer is experimentally determined by directly injecting excitons from FIrpic to PtOEP using a previously published method.[218,227] The variation in outcoupling efficiency as a function of active layer thickness is calculated using Setfos 4.6 (Fluxim) software (Appendix E: Fig. E2).

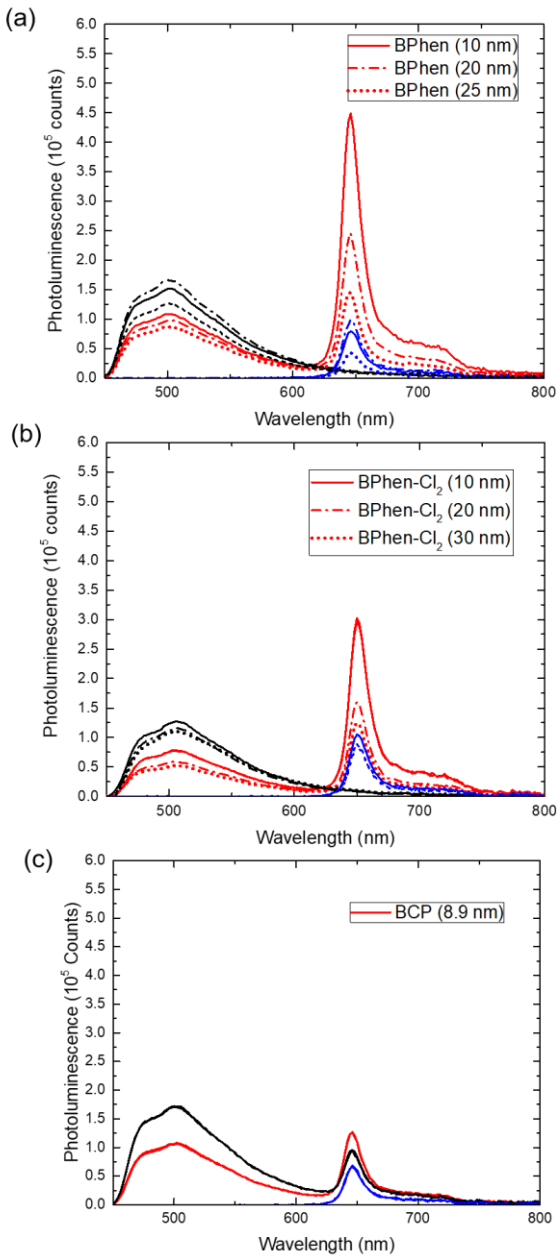

Figure 6.6 The photoluminescence spectra are collected for the multilayer structures FIrpic/mCP (10 nm)/mCP (black line); FIrpic/active layer (x nm)/5 wt.% PtOEP:mCP (red line) and mCP/ active layer(x nm)/5 wt.% PtOEP:mCP (blue line), where the active layer is (a)BPhen, (b) BPhen-Cl_2 or (c) BCP.

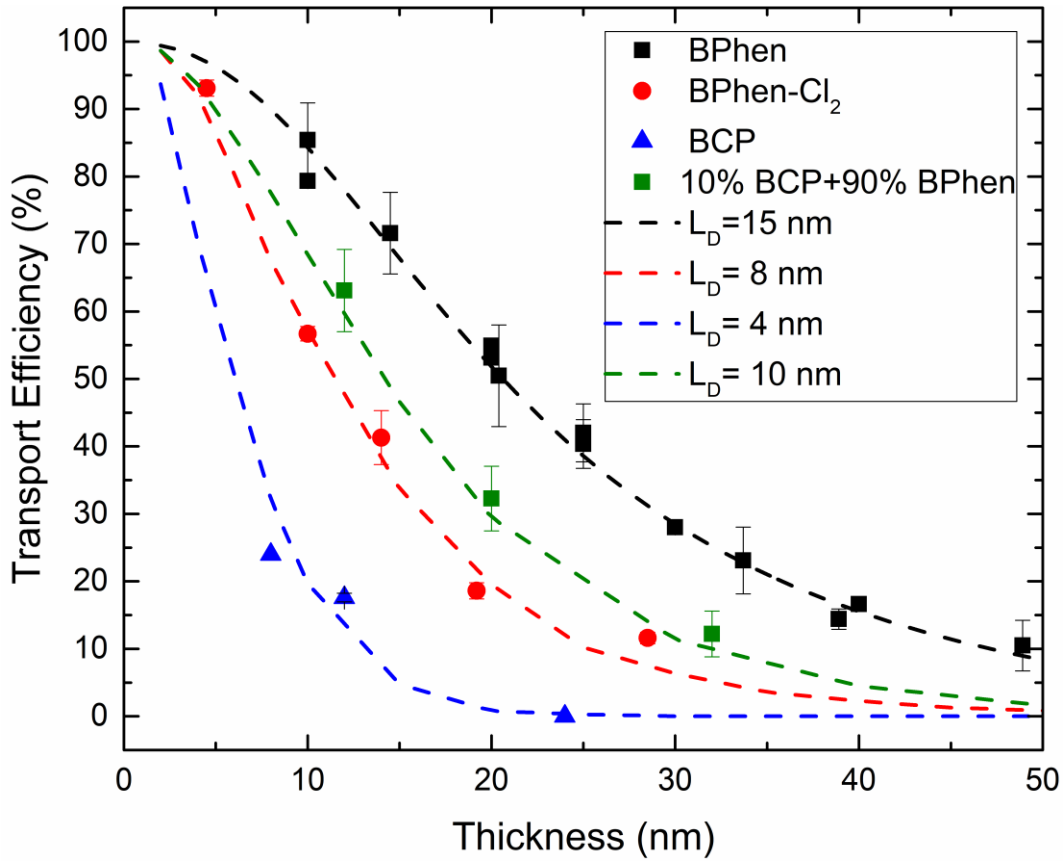

Figure 6.7 Experimental (symbols) and simulated (lines) transport efficiency as a function of active layer thickness for different values of the triplet L_D.

Figure 6.6a-c shows PL spectra for FIrpic and PtOEP with an active layer of BPhen, BPhen-Cl_2, or BCP, for cases with and without injection of excitons into the active layer. The increase in PL from PtOEP due to energy transfer from FIrpic can be isolated from direct optical excitation (*i.e.* where the injection layer of FIrpic is replaced with mCP). Kinetic Monte Carlo (KMC) [218,227] modelling of the experimentally measured η_T as a function of active layer thickness results in triplet L_D values of (15.4 ± 0.4) nm for BPhen, (8.0± 0.7) nm for BPhen-Cl_2, and (4.0 ± 0.5) nm for BCP (Fig. 6.7).

The mechanism for energy transfer can be understood by first decoupling the exciton lifetime and the diffusivity. The triplet lifetime for each material is shown in Table 1 and is

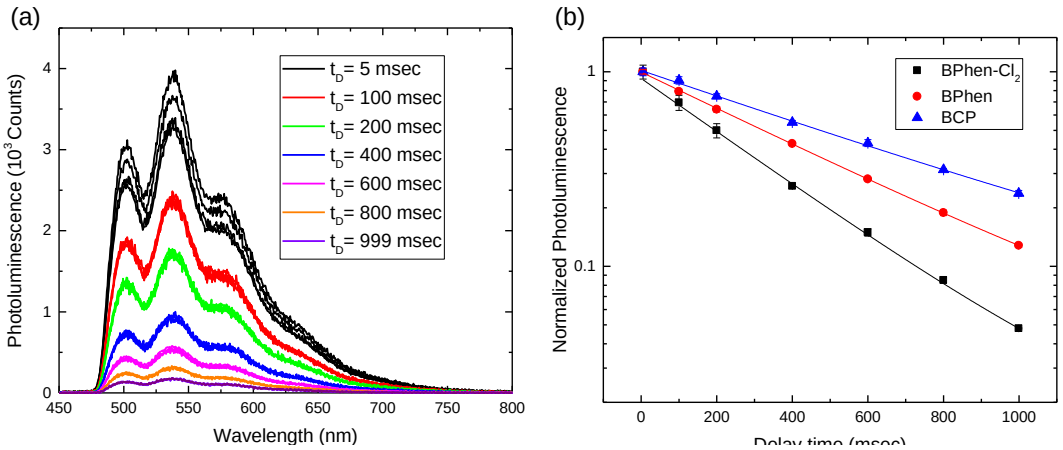

Figure 6.8 (a) Representative photoluminescence from the triplet state of BPhen-Cl_2 collected for different delay times from the trigger of a N_2 laser pulse at a wavelength of $\lambda = 337$ nm. (b) A semi-log plot between integrated photoluminescence from triplet state and delay times for phenanthroline derivatives.

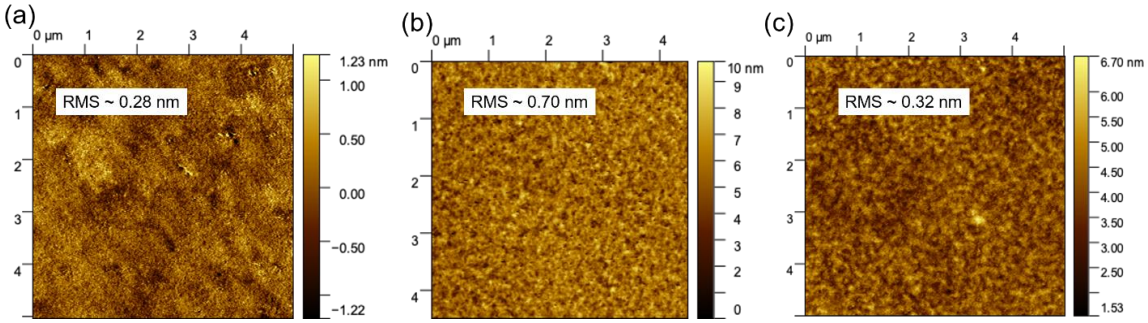

Figure 6.9 Atomic force micrographs of 30-nm-thick film of (a) BPhen (b) BPhen-Cl_2 and (c) BCP on a glass substrate. Atomic force microscopy is conducted using a Bruker Nanoscope V with a Multimode 8. Images were acquired in peak force quantitative nanomechanical (PF-QNM) mode, and AFM cantilevers were aluminum-coated n-type silicon with a nominal force constant of 0.6 N/m (HQ:NSC36/AL BS).

determined from low temperature transient phosphorescence. The trend in triplet lifetime (Table 6.2, Fig. 6.8) cannot alone explain the observed variation in triplet L_D, suggesting a change in diffusivity. This could come from changes in optical overlap, the molecular orbital radius, and the intermolecular spacing. Changes in film roughness could also lead

to differences in the extracted L_D, but this possibility is ruled out using atomic force microscopy (AFM) of as-deposited films of each active material. Films of all materials studied here show a featureless morphology with root mean square roughness < 1 nm (Fig. 6.9).

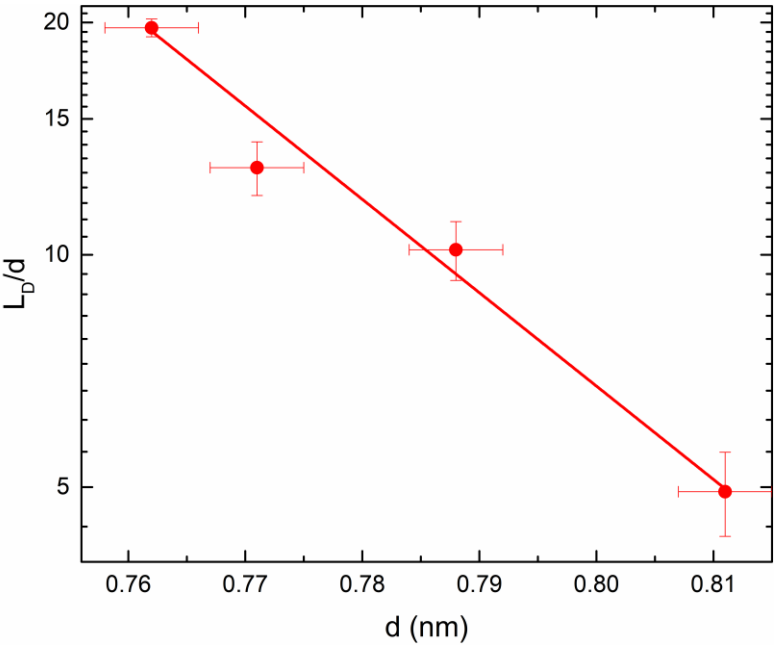

Figure 6.10 Measured triplet L_D divided by the intermolecular spacing (d) plotted as a function of the intermolecular spacing (d) for BPhen and its derivatives. The solid line is a linear fit through the data points.

The variation in triplet diffusivity is considered in terms of differences in intermolecular spacing. Indeed, Eqs. 2.8 and 2.9 in Chapter 2 suggest an exponential relationship between triplet diffusivity and intermolecular spacing, and hence the linearity of a semi-log plot between triplet (L_D/d) and intermolecular spacing can be used to check the validity of the assumed diffusion model. Figure 6.10 shows a linear fit between a semi-log plot of L_D/d and intermolecular spacing. The value of d is determined by taking the cube root of the molecular density ($\sqrt[3]{\frac{1}{\rho}}$) as measured using XRR. The intermolecular spacing varies in increasing order as (7.62 ± 0.04) Å for BPhen, (7.88 ± 0.04) Å for BPhen-Cl_2 and (8.11 ± 0.04) Å for BCP, corresponding-well with the concomitant reduction in

triplet L_D. The observed linear trend also holds for a mixture of 10 wt.% BCP in BPhen, suggesting that BCP and BPhen form a substitutional solid solution. The slope of the plot yields the molecular orbital radius as (0.37 ± 0.04 Å) (Fig. 6.10). This value is consistent with previous reports for Dexter transfer yielding ~ 0.39 Å to 2.1 Å. [258–262] In this model it is assumed that energy transfer between different spatial configurations of molecule are isotropic in nature as represented by energy transfer term containing average intermolecular spacing. However, the BPhen and its derivative molecules are assymetric in nature and it has been previously shown using first principle investigation that LUMOs and HOMOs of BCP and BPhen are more localized on the phenanthroline moeity.[263] Thus, the energy transfer will be dominated along configurations with shortest spacing between phenanthroline moeity and obtained molecular radius is weighted average of energy transfer along different directions. In future, it would be interesting to examine the role of CH_3 at different position on phenanthroline ring.

6.5 Summary

In this chapter, a study connecting the measured singlet and triplet exciton diffusion length with changes in molecular structure and intermolecular spacing. The singlet L_D values are extracted using thickness dependent photoluminescence quenching measurements while the triplet L_D values are extracted using a phosphorescent sensitizer-based methodology. For the phenanthroline derivatives considered here, the intermolecular spacing varies in increasing order as (7.62 ± 0.04) Å for BPhen, (7.88 ± 0.04) Å for BPhen-Cl_2, and (8.11 ± 0.04) Å for BCP. The singlet L_D increases from L_D <1 nm for BPhen to

(5.4 ± 1.2) nm for BPhen-Cl_2, and (3.9 ± 1.1) nm BCP, while the triplet L_D decreases from (15.4 ± 0.4) nm for BPhen to (8.0 ± 0.7) nm for BPhen-Cl_2, and (4.0 ± 0.5) nm for BCP. The variation in singlet L_D is understood using Förster transfer, considering changes in the intermolecular spacing as well as factors like the photoluminescence efficiency and optical overlap. The decrease in triplet L_D is understood more simply using Dexter transfer where the rate of energy transfer scales exponentially with intermolecular spacing. This work offers insight into the significant and differing role changes in molecular structure can play for singlet and triplet exciton transport.

7 Exciton Gating in Organic Semiconductor Thin Films

This chapter is a summary and extension of published work in physical review applied entitled “Investigation of Excitonic Gates in Organic Semiconductor Thin Films”[227] This work is supported by National Science Foundation (NSF) Electronics, Photonics and Magnetic Devices under ECCS-1509121.

7.1 Background

Chapter 3 discussed in detail the critical role of exciton transport in an organic photovoltaic cell. In an OPV, photogenerated excitons must diffuse to an electron donor-acceptor heterojunction where exciton dissociation occurs via charge transfer.[2,75,78] Exciton transport has long been recognized as a key process limiting efficiency in the simplest planar heterojunction cells. Indeed, state-of-the-art OPVs overcome this bottleneck and realize high efficiency through the use of a bulk heterojunction (BHJ) architecture where donor and acceptor materials are blended in a single layer.[40,136,137] While this approach circumvents the short exciton diffusion length (L_D) by increasing the area of the dissociating donor-acceptor interface, several works have also attempted to directly increase the value of L_D via molecular design and morphology engineering.[138,139,146,147,150,264] Indeed, the largest values of L_D have been realized in large-grained polycrystalline thin films and molecular crystals,[75,89,146–149] though the associated

anisotropy means that crystallinity alone does not guarantee long L_D in a given direction.[150–154] Prior work has also demonstrated how variations in intermolecular separation can lead to increases in the L_D by optimizing the various parameters responsible for dipole-mediated Förster energy transfer.[90,140,231,265]

In contrast, less attention has been paid to the more general problem of overcoming the diffusive and sub-diffusive nature of exciton transport in organic semiconductors. Menke et al.[171] have previously examined the idea of using multiple interfaces with an optimized molecular site imbalance to introduce asymmetry in forward and reverse exciton transport rates, pushing the system into a regime of anomalous diffusion. Practically, the site imbalance is realized by diluting the active material of interest into a wide energy gap host by different amounts on either side of the interface.[90,171,231] Indeed, this previous work found a nonlinear dependence of the mean square displacement (MSD) on time (*i.e.* $\langle x^2 \rangle \propto t^{\alpha}$, $\alpha>1$), suggesting super-diffusive transport.[171] An imbalance in energy transport rates at an interface can also arise from a difference in energy gap between the two layers. In these architectures, reverse exciton transfer is hindered due to conversation of energy. While not frequently considered in the context of exciton gating, several reports of this type of structure exist in the context of energy cascade devices in which multiple donor or acceptor layers are combined in series to realize high efficiency.[266–269] Experimentally, only the case of a single asymmetric interface has been investigated, with multiple biasing interfaces only being considered from a theoretical perspective. This chapter offer a combined theoretical-experimental study of the impact of multiple exciton gating

interfaces on exciton transport, and hence, a practical assessment of these architectures for devices.

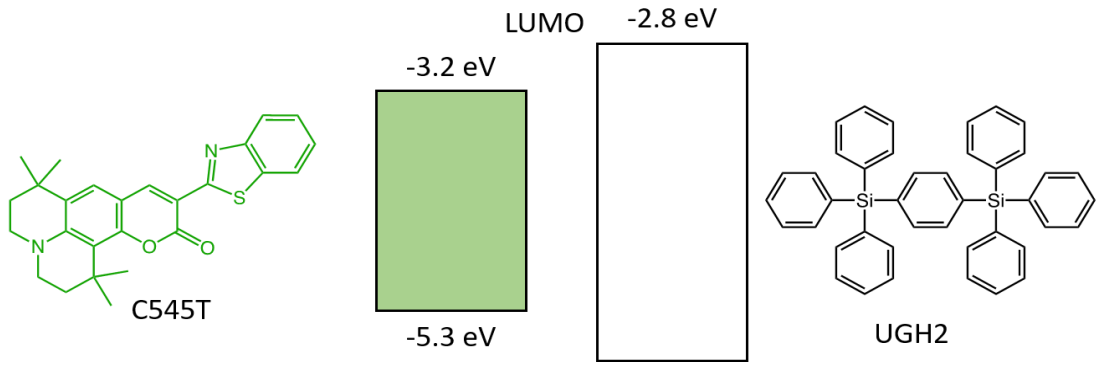

Figure 7.1 Molecular structures and energy levels for C545T and UGH2

7.2 Experimental Details

Exciton transport is examined in multilayer structures where exciton gates are formed by a molecular site imbalance across an interface. Exciton transport is probed in the archetypical fluorescent emitter, 3,6,7-tetrahydro-1,1,7,7,-tetramethyl-1H,5H,11H-10(2-benzothiazolyl) quinolizine-[9,9a,1gh] coumarin (C545T). The interfacial site imbalance is engineered by diluting C545T into a wide energy gap host material, p-bis(triphenylsilyl)benzene (UGH2).[90,231,233] In this arrangement, UGH2 is not excited and does not quench excitons from C545T (Fig. 7.1). The architectures of interest are shown in Fig. 7.2a, with the associated optical properties of each active material shown in Fig. 7.2b. In Fig. 7.2a, the gating region of the device containing C545T in various concentrations is sandwiched between an exciton injection

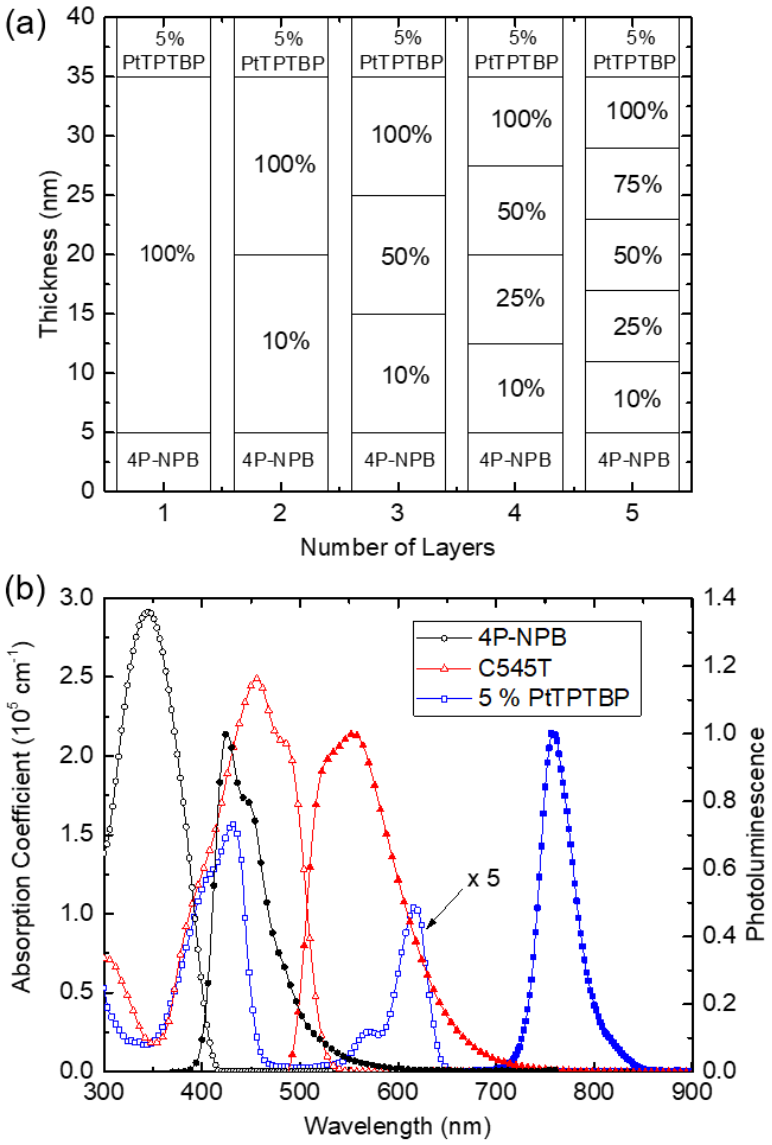

Figure 7.2 (a) Layer structure for probing the role of multiple interfacial gates. Excitons are injected from the most dilute layer of C545T in UGH2 (concentration % noted) by energy transfer from an injection layer of 4P-NPB and are collected at the neat layer using a sensitizer layer containing PtTPTBP. The thickness for each layer is optimized to maximize collection. (b) Absorption coefficient (open symbols) and normalized photoluminescence (closed symbols) of C545T, 4P-NPB and 5% PtTPTBP in UGH2. The absorption coefficient is calculated using the extinction coefficient, extracted from ellipsometric measurements on a 30-nm-thick film deposited on glass substrate. Excitons are injected into C545T by pumping 4P-NPB at a wavelength of λ=355 nm.

layer of N, N'-di-1- naphthalenyl-N,N'-diphenyl [1,1':4',1'':4'',1'''-quaterphenyl]-4,4'''-diamine (4P-NPB)[270] and an exciton collecting layer of platinum(II) tetra-phenyl-tetra-benzo-porphyrin (PtTPTBP) diluted in UGH2.[229,230,271] The PtTPTBP is diluted into a layer of UGH2 in order to increase its photoluminescence (PL) efficiency. The function of this architecture is discussed further in section 7.4. All layers are prepared by thermal vacuum sublimation (<7x10^{-7} Torr) at a deposition rate of 0.1 nm s^{-1}. All optical constants and thin film thickness are measured using a J. A. Woollam variable-angle spectroscopic ellipsometer. All of C545T, UGH2 and 4P-NPB are purchased from Luminescence Technology Corporation, while PtTPTBP is purchased from Frontier Scientific. For PL measurements on exciton gating architectures, the emission scan is carried out in two stages. First, a long pass filter with a cut off wavelength of $\lambda = 364$ nm is used to prevent pump detection while sample emission is scanned from 370 nm to 720 nm. Second, sample emission is collected from 600 nm to 900 nm using a long pass filter with a cut off wavelength of $\lambda = 600$ nm, to prevent the detection of the 4P-NPB emission double from the sample.

The exciton diffusion length of C545T in UGH2 is measured using thickness dependent PL quenching.[172] Thin films of C545T in UGH2 are deposited with and without an adjacent bottom surface quenching layer of 1,4,5,8,9,11-hexaazatriphenylene hexacarbonitrile (HATCN).[265] Under optical excitation at a wavelength of $\lambda = 460$ nm, the fraction of C545T excitons reaching the quenching interface varies depending on the thickness. A PL ratio is extracted as a function of C545T layer thickness as the ratio of the

integrated PL spectrum with and without an adjacent quenching layer. The experimentally obtained PL ratios are modelled using a 1D steady-state diffusion equation with the exciton diffusion length as the fit parameter. The exciton generation profile in this model is solved using a transfer matrix formalism.[170] Photoluminescence efficiencies are measured using an integrating sphere with previously published methods.[255] Exciton lifetimes are measured using a PicoQuant time correlated single photon counting (TCSPC) system, excited at a wavelength of $\lambda = 470$ nm using 70 ps laser pulses.

7.3 Theory of Excitonic Gates

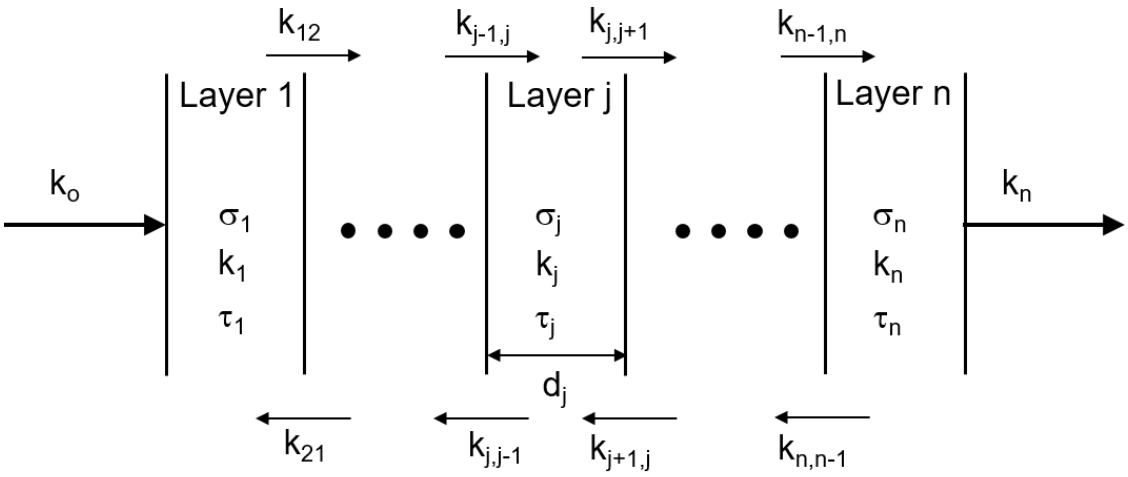

Figure 7.3 A general multilayer structure having n layers between the injection layer and sensitizer layer. Each layer j (j=1, 2, 3, ….. , n) has a thickness d_j, areal density σ_j of donor molecules in a wide gap host material, a bulk energy transfer rate k_j and an exciton lifetime τ_j. The energy transfer rate between the plane of molecules in layer i and j is represented by k_{ij} .

For an isotropic film, there is an equal probability of the exciton hopping in all directions. In a one-dimensional analog, this implies transport in the forward and reverse

directions is equally likely. When the exciton encounters an asymmetric interface with differing forward and reverse rates of energy transfer, a more detailed analysis is required.

Here, we consider the case of an interface across which there is a difference in the density of molecular sites and intermolecular spacing for a single material species (Fig. 7.3). In order to treat energy transfer from a molecule on one side of the interface to a plane of molecules on the other side of the interface, we consider a rate that varies with the intermolecular separation (d) as d^{-4} and is directly proportional to the areal density of acceptor molecules.[84,85,272] Thus, the energy transfer rate across the interface is given as:

$$k_{ij} = k_i \times \frac{\sigma_j}{\sigma_i} \times \frac{d_i^4}{d_{ij}^4} \times \frac{R_{ij}^6}{R_i^6} \quad (7.1)$$

where k_i and k_j are the respective bulk rates of Förster energy transfer in layers i and j, σ_i and σ_j are the areal densities of molecules in layer i and layer j, and R_{ij} and R_{ji} are the Förster radii for forward and reverse transfer across the interface. In considering energy transfer across an interface it is assumed that the degree of excitonic energetic disorder 2does not change with dilution .[153,175,273] Were it to change

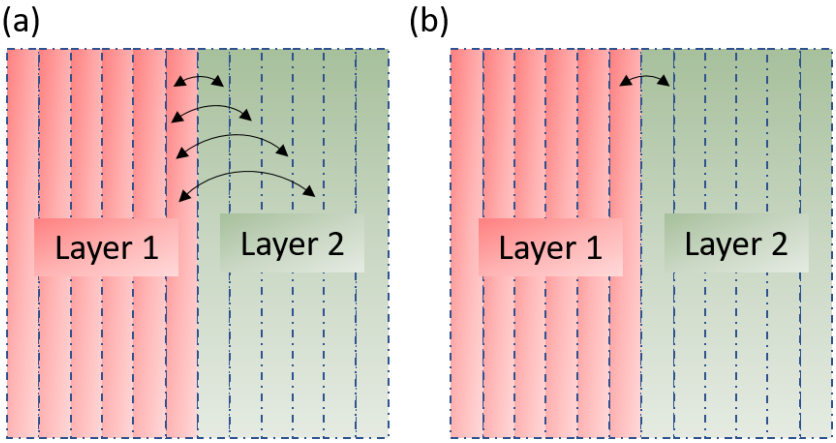

Figure 7.4 (a) KMC approach used in the present chapter considers interaction between non-adjacent bins. (b) KMC approach used by Menke et. al[171] considers only adjacent bin interaction.

substantially, disorder could add an additional source of asymmetry across the interface for the rates of energy transfer. With Eq. 7.1, a Kinetic Monte Carlo (KMC) formalism introduced in Chapter 4 is used to examine the effect of interfacial rate asymmetry on the exciton transport efficiency (η_T) across a gating architecture. Energy transfer rates are extracted from the experimental value of L_D as described in Sec. 7.4. The natural decay rate of the exciton is measured using transient fluorescence as described in Sec. 7.2. We note that the KMC approach used here differs slightly from that of Menke et. al[171] in that long-range energy transfer between non-adjacent layers is explicitly included in the calculations (Fig. 7.4).

7.4 Experimental Demonstration of Excitonic Gates

In the architectures of Fig. 7.2a, the relative role of the gates on exciton transport is considered in terms of η_T. Excitons are injected from 4P-NPB into C545T by optically pumping at a wavelength of λ=355 nm, where absorption occurs mainly in the 4P-NPB layer.[270] The exciton transport efficiency is proportional to the ratio of excitons collected by PtTPTBP to the number of excitons injected from 4P-NPB. Experimentally, η_T is calculated as the ratio of photoluminescence from PtTPTBP and 4P-NPB, while correcting for the differences in PL efficiency and optical outcoupling efficiency. These calculations are discussed further in the Appendix F, are fully determined from experimental data, and do not introduce any free parameters into the analysis.

For the architectures of Fig. 7.2a, the overall thickness of the gating region is fixed at 30 nm. Layer concentrations are selected to maximize η_T for the overall structure. For a

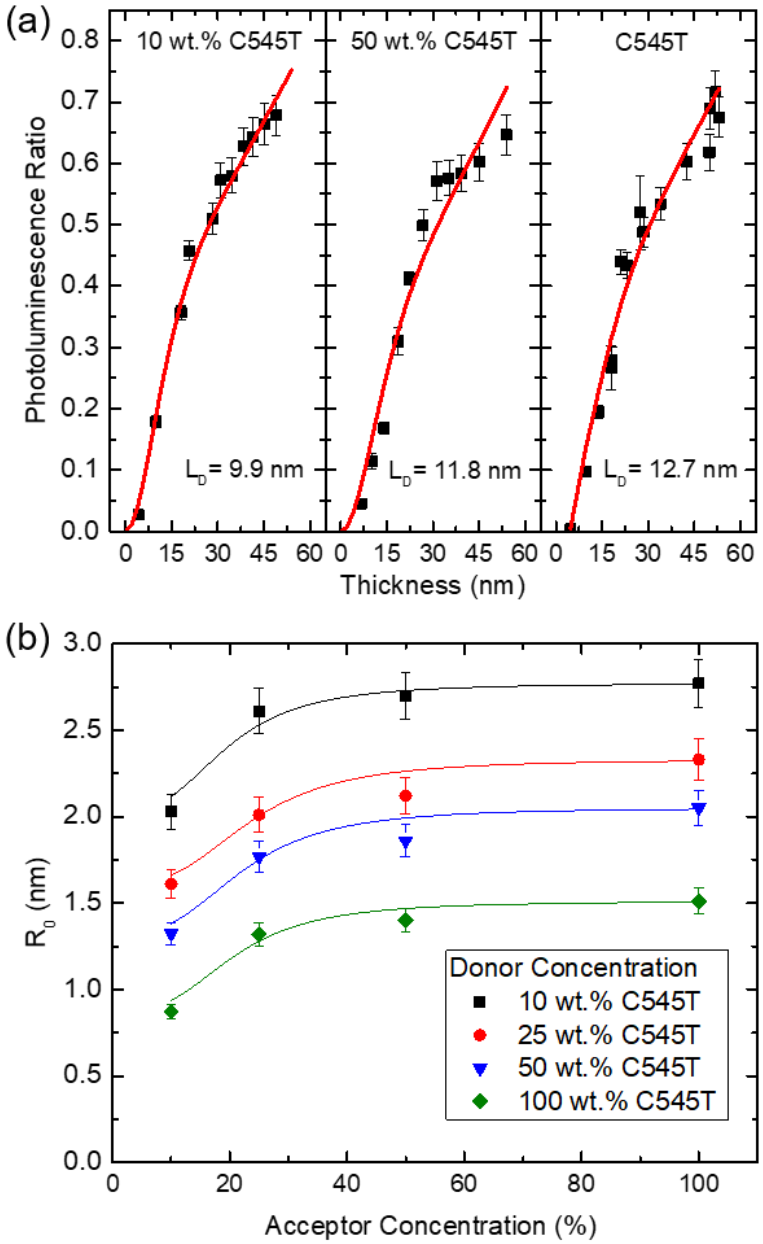

Figure 7.5 (a) Photoluminescence ratio versus thickness for three different concentrations of C545T diluted in UGH2. The L_D is extracted by fitting experimental data using a 1D steady-state diffusion equation. (b) Förster radius (R_0) as a function of acceptor layer concentration for different C545T donor layer concentrations in UGH2. The solid lines are guides for the eye.

given series of exciton gates, the transport efficiency is calculated by injecting excitons from the most dilute layer and collecting from the neat layer of the structure. The simulation of η_T depends on the bulk energy transfer rate (k_i in Eqs. 7.1) and the transfer rate between layers (k_{ij}). The k_i in each layer is extracted using Eq. 2.9 in Chapter 2 and the experimentally measured value of L_D (Fig. 7.5a).[170,272]

The extracted bulk L_D of C545T decreases with dilution in UGH2 due to increasing molecular separation. This decrease occurs despite an increase in R_0 with dilution. In contrast, the L_D of molecules like boron subphthalocyanine chloride (SubPc) and boron subnaphthalocyanine chloride (SubNc) have been shown to increase upon dilution in UGH2 due to the prevalence of an increase in R_0 over the increase in molecular separation.[90,231]

The rate of energy transfer between layers (k_{ij}) is computed by considering differences in concentration, inter-bin distance, and R_0 (Eq. 7.1). The R_0 between layers is computed from Eq. 2.5 in Chapter 2 using experimentally measured parameters such as the PL efficiency, refractive index of the donor medium, and spectral overlap integral, while the orientation factor is taken for randomly oriented dipoles.[274] Denoting layers i as j in Fig. 7.3 as the donor and acceptor, respectively, Fig. 7.5b plots the Förster radius for energy transfer (R_0) from layer i to layer j as a function of acceptor concentration for different donor concentrations of C545T in UGH2. For a fixed acceptor concentration, an increase in R_0 is observed with a reduced concentration of the donor C545T in UGH2. This observation reflects a concomitant increase in the PL efficiency from (9 ± 1) % in neat

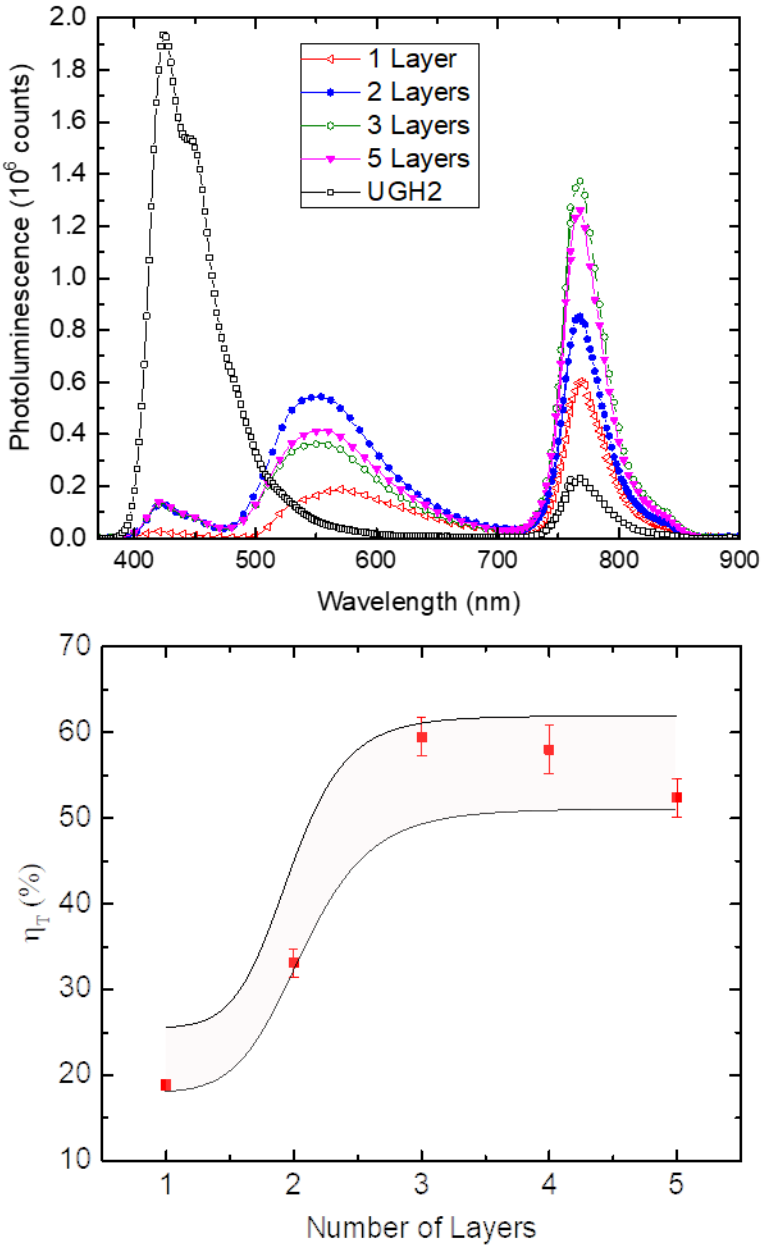

Figure 7.6 (a) Photoluminescence spectrum of the structures in Fig. 7.1a pumped at a wavelength of λ=355 nm. (b) Experimental and simulated (lines) transport efficiency as a function of number of layers. The two lines indicates the upper and lower bound of the simulated structure accounting for error in the measured L_D and layer thickness.

film to (37 ± 2) % for 10 wt.% C545T in UGH2, as well as an increase in the spectral overlap integral due to at blue shift in the fluorescence with dilution. The index of refraction also decreases with dilution from a value of 2.5 in neat film to a value of 1.7 for 10 wt.% C545T in UGH2. At a fixed donor concentration, the increase in R_0 with acceptor concentration reflects an increase in the spectral overlap integral, driven by an increase in the absorption cross-section of the acceptor layer of C545T in UGH2.

The PL intensity of PtTPTBP is tracked as a proxy for η_T as the number of layers is varied (Fig. 7.6a). Varying the number of layers changes the number of locations where the exciton experiences asymmetry in energy transfer rates, and the degree of gating and directed exciton transport. Interestingly, η_T (Fig.7.6b) is maximized when the number of layers is ≥3. This plateau is reproduced well by the associated KMC simulation shown in Fig. 7.6b as a pair of solid lines. The two lines are the upper and lower bound of η_T for the simulated structure accounting for error in the measured L_D of C545T and the layer thicknesses. The good agreement between the simulation and experiment confirm that the model has accurately captured the physics of gating interfaces.

An important feature of the KMC simulation used here is the inclusion of long-range energy transfer between non-adjacent bins in the calculations. Energy transfer between non-adjacent layers contributes 3% and 9% of the total transport efficiency for the 3 layers and 5 layers structures, respectively. This contribution will increase as the distance between non-adjacent layers approaches R_0. In considering the impact of the results of Fig. 7.6b on device design, it is important to consider the origin of the observed plateau in η_T. The

plateau is intrinsic to use of concentration to establish the gates, reflecting a tradeoff between the number of interfaces and strength of an individual gate to drive asymmetric exciton transport. While this plateau would not occur in energy-offset driven gates found in cascade OPVs,[171,231,266] such structures inherently come with an undesirable relaxation of the exciton as it migrates. In this work, the use of concentration driven exciton gates leads to a >200% increase in η_T compared to a neat film of C545T with no gates (Fig. 7.6b). This is equivalent to an effective increase in L_D from 12.7 nm to ~35 nm, further demonstrating the potential gains to be realized by engineering interfaces for enhanced exciton harvesting. The number of layers at which transport efficiency begins to plateau will depend upon the concentration range, diffusion length within each layer, intermolecular spacing and Ro between layers. If we assume the L_D does not vary significantly as a function of dilution, the number of layers at which plateau begins will vary as 6 for concentration range 1 wt.to 100 wt.% C545T, 3 for 10 wt.% to 100 wt.% C545T., 2 for 50 wt.% to 100 wt.% C545T. However, the practical limit to low concentration doping will be determined by variation in L_D. Significant decrease in L_D with dilution will overcome the gain in transport efficiency due to excitonic gates.

7.5 Summary

In conclusion, interfacial excitonic gates are experimentally created through a molecular site imbalance via dilution in a wide energy gap material. The effectiveness of these gates is demonstrated by injecting excitons from the most dilute layer and measuring the excitons collected from the neat layer. The C545T is used as a testbed to examine the

role of interfacial excitonic gates in tailoring exciton diffusion in an organic semiconductor. It is shown that the incorporation of interfaces introduces asymmetry in exciton motion, thereby improving η_T. However, the competition between the number of interfaces and the strength of an individual gate to drive asymmetric exciton transport leads to a saturation in η_T. The approach of using interfacial gates to enhance exciton transport offers new opportunities in the design of organic optoelectronic devices, and especially planar heterojunction OPVs for improved exciton harvesting.

8 Exploiting Excitonic Gates for Organic Light Emitting Devices

The previous chapter demonstrated the effect of excitonic gates in enhancing exciton transport in organic semiconductor thin films, building off prior work applying these devices in photovoltaic cells. This chapter is focused on applying entropic and energetic excitonic gates in organic light-emitting devices to engineer charge and exciton profiles in organic light-emitting devices (OLEDs).

8.1 Background

Despite the enormous progress made in OLED performance, further improvements are still required for high brightness applications. One of the important issues that remains challenging is the decrease in OLED efficiency at high brightness (the efficiency roll-off, Fig. 8.1). The external quantum efficiency (η_{EQE}) is the

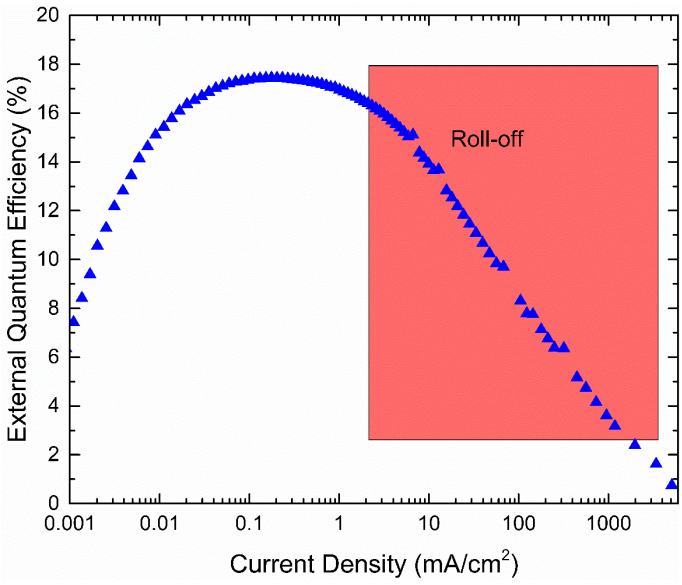

Figure 8.1 External quantum efficiency as function of current density (mA/cm^2) with significant roll-off above 1 mA/cm^2 highlighted in red.

ratio of photons emitted in the forward viewing direction divided by the number of charge carriers injected into the device. The roll-off originates from bimolecular exciton quenching mechanisms including exciton-exciton and exciton-polaron processes.[92,102,275] Besides the negative impact caused by efficiency roll-off on power consumption, it also reduces the device lifetime due to higher electrical stress needed to achieve same brightness level.[93]

High-efficiency OLEDs consists of three or more organic layers sandwiched between two electrodes. Figure 8.2 illustrates the basic structure and working principle of

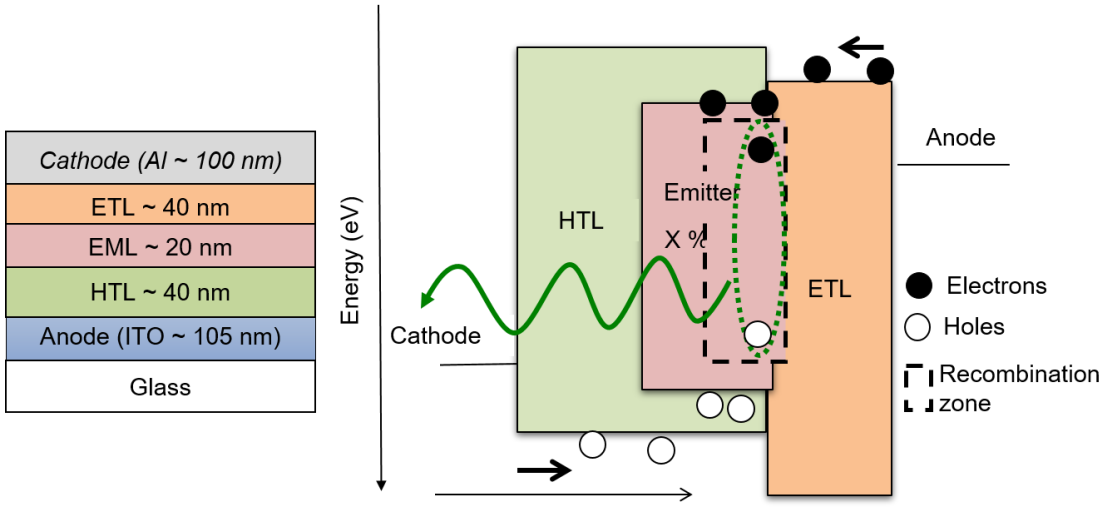

Figure 8.2 (a) Schematic representation of device architecture for an OLED. (b) Energy level diagram for an OLED. Holes and electrons are injected into the device and transported through the hole (HTL) and electron transport layers (ETL) respectively. Upon reaching the host-guest emissive layer (EML), they form excitons which may decay radiatively.

an OLED. By applying an external bias, holes and electrons are injected into the device and transported through hole and electron transport layers (HTL & ETL) to the host-guest emissive layer. Injected holes and electrons migrate to the emissive layer (EML) forming

excitons. The EML layer consists of a matrix, which is either preferentially electron or hole transporting or can be ambipolar (conducting both electron and hole). The use of heavy metals increases the spin-orbit coupling between the exciton spin angular momentum and the orbital angular momentum and the triplet state becomes emissive (Figure 1c) leading to phosphorescence. In single emissive layer OLEDs, the exciton formation zone is usually narrow (around 2 to 10 nm), and is located towards one side of the EML.[93,164,276]. For high exciton and polaron densities in the EML, bimolecular quenching mechanisms such as triplet-triplet annihilation (TTA) and triplet-polaron quenching (TPQ) may dominate recombination.

For TTA, two triplets annihilate to form an intermediate state X that can be converted to either singlet or triplet state according to the following exothermic reactions as:[92,93]

$$T_1 + T_1 \xrightarrow{k_{ss}^T} T_n + S_o \rightarrow T_1 + S_o$$

$$T_1 + T_1 \xrightarrow{k_{TT}^S} S_n + S_o \rightarrow S_1 + S_o$$

where T_1 represents the triplet excited state, S_1 the singlet excited state, and S_o the ground state of the molecule. The rate constants for generation of singlets and triplets from TTA are given as k_{TT}^S and k_{TT}^T, respectively. For phosphorescent materials, the singlet state can be immediately converted to triplet state via strong spin orbit coupling. Since this effectively leads to formation of one triplet state from two triplets, the rate of triplet loss is $\frac{1}{2}k_{TT}$. While the TTA process involves interaction between two triplet states, in the TPQ

the triplet exciton transfer its energy to a charged molecule through the following process:[93,102]

$$T_1 + h^+ \xrightarrow{k_{TP,h}} S_o + h^{+*}$$

$$T_1 + e^- \xrightarrow{k_{TP,e}} S_o + e^{-*}$$

where electron and hole quench triplet state with rate $k_{TP,h}$ and $k_{TP,e}$respectively. The TPA mainly occurs via Förster energy transfer and no orbital overlap is required for this process.[102] The time evolution of triplet population [T_1] can be described using one-dimensional rate equation as: [92,93,98]

$$\frac{d[T_1]}{dt} = -\frac{[T_1]}{\tau} - \frac{1}{2}k_{TT}[T_1]^2 - k_{Tp}[T_1][n_p] + \frac{J}{q\,W} \quad (8.1)$$

where q is the electron charge, Q is the exciton recombination zone, J is the current density (proportional to triplet generation) and τ is the triplet exciton lifetime. The n_p is the charge carrier density and can be expressed according to space charge limited current (SCLC) theory as:[102,275]

$$n_p = C\,J^{1/l+1} \text{ (8.2 a)}$$

$$C\left[\left(\frac{l+1}{2l+1}\right)\left(\frac{l+1}{l}\right)^l\left(\frac{N_t^l\,\varepsilon}{W\,e^2\mu\,N_c}\right)\right]^{1/(l+1)} \text{(8.2b)}$$

where N_t is the density of trap states, Nc the density of states at the transport level, $l = E_t/kT$ (E_t, depth of trap states), μ is the carrier mobility and W is the exciton recombination

zone. The η_{EQE} for the OLED operation can be obtained from steady-state solution of Eq. 8.1. For a single layer, the solution after Reineke et al. is: [102]

$$\frac{\eta_{EQE}}{\eta_{EQE_o}} = \Theta \left(\sqrt{\frac{\Delta^2 + \Gamma\, k_{TT}}{k_{TT}^2}} - \frac{\Delta}{k_{TT}} \right) \quad (8.3)$$

with

$$\Theta = \frac{e\, W}{\tau\, J}$$

$$\Delta = \left(\frac{1}{\tau_p} + k_{TP}\, C\, J^{1/(l+1)} \right)$$

$$\Gamma = \frac{2\, J}{e\, W}$$

where η_o is the quantum efficiency in absence of TTA and TPA. It can be seen that the behavior of η_{EQE} depends upon the four parameters k_{TP}, k_{TT}, τ and W, which can be obtained experimentally.

Based on the previous chapter, excitonic gates either energetic or entropic can be used as strategy to reduce the EQE roll-off by spatially separating charge carriers and excitons thereby reducing the overall excitonic density from the initial exciton recombination zone to an adjacent layer. An imbalance in energy transport rates at an interface can either arise from a difference in energy gap between the two layers or molecular site imbalance as demonstrated in Chapter 6. This chapter offer a combined theoretical-experimental study of the impact of exciton gating interface on efficiency role-off in OLEDs, and hence, a practical assessment of these architectures for devices.

8.2 *Experimental Details*

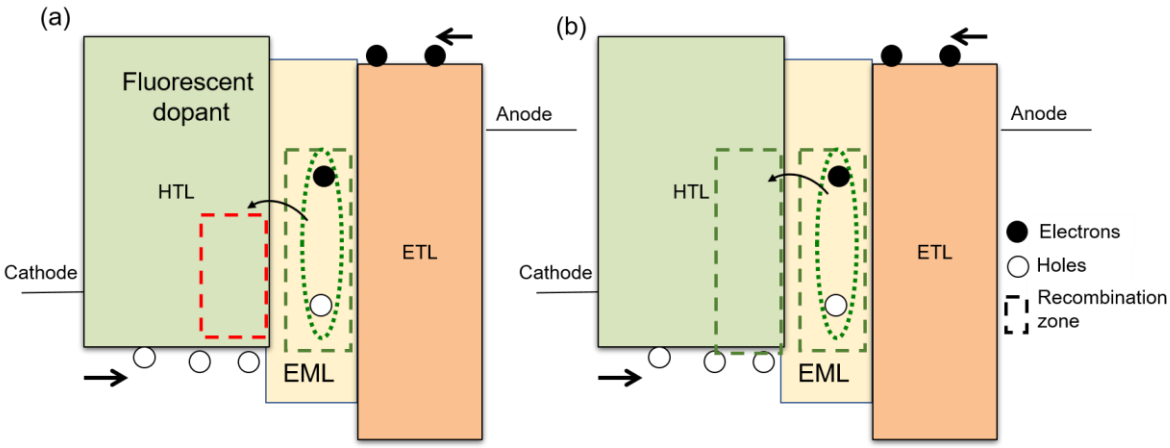

Figure 8.3 Schematic of single asymmetric architecture of OLED formed by Förster energy transfer from excitons formed in emissive layer to a fluorescent dopant (a) and phosphorescent dopant (b)

Exciton transport is examined in single asymmetric architectures of OLED where exciton gates are formed by energy transfer to a fluorescent dopant in an adjacent layer as well as through molecular site imbalance across an interface (Fig. 8.3). Exciton transport is probed in the archetypical green phosphorescent $Ir(ppy)_3$ OLED. Active materials of 4,4′-Cyclohexylidenebis[N,N-bis(4-methylphenyl)benzenamine] (TAPC), 4,4-N,N′-Dicarbazole-1,1′-biphenyl (CBP), 2,2',2"-(1,3,5-Benzinetriyl)-tris(1-phenyl-1-H-benzimidazole) (TPBi), $Ir(ppy)_3$ and 5,10,15,20-Tetraphenylbisbenz[5,6]indeno[1,2,3-cd:1′,2′,3′-lm]perylene (DBP) are purchased from Luminescence Technology Corporation. ITO coated glass substrates are sequentially cleaned using tergitol, deionized water, acetone and isopropanol in a sonication bath. Substrates are then treated UV-zone ambient for 15 minutes prior to thin film deposition. The η_{EQE} is experimentally obtained by placing

the device on the surface of large area calibrated photodetector (a Hamamatsu detector, model S3584-08 is used here) such that one is able to collect all photons emitted in forward viewing direction. Steady-state electroluminescence spectra are acquired using an Ocean Optics HR4000 Spectrometer. Energy transfer between exciton in EML to dopant in an adjacent layer is characterized by measuring transient electroluminescence (EL). The pump voltage pulse is chosen to be around 100 ns, shorter than the radiative decay lifetime of the phosphorescent molecule and larger than the charging time of the OLED (~50 ns).

8.3 Efficiency Roll-off Improvement in OLEDs

In OLED, the exciton population in a single asymmetric energetic gate between phosphorescent emissive layer and an adjacent fluorescent emitter doped layer is given by:

$$\frac{d[T_1]}{dt} = -\frac{[T_1]}{\tau_p} - \frac{1}{2}k_{TT}[T_1]^2 - k_{Tp}[\mathrm{T_1}][n_p] - \mathrm{k}_F[\mathrm{T_1}] - \frac{\mathrm{J}}{\mathrm{q\,w}} \quad (8.4)$$

$$\frac{\mathrm{d}[\mathrm{S_1}]}{\mathrm{dt}} = -\frac{[\mathrm{S_1}]}{\tau_\mathrm{s}} + \mathrm{k_F}[\mathrm{T_1}] \quad (8.5)$$

where the rate of energy transfer from the phosphorescent emitter in recombination zone to a fluorescent dopant is k_F, $[\mathrm{S_1}]$ is the singlet population, τ_s is the fluorescent emitter lifetime. The steady-state solution of Eq. 8.4 for η_{EQE} is same as Eq. 8.3 with $\Delta = \left(\frac{1}{\tau_\mathrm{p}} + \mathrm{k_F} + \mathrm{k_{TP}\ C\ J}^{1/(\mathrm{l}+1)}\right)$. Figure 8.4 shows simulated normalized η_{EQE} as a function of current density for OLED where exciton gates are formed by energy transfer to a

fluorescent dopant in an adjacent layer. The η_{EQE} is simulated for green $Ir(ppy)_3$ OLED with rate constants and exciton lifetime taken from the previously measured values as k_{TP} $= 3.3 \times 10^{-13}$ cm^3/s, $k_{TT} = 7.1 \times 10^{-12}$ cm^3/s, $\tau_p = 6.9 \times 10^{-7}$ s.[277] For the fluorescent dopant, a typical value of $\tau_s = 1 \times 10^{-9}$ s is assumed for the fluorescent lifetime. The increase in energy transfer rate k_F to a fluorescent dopant results in a slower η_{EQE} roll-off in the phosphorescent layer due to decreased triplet-polaron and triplet-triplet quenching.Experimentally, the role of the energetic excitonic gate between phosphorescent EML and fluorescent dopant is examined in $Ir(ppy)_3$-DBP system. Figure 8.5a-b show the device architecture and energy level of materials used for examining the energy transfer between $Ir(ppy)_3$ and DBP. The distance between the two layers is varied while the overall thickness of the device is fixed. The Förster radius between 15 wt.% $Ir(ppy)_3$ in CBP and 5 wt.% DBP in TAPC is 4.5 nm, calculated from Eq. 2.4 in Chapter 2. Figure 8.5d shows the steady-state electroluminescence spectra (normalized w.r.t peak) for various TAPC thickness at a

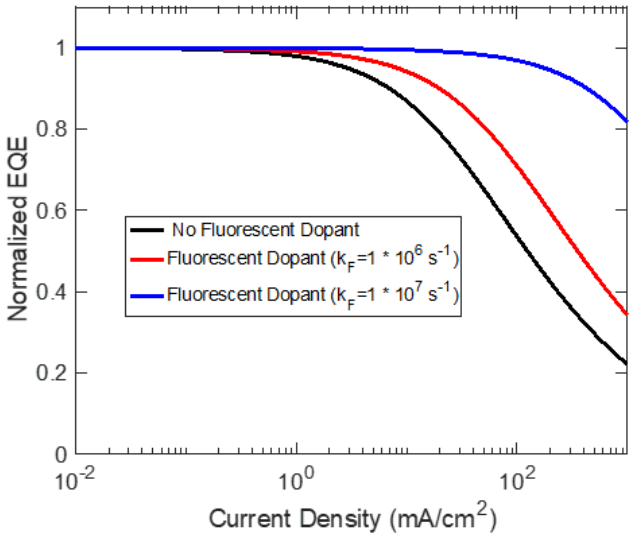

Figure 8.4 Normalized η_{EQE} as a function of current density (mA/cm^2) with no fluorophore (black line) and fluorophore (red and blue line) adjacent to $Ir(ppy)_3$ layer. The k_F is the rate of energy transfer to fluorophore.

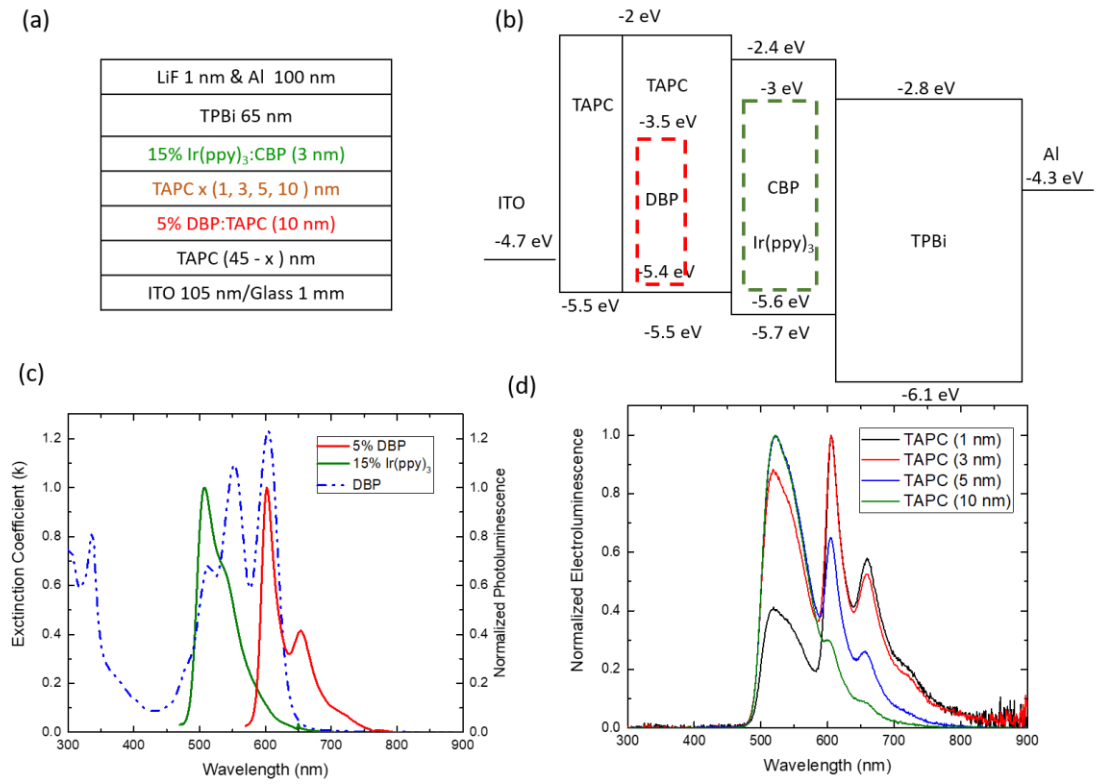

Figure 8.5 (a) Device architecture for accessing the role of a single asymmetric energetic gate between the EML and a layer of HTL doped with a fluorophore. (b) Schematic of energy level diagram for the different layers in OLED (c) Extinction coefficients (k) of DBP and normalized PL of 15 wt.% $Ir(ppy)_3$ in CBP and 5 wt.% DBP in TAPC. (d) Normalized electroluminescence measured for the device in (a) at 0.1 mA/cm^2.

current density of 0.1 mA/cm^2. An increase in TAPC thickness reduces the DBP emission which may reflect a decrease in Förster energy transfer from $Ir(ppy)_3$ and DBP. At the same time, this can result from decrease in direct exciton generation on DBP layer since increase in spacer thickness will reduced the electron leakage into DBP dopant. In order to examine the origin of the observed trend in steady-state EL spectra, transient EL decays are carried out on the devices in Fig. 8.6a. Direct exciton generation in DBP would result in fast EL decay due to the short lifetime ~ 2 ns of DBP excitons.[278] No fast EL decay component is

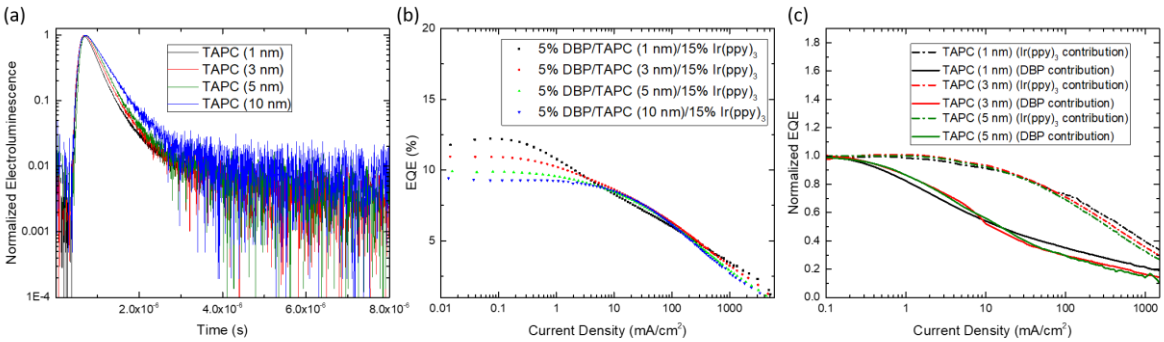

Figure 8.6 (a) Transient EL decay from the device architecture in Fig. 8.3a to assess the energy transfer between $Ir(ppy)_3$ and DBP. (b) Normalized EQE as a function of current density for $Ir(ppy)_3$ and DBP emission as the spacing between two layers is varied.

observed in Fig. 8.6a, representing the fact that the majority of excitons in DBP are generated by energy transfer from $Ir(ppy)_3$. Figure 8.6b shows the η_{EQE} as a function of current density for various spacer layer thickness between $Ir(ppy)_3$ and DBP layers. To evaluate the contribution of $Ir(ppy)_3$ and DBP to overall η_{EQE}, the η_{EQE} is collected using a 600 nm short pass filter. The contribution of each individual layer is calculated from two external quantum efficiencies, η_{EQE} and $\eta_{EQE}^{short\ pass\ 600\ nm}$ as:

$$\alpha_1\, \eta_{EQE}^{Ir(ppy)3} + (1-\alpha_1)\, \eta_{EQE}^{DBP} = \eta_{EQE}^{short\ pass\ 600\ nm} \quad (8.7\ a)$$

$$\alpha_2\, \eta_{EQE}^{Ir(ppy)3} + (1-\alpha_2)\, \eta_{EQE}^{DBP} = \eta_{EQE} \quad (8.7\ b)$$

Components α_1 and α_2 are calculate from EL spectrum at various current densities. Figure 8.6c shows normalized η_{EQE} extracted for $Ir(ppy)_3$ and DBP layer. The $Ir(ppy)_3$ layer shows slower roll-off with J_{50} (current density at which the EQE drops to half of its maximum value) varying from 324 mA/cm^2 for 5 nm TAPC to 450 mA/cm^2 for 1 nm TAPC. While for DBP η_{EQE} start to roll-off from 0.1 mA/cm^2 with J_{50} of 10 mA/cm^2. The roll-off is

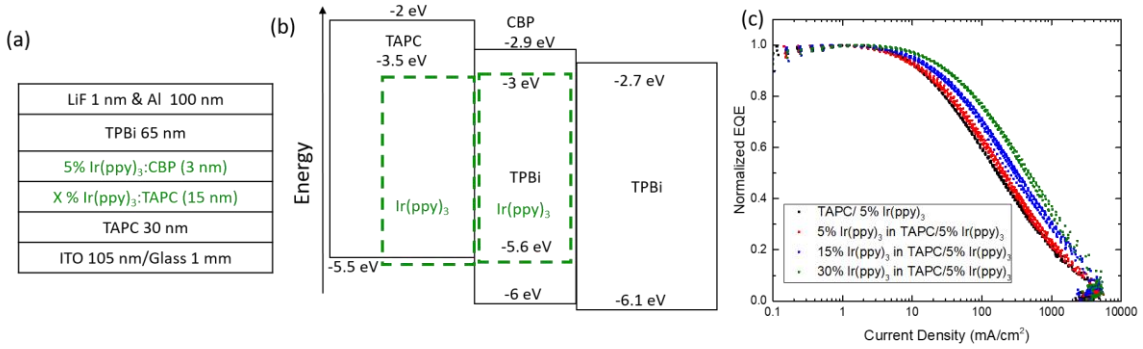

Figure 8.7 (a) Device architecture for accessing the role of single asymmetric entropic gate formed by varying the concentration of $Ir(ppy)_3$ in TAPC layer. (b) Schematic of energy level diagram for the different layers in OLED. (d) Normalized EQE as a function of current density for various concentration of $Ir(ppy)_3$ in TAPC layer

independent of the position of DBP doped in HTL, this can possibly be understood via long range singlet excitons quenching from the polarons. Previous studies have shown that singlet excitons can be quenched via Förster energy transfer with R_0 ranging from 2.5 nm to 5 nm. [100,101,279]

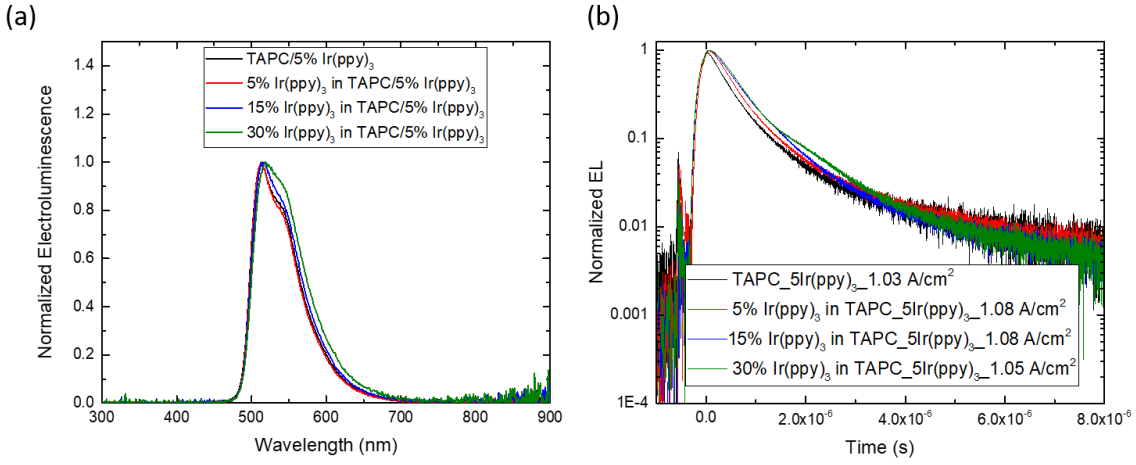

Figure 8.8 (a) Normalized electroluminescence curve measure for device architecture in 8.5(a) at 0.1 mA/cm^2. (b) (d) Transient EL decay measured for different concentration of $Ir(ppy)_3$ in TAPC layer

Efficiency roll-off is also examined for single asymmetric excitonic gate formed by varying the concentration of $Ir(ppy)_3$ in TAPC layer (Fig. 8.7a). Figure 8.7c shows the normalized η_{EQE} as a function of current density for various concentration of $Ir(ppy)_3$ in TAPC layer. Increase in $Ir(ppy)_3$ concentration in TAPC results in slower roll-off with J_{50} varying from 150 mA/cm^2 for no $Ir(ppy)_3$ concentration in TAPC layer to 470 mA/cm^2 for 30 wt. % $Ir(ppy)_3$ in TAPC. However, assessment of energy transfer could not be clearly distinct from direct generation of excitons in $Ir(ppy)_3$ doped with TAPC layer from transient EL decay curve (Fig. 8.8). The variation in dopant concentration in TAPC will also change mobility of holes in HTL layer as well as plausible shift in recombination zone.

8.4 Summary

In this chapter, a practical assessment of the role of exciton gates in reducing the efficiency role-off in OLEDs is examined. Experimentally, $Ir(ppy)_3$ is used as a testbed to experimentally examine the role of single asymmetric interfacial excitonic gates by energy transfer to a fluorescent dopant DBP representing energetic gate. The energy transfer to DBP reduces the role-off in $Ir(ppy)_3$ due to a decrease in triplet-polaron quenching and triplet-triplet annihilation. Surprising the EQE roll off in the DBP layer is severe due to long range quenching of singlet excitons and polaron. Entropic interfacial excitonic gates are also examined for $Ir(ppy)_3$ molecules, however the role of energy transfer to reduce EQE roll-off remains inconclusive.

9 Exciton Transport in Singlet Fission Materials

This chapter is a summary and extension of unpublished work entitled “Device-based probe of triplet exciton diffusion in singlet-fission materials”. This work is being submitted to the journal of physical chemistry letters. The author acknowledges collaborator Tao Zhang for photocurrent-ratio methodology published in nature communications entitled “Intrinsic measurements of exciton transport in photovoltaic cells”[206] as well as triplet diffusion length measurement of tetracene films as discussed in the last section of this chapter. This work is supported by National Science Foundation (NSF) Solid-State and Materials Chemistry under DMR-1708177 and Electronics, Photonics and Magnetic Devices under ECCS-1509121.

9.1 Background

Singlet fission is a photophysical process observed in organic semiconductors that converts a spin zero singlet exciton into two spin unity triplet excitons.[94,95,280–283] The energetic requirement to observe singlet fission is that the triplet energy must be roughly half of the associated singlet energy ($E(S_1) \approx 2E(T_1)$). Materials exhibiting singlet fission have received particular interest for applications in photoconversion. Used on their own, singlet fission absorbers are capable of generating two electrons from a single absorbed photon. When combined with conventional silicon-based photovoltaic cells, singlet-fission

materials offer a route to improve spectral coverage by direct charge generation or reduced thermalization loss via down conversion.[96,97,284,285] The latter may involve coupling the singlet fission material to an infrared-emitting species, permitting the conversion of absorbed visible light into infrared radiation that can be efficiently absorbed by silicon. In such instances, the kinetics in moving from the singlet to the triplet to the emitter must be optimized for high efficiency. While the kinetics of singlet fission have been studied extensively, specific studies of triplet migration in these materials are more challenging, as it is difficult to isolate triplet transport from the initial fission event and the migration of any remaining singlets.

Singlet fission is a multi-step process. A photogenerated singlet on one molecule interacts with a ground state neighboring molecule to form a correlated triplet pair.[286–288] The triplet pair separates into two individual mobile triplet excitons.[95,280] Direct probing of triplet exciton diffusion cannot be carried out using conventional photoluminescence-based measurements since the generated triplets are not typically luminescent.[188] Method discussed in Chapter 5 can be used to probe dark triplet excitons in singlet fission materials, however it will require near-infrared emitting(λ>1000 nm) quantum dots as a sensitizer since organic semiconductor sensitizer are not commercially unavailable. Measurement of exciton L_D will be complicated by morphology of quantum dot film.

As a result, prior work has utilized singlet exciton fluorescence as an indirect probe of triplet exciton diffusion in the limit of large triplet populations capable of singlet formation via triplet-triplet fusion.[188,289,290] In these measurements, singlet diffusion, triplet diffusion,

singlet fission, and triplet fusion may all take place, complicating the interpretation of the subsequent exciton dynamics. While non-device-based methods such as ultrafast transient absorption microscopy (TAM)[189,190,223] are capable of probing the intrinsic diffusion length of both non-radiative triplets as well as mobile singlets in fission materials, however, the measurement takes place at high photon flux which requires taking into account various bimolecular recombination rate such as triplet-triplet annihilation, singlet-triplet quenching, and triplet-triplet fusion. The measurement of the exciton diffusion length is limited by the spatial resolution of TAM which is dictated by noise due to laser fluctuation as well as detection system. It is for these reasons; that in this chapter a device-based methodology capable of specifically probing triplet diffusion in singlet-fission materials that is independent of the efficiency of singlet fission or the presence of singlet diffusion. In addition, this method can be applied at low enough light fluence to avoid complexities associated with triplet-triplet fusion. While this method has been previously demonstrated on both emissive and dark organic semiconductors, it has not previously been applied to systems where there are potentially multiple diffusing species.[157,206] In this chapter, extensively studied singlet fission material 5,12-bis((triisopropylsilyl)ethynyl)-tetracene (TIPS-tetracene) is

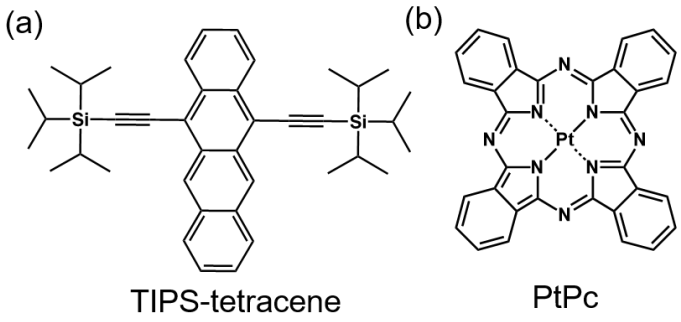

Figure 9.1 Molecular structure of (a) TIPS-tetracene and (b) PtPc used in this chapter

considered, characterized by singlet and triplet populations in equilibrium.[291] TIPS-tetracene, having same molecular core as tetracene but is made compatible to solution-based deposition techniques via addition of triisopropylsilyl (TIPS) side groups (Fig. 9.1a). The singlet fission in TIPS-tetracene have been extensively studied both in solid state as well as in solution.[292–295] It is endothermic by about 200 meV and the triplet pair separation time is highly sensitive to crystal packing.[294] In order to directly probe triplet exciton diffusion, a triplet injection layer is used to selectively excite the triplet states and isolate triplet transport from other processes.

9.2 Experimental Details

Platinum phthalocyanine (PtPc) (Fig. 9.1b), and 1,4,5,8,9,11-hexaazatriphenylene hexacarbonitrile (HATCN) are purchased from Luminescence Technology Corporation. TIPS-tetracene is supplied by Dr. Simon Dowland and Prof. Akshay Rao at the University of Cambridge. For thickness-dependent photoluminescence (PL) quenching measurements, a unity quenching efficiency is assumed for HATCN due to the favorable energy offset for electron transfer from donor material.[206,231] Photoluminescence spectra are collected using a Photon Technology International QuantaMaster 400 Fluorometer equipped with a photomultiplier detection system. Thin film samples are pumped using a monochromated Xe arc lamp at an angle of 70^{o} from substrate normal under N_2 purge. Device external quantum efficiency is calculated from the short-circuit current under monochromatic light illumination using a 300 W Oriel Xe lamp, a monochromator, an optical chopper wheel, and an SR-810 lock-in amplifier. Film thicknesses, reflectance and

transmittance spectra are measured using a J. A. Woollam variable-angle spectroscopic ellipsometer. Reflectance spectra are measured at an angle of 15º to the substrate normal. Optical constants are obtained from fitting transmittance (normal incidence) and reflectance spectra. Organic photovoltaic cells (OPVs) are fabricated on indium-tin-oxide (ITO)-coated glass substrates. The substrates are subsequently cleaned in tergitol solution, deionized water, acetone, and isopropanol, followed by exposure to UV-ozone ambient. Thin film layers are deposited at room temperature using high vacuum thermal evaporation at a deposition pressure of $<9 \times 10^{-7}$ Torr. Donor TIPS-tetracene is deposited at 0.2 nm/s.

9.3 IQE Ratio Methodology

The singlet fission process in organic semiconductor materials can be classified as exothermic or endothermic based on the energetic alignment between the singlet energy and twice the triplet energy. The process is exothermic for materials such as pentacene, where the singlet energy exceeds that of the triplet pair ($E(S_1) > 2E(T_1)$).[296] This leads to the rapid and complete conversion of the singlet state, meaning only the triplet will contribute to photocurrent in an OPV when paired with an acceptor such as C_{60}.[297] For endothermic materials such as tetracene or TIPS-tetracene,[296] the conversion is incomplete due to slower and thus both states may contribute to photocurrent in an OPVs.[298]

Photocurrent based measurement previously as described in chapter 4 is often used to measure exciton L_D of non-luminescent dark excitonic materials.[158,159,169,201–206] The extraction of L_D by fitting OPV external quantum efficiency (η_{EQE}) spectra often yield an underestimate due to interfacial charge transfer (CT) state recombination prior to charge

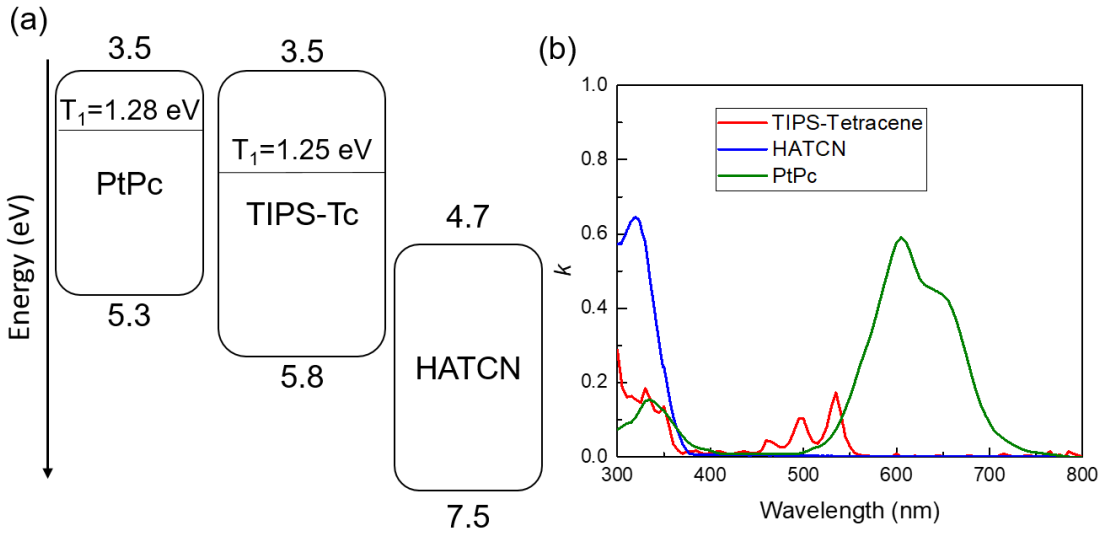

Figure 9.2 (a) Energy levels for direct injection measurement of TIPS-tetracene triplet L_D. (b) Extinction coefficients (k) of TIPS-tetracene, HATCN, and PtPc thin films.

collection. The photocurrent-ratio methodology overcomes this limitation by instead fitting a ratio of donor-to-acceptor internal quantum efficiency (η_{IQE}). The ratio cancels out the unknown efficiency of CT state separation (η_{CS}) since these losses are independent of where the exciton is initially generated.[299,300] The free carrier collection efficiency is assumed to be unity at short-circuit, consistent with previous work.[207,219,301] The internal quantum efficiency (η_{IQE}) ratio between the donor (D) and acceptor (A) is thus expressed as:

$$\frac{\eta_{IQE}^{D}}{\eta_{IQE}^{A}} = \frac{\eta_T \eta_D^D \eta_{CS}}{\eta_D^A \eta_{CS}} = \frac{\eta_D^D}{\eta_D^A/\eta_T} \quad (9.1)$$

where η_T is the triplet yield and here represents the overall efficiency of converting singlets into mobile triplets via fission. The donor diffusion efficiency (η_D^D) will vary with donor thickness while the acceptor diffusion efficiency (η_D^A) will be constant. Since η_{T} is not

expected to vary with donor layer film thickness, it is grouped with η_D^A to create a single thickness-independent fit parameter. Thus, the shape of η_{IQE} ratio as a function of donor thickness is determined by donor η_D^D (numerator) and L_D. Thus the η_{IQE} ratio is fit to yield the donor L_D and the ratio η_D^A/η_T. If η_T is known, the acceptor L_D may also be determined.

For endothermic materials, photocurrent-ratio methodology[157,206] can be modified to treat materials where the fission efficiency is not known *a priori* by selectively injecting triplets into the fission material. For example, a triplet injection layer of PtPc (T_1 = 1.28 eV)[302] can be used to selectively inject triplets into TIPS-tetracene (1.25 eV)[294] (Fig. 9.2a) via Dexter transfer, circumventing altogether the generation, diffusion, and fission of singlets. When injection layer is considered, the ratio is no longer between donor and acceptor, but instead between the injector (I) and the acceptor (A) as:

$$\frac{\eta_{IQE}^I}{\eta_{IQE}^A} = \frac{\eta_T \eta_D^I \eta_{CS}}{\eta_D^A \eta_{CS}} = \frac{\eta_D^I}{\eta_D^A/\eta_T} \quad (9.2)$$

where η_T reflects the efficiency with which triplets are formed in the injector and injected into TIPS-tetracene. As triplet energy transfer is typically short-range, triplet exciton generation in TIPS-tetracene is assumed to occur only in the first monolayer. The donor diffusion efficiency (η_D^I) will vary with donor thickness while the acceptor diffusion efficiency (η_D^A) will be constant. Since η_{T} is not expected to vary with donor layer film thickness, it is grouped with η_D^A to create a single thickness-independent fit parameter. Thus, the shape of η_{IQE} ratio as a function of donor thickness is determined by donor η_D^I

(numerator) and L_D. Thus the η_{IQE} ratio is fit to yield the donor L_D and the ratio η_D^A/η_T. If η_T is known, the acceptor L_D may also be determined.

In TIPS-tetracene, the functionalization of tetracene core changes the ionization potential for charge carriers in thin films by 0.38 eV.[303] Therefore with TIPS-tetracene, commonly used acceptor material C_{60} cannot be used due to higher value of CT state energy (1.5 eV estimated from HOMO and LUMO energy level) than TIPS-tetracene triplet energy (1.25 eV).[294] HATCN is selected as an acceptor layer to dissociate TIPS-tetracene triplets due to its deeper LUMO energy level of 5 eV[304] compared to C_{60} (4.3 eV)[305], with the CT state energy lower than the TIPS-tetracene triplet energy (Fig. 9.3).[305] Figure 9.2b shows the extinction coefficients of TIPS-tetracene, HATCN, and PtPc. Figure 9.4a shows the OPV architecture for measurement of η_{EQE} for various TIPS-tetracene thickness. The η_{EQE} are measured for both thermal evaporated TIPS-Tetracene layers (Fig. 9.4b) and spin coated films, however the triplet L_D could not be probed for solution deposited films due to low reproducibility and plausible morphology

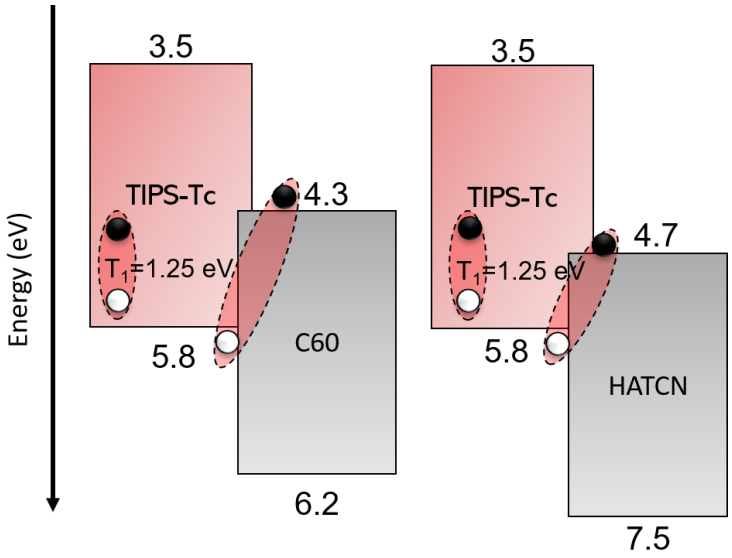

Figure 9.3 Schematic of energy levels and CT sate energy for dissociation of TIPS-Tc triplet excitons.

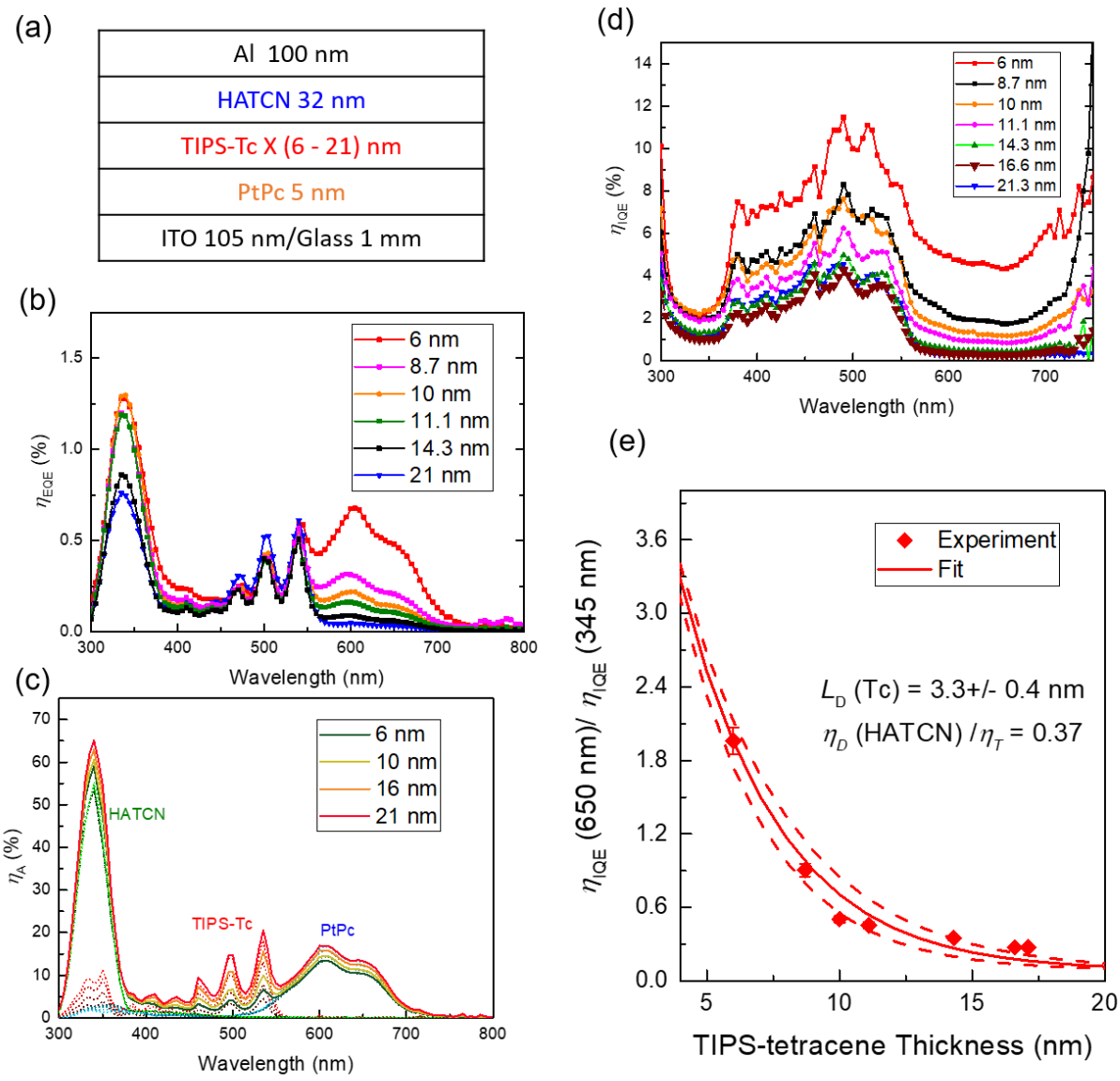

Figure 9.4 (a) Device architecture for TIPS-tetracene triplet L_D measurements. (b) The η_{EQE} spectra measured at short-circuit for different TIPS-tetracene layer thicknesses. (c) The η_A spectra of the different active layers calculated using a transfer matrix model. (d) The η_{IQE} spectra calculated by dividing the η_{EQE} spectra with the η_A spectra in (b). (e) Internal quantum efficiency ratio as a function of TIPS-tetracene layer thickness.

variation between different film thicknesses. The η_{IQE} (Fig. 9.4 d) is obtained by diving η_{EQE} (Fig. 9.4 b) with absorption efficiency η_A (Fig. 9.4 c). The injection layer η_{IQE} is extracted at $\lambda = 650$ nm (in the absence of absorption from TIPS-tetracene and HATCN), while the acceptor η_{IQE} is extracted at $\lambda = 345$ nm. Fitting the triplet injector-acceptor η_{IQE} ratio as a function of TIPS-tetracene thickness yields a L_D of (3.3 ± 0.4) nm (Fig. 9.4e). For comparison, the singlet L_D is also measured with thickness-dependent PL quenching technique (Figure 9.5), as previously described in Chapter 4, yields a triplet L_D of (7.1 ± 1.4) nm.

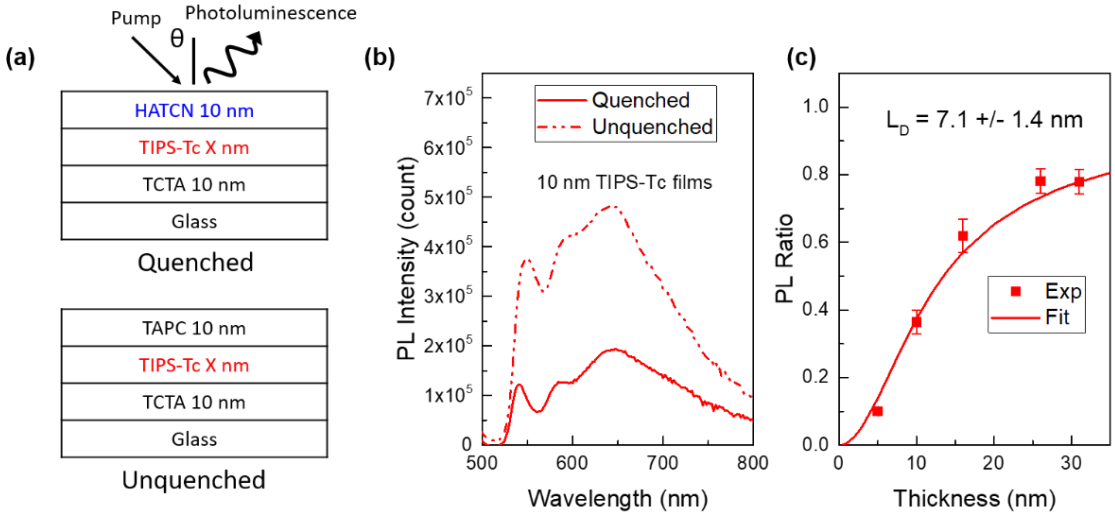

Figure 9.5 (a) Architectures for TIPS-tetracene singlet L_D measurements. Films are all pumped with $\lambda = 470$ nm light with an incident angle of 70°. (b) Representative PL spectra (10-nm-thick TIPS-tetracene) for the samples in (a). (c) The PL ratio of TIPS-tetracene films as a function of TIPS-tetracene thickness.

A triplet L_D of (32.1 ± 2.6) nm is extracted from vacuum deposited film tetracene films by group member Tao Zhang using similar photocurrent ratio methodology (unpublished). The triplet lifetime in polycrystalline tetracene films has been show to range from (40-200)

ns depending upon the morphology[306], which results in a diffusivity of (0.5×10^{-4} to 2.50×10^{-4}) cm^2s^{-1}. While for TIPS-tetracene, a triplet lifetime of 570 ns [294] results in a diffusivity of (1.9×10^{-7}) cm^2s^{-1}. A factor of 10 difference in triplet L_D between TIPS-tetracene and tetracene is consistent with Chapter 6 studying the effect of functionalization on triplet diffusion length in a phenanthroline based molecules.[245] The difference in triplet L_D can be understood using a Dexter transfer mechanism where energy transfer scales exponentially with intermolecular spacing. In thin film, previous studies have shown that the herringbone arrangement of tetracene molecule results in an average molecular densities of 3.34 nm^{-3},[307,308] while loose 1D chain type of arrangement in polycrystalline TIPS-tetracene thin film results in an molecular density of 1.10 nm^{-3} with little overlap between tetracene cores.[294] The value of average intermolecular spacing (d) as determined by taking the cube root of the molecular density ($\sqrt[3]{\frac{1}{\rho}}$) varies in increasing order as of 6.69 for tetracene and 9.69 Å for TIPS-tetracene respectively. If we assume that optical overlap is similar for these molecules, the ratio of diffusivity derived from Dexter transfer energy transfer (Eq. 2.8 and 2.9) is equivalent to experimental value for the molecular orbital radius of 0.38 Å. This value is consistent with the value of molecular orbital radius we calculated for phenanthroline molecules. Other factors such as crystalline order in TIPS-tetracene film can also play a critical role in exciton transport. Previously, systematic study of crystalline order and singlet exciton diffusion have shown enhancement in L_D from (6.5 $\pm$ 1.0) nm to (21.5 $\pm$ 2.5) nm for increase in grain size to 0 to 400 nm for PTCDA films.[146] This increment is caused due to decrease in non-radiative quenching of excitons at grain

boundaries. Similar effect can also play a role between tetracene and TIPS-tetracene for triplet excitons. The film morphology and processing condition also plays a critical in determining the triplet transport in singlet fission materials.[223]

9.4 Summary

In this chapter, a study to probe triplet L_D using a photocurrent ratio method with a triplet injector for endothermic singlet fission material, TIPS-tetracene is presented. The method allows simple estimate of triplet L_D length in isolation of singlet diffusion, triplet fusion and singlet fission taking place in the material. By measuring the IQE ratio for the material of interest, triplet L_D of (3.3 ± 0.4) nm is obtained for TIPS-tetracene. The low triplet L_D of TIPS-tetracene as compared to tetracene (32.1 ± 2.6) nm is understood using Dexter transfer where the rate of energy transfer scales exponentially with intermolecular spacing.

10 Future Work

In Chapter 5, a sensitizer approach to probe long-lived dark exciton transport has been established. Further, a systematic study in determining the impact of subtle changes in molecular structure on the singlet and triplet exciton diffusion lengths is presented. Future work is envisioned that leverages the sensitizer-based approach for various studies such as studying the effect of molecular orientation on dark triplet L_D, and measurement of dark CT state transport in donor-acceptor mixtures.

10.1 Impact of Molecular Orientation on Exciton Diffusion

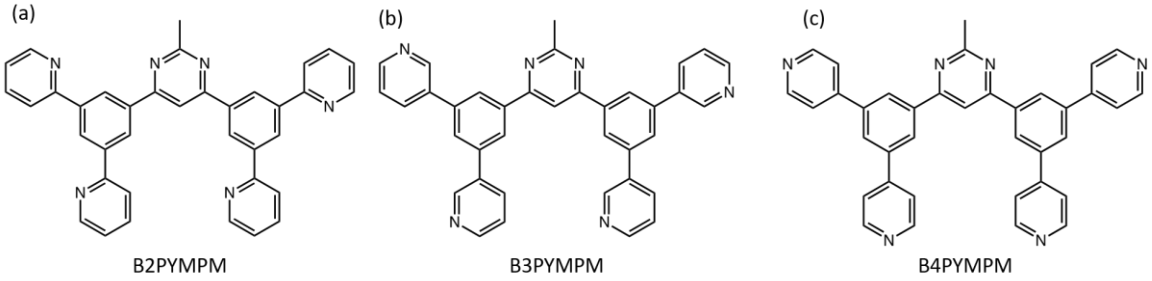

Figure 10.1 Molecular structures of (a) 4,6-Bis(3,5-di(pyridin-2-yl)phenyl)-2-methylpyrimidine (B2PymPm), (b) 4,6-Bis(3,5-di(pyridin-3-yl)phenyl)-2-methylpyrimidine (B3PymPm) and (c) 4,6-Bis(3,5-di(pyridin-4-yl)phenyl)-2-methylpyrimidine (B4PymPm).

In small molecule OLEDs, vacuum deposited amorphous films are generally used for their simplicity in fabricating multilayer structure with flat interfaces and high purity. In amorphous thin films molecular orientation is generally assumed to be random and isotropic. Recent studies have investigated the effect of intermolecular interaction and subsequent horizontal molecular orientation in OLEDs.[309–311] Yokoyama et al. has shown that by designing a family of isomers with 2-methylpyrimidine core structure molecules to

have strong intermolecular hydrogen bonds, one can control molecular stacking in vacuum-deposited organic thin films (Fig. 10.1 and Fig. 10.2).[312] In their study, they provided a systematic contrast in molecular orientation and permanent dipole due to differences in intermolecular hydrogen bonding.[312] The horizontal alignment of molecules via hydrogen bonding lead to 100 times improvement in carrier mobility in direction of stacking in thin film (Fig. 10.2). The question, remains how molecular stacking and orientation will rigorously affect the exciton L_D. For singlet excitons, the order is contained in the molecular orientation factor, κ^2, which represents orientation between transition dipole moments of donor and acceptor molecules. The κ^2 in Förster energy transfer rate (Eq. 2.4) is defined as:

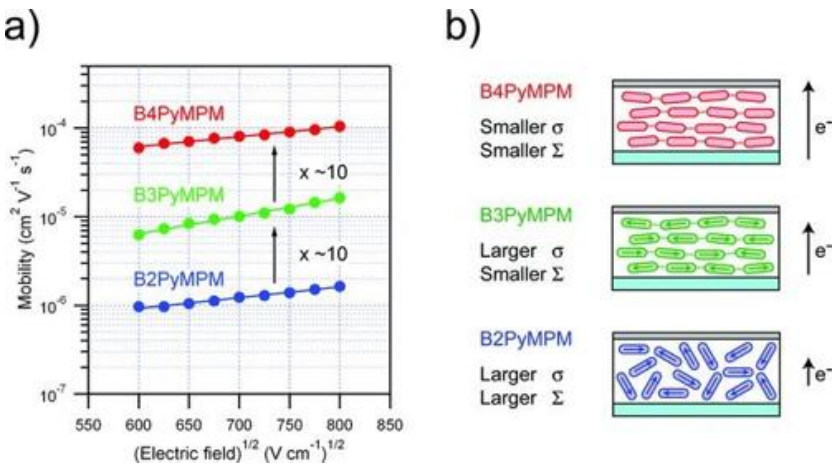

Figure 10.2 (a) Dependences of electron mobilities of B2–B4PyMPM films on electric field obtained by TOF measurements at 298K b) Schematic illustration of the effects of the molecular orientation and the permanent dipole moment on the electrical properties of the B2PyMPM, B3PyMPM and B4PyMPM devices. The B3PyMPM and B4PyMPM molecules are bound by the intermolecular hydrogen bonds and form the stacking structure in the films. The arrows in the molecules indicate the large permanent dipole moments of the molecules. (Reprinted by permission from John Wiley and Sons: Advanced Functional Materials ref. 312, copyright 2011.)

$$\kappa^2 = [\cos(\theta_{AD}) - 3\ \cos(\theta_A)\cos(\theta_D)]^2 \quad (10.1)$$

where θ_{AD} is the angle between donor and acceptor transition dipoles and θ_A, θ_D are the angle between respective dipole of the molecule and the molecular stacking direction. For randomly oriented rigid molecules κ^2 has a value of 0.476 [80]. The value of κ^2 ranges between 0 and 4 (Fig. 10.3). For perfectly aligned molecules, the value of κ^2 increases only for certain stacking direction and goes to zero for the at 54.7°. The κ^2 is also zero for the completely orthogonal transition dipole moments. For Dexter type energy transfer, the exciton hopping requires orbital overlap with adjacent acceptor molecules. Hence, there can be no energy transfer if the orbitals between molecules are perfectly orthogonal. The optimal molecular stacking for Dexter and Förster energy transfer may not necessarily be same.

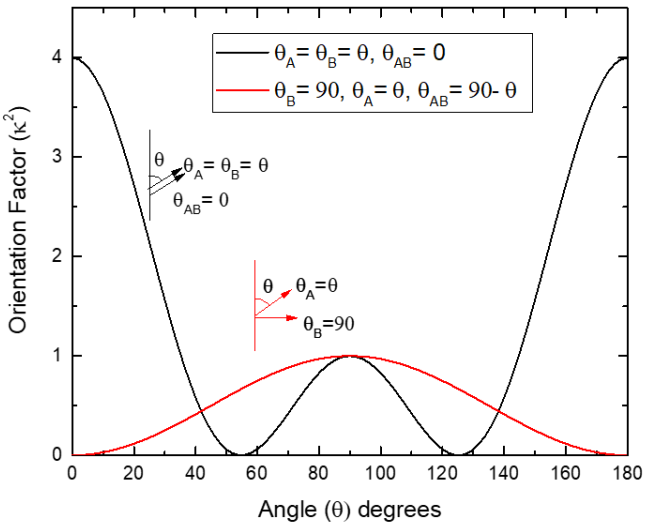

Figure 10.3 Dipole orientation factor (κ^2) in Förster energy transfer rate as a function of in-plane dipole arrangement

For the family of isomers presented in Fig. 10.1, phosphorescent sensitizer methodology and thickness dependent PL quenching can help to probe triplet and singlet states respectively. With the sensitizer-based approach of Ch. 5 excitons can be injected from an adjacent thermally activated delayed fluorescence (TADF) injector 9-(4-(4,6-

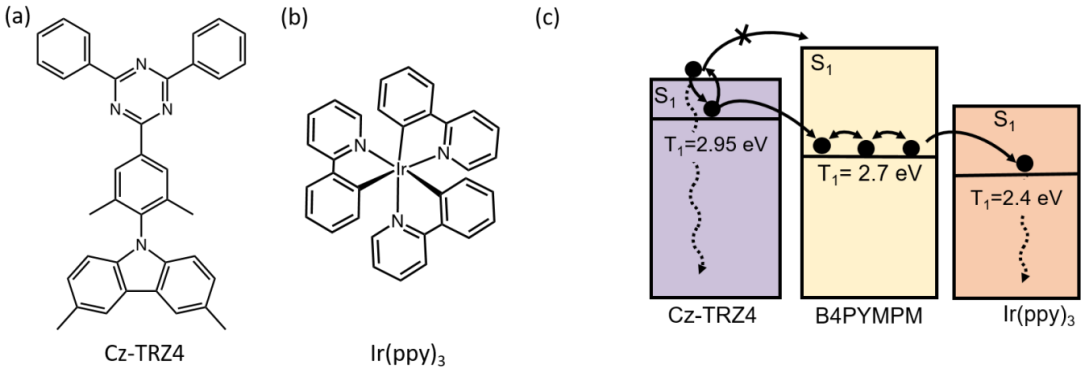

Figure 10.4 Molecular structures of (a) TADF injector Cz-TRZ4 and (b) phosphorescent sensitizer $Ir(ppy)_3$. (c) A generalized scheme for probing the diffusion length of non-radiative triplet excitons in family of isomers presented in Fig. 10.1. Excitons are injected into the transport layer by energy transfer from an adjacent TADF injection layer. Excitons diffuse through the material of interest (transport layer) before undergoing energy transfer to the phosphorescent sensitizer layer. The triplet energy levels of the three layers are selected to ensure downhill energy transfer from the injection layer to the sensitizer layer.

diphenyl-1,3,5-triazin-2-yl)-2,6-dimethylphenyl)-3,6-dimethyl-9H-carbazole (Cz-TRZ4) with a triplet energy of 2.95 eV [313] (Fig 10.4). The injected excitons that diffuse through the full thickness of the transport layer is sensed by energy transfer to phosphorescent $Ir(ppy)_3$ layer.

10.2 Measurement of Dark CT state transport

In OPVs, CT states are the intermediates that are generated when excitons reach the donor-acceptor interface. In BHJ OPVs, CT states are formed in disordered D-A mixtures. The η_{CS} of CT state depends on both material properties (i.e. conjugation length, energetic offset and reorganization energy) and film properties (degree of crystallinity, alignment of molecular orbital of donor and acceptor).[314] If CT states can diffuse within the mixture,

they might be able to reach other sites where charge separation is easier. Thus, a long-range CT migration can potentially facilitate free charge carrier generation and reduce geminate losses in OPVs.

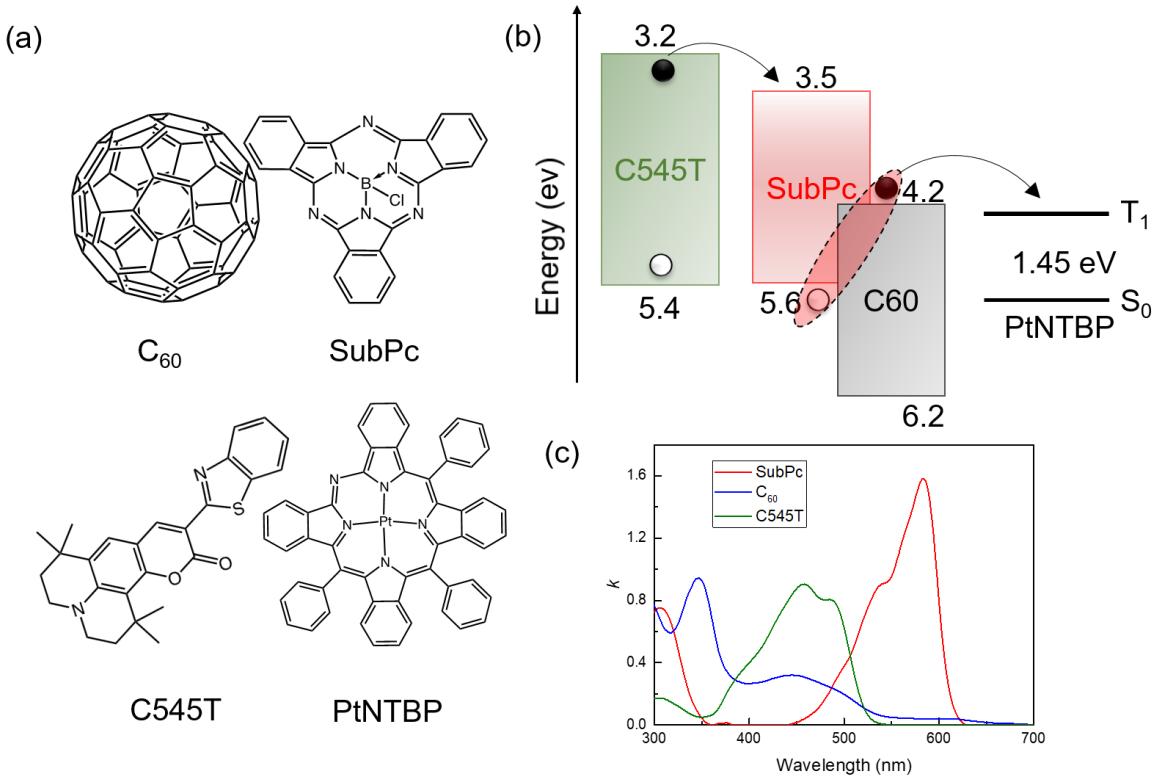

Figure 10.5 Molecular structures of (a) C_{60}, SubPc, injector C545T and phosphorescent sensitizer PtNTBP. (b) Scheme for probing the diffusion length of non-radiative CT exciton in SubPc:C_{60} mixture. Excitons are injected into the SubPc by energy transfer from an adjacent C545T injection layer. The exciton in SubPc forms a CT state with C_{60} and will diffuse through SubPc:C_{60} mixture before undergoing energy transfer to the PtNTBP sensitizer layer.

Previously, these states were assumed to be immobile, however recent studies have observed their diffusion.[315,316] Deotare et al. measured the diffusion of emissive CT states in a mixtures of m-MTDATA-3TPYMB and reported a L_D of 5-10 nm for these states. Most

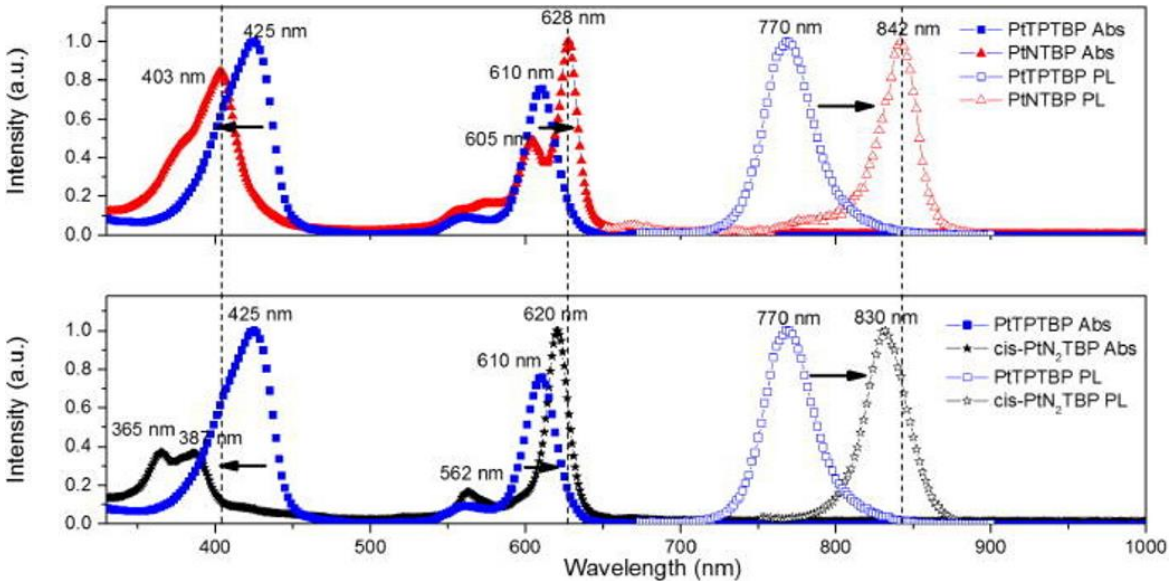

Figure 10.6 Comparison of normalized absorption (filled) and photoluminescence (open) spectra of PtTPTBP used in Chapter 6, PtNTBP, and cis-PtN2TBP in a dilute solution of tetrahydrofuran at room temperature. (Reprinted by permission from AIP Publishing: Applied Physics Letters ref. 321, copyright 2016.)

of the CT states found in OPVs are optically dark at room temperature.[68,69,317–320] Conventional photoluminescence-based techniques are inadequate in measuring the L_D of these states. The phosphorescent sensitizer methodology presented in Chapter 5 can be used to measure the diffusion length of dark CT states. Figure 10.5 illustrates the proposed dark CT state formed for a mixture of boron subphthalocyanine chloride (SubPc) and C_{60}. The CT state energy of the system as previously determined from bulk heterojunction electroluminescence as 1.55 eV.[69] Excitons can be injected into SubPc by Förster energy transfer from an adjacent C545T injection layer. The exciton in SubPc will form a CT state and diffuse through the full thickness of the mixed SubPc:C_{60} layer before undergoing energy transfer to the phosphorescent Pt (II) aza-triphenyltetrabenzoporphyrin

(PtNTBP)[321] sensitizer. Besides the selection of active materials, changing mixture composition can also tune charge transport properties and thus impact CT diffusion if the transport mechanism relies on charge carrier motion. With a growing capability of tuning CT state diffusion, it would be necessary to also explore the impact of CT state diffusion on the performance of organic optoelectronic devices. For OPVs, understanding whether CT state diffusion helps or frustrates charge separation could have important implications in determining future device design.

11 Conclusions

This thesis explores fundamental questions related to the measurement and engineering of the excited state in organic semiconductor thin films. In Chapter 5, a novel sensitizer-based technique is established to probe dark, long-lived triplet states. In this technique the ability to selectively pump singlet and triplet states by varying the injection layer helped to unravel the role of spin transport for a given material. The validity of the technique is confirmed by first extracting the L_D of luminescent singlet excitons in thin films of Alq_3, and comparing the result to conventional photoluminescence measurements. Chapter 6 offers insight into the role of molecular structure in exciton transport in phenanthroline derivatives. A study connecting the measured singlet and triplet exciton diffusion length with changes in molecular structure and intermolecular spacing was presented.

Novel solar cell architecture is developed in Chapter 7 that exploits exciton gating to bias exciton migration in organic semiconductor thin films. The excitonic gates are experimentally created through a molecular site imbalance via dilution in a wide energy gap material. The effectiveness of these gates is demonstrated by injecting excitons from the most dilute layer and measuring the excitons collected from the neat layer. The incorporation of interfaces introduces asymmetry in exciton hopping thereby overcoming the diffusive nature of energy transport. Chapter 8 offers insight into the role of excitonic gates in overcoming the efficiency roll-off at high brightness.

A device-based methodology is presented in Chapter 9, capable of specifically probing triplet diffusion in singlet-fission materials that is independent of the efficiency of singlet fission or the presence of singlet diffusion. Furthermore, the method is applied at low light fluence to avoid the complexities associated with triplet-triplet fusion. Finally, Chapter 10 presents future directives that leverages the techniques developed in this thesis for various studies such as studying the effect of molecular orientation on dark triplet L_D, and measurement of dark CT state transport in donor-acceptor mixture.

The result from this thesis provide insights in building efficient organic optoelectronic devices. The novel sensitizer technique in Chapter 5 can enable efficient screening of materials for long triplet L_D which is critical for OPVs architectures employing triplet excitons. The role of subtle changes in molecular structure on the singlet and triplet exciton L_D in Chapter 6 provide understanding of molecular design for long exciton L_D. The exciton gating architectures in Chapter 7 enabled efficient exciton transport in organic semiconductor films. The device-based methodology presented in Chapter 9 can enable efficient screening of singlet-fission materials that can be used in OPVs. It is hoped that this thesis allows others to deepen their understanding in building efficient organic optoelectronic devices that improves the lives on this planet.

12 Bibliography

1. Inganäs, O. Organic Photovoltaics over Three Decades. *Adv. Mater.* **30**, 1800388 (2018).
2. Hedley, G. J., Ruseckas, A. & Samuel, I. D. W. W. Light Harvesting for Organic Photovoltaics. *Chem. Rev.* **117**, 796–837 (2017).
3. Yin, Y., Ali, M. U., Xie, W., Yang, H. & Meng, H. Evolution of white organic light-emitting devices: from academic research to lighting and display applications. *Mater. Chem. Front.* **3**, 970–1031 (2019).
4. Zou, S.-J. *et al.* Recent advances in organic light-emitting diodes: toward smart lighting and displays. *Mater. Chem. Front.* **4**, 788–820 (2020).
5. Chen, H. W., Lee, J. H., Lin, B. Y., Chen, S. & Wu, S. T. Liquid crystal display and organic light-emitting diode display: present status and future perspectives. *Light: Science and Applications* (2018) doi:10.1038/lsa.2017.168.
6. Liu, Y.-F., Feng, J., Bi, Y.-G., Yin, D. & Sun, H.-B. Recent Developments in Flexible Organic Light-Emitting Devices. *Adv. Mater. Technol.* **4**, 1800371 (2019).
7. Sarma, K. Recent progress in OLED and flexible displays and their potential for application to aerospace and military display systems. in *Display Technologies and Applications for Defense, Security, and Avionics IX; and Head- and Helmet-Mounted Displays XX* (eds. Desjardins, D. D., Sarma, K. R., Marasco, P. L. & Havig, P. R.) 94700J (2015). doi:10.1117/12.2180172.

8. Myny, K. *et al.* Organic RFID Tags. in *Radio Frequency Identification Fundamentals and Applications Design Methods and Solutions* (InTech, 2010). doi:10.5772/7985.

9. Myny, K. *et al.* Organic RFID Tags. in *Radio Frequency Identification Fundamentals and Applications Design Methods and Solutions* (2010). doi:10.5772/7985.

10. Myny, K. *et al.* Organic RFID transponder chip with data rate compatible with electronic product coding. *Org. Electron.* **11**, 1176–1179 (2010).

11. Lan, Z. *et al.* Near-infrared and visible light dual-mode organic photodetectors. *Sci. Adv.* **6**, eaaw8065 (2020).

12. Cnops, K. Phthalocyanine-based organic solar cells and photodetectors. (2015).

13. Dye, C. *et al.* Transparent Organic Photodetector using a Near-Infrared Absorbing. 1–6 (2015) doi:10.1038/srep09439.

14. Pace, G., Grimoldi, A., Sampietro, M., Natali, D. & Caironi, M. Printed photodetectors. *Semicond. Sci. Technol.* **30**, 104006 (2015).

15. Natali, D. & Caironi, M. Organic photodetectors. in *Photodetectors* 195–254 (Elsevier, 2016). doi:10.1016/B978-1-78242-445-1.00007-5.

16. Cruz, H. *et al.* Development of e-nose biosensors based on organic semiconductors towards low-cost health care diagnosis in gynecological diseases. *Mater. Today Proc.* **4**, 11544–11553 (2017).

17. Wang, N., Yang, A., Fu, Y., Li, Y. & Yan, F. Functionalized Organic Thin Film

Transistors for Biosensing. *Acc. Chem. Res.* **52**, 277–287 (2019).

18. Sokolov, A. N., Roberts, M. E. & Bao, Z. Fabrication of low-cost electronic biosensors. *Mater. Today* **12**, 12–20 (2009).

19. Hopkins, J., Fidanovski, K., Lauto, A. & Mawad, D. All-Organic Semiconductors for Electrochemical Biosensors: An Overview of Recent Progress in Material Design. *Front. Bioeng. Biotechnol.* **7**, (2019).

20. Janietz, S., Gruber, B., Schattauer, S. & Schulze, K. Integration of OLEDs in Textiles. *Adv. Sci. Technol.* **80**, 14–21 (2012).

21. Lim, T. H., Kim, S. H. & Oh, K. W. Fabrication of Organic Materials for Electronic Textiles. in *Handbook of Smart Textiles* 739–773 (Springer Singapore, 2015). doi:10.1007/978-981-4451-45-1_13.

22. Ismailova, E. Engineering organic electronic materials for the development of smart textiles. in *2019 IEEE International Conference on Flexible and Printable Sensors and Systems (FLEPS)* 1–3 (IEEE, 2019). doi:10.1109/FLEPS.2019.8792283.

23. Benight, S. J., Wang, C., Tok, J. B. H. & Bao, Z. Stretchable and self-healing polymers and devices for electronic skin. *Prog. Polym. Sci.* **38**, 1961–1977 (2013).

24. Lee, Y. H. *et al.* Recent advances in organic sensors for health self-monitoring systems. *Journal of Materials Chemistry C* (2018) doi:10.1039/c8tc02230e.

25. Rodgers, M. M., Pai, V. M. & Conroy, R. S. Recent Advances in Wearable Sensors for Health Monitoring. *IEEE Sens. J.* **15**, 3119–3126 (2015).

26. Meyer, J., Görrn, P. & Riedl, T. Transparent OLED displays. in *Organic Light-*

Emitting Diodes (OLEDs) 512–547 (Elsevier, 2013). doi:10.1533/9780857098948.3.512.

27. Ma, R.-Q. *et al.* Flexible active-matrix OLED displays: Challenges and progress. *J. Soc. Inf. Disp.* (2008) doi:10.1889/1.2835025.

28. LG OLED65R9PUA: R9 Rollable 4K OLED TV at CES 2019. https://www.lg.com/us/tvs/lg-OLED65R9PUA-signature-oled-4k-tv.

29. LG 55EW5F-A: Transparent OLED Digital Signage | LG USA Business. https://www.lg.com/us/business/oled-displays/lg-55EW5F-A.

30. Transparent OLED Screen | Self-Lighting Transparent Signage Display. https://prodisplay.com/products/transparent-oled-screen/.

31. Heliatek | Global leader for organic solar films. https://www.heliatek.com/.

32. Mulligan, C. J. *et al.* A projection of commercial-scale organic photovoltaic module costs. *Sol. Energy Mater. Sol. Cells* **120**, 9–17 (2014).

33. Gambhir, A., Sandwell, P. & Nelson, J. The future costs of OPV – A bottom-up model of material and manufacturing costs with uncertainty analysis. *Sol. Energy Mater. Sol. Cells* **156**, 49–58 (2016).

34. Krebs, F. C., Espinosa, N., Hösel, M., Søndergaard, R. R. & Jørgensen, M. 25th Anniversary Article: Rise to Power - OPV-Based Solar Parks. *Adv. Mater.* **26**, 29–39 (2014).

35. Forrest, S. R. The path to ubiquitous and low-cost organic electronic appliances on plastic. *Nature* **428**, 911–918 (2004).

36. WINDOWS – Ubiquitous Energy, Inc. https://ubiquitous.energy/windows/.

37. Cui, Y. *et al.* Over 16% efficiency organic photovoltaic cells enabled by a chlorinated acceptor with increased open-circuit voltages. *Nat. Commun.* **10**, 2515 (2019).

38. Fan, B. *et al.* Achieving over 16% efficiency for single-junction organic solar cells. *Sci. China Chem.* **62**, 746–752 (2019).

39. Yan, T. *et al.* 16.67% Rigid and 14.06% Flexible Organic Solar Cells Enabled by Ternary Heterojunction Strategy. *Adv. Mater.* (2019) doi:10.1002/adma.201902210.

40. Meng, L. *et al.* Organic and solution-processed tandem solar cells with 17.3% efficiency. *Science (80-.).* **361**, 1094 LP – 1098 (2018).

41. NEWS – Ubiquitous Energy, Inc. http://ubiquitous.energy/world-record/.

42. Köhler, A. & Bässler, H. *Electronic Processes in Organic Semiconductors*. *Electronic Processes in Organic Semiconductors: An Introduction* (Wiley-VCH Verlag GmbH & Co. KGaA, 2015). doi:10.1002/9783527685172.

43. Köhler, A. & Bässler, H. Triplet states in organic semiconductors. *Mater. Sci. Eng. R Reports* **66**, 71–109 (2009).

44. Köhler, A. & Beljonne, D. The singlet-triplet exchange energy in conjugated polymers. *Adv. Funct. Mater.* (2004) doi:10.1002/adfm.200305032.

45. Köhler, A. & Bässler, H. The Electronic Structure of Organic Semiconductors. in *Electronic Processes in Organic Semiconductors* 1–86 (Wiley-VCH Verlag GmbH & Co. KGaA, 2015). doi:10.1002/9783527685172.ch1.

46. Turro, N. J., Ramamurthy, V. & Scaiano, J. C. Quantum Yields for Emission. in *Principles of Molecular Photochemistry: an Introduction* (2009).

47. Pope, M. & Swenberg, C. E. *Electronic Processes in Organic Electronics*. *Oxford Univ. Press USA 2nd Ed.* vol. 209 (Springer Japan, 2015).

48. Marcus, R. A. & Sutin, N. Electron transfers in chemistry and biology. *Biochim. Biophys. Acta - Rev. Bioenerg.* **811**, 265–322 (1985).

49. Jortner, J. Temperature dependent activation energy for electron transfer between biological molecules. *J. Chem. Phys.* **64**, 4860–4867 (1976).

50. Hood, S., Zarrabi, N., Meredith, P., Kassal, I. & Armin, A. Measuring Energetic Disorder in Organic Semiconductors Using the Photogenerated Charge-Separation Efficiency. *J. Phys. Chem. Lett.* **10**, 3863–3870 (2019).

51. Bussolotti, F. *et al.* Hole-phonon coupling effect on the band dispersion of organic molecular semiconductors. *Nat. Commun.* **8**, 173 (2017).

52. De Sio, A. & Lienau, C. Vibronic coupling in organic semiconductors for photovoltaics. *Phys. Chem. Chem. Phys.* **19**, 18813–18830 (2017).

53. Robinson, G. W. & Frosch, R. P. Electronic excitation transfer and relaxation. *J. Chem. Phys.* (1963) doi:10.1063/1.1733823.

54. OWEN, E. D. Molecular Spectroscopy of the Triplet State. *Photochem. Photobiol.* (1970) doi:10.1111/j.1751-1097.1970.tb05998.x.

55. Kawamura, Y. *et al.* 100% phosphorescence quantum efficiency of Ir(III) complexes in organic semiconductor films. *Appl. Phys. Lett.* **86**, 071104 (2005).

56. Siebrand, W. Radiationless transitions in polyatomic molecules. I. Calculation of Franck-Condon factors. *J. Chem. Phys.* (1967) doi:10.1063/1.1840685.

57. Siebrand, W. & Williams, D. F. Radiationless transitions in polyatomic molecules. III. Anharmonicity, isotope effects, and singlet-to-ground-state transitions in aromatic hydrocarbons. *J. Chem. Phys.* (1968) doi:10.1063/1.1670318.

58. Siebrand, W. Radiationless Transitions in Polyatomic Molecules. II. Triplet-Ground-State Transitions in Aromatic Hydrocarbons. *J. Chem. Phys.* **47**, 2411–2422 (1967).

59. Siebrand, W. Mechanism of Radiationless Triplet Decay in Aromatic Hydrocarbons and the Magnitude of the Franck—Condon Factors. *J. Chem. Phys.* **44**, 4055–4057 (1966).

60. Robinson, G. W. & Frosch, R. P. Theory of Electronic Energy Relaxation in the Solid Phase. *J. Chem. Phys.* **37**, 1962–1973 (1962).

61. Burland, D. M. & Robinson, G. W. Is the Breakdown of the Born-Oppenheimer Approximation Responsible for Internal Conversion in Large Molecules? *Proc. Natl. Acad. Sci.* **66**, 257–264 (1970).

62. La Rocca, G. . Wannier–Mott Excitons in Semiconductors. in 97–128 (2003). doi:10.1016/S1079-4050(03)31002-6.

63. Itskos, G. *et al.* Efficient dipole-dipole coupling of Mott-Wannier and Frenkel excitons in (Ga,In)N quantum well/polyfluorene semiconductor heterostructures. *Phys. Rev. B* **76**, 035344 (2007).

64. Nepurek, S. & Sworakowski, J. Use of space-charge-limited current measurements

to determine the properties of energetic distributions of bulk traps. *J. Appl. Phys.* **51**, 2098 (1980).

65. Brédas, J.-L., Beljonne, D., Coropceanu, V. & Cornil, J. Charge-Transfer and Energy-Transfer Processes in π-Conjugated Oligomers and Polymers: A Molecular Picture. *Chem. Rev.* **104**, 4971–5004 (2004).

66. Scheidler, M. *et al.* Monte Carlo study of picosecond exciton relaxation and dissociation in poly(phenylenevinylene). *Phys. Rev. B* **54**, 5536–5544 (1996).

67. Beljonne, D., Curutchet, C., Scholes, G. D. & Silbey, R. J. Beyond Förster Resonance Energy Transfer in Biological and Nanoscale Systems. *J. Phys. Chem. B* **113**, 6583–6599 (2009).

68. Zhu, X.-Y., Yang, Q. & Muntwiler, M. Charge-transfer excitons at organic semiconductor surfaces and interfaces. *Acc. Chem. Res.* **42**, 1779–1787 (2009).

69. Zou, Y. & Holmes, R. J. Correlation between the Open-Circuit Voltage and Charge Transfer State Energy in Organic Photovoltaic Cells. *ACS Appl. Mater. Interfaces* **7**, 18306–18311 (2015).

70. Zheng, Z., Tummala, N. R., Fu, Y. T., Coropceanu, V. & Brédas, J. L. Charge-Transfer States in Organic Solar Cells: Understanding the Impact of Polarization, Delocalization, and Disorder. *ACS Appl. Mater. Interfaces* (2017) doi:10.1021/acsami.7b02193.

71. Ichida, M., Nakamura, A., Shinohara, H. & Saitoh, Y. Observation of triplet state of charge-transfer excitons in C60 thin film. *Chem. Phys. Lett.* (1998)

doi:10.1016/S0009-2614(98)00480-1.

72. Kafle, T. R., Kattel, B., Wang, T. & Chan, W.-L. The relationship between the coherent size, binding energy and dissociation dynamics of charge transfer excitons at organic interfaces. *J. Phys. Condens. Matter* **30**, 454001 (2018).

73. Zhu, T. *et al.* Highly mobile charge-transfer excitons in two-dimensional WS 2 /tetracene heterostructures. *Sci. Adv.* **4**, eaao3104 (2018).

74. Xiao, J., Zhao, M., Wang, Y. & Zhang, X. Excitons in atomically thin 2D semiconductors and their applications. *Nanophotonics* **6**, (2017).

75. Menke, S. M. & Holmes, R. J. Exciton diffusion in organic photovoltaic cells. *Energy Environ. Sci.* **7**, 499–512 (2014).

76. Powell, R. C. & Soos, Z. G. Singlet exciton energy transfer in organic solids. *J. Lumin.* **11**, 1–45 (1975).

77. Diab, H. *et al.* Impact of Reabsorption on the Emission Spectra and Recombination Dynamics of Hybrid Perovskite Single Crystals. *J. Phys. Chem. Lett.* **8**, 2977–2983 (2017).

78. Mikhnenko, O. V., Blom, P. W. M. M. & Nguyen, T.-Q. Q. Exciton diffusion in organic semiconductors. *Energy Environ. Sci.* **8**, 1867–1888 (2015).

79. Főrster, T. 10th Spiers Memorial Lecture. Transfer mechanisms of electronic excitation. *Discuss. Faraday Soc.* **27**, 7–17 (1959).

80. Baumann, J. & Fayer, M. D. Excitation transfer in disordered two-dimensional and anisotropic three-dimensional systems: Effects of spatial geometry on time-resolved

observables. *J. Chem. Phys.* **85**, 4087–4107 (1986).

81. Koeppe, R. & Sariciftci, N. S. Photoinduced charge and energy transfer involving fullerene derivatives. *Photochem. Photobiol. Sci.* **5**, 1122 (2006).

82. Luhman, W. a. & Holmes, R. J. Investigation of Energy Transfer in Organic Photovoltaic Cells and Impact on Exciton Diffusion Length Measurements. *Adv. Funct. Mater.* **21**, 764–771 (2011).

83. Scholes, G. D. L <scp>ONG</scp> -R <scp>ANGE</scp> R <scp>ESONANCE</scp> E <scp>NERGY</scp> T <scp>RANSFER IN</scp> M <scp>OLECULAR</scp> S <scp>YSTEMS</scp>. *Annu. Rev. Phys. Chem.* **54**, 57–87 (2003).

84. Scully, S. R., Armstrong, P. B., Edder, C., Fréchet, J. M. J. & McGehee, M. D. Long-Range Resonant Energy Transfer for Enhanced Exciton Harvesting for Organic Solar Cells. *Adv. Mater.* **19**, 2961–2966 (2007).

85. Haynes, D. R., Tokmakoff, A. & George, S. M. Distance dependence of electronic energy transfer between donor and acceptor adlayers: p -terphenyl and 9,10-diphenylanthracene. *J. Chem. Phys.* **100**, 1968–1980 (1994).

86. Reid, O. G. & Rumbles, G. Resonance Energy Transfer Enables Efficient Planar Heterojunction Organic Solar Cells. *J. Phys. Chem. C* **120**, acs.jpcc.5b10276 (2016).

87. Paquin, F., Rivnay, J., Salleo, A., Stingelin, N. & Silva, C. Multi-phase semicrystalline microstructures drive exciton dissociation in neat plastic semiconductors. *J. Mater. Chem. C* **3**, 10715–10722 (2015).

88. Dexter, D. L. A Theory of Sensitized Luminescence in Solids. *J. Chem. Phys.* **21**, 836 (1953).

89. Powell, R. C. REVIEW ARTICLE SINGLET EXCITON ENERGY TRANSFER IN ORGANIC SOLIDS Richard C. POWELL. **11**, (1975).

90. Menke, S. M., Luhman, W. A. & Holmes, R. J. Tailored exciton diffusion in organic photovoltaic cells for enhanced power conversion efficiency. *Nat. Mater.* **12**, 152–157 (2013).

91. Bouchaud, J. P. & Georges, A. Anomalous diffusion in disordered media: Statistical mechanisms, models and physical applications. *Phys. Rep.* **195**, 127–293 (1990).

92. Baldo, M. A., Adachi, C. & Forrest, S. R. Transient analysis of organic electrophosphorescence. II. Transient analysis of triplet-triplet annihilation. *Phys. Rev. B* **62**, 10967–10977 (2000).

93. Murawski, C., Leo, K. & Gather, M. C. Efficiency roll-off in organic light-emitting diodes. *Adv. Mater.* **25**, 6801–6827 (2013).

94. Rao, A. & Friend, R. H. Harnessing singlet exciton fission to break the Shockley–Queisser limit. *Nat. Rev. Mater.* **2**, 17063 (2017).

95. Xia, J. *et al.* Singlet Fission: Progress and Prospects in Solar Cells. *Adv. Mater.* **29**, 1601652 (2017).

96. Einzinger, M. *et al.* Sensitization of silicon by singlet exciton fission in tetracene. *Nature* **571**, 90–94 (2019).

97. Futscher, M. H., Rao, A. & Ehrler, B. The Potential of Singlet Fission Photon

Multipliers as an Alternative to Silicon-Based Tandem Solar Cells. *ACS Energy Lett.* **3**, 2587–2592 (2018).

98. Erickson, N. C. & Holmes, R. J. Engineering Efficiency Roll-Off in Organic Light-Emitting Devices. *Adv. Funct. Mater.* **24**, 6074–6080 (2014).

99. Verreet, B. *et al.* Reducing exciton-polaron annihilation in organic planar heterojunction solar cells. *Phys. Rev. B* **90**, 1–8 (2014).

100. Coehoorn, R., Zhang, L., Bobbert, P. A. & Van Eersel, H. Effect of polaron diffusion on exciton-polaron quenching in disordered organic semiconductors. *Phys. Rev. B* (2017) doi:10.1103/PhysRevB.95.134202.

101. Bolinger, J. C., Traub, M. C., Adachi, T. & Barbara, P. F. Ultralong-Range Polaron-Induced Quenching of Excitons in Isolated Conjugated Polymers. *Science (80-.).* **331**, 565–567 (2011).

102. Reineke, S., Walzer, K. & Leo, K. Triplet-exciton quenching in organic phosphorescent light-emitting diodes with Ir-based emitters. *Phys. Rev. B - Condens. Matter Mater. Phys.* **75**, 1–13 (2007).

103. Drechsel, J. & Fröb, H. Deposition of Functional Organic Thin Layers by Means of Vacuum Evaporation. *Vak. Forsch. und Prax.* **20**, 15–20 (2008).

104. Taylor, D. M. Vacuum-thermal-evaporation: the route for roll-to-roll production of large-area organic electronic circuits. *Semicond. Sci. Technol.* **30**, 054002 (2015).

105. Patchett, E. R. *et al.* A high-yield vacuum-evaporation-based R2R-compatible fabrication route for organic electronic circuits. *Org. Electron.* **15**, 1493–1502

(2014).

106. Sze, S. M. & Ng, K. K. *Physics of Semiconductor Devices*. *Physics of Semiconductor Devices* (John Wiley & Sons, Inc., 2006). doi:10.1002/0470068329.

107. Campbell, S. A. *Fabrication Engineering at the Micro- and Nanoscale Third Edition*. (2008).

108. Udhardt, C. *et al.* Optical observation of different conformational isomers in rubrene ultra-thin molecular films on epitaxial graphene. *Thin Solid Films* **598**, 271–275 (2016).

109. Forrest, S. R. Ultrathin Organic Films Grown by Organic Molecular Beam Deposition and Related Techniques. *Chem. Rev.* **97**, 1793–1896 (1997).

110. Schreiber, F. Organic molecular beam deposition: Growth studies beyond the first monolayer. *Phys. status solidi* **201**, 1037–1054 (2004).

111. Kowarik, S., Gerlach, A. & Schreiber, F. Organic molecular beam deposition: fundamentals, growth dynamics, and in situ studies. *J. Phys. Condens. Matter* **20**, 184005 (2008).

112. Pola, J. *et al.* Laser Ablative Structural Modification of Poly(ethylene- a lt -maleic anhydride). *Chem. Mater.* **15**, 3887–3893 (2003).

113. Blanchet, G. B., Fincher, C. R. & Malajovich, I. Laser evaporation and the production of pentacene films. *J. Appl. Phys.* **94**, 6181–6184 (2003).

114. Wada, T. & Ueda, N. The effect of carrier gas flow rate and source cell temperature on low pressure organic vapor phase deposition simulation by direct simulation

Monte Carlo method. *J. Appl. Phys.* **113**, 154503 (2013).

115. Käfer, D. & Witte, G. Growth of crystalline rubrene films with enhanced stability. *Phys. Chem. Chem. Phys.* **7**, 2850 (2005).

116. Benzinger, J. B. Organic Vapor Phase Deposition for Optoelectronic Devices. *Princet. Univ.* (2008).

117. Burrows, P. E. *et al.* Organic vapor phase deposition: a new method for the growth of organic thin films with large optical non-linearities. *J. Cryst. Growth* **156**, 91–98 (1995).

118. Lunt, R. R., Lassiter, B. E., Benziger, J. B. & Forrest, S. R. Organic vapor phase deposition for the growth of large area organic electronic devices. *Appl. Phys. Lett.* **95**, 233305 (2009).

119. Baldo, M. *et al.* Organic Vapor Phase Deposition. *Adv. Mater.* **10**, 1505–1514 (1998).

120. Arias, A. C. *et al.* All jet-printed polymer thin-film transistor active-matrix backplanes. *Appl. Phys. Lett.* **85**, 3304–3306 (2004).

121. Sirringhaus, H. *et al.* High-Resolution Inkjet Printing of All-Polymer Transistor Circuits. *Science (80-.).* **290**, 2123–2126 (2000).

122. Burns, S. E., Cain, P., Mills, J., Wang, J. & Sirringhaus, H. Inkjet Printing of Polymer Thin-Film Transistor Circuits. *MRS Bull.* **28**, 829–834 (2003).

123. Kawase, T., Sirringhaus, H., Friend, R. H. & Shimoda, T. Inkjet Printed Via-Hole Interconnections and Resistors for All-Polymer Transistor Circuits. *Adv. Mater.* **13**, 1601–1605 (2001).

124. Kawase, T., Shimoda, T., Newsome, C., Sirringhaus, H. & Friend, R. H. Inkjet printing of polymer thin film transistors. *Thin Solid Films* **438**–**439**, 279–287 (2003).

125. Jabbour, G. E., Radspinner, R. & Peyghambarian, N. Screen printing for the fabrication of organic light-emitting devices. *IEEE J. Sel. Top. Quantum Electron.* **7**, 769–773 (2001).

126. Pardo, D. A., Jabbour, G. E. & Peyghambarian, N. Application of Screen Printing in the Fabrication of Organic Light-Emitting Devices. *Adv. Mater.* **12**, 1249–1252 (2000).

127. Cour, I. *et al.* Origin of stress and enhanced carrier transport in solution-cast organic semiconductor films. *J. Appl. Phys.* **114**, 093501 (2013).

128. Na, J. Y., Kang, B., Sin, D. H., Cho, K. & Park, Y. D. Understanding Solidification of Polythiophene Thin Films during Spin-Coating: Effects of Spin-Coating Time and Processing Additives. *Sci. Rep.* **5**, 13288 (2015).

129. Wei Chou, K. *et al.* Late stage crystallization and healing during spin-coating enhance carrier transport in small-molecule organic semiconductors. *J. Mater. Chem. C* **2**, 5681–5689 (2014).

130. Ahmadian-Yazdi, M. R., Zabihi, F., Habibi, M. & Eslamian, M. Effects of Process Parameters on the Characteristics of Mixed-Halide Perovskite Solar Cells Fabricated by One-Step and Two-Step Sequential Coating. *Nanoscale Res. Lett.* **11**, 408 (2016).

131. Toolan, D. T. W., Pullan, N., Harvey, M. J., Topham, P. D. & Howse, J. R. In Situ

Studies of Phase Separation and Crystallization Directed by Marangoni Instabilities During Spin-Coating. *Adv. Mater.* **25**, 7033–7037 (2013).

132. Lakowicz, J. R. *Principles of Fluorescence Spectroscopy Principles of Fluorescence Spectroscopy*. (2006). doi:10.1007/978-0-387-46312-4.

133. Rand, B. P., Burk, D. P. & Forrest, S. R. Offset energies at organic semiconductor heterojunctions and their influence on the open-circuit voltage of thin-film solar cells. *Phys. Rev. B* **75**, 115327 (2007).

134. Credgington, D., Jamieson, F. C., Walker, B., Nguyen, T. & Durrant, J. R. Quantification of Geminate and Non-Geminate Recombination Losses within a Solution-Processed Small-Molecule Bulk Heterojunction Solar Cell. *Adv. Mater.* **24**, 2135–2141 (2012).

135. Deibel, C., Strobel, T. & Dyakonov, V. Role of the Charge Transfer State in Organic Donor-Acceptor Solar Cells. *Adv. Mater.* **22**, 4097–4111 (2010).

136. Zhang, H. *et al.* Over 14% Efficiency in Organic Solar Cells Enabled by Chlorinated Nonfullerene Small-Molecule Acceptors. *Adv. Mater.* **30**, 1800613 (2018).

137. Yuan, J. *et al.* Single-Junction Organic Solar Cell with over 15% Efficiency Using Fused-Ring Acceptor with Electron-Deficient Core. *Joule* **3**, 1140–1151 (2019).

138. Beaujuge, P. M. & Fréchet, J. M. J. Molecular Design and Ordering Effects in π-Functional Materials for Transistor and Solar Cell Applications. *J. Am. Chem. Soc.* **133**, 20009–20029 (2011).

139. Huang, Y., Kramer, E. J., Heeger, A. J. & Bazan, G. C. Bulk Heterojunction Solar

Cells: Morphology and Performance Relationships. *Chem. Rev.* **114**, 7006–7043 (2014).

140. Mullenbach, T. K., McGarry, K. A., Luhman, W. A., Douglas, C. J. & Holmes, R. J. Connecting Molecular Structure and Exciton Diffusion Length in Rubrene Derivatives. *Adv. Mater.* **25**, 3689–3693 (2013).

141. Kanemoto, K. *et al.* Morphology-Dependent Carrier and Exciton Generations in Regioregular Poly(3-hexylthiophene) Polymer Diodes as Revealed by Bleaching Spectroscopy. *Phys. Rev. Lett.* **103**, 187402 (2009).

142. Li, Z., Zhang, X., Woellner, C. F. & Lu, G. Understanding molecular structure dependence of exciton diffusion in conjugated small molecules. *Appl. Phys. Lett.* **104**, 143303 (2014).

143. Tapping, P. C., Clafton, S. N., Schwarz, K. N., Kee, T. W. & Huang, D. M. Molecular level details of morphology dependent exciton migration in poly(3 hexylthiophene) nanostructures. *J. Phys. Chem. C* **119**, 7047–7059 (2015).

144. Brixner, T., Hildner, R., Köhler, J., Lambert, C. & Würthner, F. Exciton Transport in Molecular Aggregates – From Natural Antennas to Synthetic Chromophore Systems. *Advanced Energy Materials* vol. 7 (2017).

145. Masri, Z. *et al.* Molecular Weight Dependence of Exciton Diffusion in Poly(3-hexylthiophene). *Adv. Energy Mater.* **3**, 1445–1453 (2013).

146. Lunt, R. R., Benziger, J. B. & Forrest, S. R. Relationship between Crystalline Order and Exciton Diffusion Length in Molecular Organic Semiconductors. *Adv. Mater.*

22, 1233–1236 (2010).

147. Najafov, H., Lee, B., Zhou, Q., Feldman, L. C. & Podzorov, V. Observation of long-range exciton diffusion in highly ordered organic semiconductors. *Nat. Mater.* **9**, 938 (2010).

148. Kurrle, D. & Pflaum, J. Exciton diffusion length in the organic semiconductor diindenoperylene. *Appl. Phys. Lett.* **92**, 133306 (2008).

149. Jin, X.-H. *et al.* Long-range exciton transport in conjugated polymer nanofibers prepared by seeded growth. *Science (80-.).* **360**, 897–900 (2018).

150. Rim, S.-B., Fink, R. F., Schöneboom, J. C., Erk, P. & Peumans, P. Effect of molecular packing on the exciton diffusion length in organic solar cells. *Appl. Phys. Lett.* **91**, 173504 (2007).

151. Wei, G. *et al.* Efficient, Ordered Bulk Heterojunction Nanocrystalline Solar Cells by Annealing of Ultrathin Squaraine Thin Films. *Nano Lett.* **10**, 3555–3559 (2010).

152. Shin, H.-Y. *et al.* Exciton diffusion in near-infrared absorbing solution-processed organic thin films. *Phys. Chem. Chem. Phys.* **15**, 2867 (2013).

153. Mikhnenko, O. V. *et al.* Effect of thermal annealing on exciton diffusion in a diketopyrrolopyrrole derivative. *Phys. Chem. Chem. Phys.* **14**, 14196 (2012).

154. Rand, B. P. *et al.* The Impact of Molecular Orientation on the Photovoltaic Properties of a Phthalocyanine/Fullerene Heterojunction. *Adv. Funct. Mater.* **22**, 2987–2995 (2012).

155. Haedler, A. T. *et al.* Long-range energy transport in single supramolecular

nanofibres at room temperature. *Nature* **523**, 196–199 (2015).

156. Bjorgaard, J. A. & Köse, M. E. Simulations of singlet exciton diffusion in organic semiconductors: a review. *RSC Adv.* **5**, 8432–8445 (2015).

157. Shi, K. *et al.* Probing Enhanced Exciton Diffusion in a Triplet-Sensitized Organic Photovoltaic Cell. *J. Phys. Chem. C* **124**, 3489–3495 (2020).

158. Luhman, W. A. & Holmes, R. J. Enhanced exciton diffusion in an organic photovoltaic cell by energy transfer using a phosphorescent sensitizer. *Appl. Phys. Lett.* **94**, 153304 (2009).

159. Rand, B. P. *et al.* Organic solar cells with sensitized phosphorescent absorbing layers. *Org. Electron.* **10**, 1015–1019 (2009).

160. Popp, J., Kaiser, W. & Gagliardi, A. Impact of Phosphorescent Sensitizers and Morphology on the Photovoltaic Performance in Organic Solar Cells. *Adv. Theory Simulations* **2**, 1800114 (2019).

161. Mikhnenko, O. V., Ruiter, R., Blom, P. W. M. & Loi, M. A. Direct Measurement of the Triplet Exciton Diffusion Length in Organic Semiconductors. *Phys. Rev. Lett.* **108**, 137401 (2012).

162. Baldo, M. A., O'Brien, D. F., Thompson, M. E. & Forrest, S. R. Excitonic singlet-triplet ratio in a semiconducting organic thin film. *Phys. Rev. B* **60**, 14422–14428 (1999).

163. Luo, Y. & Aziz, H. Probing triplet-triplet annihilation zone and determining triplet exciton diffusion length by using delayed electroluminescence. *J. Appl. Phys.* **107**,

094510 (2010).

164. Baldo, M. A. & Forrest, S. R. Transient analysis of organic electrophosphorescence: I. Transient analysis of triplet energy transfer. *Phys. Rev. B* **62**, 10958-- (2000).

165. Lebental, M. *et al.* Diffusion of triplet excitons in an operational organic light-emitting diode. *Phys. Rev. B - Condens. Matter Mater. Phys.* **79**, 1–13 (2009).

166. D'Andrade, B. W., Holmes, R. J. & Forrest, S. R. Efficient Organic Electrophosphorescent White-Light-Emitting Device with a Triple Doped Emissive Layer. *Adv. Mater.* **16**, 624–628 (2004).

167. Zhou, Y. C., Ma, L. L., Zhou, J., Ding, X. M. & Hou, X. Y. Effect of a sensing layer on triplet exciton diffusion in organic films. *Phys. Rev. B* **75**, 132202 (2007).

168. Giebink, N. C. C., Sun, Y. & Forrest, S. R. R. Transient analysis of triplet exciton dynamics in amorphous organic semiconductor thin films. *Org. Electron.* **7**, 375–386 (2006).

169. Matsusue, N., Ikame, S., Suzuki, Y. & Naito, H. Charge-carrier transport and triplet exciton diffusion in a blue electrophosphorescent emitting layer. *J. Appl. Phys.* **97**, (2005).

170. Pettersson, L. a a, Roman, L. S., Ingana, O., Introduction, I. & Inganas, O. Modeling photocurrent action spectra of photovoltaic devices based on organic thin films. *J. Appl. Phys.* **86**, 487–496 (1999).

171. Menke, S. M., Mullenbach, T. K. & Holmes, R. J. Directing Energy Transport in Organic Photovoltaic Cells Using Interfacial Exciton Gates. *ACS Nano* **9**, 4543–

4552 (2015).

172. Peumans, P., Yakimov, A. & Forrest, S. R. Small molecular weight organic thin-film photodetectors and solar cells. *J. Appl. Phys.* **93**, 3693–3723 (2003).

173. Lunt, R. R., Giebink, N. C., Belak, A. a., Benziger, J. B. & Forrest, S. R. Exciton diffusion lengths of organic semiconductor thin films measured by spectrally resolved photoluminescence quenching. *J. Appl. Phys.* **105**, 053711 (2009).

174. Bergemann, K. J. & Forrest, S. R. Measurement of exciton diffusion lengths in optically thin organic films. *Appl. Phys. Lett.* **99**, 1–4 (2011).

175. Matthew Menke, S. & Holmes, R. J. Evaluating the role of energetic disorder and thermal activation in exciton transport. *J. Mater. Chem. C* **4**, 3437–3442 (2016).

176. Fielitz, T. R. Understanding and Engineering Molecular Order in Organic Semiconductors. *Univ. Minnesota Digit. Conserv.* (2017).

177. Markov, D. E., Tanase, C., Blom, P. W. M. & Wildeman, J. Simultaneous enhancement of charge transport and exciton diffusion in poly(<math display="inline"> <mi>p</mi> </math> -phenylene vinylene) derivatives. *Phys. Rev. B* **72**, 045217 (2005).

178. Markov, D. E., Hummelen, J. C., Blom, P. W. M. & Sieval, A. B. Dynamics of exciton diffusion in poly(<math display="inline"> <mi>p</mi> </math> -phenylene vinylene)/fullerene heterostructures. *Phys. Rev. B* **72**, 045216 (2005).

179. Markov, D. E., Amsterdam, E., Blom, P. W. M., Sieval, A. B. & Hummelen, J. C. Accurate Measurement of the Exciton Diffusion Length in a Conjugated Polymer

Using a Heterostructure with a Side-Chain Cross-Linked Fullerene Layer. *J. Phys. Chem. A* **109**, 5266–5274 (2005).

180. Shaw, P. E., Ruseckas, A. & Samuel, I. D. W. Exciton Diffusion Measurements in Poly(3-hexylthiophene). *Adv. Mater.* **20**, 3516–3520 (2008).

181. Hedley, G. J. *et al.* Determining the optimum morphology in high-performance polymer-fullerene organic photovoltaic cells. *Nat. Commun.* **4**, 2867 (2013).

182. Ward, A. J., Ruseckas, A. & Samuel, I. D. W. A shift from diffusion assisted to energy transfer controlled fluorescence quenching in polymer-fullerene photovoltaic blends. *J. Phys. Chem. C* (2012) doi:10.1021/jp307538y.

183. Mikhnenko, O. V. *et al.* Trap-Limited Exciton Diffusion in Organic Semiconductors. *Adv. Mater.* **26**, 1912–1917 (2014).

184. Markov, D. E. & Blom, P. W. M. Anisotropy of exciton migration in poly(<math display="inline"> <mi>p</mi> </math> -phenylene vinylene). *Phys. Rev. B* **74**, 085206 (2006).

185. Lin, J. D. A. *et al.* Systematic study of exciton diffusion length in organic semiconductors by six experimental methods. *Mater. Horiz.* **1**, 280–285 (2014).

186. Yoon, S. J., Guo, Z., dos Santos Claro, P. C., Shevchenko, E. V. & Huang, L. Direct Imaging of Long-Range Exciton Transport in Quantum Dot Superlattices by Ultrafast Microscopy. *ACS Nano* **10**, 7208–7215 (2016).

187. Irkhin, P. & Biaggio, I. Direct Imaging of Anisotropic Exciton Diffusion and Triplet Diffusion Length in Rubrene Single Crystals. *Phys. Rev. Lett.* **107**, 017402 (2011).

188. Akselrod, G. M. *et al.* Visualization of exciton transport in ordered and disordered molecular solids. *Nat. Commun.* **5**, 3646 (2014).

189. Wan, Y. *et al.* Cooperative singlet and triplet exciton transport in tetracene crystals visualized by ultrafast microscopy. *Nat. Chem.* **7**, 785–792 (2015).

190. Zhu, T., Wan, Y., Guo, Z., Johnson, J. & Huang, L. Two Birds with One Stone: Tailoring Singlet Fission for Both Triplet Yield and Exciton Diffusion Length. *Adv. Mater.* **28**, 7539–7547 (2016).

191. Wan, Y., Wiederrecht, G. P., Schaller, R. D., Johnson, J. C. & Huang, L. Transport of Spin-Entangled Triplet Excitons Generated by Singlet Fission. *J. Phys. Chem. Lett.* **9**, 6731–6738 (2018).

192. Zhu, T., Wan, Y. & Huang, L. Direct Imaging of Frenkel Exciton Transport by Ultrafast Microscopy. *Acc. Chem. Res.* **50**, 1725–1733 (2017).

193. Wan, Y., Stradomska, A., Knoester, J. & Huang, L. Direct Imaging of Exciton Transport in Tubular Porphyrin Aggregates by Ultrafast Microscopy. *J. Am. Chem. Soc.* **139**, 7287–7293 (2017).

194. Pandya, R. *et al.* Femtosecond Transient Absorption Microscopy of Singlet Exciton Motion in Side-Chain Engineered Perylene-Diimide Thin Films. *J. Phys. Chem. A* **124**, 2721–2730 (2020).

195. Lewis, A. J. *et al.* Singlet exciton diffusion in MEH-PPV films studied by exciton-exciton annihilation. *Org. Electron.* (2006) doi:10.1016/j.orgel.2006.05.009.

196. Ruseckas, A. *et al.* Singlet energy transfer and singlet-singlet annihilation in light-

emitting blends of organic semiconductors. *Appl. Phys. Lett.* (2009) doi:10.1063/1.3253422.

197. Gulbinas, V. *et al.* Exciton diffusion and relaxation in methyl-substituted polyparaphenylene polymer films. *J. Chem. Phys.* **127**, 144907 (2007).

198. Stevens, M. A., Silva, C., Russell, D. M. & Friend, R. H. Exciton dissociation mechanisms in the polymeric semiconductors poly(9,9-dioctylfluorene) and poly(9,9-dioctylfluorene-co-benzothiadiazole). *Phys. Rev. B* **63**, 165213 (2001).

199. Nickel, B., Borowicz, P., Ruth, A. A. & Troe, J. Application of Smoluchowski's generalized theory to the kinetics of triplet-triplet annihilation of anthracene in viscous solution after long-pulse excitation. *Phys. Chem. Chem. Phys.* (2004) doi:10.1039/b316805k.

200. Wünsche, J., Reineke, S., Lüssem, B. & Leo, K. Measurement of triplet exciton diffusion in organic light-emitting diodes. *Phys. Rev. B* **81**, 245201 (2010).

201. Tabachnyk, M., Ehrler, B., Bayliss, S., Friend, R. H. & Greenham, N. C. Triplet diffusion in singlet exciton fission sensitized pentacene solar cells. *Appl. Phys. Lett.* **103**, 153302 (2013).

202. Menke, S. M., Lindsay, C. D. & Holmes, R. J. Optical spacing effect in organic photovoltaic cells incorporating a dilute acceptor layer. *Appl. Phys. Lett.* **104**, 243302 (2014).

203. Shao, Y. & Yang, Y. Efficient organic heterojunction photovoltaic cells based on triplet materials. *Adv. Mater.* (2005) doi:10.1002/adma.200501297.

204. Rand, B. P. *et al.* Photocurrent enhancement in polymer:Fullerene bulk heterojunction solar cells doped with a phosphorescent molecule. *Appl. Phys. Lett.* (2009) doi:10.1063/1.3257383.

205. Siegmund, B. *et al.* Exciton Diffusion Length and Charge Extraction Yield in Organic Bilayer Solar Cells. *Adv. Mater.* **29**, 1–5 (2017).

206. Zhang, T., Dement, D. B., Ferry, V. E. & Holmes, R. J. Intrinsic measurements of exciton transport in photovoltaic cells. *Nat. Commun.* **10**, 1156 (2019).

207. Mullenbach, T. K., Curtin, I. J., Zhang, T. & Holmes, R. J. Probing dark exciton diffusion using photovoltage. *Nat. Commun.* **8**, 14215 (2017).

208. Curtin, I. J. & Holmes, R. J. Decoupling Photocurrent Loss Mechanisms in Photovoltaic Cells Using Complementary Measurements of Exciton Diffusion. *Adv. Energy Mater.* **8**, 1702339 (2018).

209. Mullenbach, T. K. & Holmes, R. J. Relating photocurrent, photovoltage, and charge carrier density to the recombination rate in organic photovoltaic cells. *Appl. Phys. Lett.* **107**, 123303 (2015).

210. Cheyns, D. *et al.* Analytical model for the open-circuit voltage and its associated resistance in organic planar heterojunction solar cells. *Phys. Rev. B* **77**, 165332 (2008).

211. Giebink, N. C., Wiederrecht, G. P., Wasielewski, M. R. & Forrest, S. R. Ideal diode equation for organic heterojunctions. I. Derivation and application. *Phys. Rev. B* **82**, 155305 (2010).

212. Kroeze, J. E., Savenije, T. J., Vermeulen, M. J. W. & Warman, J. M. Contactless determination of the photoconductivity action spectrum, exciton diffusion length, and charge separation efficiency in polythiophene-sensitized TiO2 bilayers. *J. Phys. Chem. B* **107**, 7696–7705 (2003).

213. Huijser, A., Savenije, T. J., Kroeze, J. E. & Siebbeles, L. D. A. Exciton Diffusion and Interfacial Charge Separation in m eso -Tetraphenylporphyrin/TiO 2 Bilayers: Effect of Ethyl Substituents. *J. Phys. Chem. B* **109**, 20166–20173 (2005).

214. Kroeze, J. E., Savenije, T. J., Vermeulen, M. J. W. & Warman, J. M. Contactless Determination of the Photoconductivity Action Spectrum, Exciton Diffusion Length, and Charge Separation Efficiency in Polythiophene-Sensitized TiO 2 Bilayers. *J. Phys. Chem. B* **107**, 7696–7705 (2003).

215. Kroeze, J. E., Koehorst, R. B. M. & Savenije, T. J. Singlet and Triplet Exciton Diffusion in a Self-Organizing Porphyrin Antenna Layer. *Adv. Funct. Mater.* **14**, 992–998 (2004).

216. Kroeze, J. E., Koehorst, R. B. M. & Savenije, T. J. Singlet and triplet exciton diffusion in a self-organizing porphyrin antenna layer. *Adv. Funct. Mater.* **14**, 992–998 (2004).

217. Huijser, A., Savenije, T. J., Kroeze, J. E. & Siebbeles, L. D. a. Exciton diffusion and interfacial charge separation in meso-tetraphenylporphyrin/TiO2 bilayers: effect of ethyl substituents. *J. Phys. Chem. B* **109**, 20166–20173 (2005).

218. Rai, D. & Holmes, R. J. Measurement of the triplet exciton diffusion length in

organic semiconductors. *J. Mater. Chem. C* **7**, 5695–5701 (2019).

219. Zhang, T. & Holmes, R. J. Photovoltage as a quantitative probe of carrier generation and recombination in organic photovoltaic cells. *J. Mater. Chem. C* **5**, 11885–11891 (2017).

220. Felter, K. M., Caselli, V. M., Günbaş, D. D., Savenije, T. J. & Grozema, F. C. Interplay between Charge Carrier Mobility, Exciton Diffusion, Crystal Packing, and Charge Separation in Perylene Diimide-Based Heterojunctions. *ACS Appl. Energy Mater.* **2**, 8010–8021 (2019).

221. Park, J., Reid, O. G. & Rumbles, G. Photo-induced carrier generation and recombination dynamics probed by combining time-resolved microwave conductivity and transient absorption spectroscopy. in (eds. Hayes, S. C. & Bittner, E. R.) 95490O (2015). doi:10.1117/12.2186340.

222. Savenije, T. J., Ferguson, A. J., Kopidakis, N. & Rumbles, G. Revealing the Dynamics of Charge Carriers in Polymer:Fullerene Blends Using Photoinduced Time-Resolved Microwave Conductivity. *J. Phys. Chem. C* **117**, 24085–24103 (2013).

223. Grieco, C. *et al.* Dynamic Exchange During Triplet Transport in Nanocrystalline TIPS-Pentacene Films. *J. Am. Chem. Soc.* **138**, 16069–16080 (2016).

224. Baldo, M. A. *et al.* Highly efficient phosphorescent emission from organic electroluminescent devices. *Nature* **395**, 151 (1998).

225. Wu, M. *et al.* Solid-state infrared-to-visible upconversion sensitized by colloidal

nanocrystals. *Nat. Photonics* **10**, 31–34 (2016).

226. Thompson, N. J. *et al.* Energy harvesting of non-emissive triplet excitons in tetracene by emissive PbS nanocrystals. *Nat. Mater.* **13**, 1039–1043 (2014).

227. Rai, D. & Holmes, R. J. Investigation of Excitonic Gates in Organic Semiconductor Thin Films. *Phys. Rev. Appl.* **11**, 014048 (2019).

228. Caplins, B. W., Mullenbach, T. K., Holmes, R. J. & Blank, D. A. Intermolecular Interactions Determine Exciton Lifetimes in Neat Films and Solid State Solutions of Metal-Free Phthalocyanine. *J. Phys. Chem. C* **119**, 27340–27347 (2015).

229. Erickson, N. C. & Holmes, R. J. Investigating the Role of Emissive Layer Architecture on the Exciton Recombination Zone in Organic Light-Emitting Devices. *Adv. Funct. Mater.* **23**, 5190–5198 (2013).

230. Hershey, K. W., Suddard-Bangsund, J., Qian, G. & Holmes, R. J. Decoupling degradation in exciton formation and recombination during lifetime testing of organic light-emitting devices. *Appl. Phys. Lett.* **111**, 113301 (2017).

231. Menke, S. M. & Holmes, R. J. Energy-Cascade Organic Photovoltaic Devices Incorporating a Host–Guest Architecture. *ACS Appl. Mater. Interfaces* **7**, 2912–2918 (2015).

232. Kim, Y. K., Won Kim, J. & Park, Y. Energy level alignment at a charge generation interface between 4, 4′ -bis(N -phenyl-1-naphthylamino)biphenyl and 1,4,5,8,9,11-hexaazatriphenylene- hexacarbonitrile. *Appl. Phys. Lett.* **94**, 1–4 (2009).

233. Holmes, R. J. *et al.* Blue organic electrophosphorescence using exothermic host–

guest energy transfer. *Appl. Phys. Lett.* **82**, 2422–2424 (2003).

234. Kato, T., Mori, T. & Mizutani, T. Effect of fabrication conditions on photoluminescence and absorption of hole transport materials. *Thin Solid Films* **393**, 109–113 (2001).

235. Ding, J. *et al.* Design of star-shaped molecular architectures based on carbazole and phosphine oxide moieties: towards amorphous bipolar hosts with high triplet energy for efficient blue electrophosphorescent devices. *J. Mater. Chem.* **20**, 8126 (2010).

236. Brinkmann, M. *et al.* Correlation between Molecular Packing and Optical Properties in Different Crystalline Polymorphs and Amorphous Thin Films of mer -Tris(8-hydroxyquinoline)aluminum(III). *J. Am. Chem. Soc.* **122**, 5147–5157 (2000).

237. Yost, S. R., Hontz, E., Yeganeh, S. & Van Voorhis, T. Triplet vs Singlet Energy Transfer in Organic Semiconductors: The Tortoise and the Hare. *J. Phys. Chem. C* **116**, 17369–17377 (2012).

238. Menke, S. M. & Holmes, R. J. Exciton Transport in an Organic Semiconductor Exhibiting Thermally Activated Delayed Fluorescence. *J. Phys. Chem. C* **120**, 8502–8508 (2016).

239. Hu, Z., Huang, F. & Cao, Y. Layer-by-Layer Assembly of Multilayer Thin Films for Organic Optoelectronic Devices. *Small Methods* **1**, 1700264 (2017).

240. Murrey, T. L. *et al.* Additive solution deposition of multi-layered semiconducting polymer films for design of sophisticated device architectures. *J. Mater. Chem. C* **7**, 953–960 (2019).

241. Lassiter, B. E., Zimmerman, J. D. & Forrest, S. R. Tandem organic photovoltaics incorporating two solution-processed small molecule donor layers. *Appl. Phys. Lett.* **103**, 123305 (2013).

242. Aizawa, N. *et al.* Solution-processed multilayer small-molecule light-emitting devices with high-efficiency white-light emission. *Nat. Commun.* **5**, 5756 (2014).

243. Wang, S. *et al.* Solution-processed multilayer green electrophosphorescent devices with self-host iridium dendrimers as the nondoped emitting layer: achieving high efficiency while avoiding redissolution-induced batch-to-batch variation. *Chem. Commun.* **53**, 5128–5131 (2017).

244. Dao, Q.-D., Fujii, A. & Ozaki, M. Fabrication of tandem solar cells with all-solution processed multilayer structure using non-peripherally substituted octahexyl tetrabenzotriazaporphyrins. *Jpn. J. Appl. Phys.* **55**, 03DB01 (2016).

245. Rai, D., Bangsund, J. S., Barriocanal, J. G. & Holmes, R. J. Impact of molecular structure on singlet and triplet exciton diffusion in phenanthroline derivatives. *J. Mater. Chem. C* (2020) doi:10.1039/D0TC00716A.

246. Grover, M. & Silbey, R. Exciton Migration in Molecular Crystals. *J. Chem. Phys.* **54**, 4843–4851 (1971).

247. Wu, C., Djurovich, P. I. & Thompson, M. E. Study of energy transfer and triplet exciton diffusion in hole-transporting host materials. *Adv. Funct. Mater.* **19**, 3157–3164 (2009).

248. Lu, Q., Chen, B. Y., Yang, W. Q., Zhang, T. L. & Lyu, Z. Y. Improved efficiency and

its roll-off of organic light-emitting diodes with double electron transport layers. *Faguang Xuebao/Chinese J. Lumin.* (2015) doi:10.3788/fgxb20153609.1053.

249. Han, S., Wang, L., Lei, G. & Qiu, Y. A Study on the Performances of White Organic Light-Emitting Diodes and the Morphologies of Their Hole-Blocking Layers. *Jpn. J. Appl. Phys.* **44**, L182–L185 (2005).

250. Earmme, T. & Jenekhe, S. A. High-performance multilayered phosphorescent OLEDs by solution-processed commercial electron-transport materials. *J. Mater. Chem.* **22**, 4660 (2012).

251. Kim, S. Y., Shim, H. Y., Seo, J. H., Kim, Y. K. & Kim, J. H. Determination of the exciton recombination zone in white OLEDs based on a blue emitting layer of 4 ' 4-bis(2,2 '-diphenyl vinyl)-1,1 '-biphenyl. *J. Korean Phys. Soc.* **49**, 1247–1251 (2006).

252. Patil, B. R. *et al.* Area dependent behavior of bathocuproine (BCP) as cathode interfacial layers in organic photovoltaic cells. *Sci. Rep.* (2018) doi:10.1038/s41598-018-30826-7.

253. Jafari, F. *et al.* Inverted organic solar cells with non-clustering bathocuproine (BCP) cathode interlayers obtained by fullerene doping. *Sci. Rep.* **9**, 10422 (2019).

254. Lee, J. *et al.* Electron transport mechanism of bathocuproine exciton blocking layer in organic photovoltaics. *Phys. Chem. Chem. Phys.* (2016) doi:10.1039/c5cp07099f.

255. Kawamura, Y., Sasabe, H. & Adachi, C. Simple Accurate System for Measuring Absolute Photoluminescence Quantum Efficiency in Organic Solid-State Thin

Films. *Jpn. J. Appl. Phys.* **43**, 7729–7730 (2004).

256. Xiang, H. F., Xu, Z. X., Roy, V. A. L., Che, C. M. & Lai, P. T. Method for measurement of the density of thin films of small organic molecules. *Rev. Sci. Instrum.* **78**, 034104 (2007).

257. Awaji, N. *et al.* High-precision x-ray reflectivity study of ultrathin SiO 2 on Si. *J. Vac. Sci. Technol. A Vacuum, Surfaces, Film.* **14**, 971–976 (1996).

258. Merkel, P. B. & Dinnocenzo, J. P. Experimental and Theoretical Study of Triplet Energy Transfer in Rigid Polymer Films. *J. Phys. Chem. A* **112**, 10790–10800 (2008).

259. Li, Z., Lee, W. E. & Galley, W. C. Distance dependence of the tryptophan-disulfide interaction at the triplet level from pulsed phosphorescence studies on a model system. *Biophys. J.* **56**, 361–367 (1989).

260. Strambini, G. B. & Galley, W. C. The distance dependence of triplet-triplet energy transfer at intermediate intermolecular separations with acetophenone-indole. *Chem. Phys. Lett.* **39**, 257–260 (1976).

261. Curutchet, C. & Voityuk, A. A. Distance Dependence of Triplet Energy Transfer in Water and Organic Solvents: A QM/MD Study. *J. Phys. Chem. C* **116**, 22179–22185 (2012).

262. Kandada, A. R. S. *et al.* Ultrafast Energy Transfer in Ultrathin Organic Donor/Acceptor Blend. *Sci. Rep.* **3**, 2073 (2013).

263. Li, H., Bŕdas, J. L. & Lennartz, C. First-principles theoretical investigation of the

electronic couplings in single crystals of phenanthroline-based organic semiconductors. *J. Chem. Phys.* **126**, (2007).

264. Gasparini, N. *et al.* The Physics of Small Molecule Acceptors for Efficient and Stable Bulk Heterojunction Solar Cells. *Adv. Energy Mater.* **8**, 1703298 (2018).

265. Curtin, I. J., Blaylock, D. W. & Holmes, R. J. Role of impurities in determining the exciton diffusion length in organic semiconductors. *Appl. Phys. Lett.* **108**, 163301 (2016).

266. Cnops, K. *et al.* 8.4% efficient fullerene-free organic solar cells exploiting long-range exciton energy transfer. *Nat. Commun.* **5**, 3406 (2014).

267. Schlenker, C. W. *et al.* Cascade Organic Solar Cells. *Chem. Mater.* **23**, 4132–4140 (2011).

268. Barito, A. *et al.* Universal Design Principles for Cascade Heterojunction Solar Cells with High Fill Factors and Internal Quantum Efficiencies Approaching 100%. *Adv. Energy Mater.* **4**, 1400216 (2014).

269. Nikolis, V. C. *et al.* Reducing Voltage Losses in Cascade Organic Solar Cells while Maintaining High External Quantum Efficiencies. *Adv. Energy Mater.* **7**, 1700855 (2017).

270. Schwartz, G., Pfeiffer, M., Reineke, S., Walzer, K. & Leo, K. Harvesting Triplet Excitons from Fluorescent Blue Emitters in White Organic Light-Emitting Diodes. *Adv. Mater.* **19**, 3672–3676 (2007).

271. Sun, Y. *et al.* Photophysics of Pt-porphyrin electrophosphorescent devices emitting

in the near infrared. *Appl. Phys. Lett.* **90**, 213503 (2007).

272. Scully, S. R. & McGehee, M. D. Effects of optical interference and energy transfer on exciton diffusion length measurements in organic semiconductors. *J. Appl. Phys.* **100**, 1–5 (2006).

273. Athanasopoulos, S., Emelianova, E. V, Walker, A. B. & Beljonne, D. Exciton diffusion in energetically disordered organic materials. *Phys. Rev. B* **80**, 195209 (2009).

274. Dale, R. E., Eisinger, J. & Blumberg, W. E. The orientational freedom of molecular probes. The orientation factor in intramolecular energy transfer. *Biophys. J.* **26**, 161–193 (1979).

275. Zamani Siboni, H. & Aziz, H. Triplet-polaron quenching by charges on guest molecules in phosphorescent organic light emitting devices. *Appl. Phys. Lett.* **101**, 063502 (2012).

276. Weichsel, C. *et al.* Storage of charge carriers on emitter molecules in organic light-emitting diodes. *Phys. Rev. B* **86**, 075204 (2012).

277. Hershey, K. W. & Holmes, R. J. Unified analysis of transient and steady-state electrophosphorescence using exciton and polaron dynamics modeling. *J. Appl. Phys.* **120**, 195501 (2016).

278. Ferschke, T., Hofmann, A., Brütting, W. & Pflaum, J. Application of Fluorescent Molecules as Noninvasive Sensors for Optoelectronic Characterization on Nanometer Length Scales. *ACS Appl. Electron. Mater.* **2**, 186–194 (2020).

279. Montilla, F., Ruseckas, A. & Samuel, I. D. W. Exciton–Polaron Interactions in Polyfluorene Films with β-Phase. *J. Phys. Chem. C* **122**, 9766–9772 (2018).

280. Miyata, K., Conrad-Burton, F. S., Geyer, F. L. & Zhu, X.-Y. Triplet Pair States in Singlet Fission. *Chem. Rev.* **119**, 4261–4292 (2019).

281. Basel, B. S. *et al.* Pentacenes: A Molecular Ruler for Singlet Fission. *Trends Chem.* **1**, 11–21 (2019).

282. Felter, K. M. & Grozema, F. C. Singlet Fission in Crystalline Organic Materials: Recent Insights and Future Directions. *J. Phys. Chem. Lett.* **10**, 7208–7214 (2019).

283. Piland, G. B., Burdett, J. J., Dillon, R. J. & Bardeen, C. J. Singlet Fission: From Coherences to Kinetics. *J. Phys. Chem. Lett.* **5**, 2312–2319 (2014).

284. MacQueen, R. W. *et al.* Crystalline silicon solar cells with tetracene interlayers: the path to silicon-singlet fission heterojunction devices. *Mater. Horizons* **5**, 1065–1075 (2018).

285. Pazos-Outón, L. M. *et al.* A Silicon–Singlet Fission Tandem Solar Cell Exceeding 100% External Quantum Efficiency with High Spectral Stability. *ACS Energy Lett.* **2**, 476–480 (2017).

286. Burdett, J. J., Gosztola, D. & Bardeen, C. J. The dependence of singlet exciton relaxation on excitation density and temperature in polycrystalline tetracene thin films: Kinetic evidence for a dark intermediate state and implications for singlet fission. *J. Chem. Phys.* **135**, 214508 (2011).

287. Chan, W.-L. *et al.* Observing the Multiexciton State in Singlet Fission and Ensuing

Ultrafast Multielectron Transfer. *Science (80-.).* **334**, 1541–1545 (2011).

288. Zimmerman, P. M., Zhang, Z. & Musgrave, C. B. Singlet fission in pentacene through multi-exciton quantum states. *Nat. Chem.* **2**, 648–652 (2010).

289. Tayebjee, M. J. Y., Clady, R. G. C. R. & Schmidt, T. W. The exciton dynamics in tetracene thin films. *Phys. Chem. Chem. Phys.* **15**, 14797 (2013).

290. Zhu, T. & Huang, L. Exciton Transport in Singlet Fission Materials: A New Hare and Tortoise Story. *J. Phys. Chem. Lett.* **9**, 6502–6510 (2018).

291. Jadhav, P. J., Mohanty, A., Sussman, J., Lee, J. & Baldo, M. A. Singlet Exciton Fission in Nanostructured Organic Solar Cells. *Nano Lett.* **11**, 1495–1498 (2011).

292. Pace, N. A. *et al.* Dynamics of singlet fission and electron injection in self-assembled acene monolayers on titanium dioxide. *Chem. Sci.* **9**, 3004–3013 (2018).

293. Stern, H. L. *et al.* Identification of a triplet pair intermediate in singlet exciton fission in solution. *Proc. Natl. Acad. Sci. U. S. A.* **112**, 7656–7661 (2015).

294. Stern, H. L. *et al.* Vibronically coherent ultrafast triplet-pair formation and subsequent thermally activated dissociation control efficient endothermic singlet fission. *Nat. Chem.* **9**, 1205–1212 (2017).

295. Dover, C. B. *et al.* Endothermic singlet fission is hindered by excimer formation. *Nat. Chem.* **10**, 305–310 (2018).

296. Zimmerman, P. M., Bell, F., Casanova, D. & Head-Gordon, M. Mechanism for Singlet Fission in Pentacene and Tetracene: From Single Exciton to Two Triplets. *J. Am. Chem. Soc.* **133**, 19944–19952 (2011).

297. Zhang, Y. J. *et al.* A simple and cost effective experimental method for verifying singlet fission in pentacene–C 60 solar cells. *RSC Adv.* **5**, 29718–29722 (2015).

298. Wu, T. C. *et al.* Singlet fission efficiency in tetracene-based organic solar cells. *Appl. Phys. Lett.* **104**, 193901 (2014).

299. Kurpiers, J. *et al.* Probing the pathways of free charge generation in organic bulk heterojunction solar cells. *Nat. Commun.* **9**, 2038 (2018).

300. Vandewal, K. *et al.* Efficient charge generation by relaxed charge-transfer states at organic interfaces. *Nat. Mater.* **13**, 63–68 (2014).

301. Nakano, K. *et al.* Anatomy of the energetic driving force for charge generation in organic solar cells. *Nat. Commun.* **10**, 2520 (2019).

302. Minami, N. Photocurrent spectra of phthalocyanine thin-film electrodes in the visible to near-infrared. *J. Chem. Soc. Faraday Trans. 2* **78**, 1871 (1982).

303. Griffith, O. L., Jones, A. G., Anthony, J. E. & Lichtenberger, D. L. Intermolecular Effects on the Hole States of Triisopropylsilylethynyl-Substituted Oligoacenes. *J. Phys. Chem. C* **114**, 13838–13845 (2010).

304. Oh, E. *et al.* Energy level alignment at the interface of NPB/HAT-CN/graphene for flexible organic light-emitting diodes. *Chem. Phys. Lett.* **668**, 64–68 (2017).

305. Wang, H., He, Y., Li, Y. & Su, H. Photophysical and Electronic Properties of Five PCBM-like C 60 Derivatives: Spectral and Quantum Chemical View. *J. Phys. Chem. A* **116**, 255–262 (2012).

306. Burdett, J. J., Müller, A. M., Gosztola, D. & Bardeen, C. J. Excited state dynamics

in solid and monomeric tetracene: The roles of superradiance and exciton fission. *J. Chem. Phys.* (2010) doi:10.1063/1.3495764.

307. Robertson, J. M., Sinclair, V. C. & Trotter, J. The crystal and molecular structure of tetracene. *Acta Crystallogr.* **14**, 697–704 (1961).

308. Morisaki, H. *et al.* Large surface relaxation in the organic semiconductor tetracene. *Nat. Commun.* **5**, 5400 (2014).

309. Kim, D. H. *et al.* Organic light emitting diodes with horizontally oriented thermally activated delayed fluorescence emitters. *J. Mater. Chem. C* **5**, 1216–1223 (2017).

310. Zhao, L. *et al.* Horizontal molecular orientation of light-emitting oligofluorenes in spin-coated glassy organic thin films. *J. Mater. Chem. C* **4**, 11557–11565 (2016).

311. Yokoyama, D. Molecular orientation in small-molecule organic light-emitting diodes. *J. Mater. Chem.* **21**, 19187 (2011).

312. Yokoyama, D., Sasabe, H., Furukawa, Y., Adachi, C. & Kido, J. Molecular Stacking Induced by Intermolecular C-H···N Hydrogen Bonds Leading to High Carrier Mobility in Vacuum-Deposited Organic Films. *Adv. Funct. Mater.* **21**, 1375–1382 (2011).

313. Cui, L. *et al.* Controlling Singlet–Triplet Energy Splitting for Deep-Blue Thermally Activated Delayed Fluorescence Emitters. *Angew. Chemie Int. Ed.* **56**, 1571–1575 (2017).

314. Proctor, C. M., Kuik, M. & Nguyen, T. Q. Charge carrier recombination in organic solar cells. *Progress in Polymer Science* (2013)

doi:10.1016/j.progpolymsci.2013.08.008.

315. Unuchek, D. *et al.* Room-temperature electrical control of exciton flux in a van der Waals heterostructure. *Nature* **560**, 340–344 (2018).

316. Deotare, P. B. *et al.* Nanoscale transport of charge-transfer states in organic donor–acceptor blends. *Nat. Mater.* **14**, 1130–1134 (2015).

317. Vandewal, K., Tvingstedt, K., Gadisa, A., Inganäs, O. & Manca, J. V. Relating the open-circuit voltage to interface molecular properties of donor:acceptor bulk heterojunction solar cells. *Phys. Rev. B - Condens. Matter Mater. Phys.* (2010) doi:10.1103/PhysRevB.81.125204.

318. Piersimoni, F. *et al.* Influence of fullerene ordering on the energy of the charge-transfer state and open-circuit voltage in polymer:fullerene solar cells. *J. Phys. Chem. C* (2011) doi:10.1021/jp110982m.

319. Veldman, D., Meskers, S. C. J. & Janssen, R. a. J. The Energy of Charge-Transfer States in Electron Donor–Acceptor Blends: Insight into the Energy Losses in Organic Solar Cells. *Adv. Funct. Mater.* **19**, 1939–1948 (2009).

320. Rosenow, T. C., Walzer, K. & Leo, K. Near-infrared organic light emitting diodes based on heavy metal phthalocyanines. *J. Appl. Phys.* **103**, (2008).

321. Huang, L., Park, C. D., Fleetham, T. & Li, J. Platinum (II) azatetrabenzoporphyrins for near-infrared organic light emitting diodes. *Appl. Phys. Lett.* (2016) doi:10.1063/1.4971363.

13 Appendices

A: List of Publications

1. **D. Rai** and R. J. Holmes, *Investigation of Excitonic Gates in Organic Semiconductor Thin films*, Phys. Rev. Appl., 11, 014048 (2019).
2. **D. Rai** and R. J. Holmes, *Measurement of the Triplet Diffusion Length in Organic Semiconductor*, J. Mater. Chem. C ,7, 5695-5701 (2019).
3. **D. Rai,** J. S. Bangsund, J. G. Barriocanal and R. J. Holmes, *Impact of molecular structure change on exciton diffusion in BPhen Derivatives*, Mater. Chem. C, 2020, Advance Article
4. K. Shi, I. J. Curtin, A. T. Healy, T. Zhang, **D. Rai**, D. A. Blank, and R. J. Holmes, *Probing Enhanced Exciton Diffusion in a Triplet-Sensitized Organic Photovoltaic Cell*, J. Phys. Chem. C, 124, 6, 3489-3495 (2020).
5. T. Zhang, **D. Rai**, and R. J. Holmes, *Investigation of Dark Exciton Diffusion in Singlet Fission Materials* (Preparation).

B: List of Presentations

1. **D. Rai**, R. J. Holmes, *Measurement of the Triplet Exciton Diffusion Length in Organic Semiconductor Thin Films*, Materials Research Society Spring Meeting, 2018, Phoenix AZ.
2. **D. Rai**, R. J. Holmes, *Measurement of the Triplet Exciton Diffusion Length in Organic Semiconductor Thin Films*, IPrime Annual Meeting, 2018, Minneapolis, MN.

C: Copyright and Permissions

Chapter 4: Figure 4.5 was reproduced by permission from "Irkhin, P. & Biaggio, I. Direct Imaging of Anisotropic Exciton Diffusion and Triplet Diffusion Length in Rubrene Single Crystals. *Phys. Rev. Lett.* **107**, 017402 (2011)" Copyright 2011, American Physical Society.

Chapter 4: Figure 4.8 was reproduced from "Mullenbach, T. K., Curtin, I. J., Zhang, T. & Holmes, R. J. Probing dark exciton diffusion using photovoltage. *Nat. Commun.* **8**, 14215 (2017)" under Creative Commons Attribution 4.0 International License, Copyright 2017, Springer nature.

Chapter 5: All or portions of some figures were reproduced or adapted from "Rai, D. & Holmes, R. J. Measurement of the triplet exciton diffusion length in organic semiconductors. *J. Mater. Chem. C* **7**, 5695–5701 (2019)" under Copyright 2019, The Royal Society of Chemistry.

Chapter 6: All or portions of some figures were reproduced or adapted from "Rai, D., Bangsund, J. S., Barriocanal, J. G. & Holmes Measurement of the triplet exciton diffusion length in organic semiconductors. *J. Mater. Chem. C* **7**, 5695–5701 (2019)" under Copyright 2019, The Royal Society of Chemistry.

Chapter 7: All or portions of some figures were reproduced or adapted from "Rai, D. & Holmes, R. J. Investigation of Excitonic Gates in Organic Semiconductor Thin Films. *Phys. Rev. Appl.* **11**, 014048 (2019)." Copyright 2019 from American Physical Society.

Chapter 10: Figure 10.2 was reproduced by permission from "Yokoyama, D., Sasabe, H., Furukawa, Y., Adachi, C. & Kido, J. Molecular Stacking Induced by Intermolecular C-H···N Hydrogen Bonds Leading to High Carrier Mobility in Vacuum-Deposited Organic Films. *Adv. Funct. Mater.* **21**, 1375–1382 (2011)" Copyright 2011, John Wiley and Sons.

Chapter 11: Figure 10.5 was reproduced by permission from "Huang, L., Park, C. D., Fleetham, T. & Li, J. Platinum (II) azatetrabenzoporphyrins for near-infrared organic light emitting diodes. *Appl. Phys. Lett.* (2016)" Copyright 2016, AIP Publishing, LLC.

D: Supporting Information for Chapter 5

Outcoupled Photoluminescence Efficiency Ratio

The outcoupled PL efficiency can be calculated by direct injection of excitons into the sensitizer from an adjacent layer as shown in Fig. D1, thereby setting η_T equal to 1.

$$\frac{\eta_{Sensitizer}^{PL}}{\eta_{Injector}^{PL}} = \frac{\Delta PL^{Sensitizer}}{\Delta PL^{Injector}} \quad \text{(D1)}$$

where $\Delta PL^{Sensitizer}$ and $\Delta PL^{Injector}$ are the change in photoluminescence (PL) of the injector and sensitizer layers in the case when the two layers are adjacent to each other and when each layer is replaced by the wide gap exciton blocking layer.

$$\Delta PL_{Injector} = PL^{Injector} - PL_{Sensitizer}^{Injector}$$
$$\Delta PL_{Sensitizer} = PL_{Injector}^{Sensitizer} - PL^{Sensitizer}$$

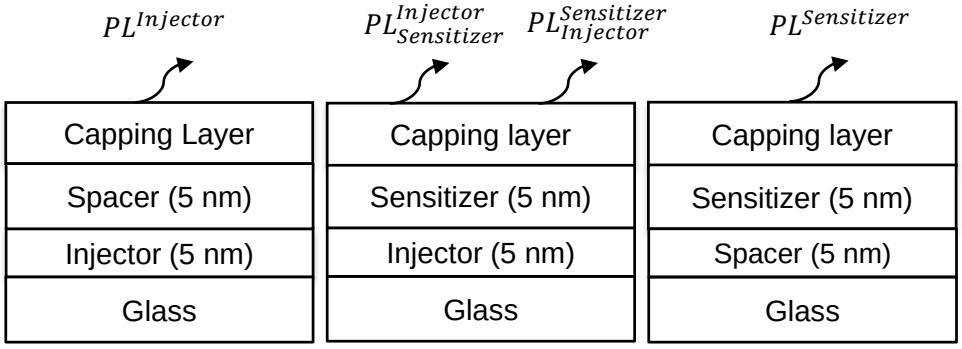

Figure D1: Architecture for extracting the outcoupled PL efficiency ratio.

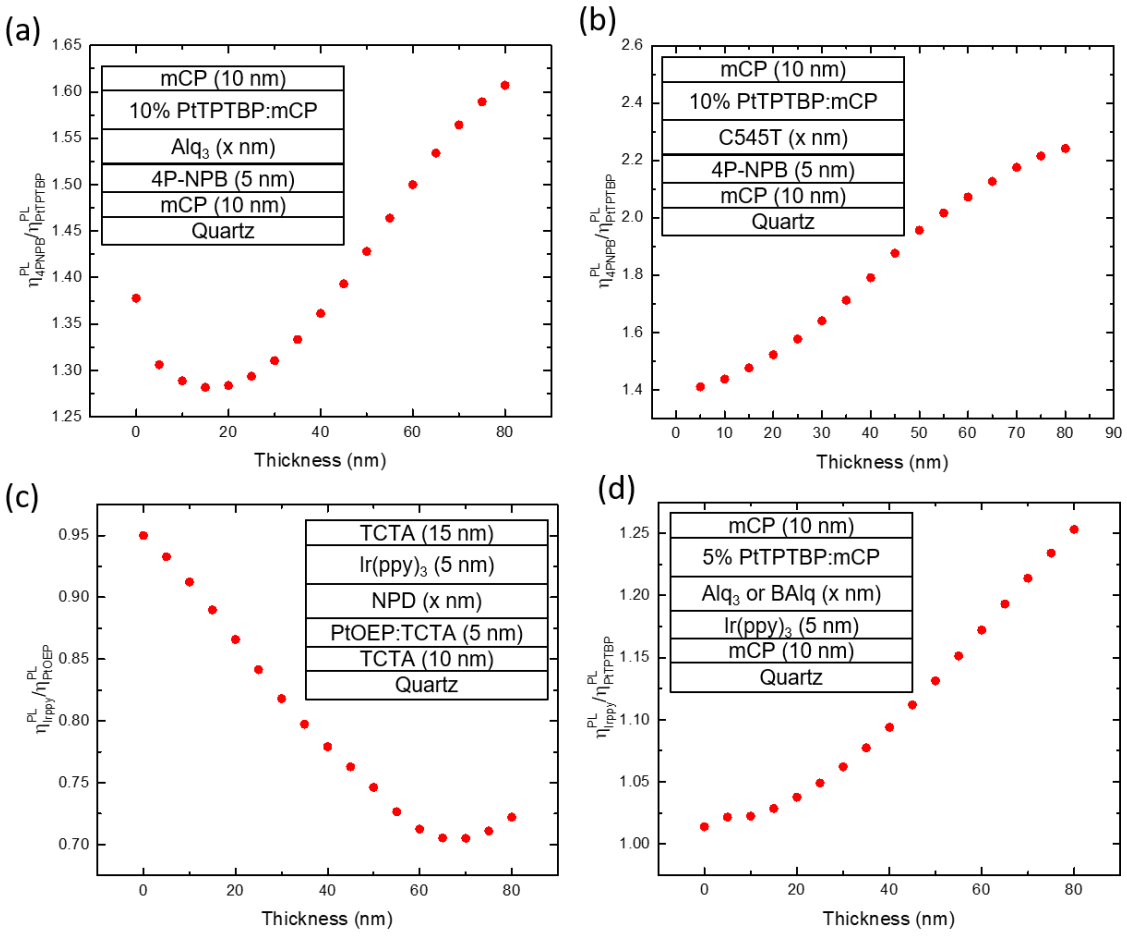

Figure D2 The simulated outcoupled photoluminescence efficiency ratio of injector and sensitizer ($\eta^{PL}_{Injector}/\eta^{PL}_{sensitizer}$) for (a) Alq_3 singlet measurement (b) C545T singlet measurement (c) NPD triplet measurement and (d) Alq_3 or BAlq triplet measurement as a function of active layer thickness using Setfos 4.6 (Fluxim) software.

E: Supporting Information for Chapter 6

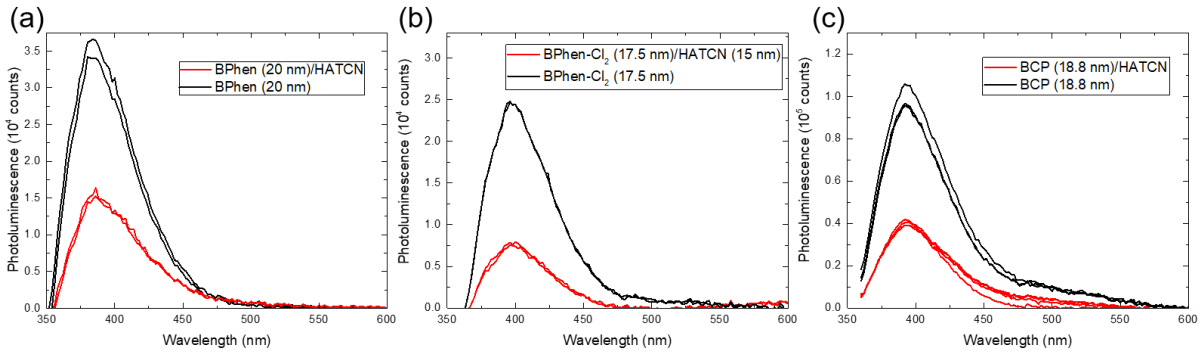

Figure E1: Photoluminescence spectra of quenched and unquenched sample of (a) BPhen (b) BPhen-Cl_2 (c) BCP.

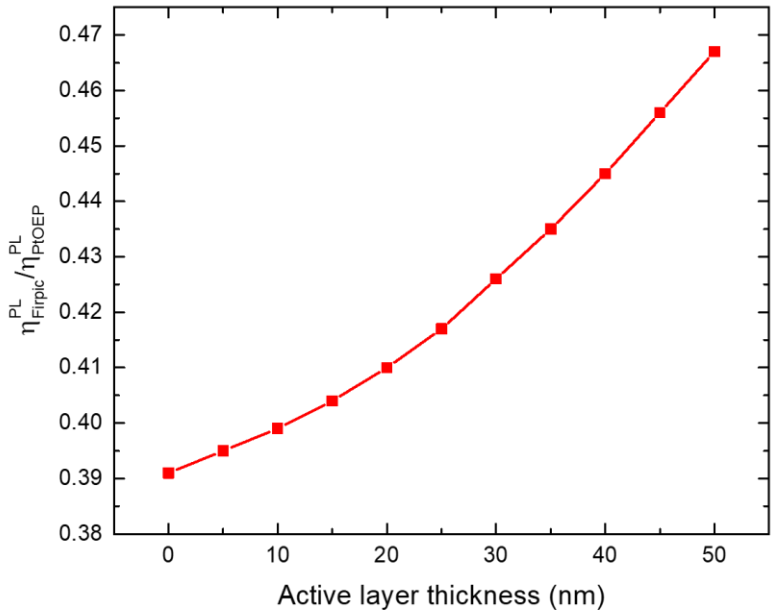

Figure E2: The simulated outcoupled photoluminescence efficiency ratio ($\eta^{PL}_{Firpic}/\eta^{PL}_{PtOEP}$) of FIrpic and PtOEP as a function of active layer thickness using Setfos 4.6 (Fluxim) software. The structure is simulated for FIrpic/active layer (x nm)/5 wt.% PtOEP, where the active layer is BPhen and its derivatives. The outcoupled photoluminescence efficiency ratios are same for all the three active layers due to similarity in optical constants.

F: Supporting Information for Chapter 7

Outcoupled Photoluminescence Efficiency Ratio

The transport efficiency (η_T) in Fig. 7.6b is extracted by comparing the photoluminescence from the injector and sensitizer layers in the case where the gating structure is present, and where it is replaced with an exciton blocking layer. In this way, the increase (decrease) in photoluminescence from the sensitizer (injector) due to energy transfer can be isolated from direct optical excitation (i.e. the case of an exciton blocking layer in place of the gating structure). The architectures associated with these measurements are shown in Fig. F1a. The η_T is therefore calculated as:

$$\eta_T = \frac{\Delta PL^{PtTPTBP}}{\Delta PL^{4P-NPB}} \times \frac{\eta_{4P-NPB}^{PL}}{\eta_{PtTPTBP}^{PL}} \times \frac{\eta_{4P-NPB}^{OC}}{\eta_{PtTPTBP}^{OC}} \quad \text{(F1)}$$

Similarly, the architectures used to measure the outcoupled PL efficiency ratio are shown in Fig. F1b. The 4P-NPB injection layer is adjacent to the sensitizer layer of 5 wt.% PtTPTBP diluted in UGH2, allowing for the direct injection of excitons into sensitizer. Thus, the exciton injection rate from 4P-NPB is equal to the exciton collection rate at the layer containing PtTPTBP. The rate of injection is calculated from Fig. F2 based on the reduction in PL from 4P-NPB (PL^{4P-NPB}) when adjacent to the sensitizer layer ($PL_{PtTPTBP}^{4P-NPB}$). The corresponding collection rate is extracted from the measured increase in PL from PtTPTBP ($PL^{PtTPTBP}$) when adjacent to 4P-NPB ($PL_{4P-NPB}^{PtTPTBP}$).

The outcoupled PL efficiency ratio is thus calculated as:

$$\frac{PL^{4P-NPB} - PL_{PtTPTBP}^{4P-NPB}}{\eta_{4P-NPB}^{PL} \times \eta_{4P-NPB}^{OC}} = \frac{PL_{4P-NPB}^{PtTPTBP} - PL^{PtTPTBP}}{\eta_{PtTPTBP}^{PL} \times \eta_{PtTPTBP}^{OC}} \quad \text{(F2)}$$

$$\frac{\eta_{PtTPTBP}^{PL}\times\eta_{PtTPTBP}^{OC}}{\eta_{4P-NPB}^{PL}\times\eta_{4P-NPB}^{OC}} = \frac{PL_{4P-NPB}^{PtTPTBP} - PL^{PtTPTBP}}{PL^{4P-NPB} - PL_{PtTPTBP}^{4P-NPB}} = 0.79 \quad \text{(F3)}$$

where η_{4P-NPB}^{PL} and $\eta_{PtTPTBP}^{PL}$ are the PL efficiencies of 4P-NPB and 5 wt.% PtTPTBP diluted in UGH2, η_{4P-NPB}^{OC} and $\eta_{PtTPTBP}^{OC}$ are the outcoupling efficiency in 4P-NPB and 5 wt.% PtTPTBP.

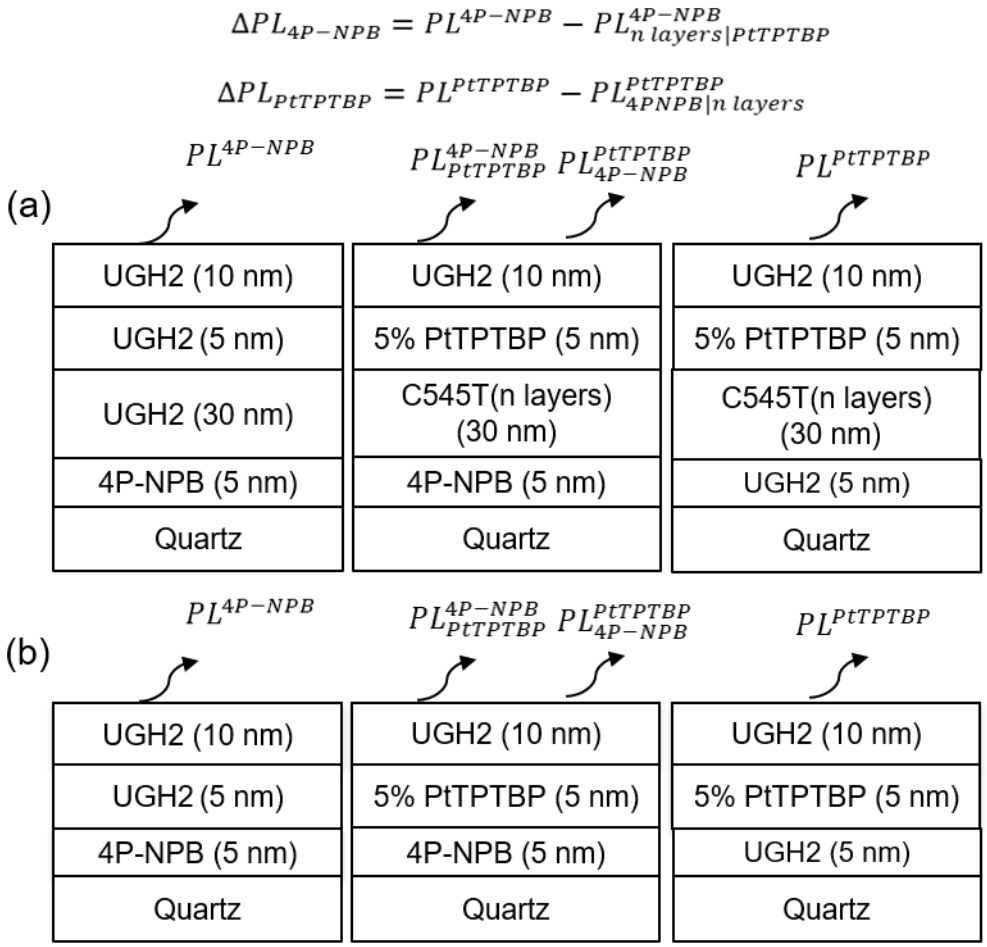

Figure F1: (a) Generalized scheme for measuring transport efficiency in Fig. 7.6b. The C545T (n layers) represents multiple interfacial gates as illustrated in Fig. 7.2a. **(b)**

Architecture for extracting the outcoupled PL efficiency ratio of 4P-NPB and 5 wt.% PtTPTBP in UGH2.

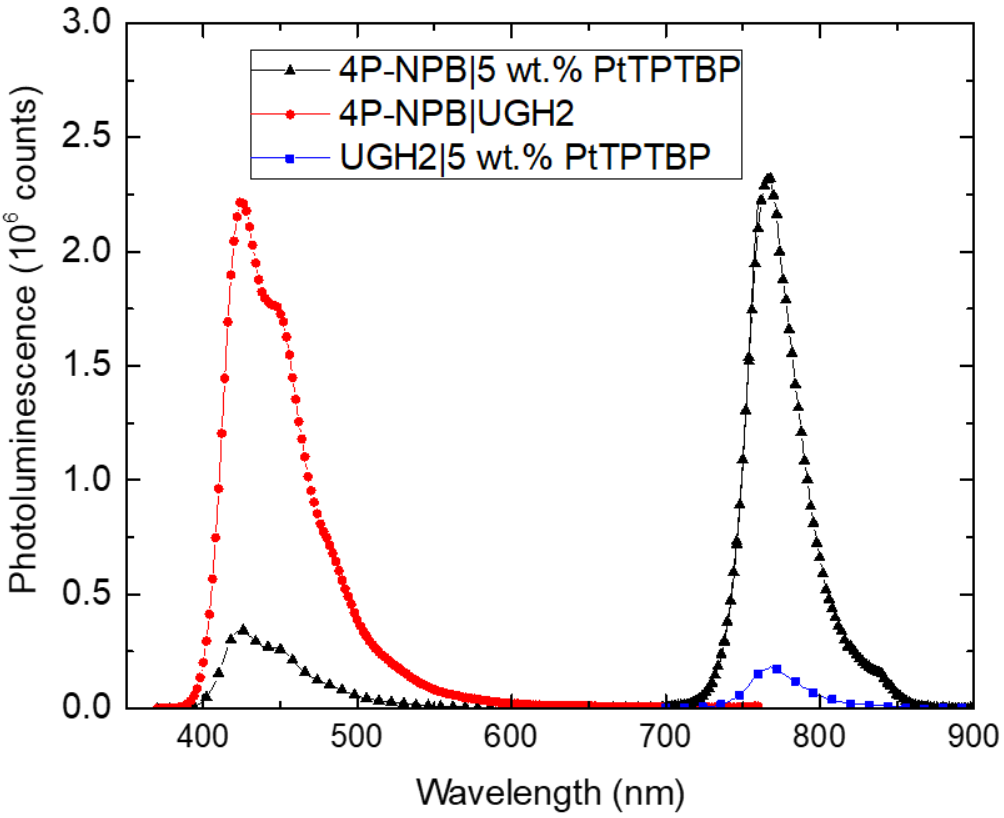

Figure F2: Photoluminescence spectra for the structures of Fig. F1b used to measure the outcoupled photoluminescence efficiency at a pump wavelength of λ=355 nm.

G: Optical Transfer Matrix Code (Matlab)

```
% Modeling Photocurrent action spectra of Photovoltaic Devices
RI=xlsread('RI.xlsx',1); %optical constants
spectrum=xlsread('SS.xlsx',1);
d=xlsread('RI.xlsx',2);  % thickness

%SS=interp1(spectrum(:,1),spectrum(:,2),300:1:840);
%file=fopen('SS.txt','w');
%fprintf(file,'%6.2f %12.8f\n',[(300:1:840); SS]);
%fclose(file);

%Alq3=interp1(spectrum(:,1),spectrum(:,4),300:2:800);
% NTU_k=interp1(spectrum(:,3),spectrum(:,5),300:1:1190);
% RI(:,10)=NTU_n;
% RI(:,11)=NTU_k;
m=length(d);
n=length(RI);
n=n-350;
q=zeros(n,m);
phio=0; % angle of incidence
lamda=590;
%L=zeros(1,4);
%L=[10.7,13.6,10.7,25];
L1=10.7; % difussion length inside SubPC
L2=15;% diffusion length inside C60
%Total Total reflection and Transmission coefficient
Rs=zeros(1,n);
Rp=zeros(1,n);
Jsc=0;

% Fresnel reflection coefficients
rs=zeros(1,m-1,n);
rp=zeros(1,m-1,n);
% Fresnel Transmission Coefficents
ts=zeros(1,m-1,n);
tp=zeros(1,m-1,n);
% Interface Materix
Is=zeros(2,2,m-1,n);
Ip=zeros(2,2,m-1,n);
% Layer(phase matrix)
 Ls=zeros(2,2,m-2,n);
 Lp=zeros(2,2,m-2,n);

 % Photcurrent

Jp1=zeros(1,n);
Jp2=zeros(1,n);
```

```
IPCE=zeros(1,n);
EQE_ss=zeros(1,n);
z=590;
for p=1:n % Iterating at each wavelength

% s polarized or TE Waves (Electric field perpendicular to the plane of
incidence)
for i=1:m;
 q(p,i)=((RI(p,2*i)+RI(p,2*i+1)*1i)^2- (RI(p,2)+RI(p,3)*1i)^2 *
sin(phio))^(0.5);
end
for i=1:m-1
 rs(1,i,p)=(q(p,i)-q(p,i+1))/(q(p,i)+q(p,i+1));
 ts(1,i,p)=2*q(p,i)/(q(p,i)+q(p,i+1));
end
% p polarized or TM Waves (Electric field parallel to the plane of
incidence)
for i=2:m;
 rp(1,i-1,p)=((RI(p,2*i+2)+RI(p,2*i+3)*1i)^2 *q(p,i-1)-q(p,i)*
(RI(p,2*i)+RI(p,2*i+1)*1i)^2)/((RI(p,2*i+2)+RI(p,2*i+3)*1i)^2 *q(p,i-
1)+q(p,i)* (RI(p,2*i)+RI(p,2*i+1)*1i)^2);
 tp(1,i-1,p)=(2*(RI(p,2*i)+RI(p,2*i+1)*1i)*(RI(p,2*i+2)+RI(p,2*i+3)*1i)
*q(p,i-1))/((RI(p,2*i+2)+RI(p,2*i+3)*1i)^2 * q(p,i-1)+q(p,i)*
(RI(p,2*i)+RI(p,2*i+1)*1i)^2);
end



for i=1:m-1;
  Is(:,:,i,p)=[1, rs(1,i,p);rs(1,i,p),1]/ts(1,i,p);
  Ip(:,:,i,p)=[1, rp(1,i,p);rp(1,i,p), 1]/tp(1,i,p);
end

for k=1:m-2
 E=(2*pi*q(p,k+1)*d(k+1))/RI(p,1);
 Ls(:,:,k,p)=[exp(-E*1i) 0; 0 exp(E*1i)];
 Lp(:,:,k,p)=[exp(-E*1i) 0; 0 exp(E*1i)];
end

% Total System Scattering Matrix
Ss=[1,0;0,1];
Sp=[1,0;0,1];
for i=1:m-2
Ss(:,:)=Ss(:,:)*Is(:,:,i,p)*Ls(:,:,i,p) ;
Sp(:,:)=Sp(:,:)*Ip(:,:,i,p)*Lp(:,:,i,p);
end
Ss(:,:)=Ss(:,:)*Is(:,:,m-1,p);
Sp(:,:)=Sp(:,:)*Ip(:,:,m-1,p);

%Total Total reflection and Transmission coefficient
```

```
Rs(p)=Ss(2,1)/Ss(1,1);
Rp(p)=Sp(2,1)/Sp(1,1);
Ts=1/Ss(1,1);
Tp=1/Sp(1,1);

%To get index for lamda
if RI(p,1)==lamda
  w=p;
end




% Calculation of internal electric field in layer j
% the layer system matrix system can be divided in two subsets
Ss_j1=ones(2,2,m-2);
Ss_j2=ones(2,2,m-2);
Sp_j1=ones(2,2,m-2);
Sp_j2=ones(2,2,m-2);

rs_j1=ones(1,m-2);
rs_j2=ones(1,m-2);
rs_j3=ones(1,m-2);
rp_j1=ones(1,m-2);
rp_j2=ones(1,m-2);

ts_j1=ones(1,m-2);
ts_j2=ones(1,m-2);
ts_j=ones(1,m-2);
tp_j1=ones(1,m-2);
tp_j2=ones(1,m-2);



% calculations can be reduced here


for u=1:m-2
  Ss_j1(:,:,u)=[1,0;0,1];
  Ss_j2(:,:,u)=[1,0;0,1];
  Sp_j1(:,:,u)=[1,0;0,1];
  Sp_j2(:,:,u)=[1,0;0,1];



  for v=1:u-1
 Ss_j1(:,:,u)=Ss_j1(:,:,u)*Is(:,:,v,p)*Ls(:,:,v,p);
Sp_j1(:,:,u)=Sp_j1(:,:,u)*Ip(:,:,v,p)*Lp(:,:,v,p);
```

```
  end


 for v=u+1:m-2
Ss_j2(:,:,u)=Ss_j2(:,:,u)*Is(:,:,v,p)*Ls(:,:,v,p);
Sp_j2(:,:,u)=Sp_j2(:,:,u)*Ip(:,:,v,p)*Lp(:,:,v,p);
 end
Ss_j1(:,:,u)=Ss_j1(:,:,u)*Is(:,:,u,p);
Ss_j2(:,:,u)=Ss_j2(:,:,u)*Is(:,:,m-1,p);
Sp_j1(:,:,u)=Sp_j1(:,:,u)*Ip(:,:,u,p);
Sp_j2(:,:,u)=Sp_j2(:,:,u)*Ip(:,:,m-1,p);

rs_j1(u)=Ss_j1(2,1,u)/Ss_j1(1,1,u);
rs_j2(u)=Ss_j2(2,1,u)/Ss_j2(1,1,u);
rs_j3(u)=-Ss_j1(1,2,u)/Ss_j1(1,1,u);

rp_j1(u)=Ss_j1(2,1,u)/Ss_j1(1,1,u);
rp_j2(u)=Ss_j2(2,1,u)/Ss_j2(1,1,u);

ts_j1(u)=1/Ss_j1(1,1,u);
ts_j2(u)=1/Ss_j2(1,1,u);
tp_j1(u)=1/Ss_j1(1,1,u);
tp_j2(u)=1/Ss_j2(1,1,u);
end



clear j
E_x=[];
n_x=[];

s=0;
% Electric Field Calculations
for i=1:m-2
x=0:0.05:d(i+1);
l=length(x);
E1=zeros(1,l);
E2=zeros(1,l);
E3=zeros(1,l);
c=2.998*10^8;
eo=8.854*10^-12;
Q=zeros(1,l);
Eo=20;
E=(2*pi*q(p,i+1))/RI(p,1);
ts_j(i)=ts_j1(i)/(1-rs_j3(i)*rs_j2(i)*exp(2*E*d(i+1)*1i));
alpha=(4*pi*RI(p,2*(i+2)+1))/RI(p,1);
R=(4*pi/RI(p,1));
for k=1:l
E1(k)=Eo*(Ss_j2(1,1,i)*exp(-E*(d(i+1)-
x(k))*1i)+Ss_j2(2,1,i)*exp(E*(d(i+1)-
```

```
x(k))*1i))/(Ss_j1(1,1,i)*Ss_j2(1,1,i)*exp(-
E*(d(i+1))*1i)+Ss_j1(1,2,i)*Ss_j2(2,1,i)*exp(E*d(i+1)*1i));
E2(k)=Eo*(Sp_j2(1,1,i)*exp(-E*(d(i+1)-
x(k))*1i)+Sp_j2(2,1,i)*exp(E*(d(i+1)-
x(k))*1i))/(Sp_j1(1,1,i)*Sp_j2(1,1,i)*exp(-
E*(d(i+1))*1i)+Sp_j1(1,2,i)*Sp_j2(2,1,i)*exp(E*d(i+1)*1i));
E3(k)=ts_j(i)*(exp(E*x(k)*1i)+rs_j2(i)*exp(E*(2*d(i+1)-x(k))*1i));
Q(k)=0.5*(c*eo*alpha*(RI(p,2*(i+2))*abs(E1(k))^2));
end


if (i==2)

  Io=0.5*c*eo*spectrum(p,3)*Eo^2*exp(-R*spectrum(p,4)*3*10^6);


end


E_x=[E_x,E3];

n_x=[n_x,x+s];
s=s+d(i+1);

end

% Exciton Transport-- Difussion Equation


N1=[]; n_x=[]; N1d=[];

ph=(Io*RI(p,1))/(1.986*10^2); % Number of incident photons at the
device per unit area per unit time
r=0;


 i=3; %% 1% SubPc Layer

% Exciton transport-diffusion Equaiton
D=228.98;
rho=abs(Ss_j2(2,1,i-1)/Ss_j2(1,1,i-1));
delta=angle(Ss_j2(2,1,i-1)/Ss_j2(1,1,i-1));
b=double(1/L1);
x=0:0.1:d(i);
l=length(x);
N=zeros(1,l);
Nd=zeros(1,l);
a=((4*pi/RI(p,1))*RI(p,2*(i+1)+1));
```

```
T=(RI(p,2*(i+1))/RI(p,4))*abs(ts_j(i-1))^2;

t1=0.8; % Quantum efficiency of exciton generation
t2=1; %Efficiency of excition dissociation at the interface

C1=(rho^2*exp(-2*a*d(i)));
C2=(((b^2-a^2)/(b^2+(4*pi*RI(p,2*(i+1))/RI(p,1))^2))*2*rho*exp(-
a*d(i)));
R=4*(pi/RI(p,1));
A=((-(a*exp(b*d(i))+b*exp(-a*d(i)))+C1*(a*exp(b*d(i))-
b*exp(a*d(i)))+C2*(exp(b*d(i))*sin(4*pi*RI(p,2*(i+1))*d(i)/RI(p,1)+delt
a)*RI(p,2*(i+1))*(4*pi/RI(p,1))-b*cos(delta)))/((exp(-
b*d(i))+exp(b*d(i)))*b));
B=-((-a*exp(-b*d(i))+b*exp(-a*d(i)))+C1*(a*exp(-
b*d(i))+b*exp(a*d(i)))+C2*(exp(-
b*d(i))*RI(p,2*(i+1))*(4*pi/RI(p,1))*sin(4*pi*RI(p,2*(i+1))*d(i)/RI(p,1
)+delta)+b*cos(delta)))/((exp(-b*d(i))+exp(b*d(i)))*b);
K1=((t1*a*T*ph)/(D*(b^2-a^2)));
%RF=(exp(-R*RI(p,5)*d(1)))*(exp(-R*RI(p,7)*d(2))*(exp(-
R*RI(p,9)*d(3))));
RF=1;
for k=1:l
N(1,k)=K1*RF*((A * exp(-b*x(k))+B* exp(b*x(k))+exp(-a*x(k))+ C1 *exp(a
* x(k))+ C2 * cos((4*pi*RI(p,2*(i+1))*(d(i)-x(k))/RI(p,1))+ delta)));
Nd(1,k)=K1*RF*((-b*A * exp(-b*x(k))+B*b* exp(b*x(k))-a*exp(-a*x(k))+
C1*a *exp(a * x(k))+ C2
*(4*pi*RI(p,2*(i+1))/RI(p,1))*sin((4*pi*RI(p,2*(i+1))*(d(i)-
x(k)))/RI(p,1)+ delta)));
end
Jp1(p)=-D*t2* Nd(1,l)*1.6*10^-19;

n_x=[n_x,x+r];
r=r+d(i);
N1=[N1,N];
N1d=[N1d,Nd];
%%%%%%%%%%%%%%%%%%%%%%%%%%%%%%%%


%%%%%%%%%%%%%%%%%%%%%%%%%%%%%%%%%%%%
i=4; %% C60 Layer

D=500; % Diffusion Coefficient
rho=abs(Ss_j2(2,1,i-1)/Ss_j2(1,1,i-1));
delta=angle(Ss_j2(2,1,i-1)/Ss_j2(1,1,i-1));
b=double(1/L2);
x=0:0.1:d(i);
l=length(x);
N=zeros(1,l);
Nd=zeros(1,l);
```

```
a=(4*pi/RI(p,1))*RI(p,2*(i+1)+1);

T=(RI(p,2*(i+1))/RI(p,4))*abs(ts_j(i-1))^2;

t2=1; % Quantum efficiency of exciton generation


C1=double(rho^2*exp(-2*a*d(i)));
C2=double(((b^2-a^2)/(b^2+(4*pi*RI(p,2*(i+1))/RI(p,1))^2))*2*rho*exp(-
a*d(i)));

A=double(-a*exp(-a*d(i))-b*exp(b*d(i))+C1*(a*exp(a*d(i))-b*
exp((b*d(i))))+C2*(-
b*exp(b*d(i))*cos((4*pi*RI(p,2*(i+1))*d(i))/RI(p,1)+delta)+RI(p,2*(i+1)
)*(4*pi/RI(p,1))*sin(delta)))/((exp(-b*d(i))+exp((b*d(i))))*b);
B=-double((-a*exp(-a*d(i)))+b*exp(-b*d(i))+C1*(a*exp(a*d(i))+b*exp(-
b*d(i)))+C2*(b*exp(-
b*d(i))*cos((4*pi*RI(p,2*(i+1))*d(i))/RI(p,1)+delta)+RI(p,2*(i+1))*(4*p
i/RI(p,1))*sin(delta)))/((exp(-b*d(i))+exp(b*d(i)))*b);
K2=((t1*a*T*ph)/(D*(b^2-a^2)));
%RF=exp(-(R*RI(p,5))*d(1))*exp(-R*RI(p,7)*d(2))*exp(-R*RI(p,9)*d(3));
%exp(-R*RI(p,11)*d(4));
RF=1;
for k=1:l
N(1,k)=K2*RF*double((A * exp(-b*x(k))+B* exp(b*x(k))+exp(-a*x(k))+ C1
*exp(a * x(k))+ C2 * cos((4*pi*RI(p,2*(i+1))*(d(i)-x(k))/RI(p,1))+
delta)));
Nd(1,k)=K2*RF*double((-b*A * exp(-b*x(k))+B*b* exp(b*x(k))-a*exp(-
a*x(k))+ C1*a *exp(a * x(k))+ C2
*(4*pi*RI(p,2*(i+1))/RI(p,1))*sin((4*pi*RI(p,2*(i+1))*(d(i)-
x(k)))/RI(p,1)+ delta)));
end

Jp2(p)=(D*t2*Nd(1,1)*1.6*10^-19);
%Jp2(p)=0;

IPCE(p)=((Jp1(p)+Jp2(p))/(RI(p,1)* Io)*1240)*10^20;

EQE_ss(p)=(IPCE(p)*SS(p));
n_x=[n_x,x+r];
r=r+d(i);
N1=[N1,N];
N1d=[N1d,Nd];
```

```
if RI(p,1)==z
figure
subplot(1,2,1);
plot(n_x,N1*10^21);
title('Exciton Density');
xlabel('Thickness(nm)');
ylabel('n(cm^-3)');


subplot(1,2,2);
plot(n_x,N1d*10^14);
title('Exciton Density Differential');
xlabel('Thickness(nm)');
ylabel('dn/dx(cm^-2)');

end

end


 figure
% subplot(2,2,1)
% plot(RI(1:n,1),abs(Rp(:)).^2);
% title('Reflectance');
% xlabel('Wavelength(nm)');
% ylabel('R');



%
% subplot(2,2,2)
plot(RI(1:n,1),Jp1(:)*10^17);
title('Photocurrent (Jp1)');
xlabel( 'Wavelength(nm)');
ylabel('Photocurrent(mA/cm^2)');


figure
%
% subplot(2,2,3)
plot(RI(1:n,1),Jp2(:)*10^17);
title('Photocurrent (Jp2)');
xlabel( 'Wavelength(nm)');
ylabel('Photocurrent(mA/cm^2)');

figure
% subplot(2,2,4)
plot(RI(1:n,1),IPCE(:));
title('IPCE');
```

```
xlabel( 'Wavelength(nm)');
ylabel('IPCE (%)');
% hold on
% plot(RI(1:n,1),EQE_ss(:));
 hold on
% plot(RI(1:n,1),EQE_ss(:));
 EQE=xlsread('EQE SUBPC.xlsx',1);
 plot(EQE(:,1),EQE(:,2));
```

H: Kinetic Monte Carlo Code (C++)

```
// Created by Deepesh Rai on 05/09/18.
// Copyright Â© 2018 Deepesh Rai. All rights reserved.

#include <fstream> //Input/output stream class to operate on files
#include <iostream> // Header that defines the standard input/output
stream objects
#include <sstream> //Header providing string stream classes
#include <string> //Strings are objects that represent sequences of
characters.
#include <vector> //Vectors are sequence containers representing arrays
that can change in size
#include <cmath> //declares a set of functions to compute common
mathematical operations and transformations
#include "mtrand.h"// Mersemne Twister Random number generator
#include <iomanip> //Header providing parametric manipulators
#include<stdlib.h>
//#include "mex.h"
using namespace std; // A namespace is like adding a new group name to
which you can add functions and other data, so that it will become
distinguishable. If we come across an object name that doesn't exist in
our current namespace, check if there exists a namespace std in which
it does exist, and use that object.

int Quenched1(double *kFnoneTrig)
{

  std::vector<int> UGH_thickness= {2,4,6,8,10,15,20,30,40,50}; // If we
want to vary the thickness of particular layer


  int nwave=1; //number of wavlength to be scanned for
  int lamda[nwave];
  int startwavelength=355;
  //Output variable
  double EQE[nwave];
  double current[nwave];

  double etaD[nwave]; // Diffusion Efficiency
  double etaA[nwave];
  double etaT[nwave]; // Transport Efficiency

  double timer[nwave];
  double intensity_factor=3.320;
  int thickness=0;
  int global=0;
  thickness=UGH_thickness.size();
 // thickness=9;
```

```
  //
  for(int l=0;l<thickness;l++)
  {


    for (int wavelength=0; wavelength<nwave;wavelength++)
    {

      // Input variables

      clock_t tStart = clock(); //Returns the processor time consumed
by the program

      //No of material layer
      const int nlayer=4; // Number of layer in the structure
      double a=UGH_thickness[l];
      double materialthickness[nlayer]={5,a,2,3}; // Thickness of each
layer

      double totalmaterial_thickness=0;

      for(int i=0;i<nlayer;i++)
      {

totalmaterial_thickness=totalmaterial_thickness+materialthickness[i];
      }

      double binthickness[nlayer]={1,1,1,1}; //size of bins


      int numbins[nlayer];// Number of bins in each layer

      int totalbins=0;//total number of bins

      for(int i=0;i<nlayer;i++)
      {
        numbins[i]=floor(materialthickness[i]/binthickness[i]);
        totalbins=totalbins+numbins[i];
        cout<<"\n"<<numbins[i];
      }
      cout<<"totalbins"<<totalbins<<endl;

      MTRand_closed mt(time(NULL)); // random number generator taking
the current time as seed
      //srand(time(NULL));

      //other device parameters
      double pi=3.14159;
      double devicearea = pow(1E-3,2)*pi;
```

```
      // Wavelength to be scanned for
      lamda[wavelength]=startwavelength+wavelength;// increment by one
at each wavelength loop
      current[wavelength]=0;
      cout<<" start wavelength"<<" "<<lamda[wavelength]<<"\n";

      double ndisoc=0; // number of dissociated excitons
      double ninjected=0;
      double lifetime[nlayer]={1E-9,1E-9,1E-9,1E-9};// exciton lifetime
in each layer



      /*Ro[0][0]=2; // Self Foster radius of layer 1
      Ro[0][1]=3.27; //Foster radius between layer 1 and layer 2
      Ro[0][2]=3.27; //Foster radius between layer 1 and layer 3
      Ro[0][3]=3.27; // Self Foster radius of layer 1 and layer 4
      Ro[0][4]=3.27; //Foster radius between layer 1 and layer 5
      Ro[0][5]=3.27; //Foster radius between layer 1 and layer 6
      Ro[0][6]=3.212; //Foster radius between layer 1 and layer 7th


      Ro[1][0]=0; // Foster radius between layer 2 and layer 1
      Ro[1][1]=1.51; //Foster radius between layer 2 and layer 2
      Ro[1][2]=1.51; //Foster radius between layer 2 and layer 3
      Ro[1][3]=1.51; // Self Foster radius of layer 2 and layer 4
      Ro[1][4]=1.51; //Foster radius between layer 2 and layer 5
      Ro[1][5]=1.51; //Foster radius between layer 2 and layer 6
      Ro[1][6]=2.78; //Foster radius between layer 2 and layer 7th


      Ro[2][0]=0; // Foster radius between layer 3 and layer 1
      Ro[2][1]=1.51; //Foster radius between layer 3 and layer 2
      Ro[2][2]=1.51; //Foster radius between layer 3 and layer 3
      Ro[2][3]=1.51; // Self Foster radius of layer 3 and layer 4
      Ro[2][4]=1.51; //Foster radius between layer 3 and layer 5
      Ro[2][5]=1.51; //Foster radius between layer 3 and layer 6
      Ro[2][6]=2.78; //Foster radius between layer 3 and layer 7th

      Ro[3][0]=0; // Foster radius between layer 4 and layer 1
      Ro[3][1]=1.51; //Foster radius between layer 4 and layer 2
      Ro[3][2]=1.51; //Foster radius between layer 4 and layer 3
      Ro[3][3]=1.51; // Self Foster radius of layer 4 and layer 4
      Ro[3][4]=1.51; //Foster radius between layer 4 and layer 5
      Ro[3][5]=1.51; //Foster radius between layer 4 and layer 6
      Ro[3][6]=2.78; //Foster radius between layer 4 and layer 7th
```

```
Ro[4][0]=0; // Foster radius between layer 5 and layer 1
Ro[4][1]=1.51; //Foster radius between layer 5 and layer 2
Ro[4][2]=1.51; //Foster radius between layer 5 and layer 3
Ro[4][3]=1.51; // Self Foster radius of layer 5 and layer 4
Ro[4][4]=1.51; //Foster radius between layer 5 and layer 5
Ro[4][5]=1.51; //Foster radius between layer 5 and layer 6
Ro[4][6]=2.78; //Foster radius between layer 5 and layer 7th

Ro[5][0]=0; // Foster radius between layer 6 and layer 1
Ro[5][1]=1.51; //Foster radius between layer 6 and layer 2
Ro[5][2]=1.51; //Foster radius between layer 6 and layer 3
Ro[5][3]=1.51; // Self Foster radius of layer 6 and layer 4
Ro[5][4]=1.51; //Foster radius between layer 6 and layer 5
Ro[5][5]=1.51; //Foster radius between layer 6 and layer 6
Ro[5][6]=2.78; //Foster radius between layer 6 and layer 7th

Ro[6][0]=0; // Foster radius between layer 7 and layer 1
Ro[6][1]=0; //Foster radius between layer 7 and layer 2
Ro[6][2]=0; //Foster radius between layer 7 and layer 3
Ro[6][3]=0; // Self Foster radius of layer 7 and layer 4
Ro[6][4]=0; //Foster radius between layer 7 and layer 5
Ro[6][5]=0; //Foster radius between layer 7 and layer 6
Ro[6][6]=0; //Foster radius between layer 7 and layer 7th */

double Ld[nlayer]={5, kFnoneTrig[0],kFnoneTrig[0], 5};
double KR[nlayer];

for(int j=0;j<nlayer;j++)
{
  KR[j]=(pow(Ld[j],2)/lifetime[j]/pow(binthickness[j],2));
}
//KR[1]=(pow(Ld[1],2)/lifetime[0]/pow(binthickness[1],2));
//Assigning Forster Radius between layers
double Ro[nlayer][nlayer];
//Assymetry factor

Ro[0][0]=KR[0]; // Self Foster radius of layer 1
Ro[0][1]=KR[0]; //Foster radius between layer 1 and layer 2
Ro[0][2]=KR[0]*1; //Foster radius between layer 1 and layer 3
Ro[0][3]=KR[0]*0; // Self Foster radius of layer 1 and layer 4
/* Ro[0][4]=KR[0]*1; //Foster radius between layer 1 and layer 5
Ro[0][5]=KR[0]*1; //Foster radius between layer 1 and layer 6
Ro[0][6]=0; //Foster radius between layer 1 and layer 7th
*/


Ro[1][0]=KR[1]*0; // Foster radius between layer 2 and layer 1
Ro[1][1]=KR[1]*1; //Foster radius between layer 2 and layer 2
Ro[1][2]=KR[1]*1; //Foster radius between layer 2 and layer 3
Ro[1][3]=KR[1]*0; // Self Foster radius of layer 2 and layer 4
```

```
      /* Ro[1][4]=KR[1]*1; //Foster radius between layer 2 and layer 5
      Ro[1][5]=KR[1]*1; //Foster radius between layer 2 and layer 6
      Ro[1][6]=KR[1]*1; //Foster radius between layer 2 and layer 7th
      */

      Ro[2][0]=0; // Foster radius between layer 3 and layer 1
      Ro[2][1]=KR[2]; //Foster radius between layer 3 and layer 2
      Ro[2][2]=KR[2]; //Foster radius between layer 3 and layer 3
       Ro[2][3]=KR[2]*kFnoneTrig[1]; // Self Foster radius of layer 3
and layer 4
      /* Ro[2][4]=0; //Foster radius between layer 3 and layer 5
      Ro[2][5]=0; //Foster radius between layer 3 and layer 6
      Ro[2][6]=0; //Foster radius between layer 3 and layer 7th
      */
       Ro[3][0]=0; // Foster radius between layer 4 and layer 1
      Ro[3][1]=0; //Foster radius between layer 4 and layer 2
      Ro[3][2]=0; //Foster radius between layer 4 and layer 3
      Ro[3][3]=0; // Self Foster radius of layer 4 and layer 4
      //Ro[3][4]=0; //Foster radius between layer 4 and layer 5
      /* Ro[3][5]=0; //Foster radius between layer 4 and layer 6
      Ro[3][6]=0; //Foster radius between layer 4 and layer 7th

      Ro[4][0]=0; // Foster radius between layer 5 and layer 1
      Ro[4][1]=KR[4]*0; //Foster radius between layer 5 and layer 2
      Ro[4][2]=KR[4]*0; //Foster radius between layer 5 and layer 3
      Ro[4][3]=KR[4]*0; // Self Foster radius of layer 5 and layer 4
      Ro[4][4]=KR[4]*0; //Foster radius between layer 5 and layer 5
      Ro[4][5]=KR[4]*0; //oster radius between layer 5 and layer 6
      Ro[4][6]=KR[4]*0.275; //Foster radius between layer 5 and layer
7th

      Ro[5][0]=0; // Foster radius between layer 6 and layer 1
      Ro[5][1]=KR[5]*1; //Foster radius between layer 6 and layer 2
      Ro[5][2]=KR[5]*1; //Foster radius between layer 6 and layer 3
      Ro[5][3]=KR[5]*1; // Self Foster radius of layer 6 and layer 4
      Ro[5][4]=KR[5]*1; //Foster radius between layer 6 and layer 5
      Ro[5][5]=KR[5]; //Foster radius between layer 6 and layer 6
      Ro[5][6]=KR[5]*0.275; //Foster radius between layer 6 and layer
7th

      Ro[6][0]=0; // Foster radius between layer 7 and layer 1
      Ro[6][1]=0; //Foster radius between layer 7 and layer 2
      Ro[6][2]=0; //Foster radius between layer 7 and layer 3
      Ro[6][3]=0; // Self Foster radius of layer 7 and layer 4
      Ro[6][4]=0; //Foster radius between layer 7 and layer 5
      Ro[6][5]=0; //Foster radius between layer 7 and layer 6
      Ro[6][6]=KR[6]; //Foster radius between layer 7 and layer 7th */


      //Assigning molecular density of each layer
      double rho[nlayer];
```

```
      rho[0]=1.19;
      rho[1]=1.37;
      rho[2]=1.37;
      rho[3]=1.37;
      /* rho[4]=1.37;
      rho[5]=1.37;
      rho[6]=0.14;*/

      double K[nlayer][nlayer]; // Rate between layers



      for (int i=0;i<nlayer;i++)
      {
        for(int j=0;j<nlayer;j++)
        {
          //K[i][j]=(pow(Ro[i][j],6)*rho[j]*(pi/2))/(lifetime[i]);
          K[i][j]=Ro[i][j];
          // cout<<K[i][j]<<" ";
        }

      }




      double goaltime=1E-7;// Total time for all events in the material

      double group=1;// Number of excitons to be transferred in each
step

      double absfactor=(lamda[wavelength])/(1.986*1e-16); // factor
used for calculation of generation rate in a material
      cout<<" absolute factor"<<" "<<absfactor<<endl;

//////////////////////////////////////////////////////////////////////
//////////

      // Reading solar spectrum factor from the file
      /// double solarspectrum[nwave];
      // solarspectrum[0]=1.37; //for lamda=590nm
      // ifstream ss;

//////////////////////////////////////////////////////////////////////
/////////


      //Assigning positions to each bin
```

```
      double binx[totalbins+1]; // variable for keeping track of
position of bins
      int c1,c2,c4;
      double c3;
      c1=0;c2=0;c3=0;c4=numbins[0];
      binx[0]=binthickness[0];
      for(int i=0; i<nlayer;i++)

      { c1=c1+numbins[i];
        for(int j=c2; j<c1;j++)
        {
          if(j==c4)
          {
            binx[j]=c3+(binthickness[i-1]+binthickness[i])/4;
            c3=c3+binthickness[i];
            c4=c4+numbins[i];
            cout<<"\n"<<binx[j];
          }
          else
          {
            binx[j]=c3+(binthickness[i])/2; // filling bins from the
last(bin2)
            c3=c3+binthickness[i];
            cout<<"\n"<<binx[j];
          }
        }
        c2=c2+numbins[i];

      }



      binx[totalbins]=c3+binthickness[nlayer-1]/2;

      //cout<<"\n"<<binx[j];




////////////////////////////////////////////////////////////////////////
/////////



      // Energy absorption factors
      double x[totalbins+1]; // variable pointng to position in
generation file
```

```
      double Q[totalbins+1]; // variable pointing to energy absorbed in
generation file
      double factor=0;

      //Loading Q from file
      ifstream fp_in;//input stream class to operate on files
      fp_in.open("/Users/Deepesh/Google Drive/Simulations/KMC
Simulations/KMC model for triplet transport efficiency/KMC model for
triplet transport efficiency/Generation_bottom_quenched/GenerationQ"+
std::to_string(UGH_thickness[l]) +"nm.txt");




      //   if(fp_in.is_open())
      //    {

      //Return to the beginning of the input file stream
      // fp_in.clear(); // set error state flag at the beginning of
file
      //fp_in.seekg(0); // sets the position of the next character to
be extracted from the input stream

      int length=0;
      int i=0;


      while(fp_in.good()!=0)
      {

        fp_in>>factor;
        if(factor==binx[i])
        {
          fp_in>>factor;
          Q[i]=factor;
          x[i]=binx[i];
          cout<<binx[i]<<" "<<factor<<"\n";
          length++;
          i++;

        }


      }
      fp_in.close();
      //else
       //  { cout<<"unable to open"<<endl;
        //   return 0;
         //}
```

```
      //Total energy absorbed
      double energyabsorbed[nwave];
      energyabsorbed[0]=0;
      for(int i=1; i<=length;i++)
      {
        energyabsorbed[wavelength]=energyabsorbed[wavelength]+
Q[i]*binthickness[0]*1e-9;
      }
      cout<<" Energy absorbed"<<" "<<energyabsorbed[wavelength]<<endl;


////////////////////////////////////////////////////////////////////////
/////////////////////////

////////////////////////////////////////////////////////////////////////
//////////////////

////////////////////////////////////////////////////////////////////////
//////////////////
      //Building overall rate matrix

      double R[totalbins+2][totalbins]; // Rate matrix

      //Fill G from Q
      c1=0;
      c2=0;
      for(int i=0; i<nlayer;i++)
      {  c1=c1+numbins[i];
        for(int j=c2;j<c1;j++)
        {
          R[0][j] = absfactor*Q[j]*devicearea*binthickness[i]*1e-9;

        }
        c2=c2+numbins[i];
      }

      cout<<endl;



      //Fill Lifetime

      c1=0;c2=0;
      for(int i=0; i<nlayer;i++)
      {  c1=c1+numbins[i];
        for(int j=c2;j<c1;j++)
        {
          R[1][j] = 1/lifetime[i];
```

```
  }
  c2=c2+numbins[i];
}
```

```
//Fill kFs /Energy transfer rates

int j=0;
c1=0;c2=0;c4=numbins[0];

for(int i=0; i<nlayer;i++)
{
  c1=c1+numbins[i];

  for(j=c2;j<c1;j++)
  {  int d=0; int e=0;
    for (int f=0; f<nlayer;f++)
    {
      d=d+numbins[f];

      for(int k=e+2; k<d+2;k++)
      {
        if(k>j+1)
        {
          R[k][j]=K[i][f]*pow((k-j-2),-4);

        }

        else
        {
          R[k][j]=K[i][f]*pow((j-k+2),-4);

        }

      }
      e=e+numbins[f];

    }

  }
```

```
        c2=c2+numbins[i];
      }

      for(int i = 2; i <totalbins+2; i++)
      {

        R[i][i-2] = 0;

      }

      for(int i = 0; i <= 1; i++)
      {
        for(int j=0; j<totalbins; j++)
        {
          cout << setw(7) << setprecision(4) << scientific << R[i][j]
<< "\t";
        }
        cout << endl<<"\n";
      }

      for(int i = 2; i <totalbins+2; i++)
      {
        for(int j=0; j<totalbins; j++)
        {
          cout << setw(7) << setprecision(4) << scientific << R[i][j]
<< "\t";
        }
        cout << endl<<"\n";
      }


////////////////////////////////////////////////////////////////////////
//////////////////////////////////////////////////////
      //


      // output of the data


////////////////////////////////////////////////////////////////////////
//////////////////////////////////////////////////////


      //Inital value of exciton densities ..reading from the file
      //Intitalize n
      int nflag=1;
      double n[totalbins+1];
      ifstream fileID;
      if (nflag== 1)
      {
```

```
        fileID.open("/Users/Deepesh/Google Drive/Simulations/KMC
Simulations/KMC model for triplet transport efficiency/KMC model for
triplet transport efficiency/initial_n.txt");

        if(fileID.is_open())

        {
          //while (fileID.good()!=0)
          {
            for(int i=0;i<totalbins;i++)
            { fileID>>n[i];
              // cout<<"\n"<<n[i]<<" ";

            }


          }


          fileID.close();

        } else
        {cout<<"unable to open file";
          return 0;
        }

      }

      //n[totalbins-1]=0;

      // case 2 fill each bin with equal number of excitons initially
      if (nflag == 0)
      {
        //Initalize n
        for (int i=0; i<totalbins; i++)
        {
          n[i] = 100;
          //cout<<n[i]<<"\t";
        }
        // cout<<endl;
        // n[totalbins] = 0;
      }
      //n[totalbins-1]=0;

////////////////////////////////////////////////////////////////////////
//////////////////////////////////////////////////////
```

```
//////////////////////////////////////////////////////////////////////////
////////////////////

//////////////////////////////////////////////////////////////////////////
////////////////////

//////////////////////////////////////////////////////////////////////////
////////////////////



      //Start of iterations
      int flag=0;
      EQE[wavelength]=0;
      timer[wavelength]=0;
      double NR[totalbins+2][totalbins];
      double cumsumacross[totalbins];
      double cumsumdown[totalbins+2][totalbins];
      double random1=0;
      double random2=0;
      // int timerloop=0;
      int iterations = 0, iterationsloop = 0; // number of iteration
      double disocrate[2000][3];
      double EQEcheck=0.001;
      int counter_gen=0; // Count for total generation event

      int counter_recomb=0; //count for total recombination event

      int counter_forward=0; //count for total forward energy transfer
event

      int counter_backward=0; //count for total Backward energy
transfer event



      //counter for different events
      double counter_event[nlayer+2][nlayer];



      int niteration=0;
      int z=1;
      ndisoc=0;
      ninjected=0;
```

```
      while (flag == 0)
      {
        counter_gen=0; // Count for total generation event

        counter_recomb=0; //count for total recombination event

        counter_forward=0; //count for total forward energy transfer
event

        counter_backward=0; //count for total Backward energy transfer
event

        ndisoc=0;
        ninjected=0;

        // Counter for Generation event in each layer
        for(int i=0; i<nlayer;i++)
        {
          counter_event[0][i]=0;//Generation in the ith layer
        }

        // Counter for Recombination event in each layer
        for(int i=0; i<nlayer;i++)
        {
          counter_event[1][i]=0;//Recombination in the ith layer
        }



        //Counter for excitons from (i-2) th layer to other layers
        for(int i=2;i<nlayer+2;i++)
        {
          for(int j=0; j<nlayer;j++)
          {
            counter_event[i][j]=0;//Energy transfer from the j th layer
to (i-2) layer
          }

        }




        //NR Matrix
        for(int i = 0; i<totalbins; i++)
        {
          NR[0][i] = R[0][i]; // Assinging the generation rate data to
NR matrix
        }
```

```
        for (int i = 1; i<totalbins+2; i++)
        {
          for(int j = 1; j<totalbins; j++)
          {
            NR[i][j] = n[j]*R[i][j]; // Assinging other rates to NR
matrix

          }

        }


        //Cumulative sum matrix
        c3=0;
        for(int i=0;i<totalbins;i++)
        {
          cumsumdown[0][i] = NR[0][i];
          for (int j = 1; j<=totalbins+1; j++)
          {
            cumsumdown[j][i] = NR[j][i]+cumsumdown[j-1][i];
          }
          // cumsumacross[i] = cumsumdown[5][i]+c3;
          // c3=c3+cumsumacross[i];
          //cout<<cumsumacross[i]<<"  ";

        }

        // cumsumacross[i] = cumsumdown[5][i]+c3;
        // c3=c3+cumsumacross[i];




        cumsumacross[0]=cumsumdown[totalbins+1][0];

        for(int i=1; i<totalbins;i++)
        {
          cumsumacross[i]=cumsumdown[totalbins+1][i]+cumsumacross[i-1];

          //cout<<cumsumacross[i]<<"  ";
        }

        //cout<<cumsumacross[i]<<"  ";

        //Begin Iterations
        while (timer[wavelength] < goaltime)
```

```
        {



          //Generate First Random Number to choose bin

          random1 = mt()*cumsumacross[totalbins-1];
          //random1=(double (rand())/RAND_MAX)*cumsumacross[totalbins-
1];
          int k = 0;
          while (random1>cumsumacross[k])
          {
            k++;
          }

          random2 = mt()*cumsumdown[totalbins+1][k];
          //random2=(double
(rand())/RAND_MAX)*cumsumdown[totalbins+1][k];
          int o = 0;
          while (random2>cumsumdown[o][k])
          {
            o++;
          }


          //        ofstream file;
          //
file.open("/Users/deepeshrai/Documents/Modelling/Super_diffusion/Super_
diffusion/random.txt",ios::app);
          //        file<< random1<< "\t" << random2<< endl;
          //        //cout << EQE[i] << "\t" << etaD[i] << "\t" <<
etaA[i] << endl;
          //        file.close();
          //



////////////////////////////////////////////////////////////////////
/
          // Carrying of event


         if(k==totalbins)
          { cout<<" Need some correction"<<endl;
            cout<<"total bins \t"<<totalbins<<endl;
            cout<<cumsumacross[totalbins]<<"
"<<cumsumacross[totalbins-1]<<endl;
```

```
}


if (o==0)
{
  n[k] = n[k] + group;
  counter_gen = counter_gen + group;

  int d=0;
  for(int i=0;i<nlayer;i++)
  {  d=d+numbins[i];

    if(k<d)
    {
      counter_event[0][i]=counter_event[0][i]+group;
      i=nlayer; // To come out from the loop
    }


  }


}



if (o==1)
{
  n[k] = n[k] - group;
  counter_recomb = counter_recomb + group;
  int d=0;

  for(int i=0;i<nlayer;i++)
  {  d=d+numbins[i];

    if(k<d)
    {
      counter_event[1][i]=counter_event[1][i]+group;
      i=nlayer; // To come out from the loop
    }


  }
}

if(o>=2)
{
```

```
            if(o<k+2)
            { counter_backward=counter_backward+1;
              n[k]=n[k]-group;
              n[o-2]=n[o-2]+group;

              int d=0;

              for(int i=0;i<nlayer;i++)
              {  d=d+numbins[i];

                if(k<d)
                {
                  int e=0;

                  for(int j=0;j<nlayer;j++)
                  {  e=e+numbins[j];

                    if(o-2<e)
                    {
counter_event[j+2][i]=counter_event[j+2][i]+group;
                      j=nlayer; // To come out from the loop
                    }


                  }


                  i=nlayer; // To come out from the loop




                }


              }

            }
            else
            { counter_forward=counter_forward+1;
              n[k]=n[k]-group;
              n[o-2]=n[o-2]+group;

              int d=0;

              for(int i=0;i<nlayer;i++)
              {  d=d+numbins[i];
```

```
                if(k<d)
                {
                  int e=0;

                  for(int j=0;j<nlayer;j++)
                  {  e=e+numbins[j];

                    if(o-2<e)
                    {

counter_event[j+2][i]=counter_event[j+2][i]+group;
                      j=nlayer; // To come out from the loop
                    }


                  }


                  i=nlayer; // To come out from the loop




                }


              }



            }


          }
          //cout<<k<<" "<<o<<" "<<endl;

          //Update dataprob, cumsumdown, and cumsum across


          for(int j = 1; j<totalbins+2; j++)
          {
            NR[j][k] = n[k]*R[j][k];
            cumsumdown[j][k]=NR[j][k]+cumsumdown[j-1][k];

          }
```

```
            if (o>=2)
            {
              for(int j = 1; j<totalbins+2; j++)
              {
                NR[j][o-2] = n[o-2]*R[j][o-2];
                cumsumdown[j][o-2]=NR[j][o-2]+cumsumdown[j-1][o-2];
              }


            }


            //Cumulative sum matrix




            cumsumacross[0]=cumsumdown[totalbins+1][0];



            for(int i=1; i<totalbins;i++)
            {
              cumsumacross[i]=cumsumdown[totalbins+1][i]+cumsumacross[i-
1];
             // cout<<n[i]<<" ";
            }




            //Determine Timestep
            timer[wavelength] = timer[wavelength] -
log(mt())/cumsumacross[totalbins-1];
            //timer[wavelength]=timer[wavelength]-log((double
(rand())/RAND_MAX))/cumsumacross[totalbins-1];


          /* if (n[k]<0)

            {


              cout << "Ran out of Excitons!" << endl;
              ofstream nexciton;//input stream class to operate on files
              nexciton.open("/Users/Deepesh/Google Drive/Simulations/KMC
Simulations/Monte_Carlo_simulation_non_nearest/3 Layers/3
Layers/nexciton/n" + std::to_string(z)+ ".txt");
```

```
    for (int i=0;i<=totalbins;i++)
    { nexciton<<n[i]<<endl;


    }
    niteration=niteration+1000;
    z++;


    flag=1;

    return 0;
  } */


  if( iterations == 1000000)
  {
    disocrate[iterationsloop][0] = (iterationsloop+1)*1000000;
    disocrate[iterationsloop][1] = timer[wavelength];
    disocrate[iterationsloop][2] = ndisoc/timer[wavelength];
    iterations = 0;
    iterationsloop = iterationsloop + 1;
  }
  else
  {
    iterations = iterations + 1;
  }

  if( iterationsloop==300)
  {
    flag=1;

  }







}

for(int i=0;i<nlayer-1;i++)
{
  ndisoc=ndisoc+counter_event[nlayer+1][i];


}
for(int i=1;i<nlayer;i++)
{
```

```
          ninjected=ninjected+counter_event[i+2][0];


        }


        EQE[wavelength] =
100*(ndisoc/(intensity_factor*devicearea*timer[wavelength]*absfactor));

        if (pow(pow(EQE[wavelength]-EQEcheck,2),.5) < 0.1)
        {
          flag = 1;
        }


        else
        {   EQEcheck = EQE[wavelength];
          iterations = 0;
          iterationsloop = 0;
          timer[wavelength] = 0;
          ndisoc=0;
          ninjected=0;
          counter_gen=0;
          global++;
        }


      }

      current[wavelength] = ndisoc*(1.6e-
19)/timer[wavelength]/devicearea/10;
      cout<<"device area"<<" "<<devicearea<<endl;
      EQE[wavelength] =
100*(ndisoc/(intensity_factor*devicearea*timer[wavelength]*absfactor));
      etaD[wavelength]=(ndisoc/counter_gen)*100 ;
      etaT[wavelength]=(ndisoc/ninjected)*100;

etaA[wavelength]=100*(counter_gen/(intensity_factor*devicearea*timer[wa
velength]*absfactor));

      cout << "Current = "<<" "<<current[wavelength]<< " mA/cm^2" <<
endl;
      cout << "EQE = " << EQE[wavelength] << " %" << endl;
      cout << "Diffusion Efficiency = " << etaD[wavelength]<< " %" <<
endl;
      cout << "Absorption Efficiency = " << etaA[wavelength] << " %" <<
endl;
      cout << "Transport Efficiency = " << etaT[wavelength]<< " %" <<
endl;
      cout << "Excitons Dissociated"<<" "<<"="<<" "<<ndisoc << endl;
```

```
      cout <<"Excitonds Generated"<<" "<<"="<<" "<<counter_gen << endl;
      cout <<"Excitonds Injected"<<" "<<"="<<" "<<ninjected<< endl;
      cout<<"Time"<<" "<<timer[wavelength]<<endl;
      cout<<"Iteration loop"<<iterationsloop<<endl;
      cout<<"Iterations"<<(iterations*iterationsloop+iterations)<<endl;
      cout<<"Number of Generation events"<<" "<<counter_gen<<endl;
      cout<<"Number of Recombination events"<<"
"<<counter_recomb<<endl;
      cout<<"Number of Forward energy Transfer event"<<"
"<<counter_forward<<endl;
      cout<<"Number of backward energy Transfer event"<<"
"<<counter_backward<<endl;

      //cout<<"Number of Forster energy Transfer event"<<"
"<<counter_event[5]<<endl;
      //cout<<"Number of other transfer events"<<"
"<<counter_event[4]<<endl;

      ofstream TE;
      TE.open("/Users/Deepesh/Google Drive/Simulations/KMC
Simulations/KMC model for triplet transport efficiency/KMC model for
triplet transport efficiency/Absolute_TE.txt",ios::app);
      TE<<etaT[wavelength]<<" ";
      TE.close();

      printf("Time taken by program %f seconds\n", (double)(clock() -
tStart)/CLOCKS_PER_SEC); //time taken by program to run
      //CLOCKS_PER_SEC-->This macro expands to an expression
representing the number of clockticks per second.


////////////////////////////////////////////////////////////////////////
/////////////////
      ofstream nfinal; //Stream class to operate on strings.
      nfinal.open("/Users/Deepesh/Google Drive/Simulations/KMC
Simulations/KMC model for triplet transport efficiency/KMC model for
triplet transport efficiency/Results/nlayers_Q.txt");
      for (int i=0; i <totalbins; i++)
      {
        nfinal << n[i] << endl; // updating the new exciton density
      }
      nfinal.close();



////////////////////////////////////////////////////////////////////////
////

      // ofstream file;
```

```
      //file.open("/Users/Deepesh/Google Drive/Documents/C545T/3-
Layered /4 layers/4 layers/EQE.txt",ios::app);
      //for (int i=0; i <nwave; i++)
      //{
      // file<< lamda[i]<<"\t"<<nlayer<<"\t"<<EQE[i] << "\t" << etaD[i]
<< "\t" << etaA[i] <<"\t"<<KFij[0]<<"\t Wavelength
\t"<<startwavelength<<endl;
      //cout << EQE[i] << "\t" << etaD[i] << "\t" << etaA[i] << endl;
      //}
      //file.close();


    }
  }
 return 0;
}


/* The gateway function */
/*
void mexFunction(
        int     nlhs,
        mxArray   *plhs[],
        int     nrhs,
        const mxArray *prhs[]
        )
{
  /* variable declarations here */
 /* double *foster;

  /* create a pointer to the real data in the input matrix */
  //foster = mxGetScalar(prhs[0]);
 /* foster=mxGetPr(prhs[0]);


  /* get dimensions of the input matrix */
  // ncols = mxGetN(prhs[0]);


 /* Quenched1(foster);
  /* Destroy array */
  // mxDestroyArray(foster);
//}
int main(int argc, const char * argv[]) {
  double Ro[2];
  Ro[0]=10;
  //Ro[1]=2.379*1.495;
 Ro[1]=10;

  //Ro[3]=0.628*0.42;
```

```
  Quenched1(Ro);

  return 0;
}
```